Proximal-to-Distal Energy Transfer in the Golf Swing

Mechanisms, Evidence, and Counterfactual Tests of Distal-Handoff Timing

Dieter Olson

2026-08-08

Abstract

Proximal-to-distal (P→D) sequencing — the ordered peaking of pelvis, thorax, arm, and club rotational speeds — is the most widely reported organizing principle of the golf downswing, and it is usually read as evidence that mechanical energy should be passed outward along the kinetic chain as early and as completely as possible. This study reviews the mechanics and the empirical literature behind that reading and asks the sharper question: *when* during the downswing should the P→D transfer occur? Double-pendulum mechanics, delayed-release simulation, optimal control, and the segmental kinetic-energy literature motivate a model hypothesis in which distal actuation is delayed while proximal speed develops and the distal handoff accelerates later. We formalize this delayed-actuation hypothesis in the language of zero-torque counterfactual (ZTCF) and zero-velocity counterfactual (ZVCF) decompositions, and test it in a reproducible two-segment golf model using an exact interaction-force decomposition, a matched-state torque-killswitch comparison, a wrist-torque timing sweep (92 torque programs), pointwise drift/control counterfactual decompositions, and Robertson-Winter style wrist-interface power accounting, all generated by committed, reproducible scripts. In this model, driving the wrist from the top produced 15.3% and 10.7% less clubhead speed than the corresponding passive-wrist programs at the two tested shoulder-torque levels, while delaying the wrist drive to the grid-selected onset produced 12.4% and 7.8% more. Of the 92 idealized commands tested, a restrain-then-drive program produced the highest speed at both shoulder-torque levels. The energy accounting shows that the selected programs move *less* energy into the club early and far more late, with negative early work by the modeled wrist actuator. That sign describes the imposed control law; it does not identify muscle action or human intent. We interpret these results against the literature and state their limitations: the primary timing estimand uses a planar 2-DOF model with a fixed hub and rigid shaft, while the later model tiers answer narrower moving-base, flexible/modal-shaft, spatial, and contact questions without supplying subject-calibrated human validation. A one-at-a-time sensitivity study spanning 13 parameter cases preserves the strategy ordering but shifts the selected onset. First-order command transitions from 20 to 50 ms also preserve the registered ordering while moving the selected program. Neither sweep is a continuous optimal-control solution or a human timing prescription. The force analysis resolves the geometric sine and cosine projections that determine whether distal centripetal and tangential forces transfer power. A separate audit of the author's prior two-hand WSCG model reconstructs all 2,801 stored samples and shows that a -19.63 N m pointwise zero-command midpoint couple is generated entirely by separated contact forces. It also distinguishes couple sign from power sign and verifies the predicted linear grip-separation and relative-orientation geometry. A matched rigid/flexible three-coordinate surrogate then separates control, momentum, gravity, joint damping, shaft elasticity, and shaft damping with closed work–energy accounting. In its reference case, flex changes delivery speed by +0.108 m/s, while gravity and joint-damping ablations are substantially larger; broad stiffness, damping, torque-cut, endpoint-window, and timestep sweeps bound the result. A forward constrained two-arm model then branches an exact same-state zero-command trajectory at 0.200 s. Its contact-force couple remains negative for the full 50 ms branch and reaches -7.43 N m; removing both grip moment arms collapses that couple exactly to zero, while timestep and projection studies bound the numerical result. A coupled extension then admits a finite-mass translating base, two constrained arms, and a two-segment compliant club in one forward KKT system. Base motion and shaft flex are endogenous; a same-state zero-command branch retains a negative force-generated couple for 50 ms, the coincident-grip control removes it exactly, and work–energy and contact-power identities close under timestep refinement. These are planar model-feasibility results, not physiological or human evidence. A separate distributed-shaft study then reuses the shared Euler–Bernoulli finite-element model to compare a first-mode reduction with a six-mode reference. Synthetic modal identification recovers its declared modulus and tip mass, mesh and work–energy gates close, and a short load pulse exposes sixty times more RMS response discrepancy than a slow pulse. This is structural verification, not equipment calibration. A subsequent planar experiment couples three transported shaft modes into the moving-base, two-hand forward solve. The current baseline reaches a 13.48% tip-deflection ratio and therefore fails its declared 5% small-deflection screen. It is retained only as an out-of-domain numerical stress test: the zero-command grip couple remains negative for about 25 ms, coincident and reversed moment-arm controls close exactly, and work–energy error decreases under timestep refinement. These checks support numerical coupling and qualitative force-couple geometry, not quantitative shaft response. A common-observable model ladder then carries reference-explicit force,

couple, velocity, angular velocity, and power through a third coordinate, prescribed hub motion, two-hand constraint geometry, and proper 3-D frame transformations. A reduced full-body extension executes nonplanar common-state inverse dynamics through MuJoCo and an independent Lagrange–Christoffel formulation. Across 20 generalized coordinates and 61 states, the maximum relative discrepancy is 2.14×10^{-11}; reversing the hand moment arm reverses a -4.32 N m force-generated couple, and coincident hands remove it exactly. Because contact loads are prescribed, passive spatial contact remains inconclusive at that tier. A six-profile subject-scaled audit then shows why local rank is insufficient: its prescribed anatomical hand points miss the declared grips by 0.171–0.616 m even though every local contact Jacobian has rank six. A bounded inverse-kinematics continuation then closes all 234 registered subject-scaled configurations while holding the club pose fixed; every sample retains rank six, stays inside broad reduced-model engineering limits, and passes a coarse nonadjacent-body bounding-sphere screen. This establishes reduced-tree geometric feasibility, not anatomical validity, contact force, passivity, timing benefit, or human strategy. All 234 closed states now enter one canonical forward-state contract with preserved position and velocity closure and zero interface preload. Native MuJoCo and Pinocchio then pass trajectory, wrench, and energy comparisons for a 54-case, 4 ms spanning initialization audit. This closes a coordinate and numerical-transport gap, not the full-horizon articulated-contact gate. A preregistered extension then advances the same 54 states through 4, 10, 25, and 50 ms under nominal conditions and nine one-factor adverse or null branches. All 2,160 horizon cases pass the declared cross-engine and work–energy gates; no failure is observed through 50 ms. The result is right-censored at that horizon and remains a reduced hand-carriage result. A subsequent reduced forward-contact experiment independently integrates MuJoCo and Pinocchio with two finite-mass hand carriages, paired compliant interfaces, and no direct club actuation. Its exact same-state driver-killswitch branch retains a negative swing-normal contact couple for 37.5 ms; coincident and reversed-moment-arm controls close exactly, trajectory and wrench gates pass, and work–energy residual decreases under timestep refinement. This supports a reduced spatial mechanism, not anatomical arms, muscle coordination, human strategy, or equipment calibration. A coupled uncertainty and control experiment then varies 12 inputs simultaneously, audits structural and practical identifiability, and compares eight preselected delayed-command programs on separate training and held-out ensembles. The net planar wrench leaves one individual-hand-force mode unidentified, the six summary observables cannot identify the full 12-parameter vector, and all eight programs are nondominated on held-out samples. An early opposing command improves lower-tail speed relative to late drive but worsens the planar face/path proxy, rejecting a universal optimum and any direct physiological interpretation. A preregistered experimental protocol then fixes synchronized motion, bilateral hand-wrench, club, ground-reaction, launch, and activation measurements; participant-level holdout; filtering; calibration; residuals; identity protection; and four outcome falsifiers. Its synthetic dry run qualifies only the fail-closed pipeline. No human outcome is analyzed, and every experimental prediction remains untested. A separate hand-path attribution study evaluates the MacKenzie force-work-per-path-length estimand in an impact-truncated double pendulum, a forward-simulated one-arm model, and a mechanically closed two-arm local sweep. Drift supplies 101.2% and 103.5% of signed hand-path force work in the two forward cases because the contemporaneous control contribution is slightly opposing; in the two-arm sweep, drift and control instead cancel with an index of 0.962. Joint- and time-resolved impulse, power, work, force-vector, and common/differential-mode results show why a large net hand-path force is a mechanical transfer observable rather than a direct measure of biological effort. A final matched-task allocation experiment separates direct wrist moments from the moment of bilateral hand forces at identical club states. Internal demands vary even when club-moment closure is exact. A separate dead-zone transmission model predicts that preserving each channel's loaded direction avoids a reversal gap, whereas reversing both modeled channels crosses zero transmission. These conditional predictions do not identify scapular action or establish a preferred human technique. A constrained-contact extension then defines frame-explicit configuration, velocity, control, and external-load contributions to reaction force and fails closed when contact allocation is nonunique. In the fixed-support double-pendulum benchmark, pointwise ZTCF predicts the modeled support-reaction waveform with componentwise R-squared values of 0.871 and 0.814 but retains large amplitude error; opposing control also makes the vertical ZTCF impulse exceed the total. This benchmark is not a bilateral human force-plate validation, and the required synchronized force-plate and whole-body kinematic experiment is specified as a falsification protocol. An advanced bridge then proves wrench–twist power invariance under proper rotations and paired reference-point transport, verifies Jacobian virtual work, and round-trips one canonical pose through the MuJoCo, Pinocchio, Drake, OpenSim, and MyoSuite coordinate adapters. The pose result is a representation check, not five-engine dynamics parity. A reduced Hill-type study demonstrates that 41 agonist–antagonist allocations can produce the same net moment while changing internal stiffness and series-energy proxies; continuous activation and series-force states make preparation history observable but do not identify anatomy or a preferred technique. A final adversarial transmission study compares clock- and state-triggered handoff under paired training and held-out perturbations. State triggering improves lower-tail delivery speed and a planar face/path proxy relative to clock timing but raises peak hand force; higher impedance changes the tradeoff, and all four registered programs remain Pareto-nondominated. A local task-Jacobian partition exposes five task-null input directions, but this is a model property rather than evidence of a neural synergy or human self-stabilization. An exact double-pendulum identifiability audit separates coefficient excitation from physical-parameter recovery. The registered synthetic trajectory excites all seven dimensionless base-coefficient directions, while the eleven-entry physical map has analytic rank seven, nullity four, and three exact nonunique parameter families. The associated Fisher screen is an oracle-kinematics lower bound only; it does not identify participant anatomy, equipment, or practical measurement performance. A bounded nonlinear follow-up then solves finite event-surface targets with exact-RK4 multiple shooting and independent replay. Both torque channels, shoulder only, and wrist only reach every registered small tangent target; the zero-authority killswitch rejects exactly the six displaced targets. Mesh, integration-step, and adverse-state controls converge, but two multistarts differ by 24.9517% in their scaled control-energy objective and fail the 5% optimality gate. The result therefore supports only local model-scenario feasibility and supplies no controller, effort, human, or coaching ranking. A global direction-aware extension then retains every event crossing under causal delay and matched state, command, and event-surface perturbations. All 6,336 registered small-stress replays preserve one positive transverse crossing, but a preregistered stress extension exposes absent and multiple crossings from 2% synthetic dimensionless stress. Channel, step-size, and horizon controls distinguish topology loss from search-window truncation. These open-loop model stresses do not estimate human variability, anatomy, fatigue, controller superiority, or a coaching strategy. A phase-resolved proximal-motion study evaluates 126 rate cases under relative-rate, absolute-rate, and exact total-kinetic-energy matching, plus 45 identical-state acceleration interventions. The large pre-impact rate trend nearly vanishes under energy matching, and increasing proximal acceleration raises interface power while reducing club angular acceleration before impact. A separate 60-program grid is more adversarial: among 26 valid impacts, release-state proximal velocity correlates negatively with impact speed and positively with negative grip work. Eight reused approximate actuator-work matches initially favor the lower-rate member but retain a load confound. A follow-on 216-program common-time screen resolves that confound: 46 independent work/load-matched pairs contain 20 favorable and 26 adverse higher-rate outcomes, with both signs retained in all nine tolerance cells. The combined result rejects proximal speed as a standalone release rule while retaining full-delivery-state and human tests as open. The resulting rotating-base, two-hand tier uses finite torso inertia, two closed arm–grip constraints, separated reactions, and a compliant distal club. Its 18-program matched- state grid finds that higher initial torso rate can accompany greater delivery speed but does not uniformly reduce braking work; exact torso, arm, and wrist killswitches are nonmonotonic. This remains a planar mechanism result. The subject-scaled articulated sequence now advances a five-fiber-per-hand grip through 50 ms and then adds passive first-mode bending and torsion under rigid, single-mode, and coupled killswitch branches. All 384 fine-grid shaft trajectories pass the registered linear-domain, work–energy, refinement, and MuJoCo–Pinocchio gates. Among 126 coupled–rigid cells matched within 5% for peak load and dissipated work, final-speed differences include 82 negative and 44 positive values. This establishes a state-dependent synthetic elastic pathway and rejects a universal shaft-speed benefit; it does not calibrate equipment or identify a human strategy. A subsequent finite-base extension adds planar ground reaction and intrinsic free moment. All 576 registered trajectories pass the declared numerical and native-engine gates, but none of 384 coupled–fixed cells meets the preregistered peak-load and total-work match. A labeled post-hoc alternative admits both speed-difference signs. The result qualifies the synthetic mechanism while leaving its isolated delivery effect unidentified. A frozen participant-held-out bilateral-wrench protocol defines the human falsifier, but no governed human outcome is available. References, analysis code, machine-readable results, and provenance are available with the document for independent inspection and reuse.

Table of contents

List of Figures

Chapter 1

Introduction

> **Scope and Evidence Categories**
>
> This document distinguishes three kinds of statement. **Empirical findings** summarize published measurements of golfers. **Model-derived findings** report deterministic simulations generated by the archived analysis code and parameter sets. **Hypotheses and interpretations** state claims that remain to be tested in higher-fidelity models or human data. The distinction matters because agreement between a simplified model and prior literature is not independent empirical confirmation.

1.1 Motivation

Subject to impact efficiency, launch angle, spin, and aerodynamic conditions, greater clubhead speed raises the available ball speed and distance. Clubhead speed has also been associated with handicap or playing standard in particular cohorts, including a 45-man sample spanning handicaps 2–27; those associations do not make it a complete measure of golf performance (Fradkin, Sherman, and Finch 2004; Hellström 2009; Hume, Keogh, and Reid 2005). The golf downswing is a widely studied example of sequenced multi-segment rotation (McPhee 2022; Dillman and Lange 1994). Under commonly used segment and angular-velocity definitions, many skilled golfers exhibit a pelvis–thorax–arm or hands–club ordering of peak speeds, often with distal speed amplification (Cheetham et al. 2008; Tinmark et al. 2010). The identified order is neither universal nor independent of coordinate, component, event, and filtering choices (Marsan et al. 2019; Lee, Ehrlich, and Cain 2026). This *kinematic sequence* resembles the broader proximal-to-distal sequencing observed in throwing and striking (Putnam 1993), but peak order alone is not a measurement of mechanical energy transfer. Treating it as such is an interpretation that has influenced applied swing descriptions (Smith et al. 2015), not an identity used in this study.

That interpretation leaves a first-order question unanswered:

> **Within a declared model or measured swing, does earlier distal actuation improve delivery, or can delayed distal actuation permit a more effective late handoff?**

For experimental contrast, the two poles are given the shorthand labels “drive early” and “retain early/release late.” These labels are not a survey of coaching doctrine, nor are model torques coaching cues. The poles imply opposite idealized torque programs and different predictions for what counterfactual decompositions of a measured swing should show. The question also connects to a long-standing thread in the modeling literature: double-pendulum analyses have argued since the 1960s that the highest clubhead speeds arise when the distal joint is *not* driven early — when release is passively or actively delayed (Cochran and Stobbs 1968; T. Jorgensen 1970; Milburn 1982; Pickering and Vickers 1999). The present study therefore tests and instruments a well-established model behavior; it does not claim novelty for the general delayed-release idea.

This study approaches the question with *counterfactual dynamics*. Two decompositions are evaluated: the **zero-torque counterfactual (ZTCF)** — the acceleration the system would exhibit at the current instant if all applied joint torques were removed, isolating what accumulated motion, gravity, and inter-segment coupling produce on their own — and the **zero-velocity counterfactual (ZVCF)** — the instantaneous acceleration at the fixed pose and retained internal state after both generalized velocity and the declared applied control are set to zero. A zero-velocity evaluation that preserves applied control is a separate, explicitly named diagnostic. Preliminary torque-removal analyses motivated the hypothesis examined throughout this document: that *restraining* the P→D handoff early in the downswing and accelerating it late may be the more effective strategy.

1.2 Research Questions

The document is organized around four questions:

- **RQ1 — Mechanism.** By what mechanical pathways does energy generated proximally reach the club, and what does each pathway imply about the *timing* of the handoff? (Section 2)
- **RQ2 — Evidence.** Where does the P→D transfer occur in measured swings, and how do skilled and less-skilled players differ — in sequence order, in magnitudes, or in transfer efficiency? (1)
- **RQ3 — Formalization.** How can "transfer early" versus "retain-early/release-late" be stated as falsifiable claims about measurable quantities, and what do the ZTCF/ZVCF counterfactuals predict under each? (Section 26)
- **RQ4 — Model test.** What does a two-link model show when the timing of the distal handoff is manipulated directly, with the energy accounting and counterfactual decompositions computed along every trajectory? (Section 28, Section 29, Section 30)

1.3 Approach and Contributions

The document makes six contributions:

1. a synthesis of the mechanics of sequenced swings, from the summation-of-speed principle through segment-interaction dynamics, parametric energy transfer, and optimal control (Section 2);
2. a methodological account of what "energy transfer" means operationally — joint power, joint-force power, segmental energy accounting, induced accelerations — and where the popular kinematic-sequence proxy fails (Section 2.5);
3. a critical review of the empirical evidence, including the directly relevant segmental kinetic-energy sequencing studies (Kenny et al. 2008; Anderson, Wright, and Stefanyshyn 2006) and the skill-level literature (1);
4. a formalization of the timing question and of the ZTCF/ZVCF counterfactual framework, including the distinction between pointwise and re-simulation counterfactuals (Section 26);
5. a **reproducible model test** on a double-pendulum golf model — 92 torque programs swept over wrist-drive onset time and profile, scored at a consistently defined impact, with pointwise drift/control decompositions and Robertson-Winter wrist-interface power accounting computed along every representative trajectory (Section 28, Section 29); and
6. a bridge from these 2-DOF results to broader tests: what the simplified model can and cannot establish, and the concrete, steps that extend the analysis to re-simulation parity, full-body engines, and motion-capture replication (Section 30, Section 32).

1.4 Reading Guide

Readers interested only in the new quantitative material can read Section 26 for the hypothesis, Section 28 for the setup, and Section 29 and Section 30 for the outcome. Readers using this document as a literature resource will find the review chapters (Section 2, 1) and the verified bibliography self-contained. Appendices document software and data availability (Section 33), reproducibility (Section 34), collect validation evidence (Section 35), and tabulate model parameters (Section 36).

Chapter 2

Mechanics of Sequenced Swings

This chapter assembles the mechanical foundations the rest of the document builds on: the dynamics formalism (Section 2.1), the summation-of-speed principle and its dynamical correction (Section 2.2), the double-pendulum tradition that made release timing an explicit variable (Section 2.3), the optimal-control literature (Section 2.4), and the operational meanings of "energy transfer" (Section 2.5).

2.1 Dynamics Formalism

Write the equation of motion of an articulated chain in standard manipulator form (Featherstone 2008):

$$M(q)\,\ddot{q} \;=\; \tau \;-\; b(q,\dot{q}), \qquad b(q,\dot{q}) \;=\; C(q,\dot{q})\,\dot{q} \;+\; g(q) \;+\; d(\dot{q}), \tag{2.1}$$

with configuration q, inertia matrix M, applied generalized torques τ, Coriolis/centripetal terms $C\dot{q}$, gravity g, and velocity-dependent dissipation d. In an articulated rigid-body model, $M(q)$ is generally configuration dependent and can contain off-diagonal terms. A generalized torque can therefore produce accelerations in coordinates other than the coordinate at which it is applied through M^{-1}; the exact pathways depend on the coordinates, inertial parameters, constraints, and instantaneous configuration. Symmetry, decoupled coordinates, or a special configuration can make a particular cross-coordinate pathway zero. This qualified coupling is the basis of induced-acceleration analysis (Zajac and Gordon 1989) and of the counterfactual decompositions of Section 26.

For the declared unconstrained manipulator model, with b independent of the current applied torque, the equation is *affine in* τ:

$$\ddot{q} = -M^{-1}b + M^{-1}\tau. \tag{2.2}$$

The accompanying tests enforce this drift–control split to numerical tolerance (Section 35). It is an exact identity for that model class, not a universal biological decomposition. Closed-loop constraints add reaction terms, contact can change mode, and muscle, tendon, or actuator states can make the mapping from neural command to generalized torque dynamic and state dependent.

2.2 The Summation-of-Speed Principle and Its Limits

An influential coaching formulation of P→D sequencing is Bunn's *summation of speed* principle: in skills demanding high end-point speed, each segment should begin its motion at the moment of peak speed of the segment proximal to it, so that distal speed is built on top of proximal speed (Bunn 1972). This is a coaching proposition, not an experimental law. Milburn applied the principle to golf with a double-pendulum analysis of the downswing and found the characteristic pattern of an initially dominant proximal (arm) rotation followed by rapid distal (club) rotation, noting that *"an initial delay in the uncocking of the wrist"* allows the arm to reach greater acceleration and the club's acceleration to be summed with the proximal segment's maximum (Milburn 1982). Note the structure of that finding: the summation principle, taken naively, prescribes *sequential initiation*; Milburn's analysis showed the benefit comes specifically from *delaying* the distal contribution.

Putnam's segment-interaction analyses gave the principle a dynamical test and exposed its limits (Putnam 1991, 1993). In a linked chain, each segment's angular acceleration depends not only on joint torques but on *motion-dependent interaction terms* — including centripetal and Coriolis terms that contain squares and products of segment angular velocities (represented within $C\dot{q}$ in Equation 2.1). The 1991 study used high-speed film from four participants performing walking, running, and kicking. It found a significant thigh–leg interaction and support for summation of segment speeds, but no support for summation of force or for a general rule that negative thigh acceleration produces positive leg acceleration (Putnam 1991). Putnam's 1993 synthesis extended the discussion to striking and throwing: distal acceleration could arise largely from motion-dependent interaction tied to proximal angular velocity, and proximal slowing could arise largely from the distal segment's motion-dependent effect. The source explicitly warned that task-dependent interaction differences must be examined before general principles are asserted (Putnam 1993).

Feltner and Dapena's 1986 inverse-dynamics study estimated resultant shoulder and elbow forces and torques in fastball pitches by eight intercollegiate pitchers (Feltner and Dapena 1986). The later two-part interaction analysis supplied the relevant decomposition: a general three-dimensional two-segment model (Feltner and Dapena 1989) and its application to the same class of pitching motion (Feltner 1989). In eight collegiate pitchers, the Part II analysis attributed rapid pre-release elbow extension primarily to the angular velocity of the upper arm and trunk rather than to elbow-extensor torque (Feltner 1989). That result is a task- and model-bounded acceleration attribution, not evidence that distal musculature is generally inactive.

Herring and Chapman obtained P→D torque onsets and beneficial late torque reversals in a sagittal three-segment throw simulation (Herring and Chapman 1992). The inputs were idealized constant joint torques switched on at varied times, with shoulder and elbow torque signs reversed instantaneously in the reversal trials. The result demonstrates a linked-system mechanism; it does not establish physiological muscle timing or the feasibility of an instantaneous human torque reversal. Two implications matter for golf. First, kinematic order does not reveal *which* torques produced it: an identical peak sequence can arise from different mixes of muscular and interaction torques. Second, the proximal deceleration observed in experts need not be an active "braking" strategy — it can be the dynamical *consequence* of the distal segment accelerating and back-reacting on the chain.

Marshall and Elliott added a task-specific measurement caution. In the tennis serve and squash forehand drive, upper-arm and forearm long-axis rotations peaked late and were important contributors to racquet-head speed (Marshall and Elliott 2000). This shows why a planar peak-ordering analysis can omit relevant three-dimensional rotations in those racquet tasks. A corresponding role for forearm rotation and wrist action in golf is a testable analogy, not a result measured by that study.

2.2.1 Foundational Sequencing Evidence Boundaries

Source	Declared Domain	Supported Finding	Boundary for This Paper
Bunn (Bunn 1972)	Coaching text	Summation-of-speed heuristic	Not an empirical validation or universal timing law
Putnam (Putnam 1991)	Four participants; walking, running, and kicking	Motion-dependent thigh–leg interaction was significant; segment-speed summation was supported	No support for summation of force or a general negative-proximal-acceleration rule

Source	Declared Domain	Supported Finding	Boundary for This Paper
Putnam (Putnam 1993)	Review and mechanics synthesis spanning kicking, striking, and throwing	Proximal angular velocity can drive distal acceleration, and distal motion can slow the proximal segment	Interaction differs across skills; task geometry must be examined before generalization
Feltner and Dapena (Feltner and Dapena 1986, 1989; Feltner 1989)	Three-dimensional pitching analysis; eight collegiate pitchers	Resultant joint loads were estimated, then angular acceleration was decomposed into torque- and motion-dependent terms	The 1986 paper alone does not provide the later decomposition; pitching attribution is not a golf or population-wide result
Herring and Chapman (Herring and Chapman 1992)	Sagittal three-segment throw simulation with constant torque inputs	P→D onsets and late P→D torque reversals improved simulated output	Idealized switches and instantaneous reversals are not muscle or neural-control evidence
Marshall and Elliott (Marshall and Elliott 2000)	Tennis serve and squash forehand drive	Long-axis rotations peaked late and contributed to racquet-head speed	Golf relevance is an analogy requiring direct three-dimensional golf measurement

These sources establish candidate mechanisms and measurement cautions. They do not make peak order a measure of energy flow, prove a universal active braking strategy, or identify one optimal golf control program.

2.3 Double-Pendulum Mechanics of the Golf Downswing

The two-lever, one-hinge model of the downswing — an "arm" link rotating about a hub, connected by a wrist hinge to a "club" link — has been the workhorse of golf mechanics since Cochran and Stobbs' *Search for the Perfect Swing* (Cochran and Stobbs 1968) and Jorgensen's dynamical analysis fitted to stroboscopic photographs of a professional swing (T. Jorgensen 1970; T. P. Jorgensen 1999); Penner's review surveys the tradition (Penner 2003). Its enduring value here is that it makes the *timing* of the P→D handoff an explicit variable (the "release": the point at which the wrist angle is allowed, or driven, to open) and exposes mechanisms by which delay can affect delivery. This lineage establishes an analytically useful reduced model, not empirical validation of a fixed hub, planar rigid shaft, or human wrist-control program. Three results anchor the analysis:

Delayed Release Increases Clubhead Speed. Pickering and Vickers, sweeping release angles in a driven double-pendulum model, found clubhead velocity at impact increases as release is delayed — the classical "late hit" (Pickering and Vickers 1999). This result supports late release for the particular fixed-hub, rigid-link, torque, release, and impact definitions examined; it does not establish that every earlier release is inferior in every model. In particular, White later found release timing to have only a second-order effect in his constant-shoulder-torque model (White 2006).

Late Wrist Torque Can Help in Actuator-Bounded Simulations. Sprigings and Neal, using a torque-driven three-segment model with physiologically bounded actuators, found that an active wrist torque applied *during the latter stages of the downswing* increased clubhead speed by approximately 9% relative to their wrist-generator-disabled condition (Sprigings and Neal 2000). Their optimization placed wrist activation when the arm was about 30° below horizontal, but the authors also reported that this time depended strongly on the assumed torque-profile shape. In a follow-up three-segment study, Sprigings and MacKenzie separated a forced 50 ms resistive delay from post-release wrist drive. The optimized forced delay increased impact speed from 44.0 to 44.7 m/s (1.6%), whereas removing active wrist torque after that delay reduced it to 38.9 m/s (Sprigings and MacKenzie 2002). These are model-conditional comparisons, not a general human timing rule or a common effect size.

Energy Transfer to the Club Can Be Largely Passive—Governed by the Changing Geometry. White analyzed an *undriven* double pendulum and showed that the transfer of kinetic energy from arms to club late in the downswing is a parametric-transfer phenomenon: as the club swings out, the effective moment of inertia of the system changes, and conservation of energy and angular momentum move kinetic energy distally without any wrist torque at all; the wrist-cock angle maintained before release is the principal efficiency-determining parameter in that model (White 2006). In White's driven sensitivity study, however, ordinary release advances or delays had little net effect, and increasing constant positive wrist torque reduced predicted distance because its efficiency gain was offset by a shorter downswing. White separately noted that selective late torque can avoid that tradeoff. Miura's modified double-link emulation predicted that moving the hub inward near impact, when the modeled centrifugal force was developed, could substantially increase clubhead velocity (Miura 2001). Nesbit and McGinnis measured one selected driver swing from each of four diverse amateur golfers and found non-circular hand paths with a shared three-phase radius pattern but substantial between-subject geometry differences (Nesbit and McGinnis 2009). Their later two-dimensional constrained optimization predicted that combined hand-path and club-angular-trajectory changes could increase impact speed for all four subjects within each subject's modeled force, torque, work, and power limits; the changes and limiting quantities were subject dependent (Nesbit and McGinnis 2014). These model-based results motivate hub-path interventions, but they do not isolate an inward-pull contribution in a human experiment.

Together these studies motivate, but do not prove, a **retain-early / release-late** hypothesis. Pickering and Vickers, Sprigings and Neal, Sprigings and MacKenzie, and Sharp identify benefits from delayed release, late wrist drive, or a negative-to-positive wrist-torque program within their respective models (Pickering and Vickers 1999; Sprigings and Neal 2000; Sprigings and MacKenzie 2002; Sharp 2009). White supports passive geometry-mediated transfer while also showing that release-delay and wrist-torque effects depend on how the downswing angle, impact event, and torque program are defined (White 2006). The numerical study in Section 29 therefore tests one specified intervention family rather than treating the literature as a prior proof of its ordering.

2.3.1 Which Double-Pendulum Parameters Are Identifiable?

The analytical model also permits an exact distinction between coefficient excitation and physical-parameter recovery. Its inverse dynamics factor as

$$\tau = Y(q, \dot{q}, \ddot{q})\,[\alpha, \beta, \delta, \gamma_1, \gamma_2, d_1, d_2]^\mathsf{T},$$

where the seven base coefficients combine eleven reduced physical entries: two masses, two centers of mass, two proximal inertias, upper-link length, gravity, plane inclination, and two damping coefficients. The exact physical-to-base Jacobian has analytic row rank seven because one declared 7×7 minor has magnitude $m_2^2 r_1 r_2 [g\cos(\phi)]^2 > 0$. Its nullity is therefore four. Three finite counterexample families independently preserve every base coefficient while changing mass–center-of-mass, lower-link coupling, or gravity–plane parameters. Consequently, even an arbitrarily long noiseless record governed by this model cannot uniquely recover the declared eleven-entry physical vector.

The registered `restrain_then_drive@0.100s` synthetic record answers the separate excitation question. After scaling each coefficient by its registered base value and generalized torque by the registered 60 N m maximum, its 700×7 dimensionless regressor has rank seven with retained condition number 180.853 under the threshold $\max(10^{-8}, 10^{-7}\bar{\sigma}_1)$. Equivalent coefficient units change the dimensionless matrix by at most 4.45×10^{-16} and preserve the rank. Two additional positive scale choices also preserve rank while changing the condition number, so every reported condition number remains inseparable from its declared scale contract.

Full rank does not imply useful finite-noise recovery. Under deliberately favorable assumptions of exact kinematics, exact model form and event timing, and independent known Gaussian torque noise, a 1 N m noise standard deviation produces a worst relative 95% half-width of 0.123 for the full record but 499 for its first 10%. These are Cramér–Rao-style oracle lower bounds. Kinematic differentiation noise, correlated sensor errors, model discrepancy, unknown noise scale, repeated participants, and held-out prediction can only weaken the practical inference. The result therefore establishes structural non-uniqueness of the declared physical map and finite-record excitation of seven base coefficients; it does not establish participant parameters, model adequacy, human mechanism, or coaching guidance. The derivation, unit and scale audits, adverse windows, exact counterexamples, and reproduction command are provided in `DOUBLE_PENDULUM_IDENTIFIABILITY.md` and the registered `double_pendulum_identifiability.json`.

2.3.2 Source-Level Contrast Matrix

The cited studies answer different questions. Keeping their contrasts separate prevents a release-delay effect, an active-wrist-torque effect, and passive energy redistribution from being treated as the same quantity.

Source	Declared Comparison	Reported Finding	Evidentiary Boundary
Pickering and Vickers (Pickering and Vickers 1999)	Release angle in a driven fixed-hub double pendulum	Impact clubhead velocity increased with later release in the tested sweep; natural release minimized supplied energy	Computational parameter study; abstract does not establish universality or a human causal effect
Sprigings and Neal (Sprigings and Neal 2000)	Physiologically constrained three-segment simulation with wrist generator enabled versus disabled	Approximately 9% clubhead-speed gain with late active wrist torque; optimum activation near 30° below horizontal	Timing depended strongly on assumed torque-profile shape
Sprigings and MacKenzie (Sprigings and MacKenzie 2002)	No forced delay (SIM-1), 50 ms resisted delay plus active release (SIM-2), and resisted delay without post-release wrist torque (SIM-3)	SIM-2 versus SIM-1: 44.7 versus 44.0 m/s (1.6%); SIM-3: 38.9 m/s	Model included activation and force–velocity limits but omitted legs, lateral torso motion, right-arm extension, and forearm rotation
White (White 2006)	Undriven transfer analysis and driven constant-shoulder-torque sensitivity study	Passive parametric redistribution; ordinary release timing had a second-order net effect; increasing constant positive wrist torque reduced predicted distance	Point-mass or rigid-link planar models; late selective torque was discussed separately from constant torque
Sharp (Sharp 2009)	Parameterized arm–club and shoulder–arm–club simulations fitted to historical expert data and optimized within torque bounds	Near-optimal programs included a negative-to-positive wrist-torque switch and delayed release	The author explicitly identifies kinematic mismatch, sparse historical data, and model-dependence

This matrix is a preregistration aid for the project: a new model or experiment must declare which row's contrast it reproduces, or define a new estimand, before its result is compared numerically.

2.4 Optimal Control and Torque Sequencing

If the timing question is posed as an optimization — what torque program maximizes clubhead speed subject to actuator limits? — the answer has been studied repeatedly, but the resulting control histories are not one estimand. Lampsa used film of his own swing to parameterize and constrain a generalized two-link model, compared computed and actual torques, and used steepest ascent to search for torques maximizing drive distance (Lampsa 1975). Sharp later reproduced the published torque parameterization, found timing differences too large for both solutions to be numerically correct, and obtained a faster model swing with a negative-to-positive wrist-torque switch (Sharp 2009). Lampsa is therefore an early demonstration of the optimization question, not an independently confirmed global optimum or evidence that a human swing is suboptimal.

Later spatial forward models increased biomechanical and club detail, but also changed the state, controls, constraints, and objective. MacKenzie and Sprigings optimized a four-degree-of-freedom model with a flexible segmented shaft for impact clubhead speed (MacKenzie and Sprigings 2009). Balzerson, Banerjee and McPhee coupled a four-degree-of-freedom golfer to a Rayleigh beam, impact, and ball-flight model and optimized carry distance (Balzerson, Banerjee, and McPhee 2016). McNally and McPhee added a pelvis, a second shoulder degree of freedom, a modeled backswing, passive joint resistance, and eccentric–concentric torque–velocity scaling, then optimized carry distance (McNally and McPhee 2018). These models contain late wrist or forearm activations, but they do not establish one universal distal-torque program. Their source-level contrasts are separated below; McPhee reviews the broader lineage (McPhee 2022).

2.4.1 Forward-Optimization Model Boundaries

Source	Declared Model and Objective	Reported Result	Evidentiary Boundary
Lampsa (Lampsa 1975)	Film-parameterized generalized two-link swing; steepest-ascent search for drive distance under penalty constraints	Computed optimal torques were compared with torques derived from the author's filmed swing, with parameter sensitivity examined	The publisher record reports necessary conditions and a numerical search, not proof of a unique global optimum; Sharp later reported a materially different reproduction and a faster admissible program (Sharp 2009)
MacKenzie and Sprigings (MacKenzie and Sprigings 2009)	Four-degree-of-freedom spatial golfer with torque generators and a segmented flexible shaft; maximize impact clubhead speed	Optimized impact speed was 41.9 m/s; torso, shoulder, wrist-ulnar-deviation, and lead-arm external-rotation generators activated at approximately 0, 0.07, 0.16, and 0.17 s	Model validation used six accepted drives from one 3-handicap male and a single 2-D camera; the model omitted lower-body energy and a trail arm, and its optimized speed was about 7 m/s below the professional comparison cited by the authors
Balzerson, Banerjee, and McPhee (Balzerson, Banerjee, and McPhee 2016)	Four-degree-of-freedom torso–lead-arm–lead-hand model, continuous flexible shaft, impact, and ball flight; maximize carry	Optimized impact speed was 41.5 m/s with 196 m carry; wrist activation was approximately 0.11–0.12 s and forearm activation approximately 0.14–0.17 s	The model omitted the lower body and trail arm and explicitly assumed negligible trail-arm power; its authors positioned pelvis rotation as unnecessary for their club-design objective, not for joint-power attribution

Source	Declared Model and Objective	Reported Result	Evidentiary Boundary
McNally and McPhee (McNally and McPhee 2018)	Six-degree-of-freedom golfer, flexible shaft, volumetric impact, and ball flight driven by 12 backswing/downswing torque generators; maximize carry	Optimized clubhead speed was 164 km/h (45.6 m/s) and carry was 257 yd	The optimizer initiated torso motion before pelvis motion, which the authors identified as inconsistent with real swings; simulated grip kinematics left the measured elite-golfer standard-deviation bands at some phases, especially late in the swing

Optimal control optimizes *within a model*. Even the direction and timing of an apparent optimum can change with hub mobility, shaft flexibility (Betzler et al. 2012; Osis and Stefanyshyn 2012), actuator parameterization, impact definition, ball-flight objective, or omitted degrees of freedom. Cross-engine validation (Section 27), intervention ablations, and held-out human kinematics are therefore required before treating any optimized timing as a biological or coaching result.

2.5 What "Energy Transfer" Means Operationally

Claims about energy transfer require an accounting framework. Four levels of analysis appear in the literature, and they are not interchangeable.

2.5.1 Joint Power and Work

For a one-degree-of-freedom joint spanning segments i and $i+1$, with net generalized joint torque τ and compatible relative joint rate $\dot{q}$, the net joint power is

$$P_{\text{joint}} = \tau \dot{q}. \tag{2.3}$$

Its time integral is the net mechanical work associated with the resultant joint moment under the declared sign convention. Positive and negative values mean net positive and negative mechanical power; they do not, by themselves, identify muscle energy generation or absorption. Resultant inverse-dynamics torque can combine agonist and antagonist forces, passive tissue moments, and other unmodeled contributions. This net work–power quantity is central to the budget of Nesbit and Serrano (Section 25.1) (Nesbit and Serrano 2005), but interpreting it physiologically requires additional muscle and tissue measurements or models.

2.5.2 Joint-Force Power and Segmental Energy Accounting

Joint moments are not the only conduit of segmental mechanical energy. For a wrench acting on one segment at joint point J, the endpoint power must use the velocity and angular velocity of that same segment, expressed in compatible frames:

$$P_{J \to i} = \mathbf{F}_{J \to i} \cdot \mathbf{v}_{J,i} + \mathbf{M}_{J \to i} \cdot \omega_i. \tag{2.4}$$

The equal-and-opposite wrench on the adjacent segment generally has a different segment angular velocity, so the two moment-power terms need not cancel. Their sum is related to the net relative joint power; the individual segment terms describe delivery to or removal from each segment. At a common ideal joint point, the internal force-power terms cancel in the whole-system sum but remain essential to each segment's energy balance.

Robertson and Winter balanced each leg segment's rate of mechanical-energy change against proximal and distal reaction-force and moment powers (Robertson and Winter 1980). Their validation used sagittal-plane force-plate and cinefilm data from two participants walking at several speeds. Agreement was acceptable except for ankle power during weight acceptance and late push-off, and the estimated joint transfers were comparable in magnitude to estimated muscle generation and absorption. The method therefore motivates full segment-level accounting; the small walking study is not a validation of golf power, three-dimensional joint-center estimates, or individual muscle energetics.

The "retain-early / release-late" hypothesis concerns the time course of declared intersegment power terms, so segment energy balances are more direct than peak angular velocities. They are still not sufficient for muscle coordination: Zajac, Neptune, and Kautz explicitly cautioned that joint powers and segment angular velocities alone cannot determine energy flow, and recommended muscle-induced acceleration and power analysis in a dynamical simulation (Zajac, Neptune, and Kautz 2002). Section 28 implements a model-level wrist-interface balance, including a residual check; it does not identify the human muscles responsible for that balance.

2.5.3 Induced Accelerations and Dynamic Coupling

In a coupled chain, a single generalized torque can induce acceleration at multiple coordinates — including coordinates it does not span — through the inverse inertia matrix when the corresponding coupling terms are nonzero (Zajac and Gordon 1989). Zajac, Neptune, and Kautz reviewed why inverse dynamics cannot by itself assign causal action to individual muscles and why muscle-driven simulations are needed for induced-acceleration and power analyses (Zajac, Neptune, and Kautz 2002). In a golf model with nonzero pathways, an early torso torque may induce club acceleration and a late wrist torque may induce proximal acceleration or deceleration. Their signs and magnitudes must be computed for the declared model and state; these are mechanical possibilities, not human-golf findings supplied by the walking literature. The ZTCF/ZVCF decompositions of Section 26 are model-level counterfactual analyses with a different intervention definition, not measurements of individual muscle action.

2.5.4 Kinematic Sequence as a Proxy — And Its Failure Modes

Peak-ordering of segment angular speeds is a *proxy* for energy flow, not a measurement of it. Marsan and colleagues analyzed driver swings from 13 golfers with seven angular-velocity component-selection methods and obtained almost as many sequences as methods for each golfer; no method could be designated the reference, although one correlated most strongly with performance in that sample (Marsan et al. 2019). Marshall and Elliott's long-axis-rotation result in two racquet tasks (Marshall and Elliott 2000) illustrates one omitted component, not a golf energy-flow validation.

"Planar" also requires a declared object and tolerance. Coleman and Rankin measured seven right-handed golfers (handicap 0–15) and found that the left-arm plane changed orientation through the downswing while the clubhead was, on average, 0.291 m from that plane at impact (Coleman and Rankin 2005). Kwon and colleagues measured 14 skilled male golfers with three clubs: the clubhead followed a well-defined functional swing plane, but shoulder and arm points occupied different motion planes and deviated substantially from the clubhead plane (Kwon et al. 2012). These results reject a single fixed plane shared by the body and club; they do not imply that a planar club model is useless for a narrowly declared mechanism.

Tests of the timing hypothesis should therefore pair an explicitly defined kinematic sequence with segment and interface power accounting (Section 2.5.2), coordinate sensitivity, and three-dimensional residuals. The sequence remains corroborating description rather than evidence of energy transfer—which is how Section 29 uses it.

Chapter 3

Interaction-Force Mechanisms in the Double Pendulum

The phrase *energy transfer* is often used as if energy were a substance that waits in one link and is then released into the next. The mechanics are more specific. A distal segment gains mechanical energy when forces acting at its moving joint and moments acting on it do positive power. Those forces can grow without a large distal actuator torque because the segment must satisfy the acceleration constraints imposed by the moving chain. Their capacity to do work depends on orientation: a large force perpendicular to joint-point velocity transmits no instantaneous translational power at that point, while a smaller force aligned with that velocity can be effective. This chapter derives those statements exactly for the double pendulum, tests them numerically, and identifies which conclusions survive when the commanded torques are removed.

3.1 The Question in Operational Form

Consider the club segment alone. It is acted on by gravity, a force at the wrist, and a net wrist moment. Its kinetic-energy rate is

$$\dot{T}_2 = \underbrace{\mathbf{F}_W \cdot \mathbf{v}_W}_{\text{joint-force power}} + \underbrace{M_W \omega_2^{\text{abs}}}_{\text{joint-moment power}} + \underbrace{m_2 \mathbf{g} \cdot \mathbf{v}_{C2}}_{\text{gravity power}} , \tag{3.1}$$

where $\mathbf{F}_W$ is the wrist force acting on the club, $\mathbf{v}_W$ is the velocity of the wrist point, M_W is the net moment acting on the club at the wrist, and $\omega_2^{\text{abs}} = \dot{\theta}_1 + \dot{\theta}_2$ is the club's absolute angular velocity. Equation 3.1 separates three questions:

1. What creates a large wrist force?
2. What orients that force so it has a useful projection onto wrist velocity?
3. What part of the resulting club-energy gain requires commanded wrist torque?

The first two questions concern dynamic coupling and geometry. The third is a counterfactual question. None can be answered from angular-speed peak order alone (Putnam 1991; Robertson and Winter 1980; Winter 2009).

3.2 Coordinate and Sign Conventions

The arm angle θ_1 and relative wrist angle θ_2 are measured from the downward vertical and from the arm, respectively. The club absolute angle is $\phi = \theta_1 + \theta_2$. In swing-plane Cartesian coordinates, x points toward the target side and y points upward. Define

$$\mathbf{u}(\theta) = \begin{bmatrix} \sin\theta \\ -\cos\theta \end{bmatrix}, \qquad \mathbf{u}_\perp(\theta) = \begin{bmatrix} \cos\theta \\ \sin\theta \end{bmatrix}. \tag{3.2}$$

$\mathbf{u}$ points along a link and $\mathbf{u}_\perp$ points in its positive angular-velocity direction. Figure 3.1 declares the free-body convention used in every calculation. $\mathbf{F}_W$ is the force *on the club*; the equal-and-opposite force acts on the arm. Positive $\mathbf{F}_W \cdot \mathbf{v}_W$ therefore means that the wrist force delivers positive instantaneous power to the club. The complete club balance still includes wrist-moment and gravity power.

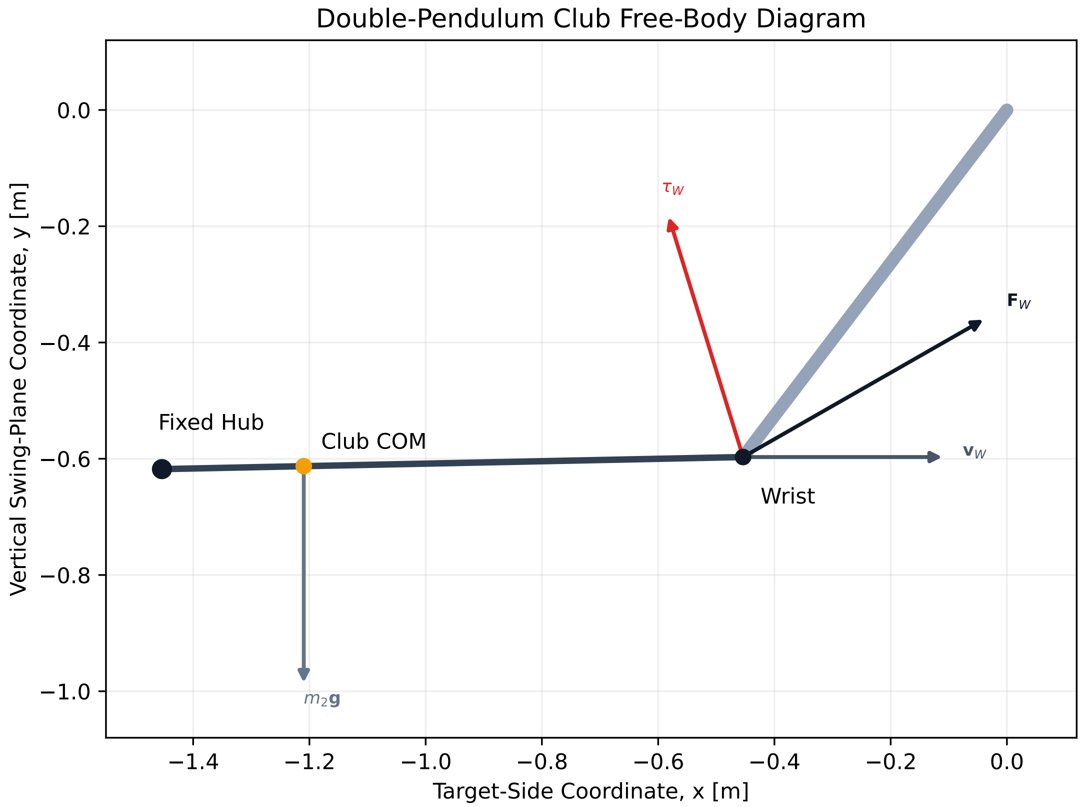

Figure 3.1: Double-Pendulum Club Free-Body Diagram

The force and moment are related but not interchangeable. Translation of the club centre of mass depends on the net force. Rotation about the centre of mass depends on both the wrist-force moment arm and M_W:

$$I_{2,C}\ddot{\phi} = (\mathbf{r}_W - \mathbf{r}_C) \times \mathbf{F}_W + M_W. \tag{3.3}$$

The executable validation checks Equation 3.3 at machine precision. This distinction becomes central in a two-hand model, where two hand forces can have a modest resultant force but a large equivalent couple.

3.3 Exact Decomposition of the Wrist Reaction Force

The wrist and club centre-of-mass positions are

$$\mathbf{r}_W = l_1\mathbf{u}(\theta_1), \qquad \mathbf{r}_{C2} = \mathbf{r}_W + l_{c2}\mathbf{u}(\phi). \tag{3.4}$$

Differentiating twice gives four acceleration terms:

$$
\begin{aligned}
\mathbf{a}_{C2} = \; & \underbrace{l_1\ddot{\theta}_1\mathbf{u}_\perp(\theta_1)}_{\text{proximal tangential}} - \underbrace{l_1\dot{\theta}_1^2\mathbf{u}(\theta_1)}_{\text{proximal centripetal}} \\
& + \underbrace{l_{c2}\ddot{\phi}\mathbf{u}_\perp(\phi)}_{\text{distal tangential}} - \underbrace{l_{c2}\dot{\phi}^2\mathbf{u}(\phi)}_{\text{distal centripetal}} .
\end{aligned} \tag{3.5}
$$

Newton's second law for the club yields

$$
\mathbf{F}_W = m_2(\mathbf{a}_{C2} - \mathbf{g}). \tag{3.6}
$$

Combining Equation 3.5 and Equation 3.6 produces five exact force components. They are not fitted regressors and do not depend on numerical differentiation.

Table 3.1: Exact Wrist-Force Components in the Planar Double Pendulum

Component	Vector Expression	Physical Meaning
Proximal tangential	$m_2 l_1 \ddot{\theta}_1 \mathbf{u}_\perp(\theta_1)$	Force needed because the wrist has tangential acceleration
Proximal centripetal	$-m_2 l_1 \dot{\theta}_1^2 \mathbf{u}(\theta_1)$	Force needed because the wrist follows a curved path
Distal tangential	$m_2 l_{c2} \ddot{\phi} \mathbf{u}_\perp(\phi)$	Force associated with club angular acceleration about the wrist
Distal centripetal	$-m_2 l_{c2} \dot{\phi}^2 \mathbf{u}(\phi)$	Force associated with the club COM curving about the wrist
Gravity reaction	$-m_2\mathbf{g}$	Wrist support needed in addition to gravity

Two cautions prevent common misreadings. First, *centripetal* describes an acceleration direction, not a separate applied agent. The joint reaction force is the physical constraint force; the named terms explain why that force is required. Second, gravity appears twice in a causal discussion: it contributes to the system accelerations through the equations of motion, and the explicit $-m_2\mathbf{g}$ term is required when the club free-body equation is solved for the wrist force. These roles must not be double-counted.

3.4 Why Zero Commanded Torque Does Not Imply Zero Force

For generalized coordinates $q = [\theta_1, \theta_2]^T$, the dynamics are

$$
\ddot{q} = M(q)^{-1}\{\tau - b(q, \dot{q})\}. \tag{3.7}
$$

Setting $\tau = 0$ leaves $\ddot{q}_0 = -M^{-1}b$, which is generally nonzero whenever gravity, velocity-dependent coupling, or damping is present. Substitution of $\ddot{q}_0$ into Equation 3.5 yields a nonzero centre-of-mass acceleration and therefore a nonzero wrist reaction force. This is the precise mechanical basis, for this declared unconstrained manipulator model, for the WSCG presentation's statement that zero *commanded* joint torque does not mean zero interaction force (Olson 2024). Passive damping remains inside b; imposed constraints or external contacts would require their reaction terms to be retained separately. The result also follows directly from standard linked-segment dynamics (Putnam 1991, 1993; Featherstone 2008).

For this unconstrained model, because the equations are affine in the declared generalized torque, the *instantaneous* acceleration has an exact split:

$$
\ddot{q}_{\text{total}} = \underbrace{-M^{-1}b}_{\ddot{q}_{\text{drift}}} + \underbrace{M^{-1}\tau}_{\ddot{q}_{\text{control}}}. \tag{3.8}
$$

At a fixed state, all velocity-squared terms in Equation 3.5 are shared between the two cases. The force split is therefore

$$\mathbf{F}_{\text{total}} = \mathbf{F}_{\text{drift}} + \mathbf{F}_{\text{control}}, \tag{3.9}$$

where $\mathbf{F}_{\text{drift}}$ is evaluated at zero commanded torque and $\mathbf{F}_{\text{control}} := \mathbf{F}_{\text{total}} - \mathbf{F}_{\text{drift}}$ is the change induced by the commanded torque at that same state. This is a local superposition at one state and under one intervention definition. It is not a muscle-force partition. Once two futures are integrated, their states diverge and the equality cannot be applied across time by subtracting unrelated samples.

Figure 3.2 shows this decomposition at six phases of the reference swing. The force scale is fixed across panels. The pointwise zero-torque force becomes large late even though the commanded torque is set to zero in that calculation; accumulated angular velocity and changing geometry continue to demand a substantial wrist constraint force.

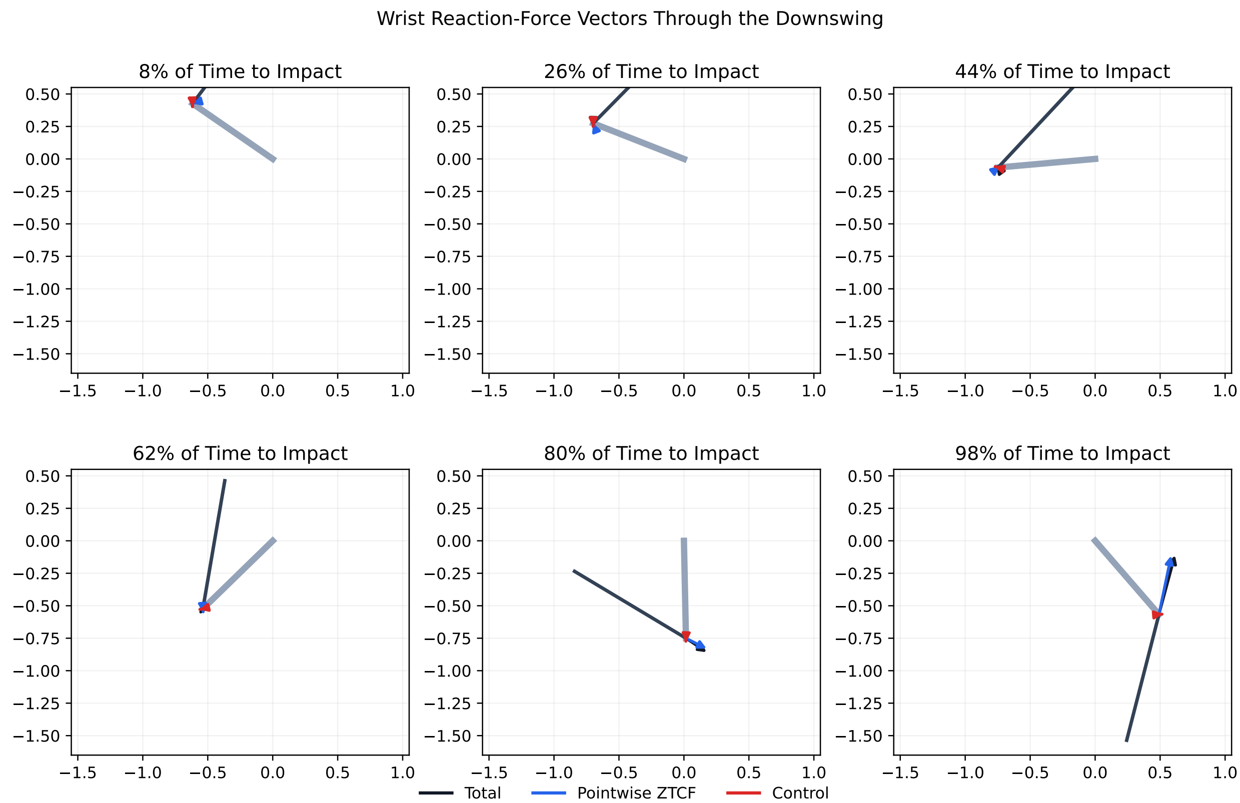

Figure 3.2: Wrist Reaction-Force Vectors Through the Downswing

3.5 Force Magnitude Is Not Transfer

The wrist velocity is

$$\mathbf{v}_W = l_1 \dot{\theta}_1 \mathbf{u}_\perp(\theta_1). \tag{3.10}$$

For any component $\mathbf{F}_k$, its contribution to club energy is $P_k = \mathbf{F}_k \cdot \mathbf{v}_W$. The dot product, not force magnitude, decides transfer. Substitution of the five components produces

$$
\begin{aligned}
P_{\text{prox,tan}} &= m_2 l_1^2 \ddot{\theta}_1 \dot{\theta}_1, \\
P_{\text{prox,cen}} &= 0, \\
P_{\text{dist,tan}} &= m_2 l_1 l_{c2} \ddot{\phi} \dot{\theta}_1 \cos\theta_2, \\
P_{\text{dist,cen}} &= -m_2 l_1 l_{c2} \dot{\phi}^2 \dot{\theta}_1 \sin\theta_2, \\
P_{g\text{-reaction}} &= m_2 g_{\text{proj}} l_1 \dot{\theta}_1 \sin\theta_1.
\end{aligned}
\tag{3.11}
$$

Equation 3.11 gives several strong results.

The proximal centripetal term does no work at a fixed circular hub path. It is radial to the arm while wrist velocity is tangential. It can be large in a force plot and still contribute exactly zero joint-force power. A mobile or noncircular hub breaks that orthogonality, which is why hand-path shaping is a separate mechanism in more complete models (Miura 2001; Nesbit and McGinnis 2009; Nesbit and McGinnis 2014).

The distal centripetal term is geometry gated. Its projection coefficient is $-\sin\theta_2$. With the club approximately 90° behind the arm ($\theta_2 \approx -90°$), the coefficient is near $+1$: a force directed toward the club's instantaneous centre can project strongly along hand motion. As the links align, this coefficient falls to zero.

The distal tangential term has the complementary gate. Its coefficient is $\cos\theta_2$: near a 90° wrist cock its projection is small, while it becomes large as the links align. The changing wrist angle therefore rotates the two projection gates toward and away from the hand-velocity direction. Which term dominates also depends on $\ddot{\phi}$, $\dot{\phi}^2$, $\dot{\theta}_1$, and the declared state; geometry alone does not determine the dominant pathway.

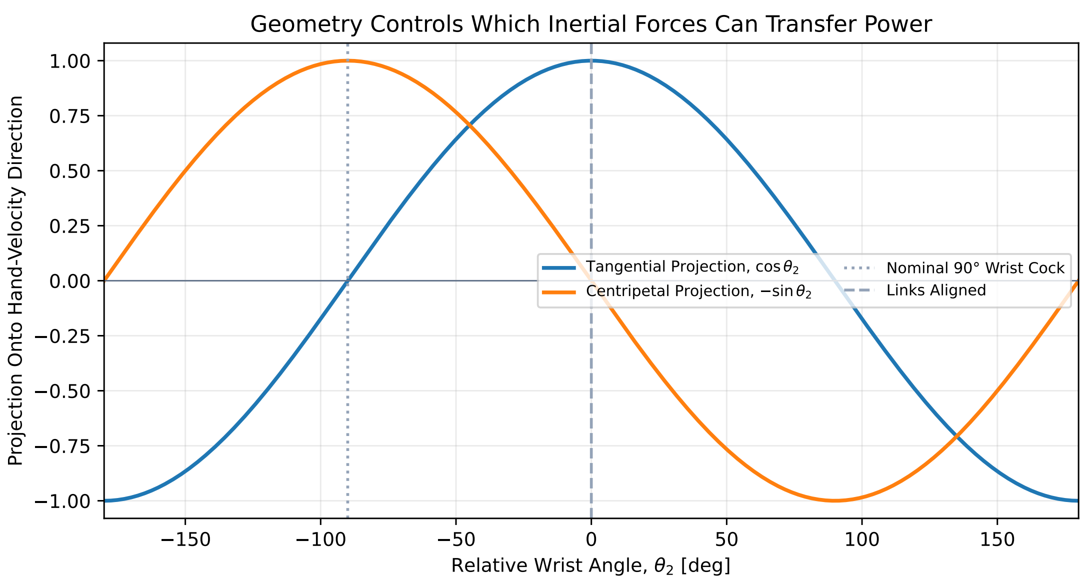

Figure 3.3: Geometry Controls Which Inertial Forces Can Transfer Power

This complementarity is one geometric mechanism available to the handoff. A compact configuration admits a large relative angle and therefore different proximal and distal absolute rates, but it does not guarantee high proximal acceleration or delayed club acceleration. As the wrist opens, the projection factors change and $\dot{\phi}^2$ may grow; whether force rises and performs positive wrist-force work must be calculated for the state and control history. White studied transfer efficiency in a reduced swing model, whereas Miura studied inward hand-path pull and parametric acceleration. They motivate separate fixed-hub and moving-hub hypotheses rather than jointly validating the present result (White 2006; Miura 2001).

3.6 Numerical Mechanism Audit

The numerical audit uses the existing reference program: 60 N · m at the shoulder, -10 N · m at the wrist until 0.10 s, and +15 N · m thereafter. Impact is the first valid upward crossing of club vertical. The program reaches that event at 0.3493 s with 38.85 m/s clubhead speed. These values describe the declared model, not a human normative target.

The exact force reconstruction reaches a peak wrist-force magnitude of 315.4 N before impact. The pointwise zero-torque case reaches 310.6 N, while the root-mean-square magnitude of the control-force increment is 16.3% of the root-mean-square total-force magnitude. The similarity is not evidence that torque is unimportant: prior torque shaped the state, and the present torque still changes the future. Under this pointwise decomposition and RMS norm, the instantaneous control-force increment is small relative to total force over the sampled interval; that result does not identify biological effort or establish the same ordering under another norm, state history, or model.

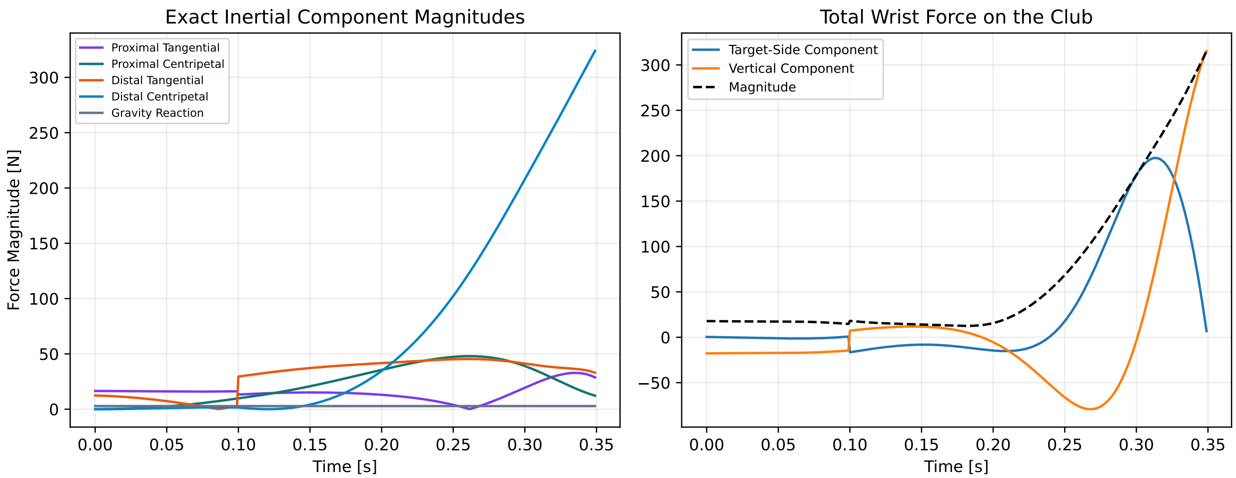

Figure 3.4: Exact Inertial Components and Total Wrist Force

Figure 3.4 exposes the mechanism behind the late rise. The distal centripetal term grows approximately with $\dot{\phi}^2$ and is the largest component near impact. Its effect on transfer is then determined by the wrist-angle projection in Equation 3.11. The discontinuity in tangential terms at 0.10 s is expected: the prescribed wrist torque switches from restraint to drive, changing angular acceleration instantaneously while position and velocity remain continuous.

The integrated wrist-force work to impact is 130.7 J. The late half contributes 131.7 J, because the early half contains small positive and negative exchanges that nearly cancel. Across the full interval, positive force work is 136.8 J and negative force work is -6.1 J. The pointwise zero-torque force integrates to 132.2 J along the *commanded states*. That last quantity is an attribution diagnostic, not the energy of a realizable zero-torque future.

The force-power traces clarify why peak-force comparisons alone are insufficient. The proximal centripetal magnitude is visible in Figure 3.4 but its power trace remains zero by geometric orthogonality. The distal centripetal pathway grows into the dominant positive term late. The distal tangential pathway is negative through much of the middle downswing and turns positive near impact. Total transfer is their signed sum with proximal tangential and gravity-reaction contributions.

3.7 Pointwise and Forward Counterfactuals

Two zero-torque questions are useful, but they must have different names.

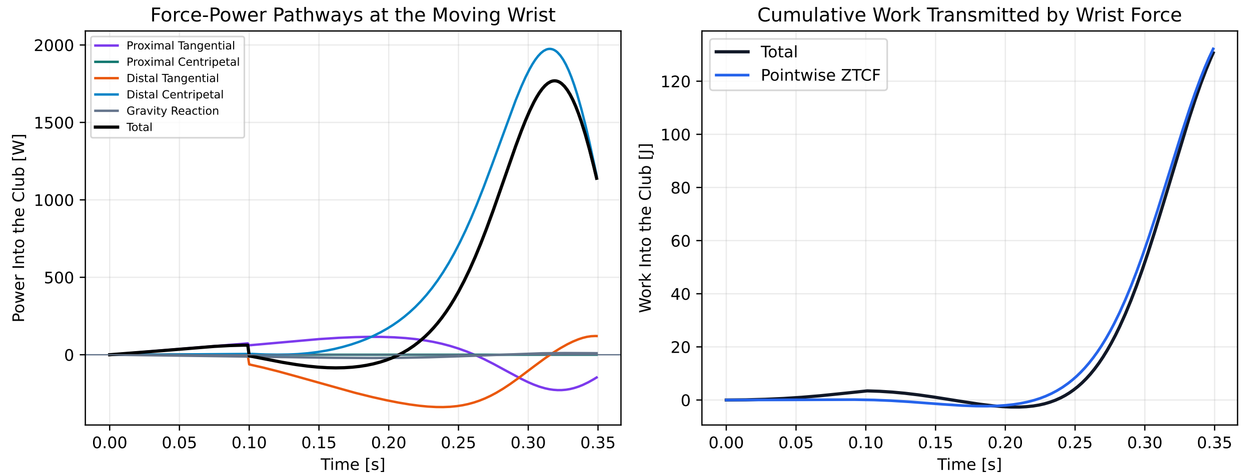

Figure 3.5: Force-Power Pathways and Cumulative Wrist-Force Work

Pointwise ZTCF asks: *At this observed state, what acceleration and reaction force would the equations require if commanded torques were zero right now?* It holds $(q, \dot{q})$ fixed independently at every recorded sample. This is an instantaneous attribution and gives the exact affine split in Equation 3.9.

Matched-state torque killswitch asks: *Starting from this state, what future trajectory follows if torque remains zero?* It initializes commanded and zero-torque rollouts at the same $(q, \dot{q}, t)$ and integrates both. Only the initial state is matched. As soon as accelerations differ, velocity, geometry, force, and power histories diverge.

The WSCG presentation constructs a trajectory-level counterfactual by applying kill switches at successive states and compiling the resulting values (Olson 2024). The present implementation makes the distinction executable. At a 0.251 s cut, the two rollouts begin with identical position and velocity, and the initial zero-torque acceleration exactly matches the pointwise drift calculation. After 0.120 s, their generalized positions differ by 0.540 rad and their generalized velocities by 8.49 rad/s. Figure 3.6 shows why a pointwise ZTCF trace cannot be interpreted as a torque-free replay of the measured motion.

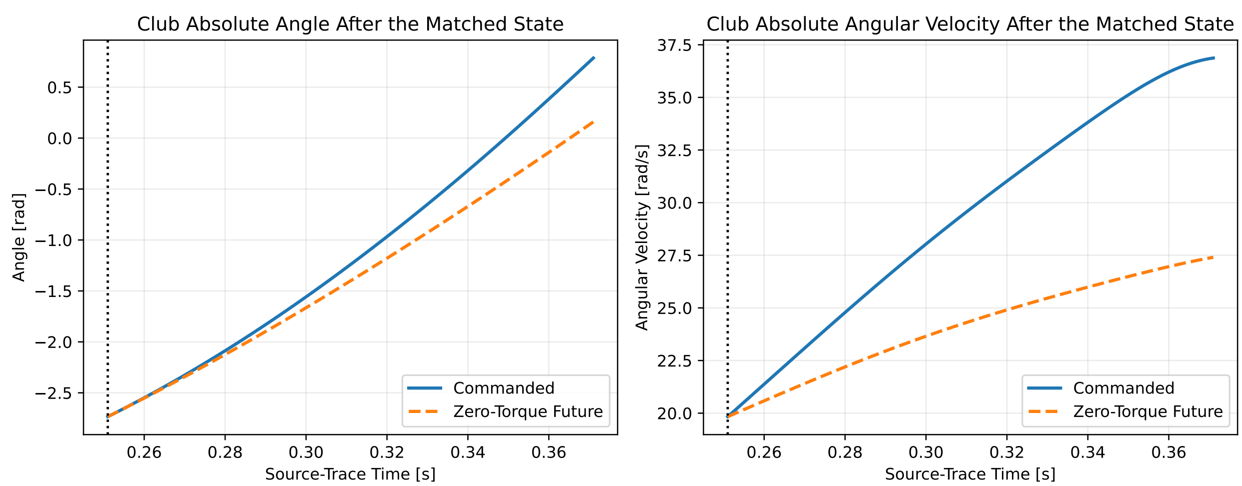

Figure 3.6: Commanded and Zero-Torque Futures From a Matched Late-Downswing State

Both counterfactuals are informative. The pointwise version isolates the force required by the state already achieved. The killswitch version tests whether that state can carry the club forward without continued control.

A robust claim of passive late-swing transfer should be supported by both: large favorable pointwise drift power and persistence of the predicted behavior over a stated killswitch horizon.

3.8 Mechanistic Hypotheses for Delivery-Speed Studies

Within this model class, the mechanism generates five testable hypotheses. They are experimental factors, not technique instructions.

1. **Early-State Hypothesis.** At matched initial conditions, programs that preserve a larger relative angle while increasing proximal rate should alter later drift-force and drift-power distributions. A preregistered comparison must report failures to reach the delivery event.
2. **Projection Hypothesis.** Around $\theta_2 = -90^\circ$, the distal centripetal coefficient is near its positive maximum, but favorable work is predicted only when the remaining signed rate terms also agree. Sweeping angle without matching state is not a causal test.
3. **Pathway-Rotation Hypothesis.** As θ_2 approaches zero, the centripetal projection decreases and the tangential projection increases. Their actual power crossover should move when acceleration, hub path, or shaft compliance is perturbed.
4. **Control-History Hypothesis.** Late wrist drive can improve delivery in the reference program even when pointwise drift accounts for most force work at the achieved states. Matched-history and killswitch comparisons can separate state preparation from instantaneous contribution.
5. **Constrained-Objective Hypothesis.** Maximizing an intermediate force, angular acceleration, or relative angle need not maximize valid delivery. Speed, orientation, actuator bounds, load, robustness, and event validity must be evaluated together (Pickering and Vickers 1999; Sprigings and Neal 2000).

These conclusions are model-conditional. A mobile hub adds radial hand velocity, a flexible shaft adds stored elastic energy, three-dimensional motion adds long-axis rotations, and a biological controller adds torque-rate and activation constraints. Each extension can change the best timing while leaving the power identity $P = \mathbf{F} \cdot \mathbf{v}$ intact.

3.9 Bridge to Two-Hand Negative Coupling

A single wrist point cannot produce an independent force couple: force and wrist moment are separate inputs. Two hands change the wrench geometry. If the lead and trail hands apply $\mathbf{F}_L$ and $\mathbf{F}_T$ at positions $\mathbf{r}_L$ and $\mathbf{r}_T$, their equivalent wrench about a reference point O is

$$\mathbf{F}_{\text{net}} = \mathbf{F}_L + \mathbf{F}_T, \qquad M_O = (\mathbf{r}_L - \mathbf{r}_O) \times \mathbf{F}_L + (\mathbf{r}_T - \mathbf{r}_O) \times \mathbf{F}_T. \tag{3.12}$$

Opposing hand-force components can cancel in $\mathbf{F}_{\text{net}}$ while adding in M_O. Consequently, a negative equivalent couple near impact does not by itself prove an actively commanded negative wrist torque. It can arise in a model from the pair of constraint forces needed to enforce two separated moving hand contacts on the club. That is a mechanism hypothesis, not a physiological inference. The WSCG two-hand planar simulation reported this pattern: similar BASE and zero-torque net club forces, substantial opposing local hand forces, and a late reversal of the equivalent couple (Olson 2024).

The registered source series are redrawn in Figure 3.7. They preserve the reported BASE and counterfactual hand-force histories; they are not claimed as a reproduction of the underlying Simscape simulation.

This evidence motivates the next model test. The two-hand study must compute the equivalent wrench from local forces, verify sign conventions through power and moment balance, compare pointwise and killswitch counterfactuals, and separate momentum, gravity, shaft flex, damping, and numerical effects. The passive-negative-couple hypothesis survives only if the sign reversal persists under those controls and across reasonable contact spacing, hub paths, and shaft parameters.

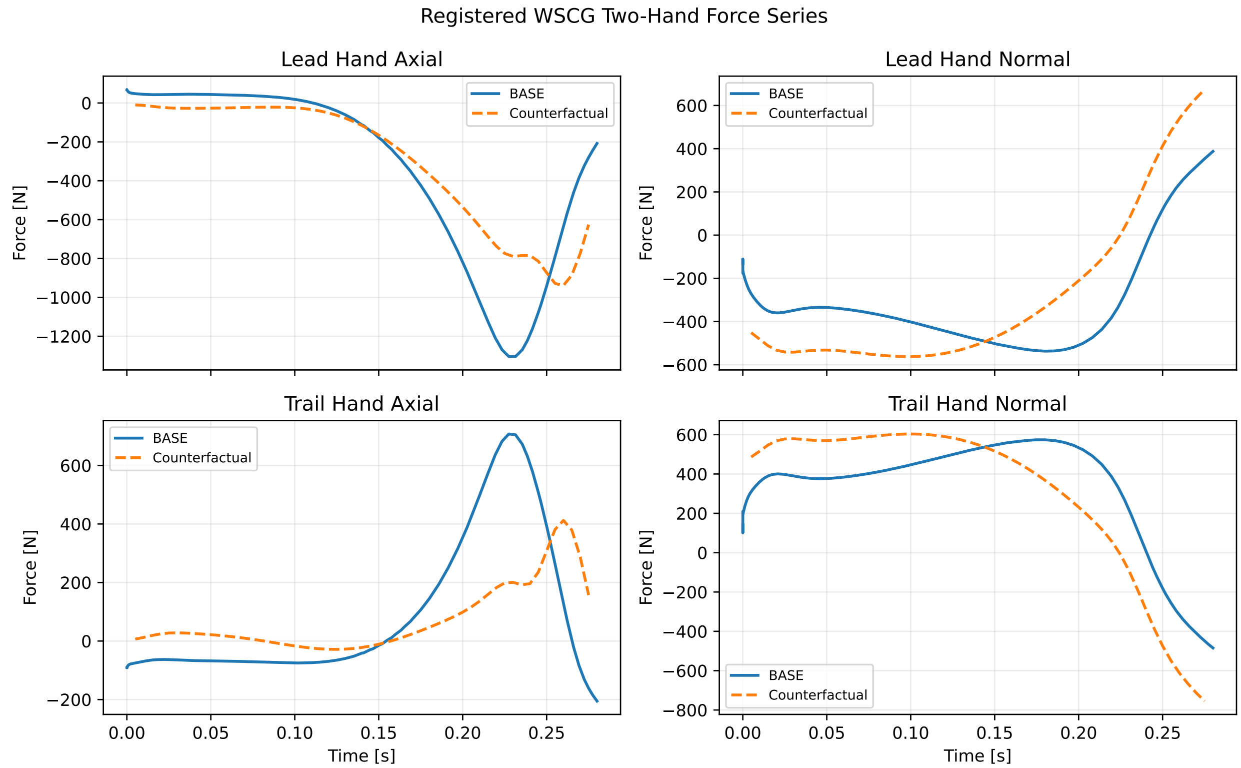

Figure 3.7: Registered WSCG Two-Hand BASE and Counterfactual Hand-Force Series

3.10 Claims, Nonclaims, and Falsification Tests

The double-pendulum evidence supports four narrow claims:

- substantial wrist reaction force can exist at zero commanded torque;
- force transfer is governed by a signed velocity projection, not force magnitude;
- wrist geometry produces exact sine and cosine gates on two major inertial power terms; and
- in the reference program, most positive wrist-force work occurs late and the pointwise drift force dominates the total-force magnitude at achieved states.

It does **not** establish that human golfers use the same torque history, that the two-hand negative couple is always passive, that more lag is always better, or that the reported parameter values are population estimates. The following tests could overturn or materially qualify the framework:

- a matched-state killswitch ensemble showing that favorable pointwise drift does not persist long enough to affect delivery;
- a two-hand wrench audit in which the negative couple disappears after gravity, shaft elasticity, damping, and numerical artifacts are separated;
- higher-order models in which hub translation or three-dimensional rotation reverses the dominant power pathway; or
- synchronized human motion and force estimates inconsistent with the modeled timing and sign structure.

These failure conditions bound the inference. The double-pendulum evidence identifies a reproducible mechanism; it does not convert behavior in one model into a population estimate or coaching prescription.

Chapter 4

Hand-Path Force Attribution Across the Model Ladder

4.1 The Observation and the Inference It Does Not Support

MacKenzie, McCourt, and Champoux analyzed drives from 76 right-handed amateur golfers with handicaps below 15 and represented the golfer's action on the driver as a resultant force at the mid-grip point plus a resultant couple (MacKenzie, McCourt, and Champoux 2020). Their path-averaged force was strongly associated with clubhead speed ($r = 0.96$); the corresponding bivariate regression entry reported $R^2 = 0.92$ in that sample. Mean linear work was 174 J, mean angular work was 39 J, mean hand-path length was 1.35 m, and mean force along the path was 129 N. These are observational between-golfer associations from one sample and shared-club protocol, not an intervention estimate or a claim that adding force while holding the trajectory and all other determinants fixed would cause the same speed change.

That result is important, but the observable must be named precisely. It is a signed mechanical line integral divided by path length,

$$\overline{F}_{\parallel} = \frac{\int_{t_a}^{t_b} \mathbf{F}_H \cdot \mathbf{v}_H \, dt}{\int_{t_a}^{t_b} \|\mathbf{v}_H\| \, dt} = \frac{W_{H,F}}{L_H}, \tag{4.1}$$

not a time average, not a force-magnitude average, and not an average of two individual hand-force magnitudes. It is also not a physiological effort measure. In a linked system, the force transmitted at the grip is the reaction required to satisfy the equations of motion and the joint constraints. Its value can contain a large contribution from gravity, velocity-dependent interaction dynamics, passive elements, prescribed-base motion, and earlier work stored in the achieved state. None of those contributions is identified by a net grip-force trace alone (Putnam 1991, 1993; Zajac and Gordon 1989). Even a specified endpoint force can admit wide ranges of muscle activation in a redundant musculoskeletal model (Sohn, McKay, and Ting 2013). That cited demonstration used static endpoint-force production in a 31-muscle cat-hindlimb model; it supports an identifiability warning, not a quantitative statement about human golf muscles or dynamic activation histories.

The correct conclusion from the 2020 study is therefore narrow and useful: golfers who produced more signed linear work per metre of hand travel also produced greater clubhead speed in that sample. The result does not establish that they experienced proportionally greater perceived effort, generated proportionally greater instantaneous muscle activation, or could obtain the same change by simply trying to pull harder along the observed path. This chapter asks the model-based question left open by that evidence: how much of the transmitted force, impulse, power, and work is present in the achieved state without the instantaneous command, and how does that attribution change with joint, phase, geometry, and model structure?

4.2 Four Distinct Counterfactual Quantities

For a control-affine model,

$$M(q)\ddot{q} + h(q, \dot{q}) = B(q)u, \tag{4.2}$$

the same-state acceleration is separated exactly as

$$\ddot{q}_{\text{total}} = \underbrace{-M^{-1}h}_{\ddot{q}_{\text{drift}}} + \underbrace{M^{-1}Bu}_{\ddot{q}_{\text{control}}}. \tag{4.3}$$

The **pointwise ZTCF sample** is the first term evaluated at the achieved state after the declared applied controls are set to zero. Repeating this operation along the achieved history produces a **stitched pointwise ZTCF trace**, not a single forward trajectory. In the analyses here, its inventory includes gravity and motion-dependent terms and includes a passive element only when that element belongs to the declared model. The **control increment** is total minus ZTCF at that identical state. The two close exactly because the state, constraints, parameters, and numerical protocol are held fixed.

The **ZVCF** is a different counterfactual: velocities are set to zero while the configuration and the declared commands are retained. Velocity-dependent terms disappear, but gravity, configuration-dependent stiffness, and the direct command generally remain. ZVCF is therefore not another name for the control increment. It answers which reactions and accelerations would remain at this configuration if the generalized velocity vanished under its stated protocol.

Finally, a **forward** or **branched ZTCF** starts a new trajectory after removing a command. It ceases to share the achieved state as soon as it is integrated. A pointwise ZTCF sample can attribute an instantaneous reaction; only a forward experiment can test persistence. Results from one experiment are not silently promoted into claims about the other.

For a constrained two-hand model, the same distinction applies to the complete Karush–Kuhn–Tucker solve,

$$\begin{bmatrix} M & -J^T \\ J & 0 \end{bmatrix} \begin{bmatrix} \ddot{q} \\ \lambda \end{bmatrix} = \begin{bmatrix} Bu - h \\ -\dot{J}\dot{q} \end{bmatrix}. \tag{4.4}$$

The contact reactions λ must be recomputed in each counterfactual. Subtracting unconstrained accelerations, assigning a residual by least squares, or comparing reactions from diverged trajectories does not provide a valid reaction-force attribution.

4.3 From Force Vectors to Transfer Metrics

At every moving interface, the path tangent is

$$\mathbf{e}_t = \frac{\mathbf{v}}{\|\mathbf{v}\|}, \qquad \|\mathbf{v}\| > v_\epsilon, \tag{4.5}$$

and the signed along-path components are

$$F_{\parallel,k} = \mathbf{F}_k \cdot \mathbf{e}_t, \qquad k \in \{\text{total}, \text{drift}, \text{control}, \text{ZVCP}\}. \tag{4.6}$$

The tangent is taken from the achieved trajectory for all pointwise additive components. Samples below the declared speed threshold are undefined rather than being assigned a convenient direction. This matters near the top of the backswing and at fixed joints.

Four integrals answer different questions:

$$\mathbf{J}_k = \int \mathbf{F}_k \, dt, \qquad J_{\parallel,k} = \int F_{\parallel,k} \, dt, \tag{4.7}$$

$$P_{F,k} = \mathbf{F}_k \cdot \mathbf{v}, \qquad W_{F,k} = \int P_{F,k} \, dt. \tag{4.8}$$

The vector impulse $\mathbf{J}$ retains direction in the global frame. The signed tangent impulse $J_\parallel$ integrates projections onto a tangent that rotates with the path, so it is not $\|\mathbf{J}\|$ and is not an energy measure. Force power weights the same signed projection by path speed; its integral is linear work. A component can dominate absolute impulse while doing little work, or do substantial work over a short high-speed interval without dominating time-integrated force.

At a joint that also transmits a couple, the complete planar wrench power is

$$P_k = \mathbf{F}_k \cdot \mathbf{v}_O + C_{O,k}\omega, \tag{4.9}$$

where the force, couple, translational velocity, and angular velocity use the same body, sign, frame, and reference point. Reporting force power and couple power separately reveals whether energy crossed an interface through translation, rotation, or opposing contributions whose net is small.

4.4 Fractions, Cancellation, and Undefined Ratios

For any additive signed quantity $X = X_d + X_c$, the familiar ratio X_d/X is useful only when X is safely separated from zero. Drift and control can oppose, so the ratio can be negative or exceed 100%; those values are physical sign information, not errors. Near cancellation, however, an arbitrarily large signed percentage is a poor summary. Each table therefore retains the raw values and reports both

$$s_d = \frac{X_d}{X}, \qquad s_c = \frac{X_c}{X}, \tag{4.10}$$

when the denominator is valid, and the cancellation-stable magnitude shares

$$m_d = \frac{|X_d|}{|X_d| + |X_c|}, \qquad m_c = \frac{|X_c|}{|X_d| + |X_c|}. \tag{4.11}$$

The companion cancellation index

$$\chi = 1 - \frac{|X|}{|X_d| + |X_c|} \tag{4.12}$$

is zero when the components reinforce and approaches one when large opposing components leave a small resultant. An attribution atlas without this guard would systematically exaggerate unstable percentages at exactly the joints and phases where the mechanics are most counterintuitive.

4.5 Model Ladder and Common Observables

The same observable contract is evaluated at three levels. Increasing model complexity is used as a stress test, not as a claim that the highest tier is a validated representation of an individual golfer.

4.5.1 Double Pendulum: Exact Minimal Mechanism

The two-link arm–club model has a fixed shoulder, a distributed-inertia arm, a distributed-inertia club, and two generalized controls. Exact equations of motion yield total and zero-command accelerations at every achieved state. The wrist reaction on the club is independently reconstructed from the club free-body equation, and the shoulder reaction is checked against the arm subsystem balance. This tier isolates the central mechanism: a large wrist reaction and positive wrist-force work can exist with zero instantaneous wrist command because the moving proximal segment, gravity, and joint geometry still constrain the club.

The fixed shoulder has no linear path and therefore no shoulder path-force estimand. It does have a transmitted couple and corresponding couple power. The wrist has both a translational path and a rotational interface. Keeping those observables separate prevents the phrase *force along the hand path* from being applied indiscriminately to every joint.

4.5.2 One-Arm Three-Link Tier: Joint-by-Joint Redistribution

The next tier introduces upper-arm, forearm, and club coordinates and reports shoulder, elbow, and wrist actions. The repository implementation uses distal point masses and is therefore a mechanism model rather than a calibrated anatomical limb. Its value is structural: adding an elbow allows the analysis to test whether drift dominance at the wrist implies drift dominance everywhere else. It does not. Each joint has a different distal subsystem, velocity, moment arm, and phase history, so force, couple, impulse, and work shares need not agree either across joints or within one joint.

4.5.3 Two-Arm Closed Loop: Constraint Reactions and Redundancy

The two-arm tier contains seven planar generalized coordinates: two relative joint pairs for the arms and a freely translating and rotating club. Four independent hand-position constraints close both hands on separated grip points. The constraint Jacobian must have row rank four, the mass matrix must remain positive definite, and both the acceleration-constraint and KKT residuals must satisfy declared tolerances. Singular poses fail closed.

This construction avoids a common but consequential shortcut in which the club translation is implicitly anchored to one hand and the second contact is added as if it supplied two further independent constraints. Such a model can return numbers from a least-squares solve while failing to identify the individual contact reactions required for the scientific claim.

4.6 Reference-Case Attribution Results

The three reference cases apply one observable contract but do not pretend to be three measurements of the same swing. The double pendulum is a forward simulation truncated at its first valid club-vertical impact (0.3493 s). The one-arm model is a forward simulation over a declared 0.400 s window. The two-arm closed loop is a 0.400 s, constraint-consistent **local kinematic sweep** with only 0.0425 m of mid-grip travel. Its line integrals diagnose the prescribed path; they are not realized forward-simulation work and are not scaled up to a full downswing.

Table 4.1 reports the MacKenzie-compatible primary estimand at the wrist for the open-chain models and at the mid-grip resultant for the closed loop. Drift is the stitched pointwise ZTCF contribution. Total equals drift plus control at the achieved state. The zero-velocity control-preserved evaluation (ZVCP) is displayed in a separate column because it is not an additive component of that equality; its force is projected on the achieved velocity only to make the diagnostic comparable in units. ZVCP is not canonical ZVCF.

Table 4.1: Primary Hand-Path Force-Work Attribution in the Declared Reference Cases

Model Tier	Path (m)	Total Work (J)	Drift Work (J)	Control Work (J)	ZVCP Projected Diagnostic (J)	$\overline{F}_{\parallel}$ Total / Drift / Control (N)
Double pendulum	2.2241	130.794	132.375	-1.580	-1.588	58.807 / 59.517 / -0.711
One-arm three-link	2.7336	27.802	28.781	-0.979	-1.827	10.170 / 10.528 / -0.358
Two-arm closed loop	0.0425	-0.00381	-0.05236	+0.04855	+0.00188	-0.0898 / -1.2330 / +1.1432

The first two rows answer the central inference question directly. In the double pendulum, the drift contribution is 101.2% of signed force work and the control increment is -1.2%; in cancellation-stable magnitude terms the split is 98.8% drift and 1.2% control. In the one-arm case, the signed split is 103.5% drift and -3.5% control, while the magnitude split is 96.7% and 3.3%. Thus a positive net force-work-per-path-length value can be generated mostly by the state-dependent reaction even while the current command contribution opposes the hand path. The result is about mechanical attribution within the declared trajectories. It does not imply that the achieved states were obtained without earlier control or biological effort.

The two-arm row exposes the opposite interpretive hazard. Drift and control work are individually about an order of magnitude larger than their net and oppose one another. Their magnitude shares are 51.9% and 48.1%, but the cancellation index is 0.962. A signed percentage of the near-zero resultant would exceed 1,000% and obscure the mechanics. Raw work, magnitude shares, and the cancellation index are therefore the defensible summary.

Figure 4.1 shows why the integrated results cannot be inferred from a force peak alone. In the double pendulum, the late positive rise is almost entirely drift. In the one-arm model, drift changes sign and then becomes strongly positive while control remains opposing late. In the two-arm local sweep, much larger opposing drift and control components leave a small net resultant. The dashed ZVCP trace stays distinct from the control increment even when the two happen to be close over part of a history.

Figure 4.2 retains vector direction rather than only the along-path scalar. All four splits use one force-arrow scale within each model row, and both two-hand contacts are shown. The achieved path tangent is a geometric reference, not an additional force. A control vector can therefore look counterintuitive in global coordinates while its tangent projection, normal component, and future geometric effect remain separately identifiable.

Figure 4.3 separates the target-direction component of global vector impulse from force work. For example, the two-arm sweep has a positive 5.57 N s target-direction resultant assembled from -0.40 N s drift and +5.97 N s control, yet its net force work is nearly zero because work also depends on the direction and speed of the mid-grip path. ZVCF bars are again same-configuration projections, not a third additive share.

4.6.1 Every Joint and Time Window

The joint atlas uses total-wrench work, including both force and couple power. Each horizontal bar in Figure 4.4 is $|W_d|/(|W_d| + |W_c|)$ for one joint and one normalized time quartile. The cross is plotted at the corresponding cancellation index when that index is at least 0.25. This presentation keeps all 36 model–joint–window combinations visible without converting cancellation into unstable signed percentages.

The atlas rejects a system-wide label such as “drift dominated.” In the double pendulum, shoulder total-wrench work remains control dominated in all four windows, while wrist drift share rises from less than 1%

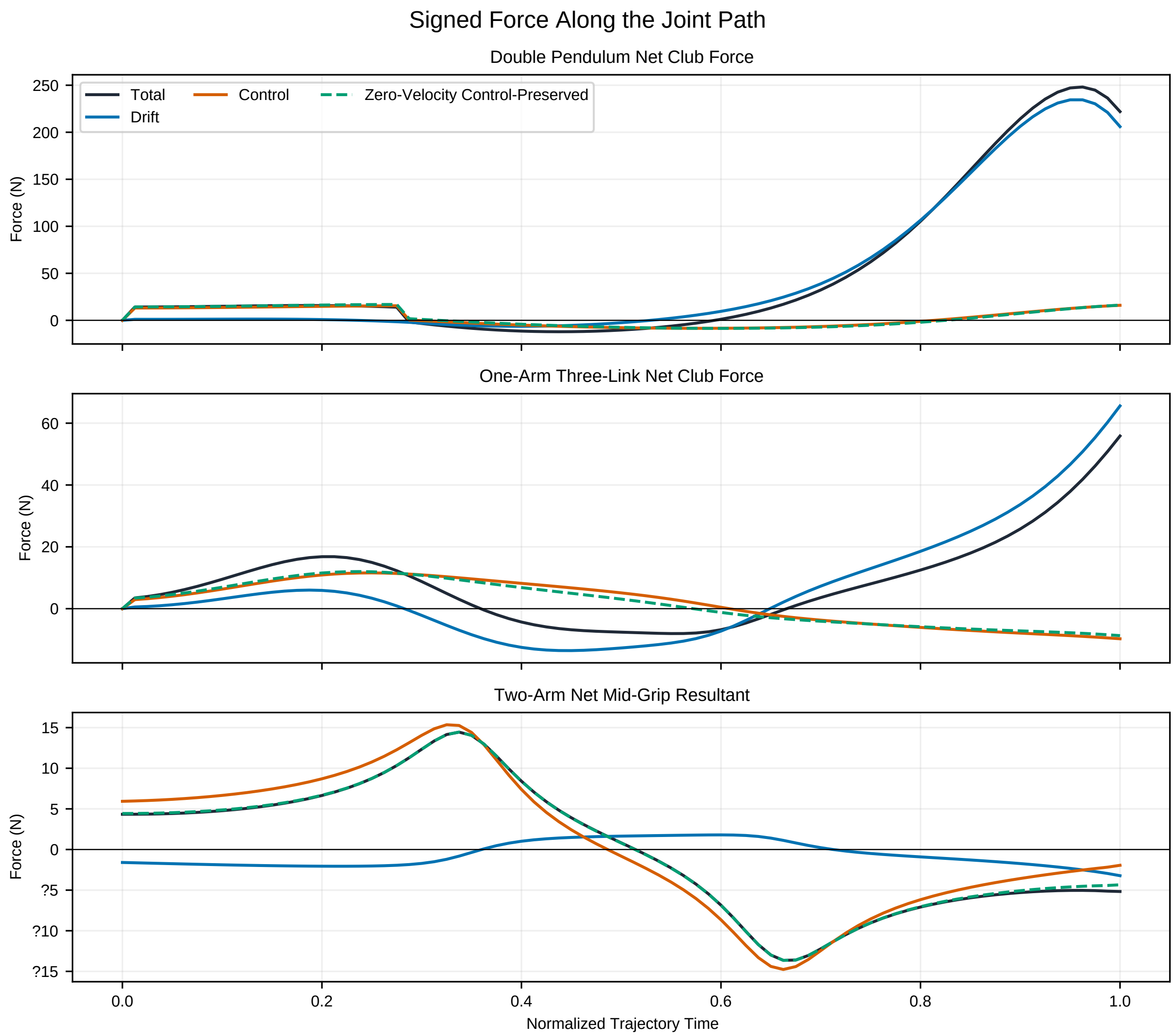

Figure 4.1: Signed Force Along the Achieved Hand Path for the Three Reference Cases

Figure 4.2: Total, Drift, Control, and Zero-Velocity Control-Preserved Force Vectors at Normalized Time Quartiles

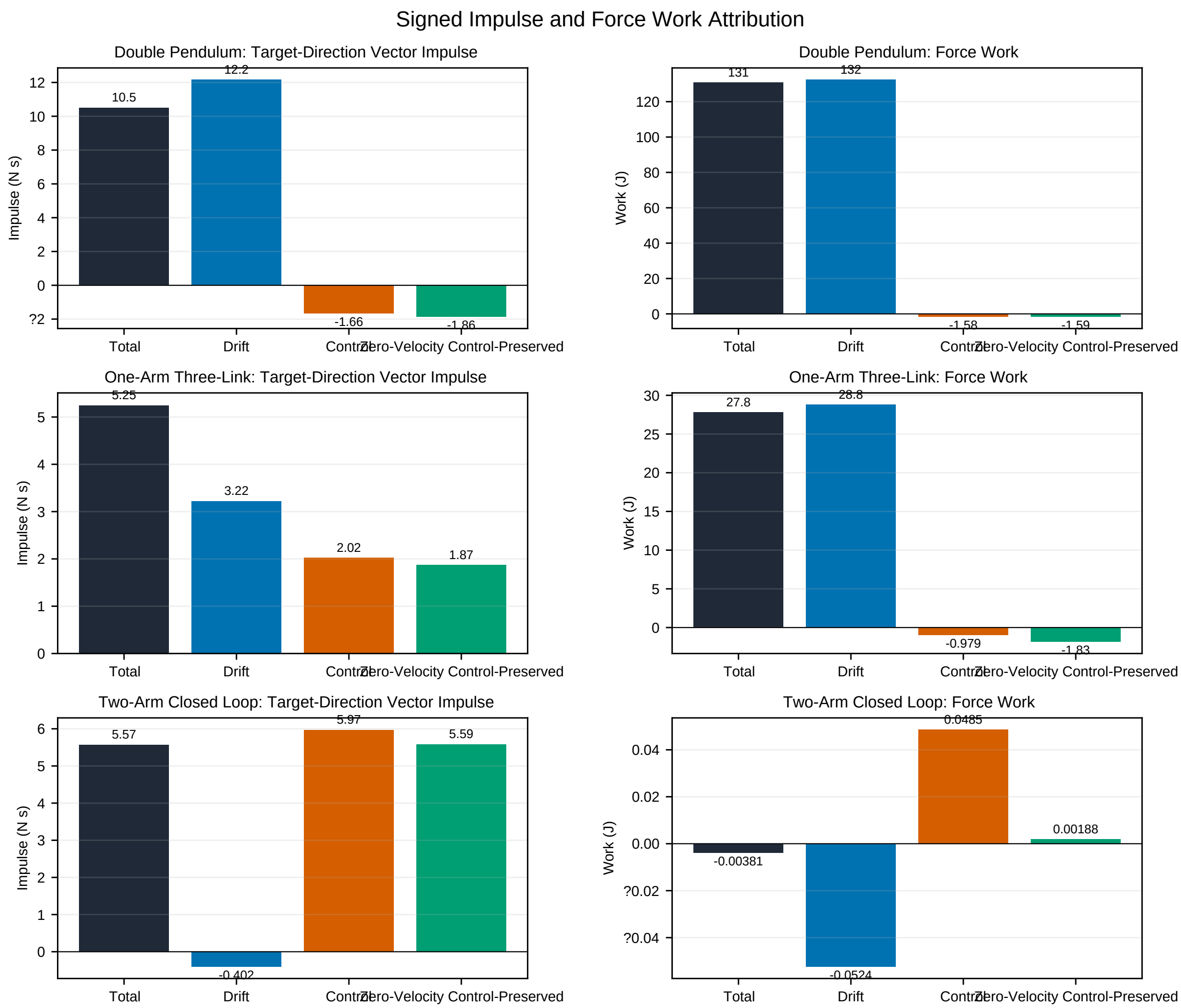

Figure 4.3: Signed Target-Direction Impulse and Force-Work Attribution

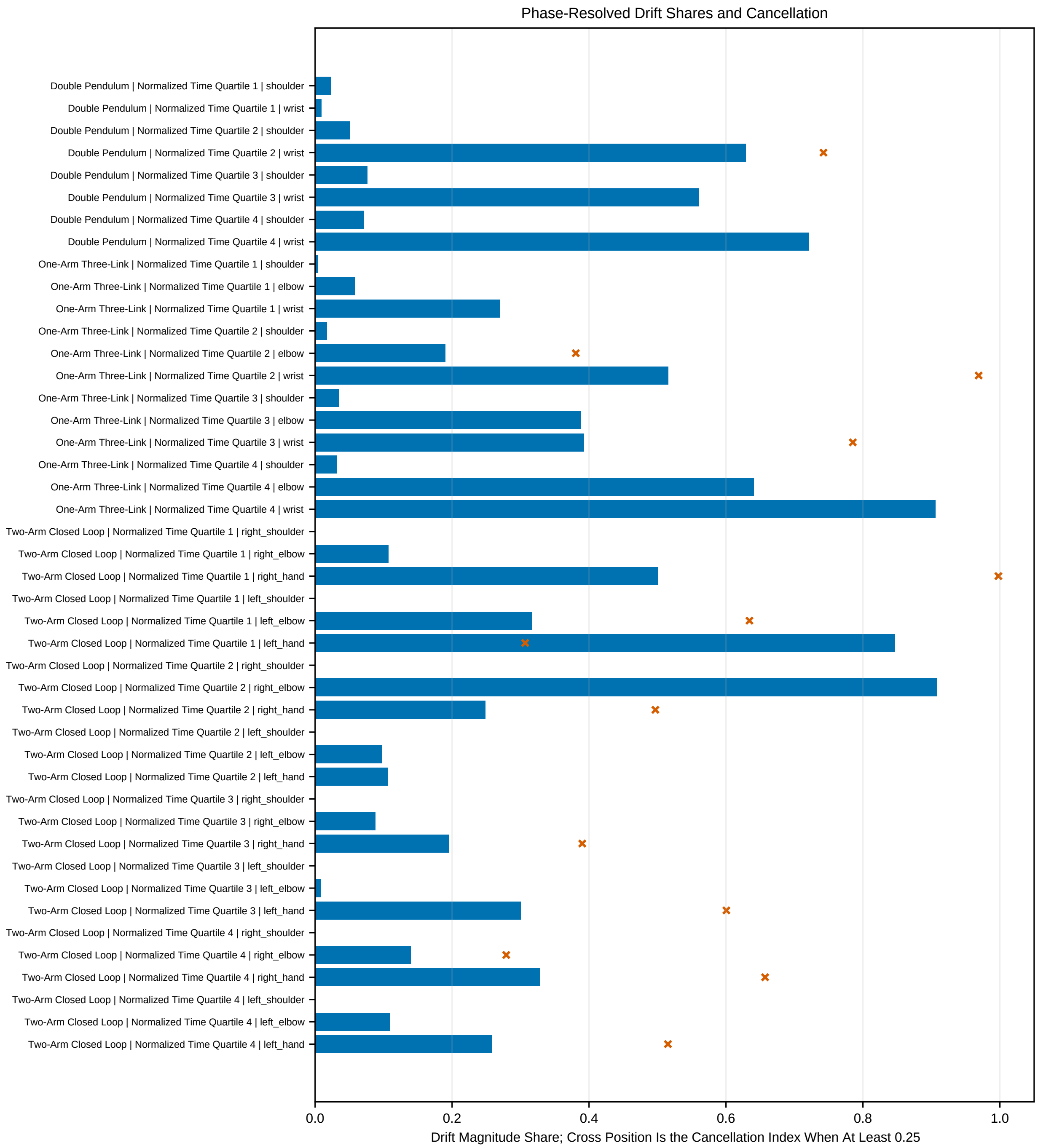

Figure 4.4: Phase-Resolved Drift Work Shares and Cancellation for Every Joint

in the first window to roughly 63%, 56%, and 72% thereafter. In the one-arm case, the shoulder is control dominated throughout, whereas the elbow and wrist become strongly drift influenced late. The two-arm model adds left/right asymmetry and contact redundancy: a drift-dominant hand contact can coexist with a control-dominant shoulder or elbow during the same interval. The exact raw work values and signed shares remain in the JSON evidence rather than being recoverable only from bar lengths.

Power requires an instantaneous guard analogous to the work guard:

$$m_{P,d}(t) = \frac{|P_d(t)|}{|P_d(t)| + |P_c(t)|}, \qquad \chi_P(t) = 1 - \frac{|P_d(t) + P_c(t)|}{|P_d(t)| + |P_c(t)|}. \tag{4.13}$$

Near-zero denominators are undefined and masked. Figure 4.5 plots $m_{P,d}$ for every joint; crosses identify samples with $\chi_P \geq 0.25$. The rapid excursions are a substantive result: an integrated work share can be stable even though the instantaneous power allocation changes quickly or passes through near cancellation. This is why a single peak-power fraction is not substituted for the time history.

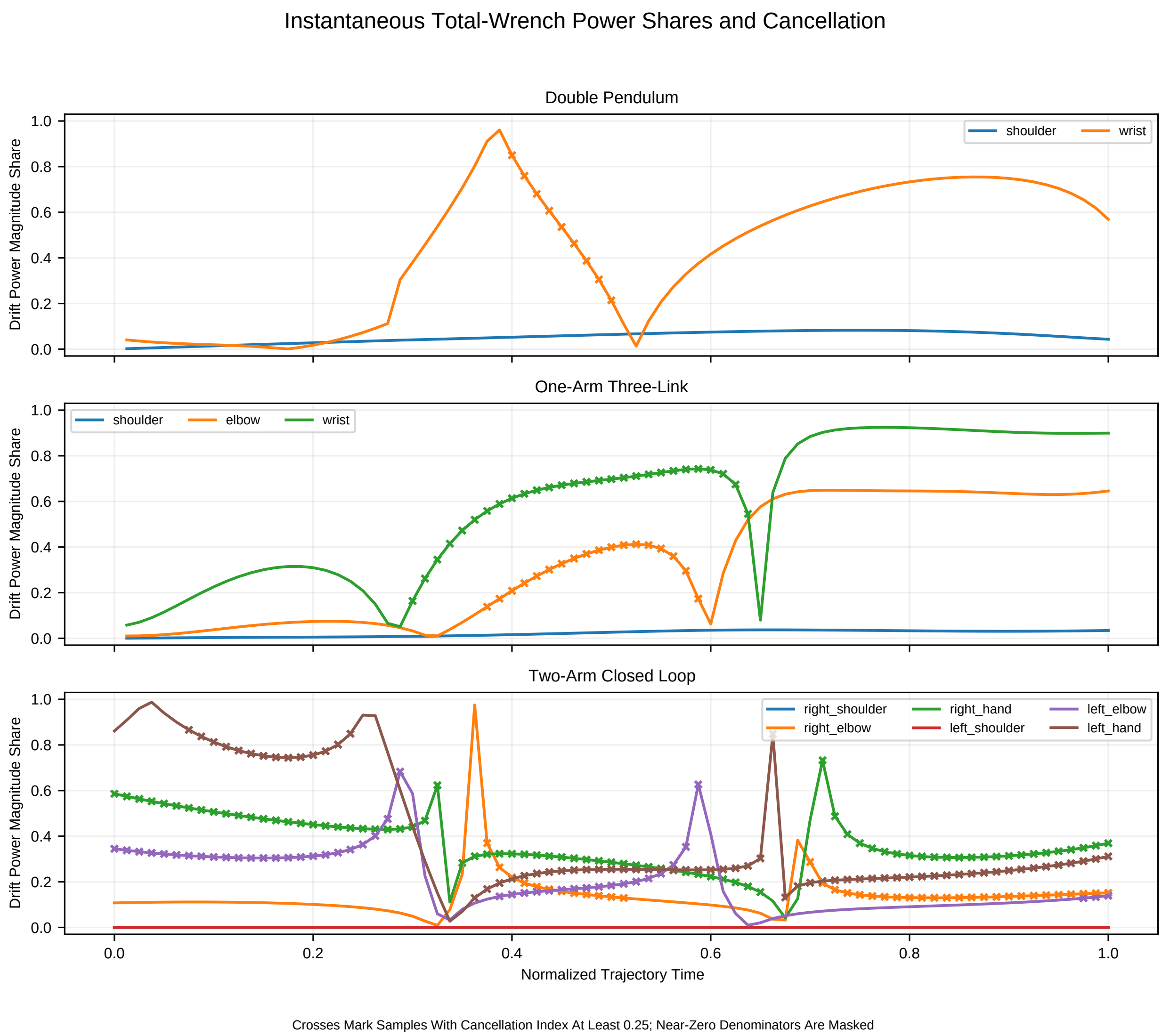

Figure 4.5: Instantaneous Drift Power Shares and Cancellation for Every Joint

4.6.2 Numerical Closure and Resolution Sensitivity

For all three tiers, the maximum additive force and couple residual is below 1.8×10^{-15} in SI units, the maximum power residual is below 2.3×10^{-13} W, and the maximum cumulative-work residual is below 5.7×10^{-14} J. The four windows cover every integration interval once and only once. Coarsening the stored histories from 81 to 41 samples changes primary force work by 0.044 J in the double pendulum, 0.059 J in the one-arm case, and less than 0.001 J in the two-arm sweep. At 21 samples, the respective changes are 1.11 J, 0.29 J, and less than 0.001 J. These are quadrature and sampling checks, not parameter uncertainty or biological validation.

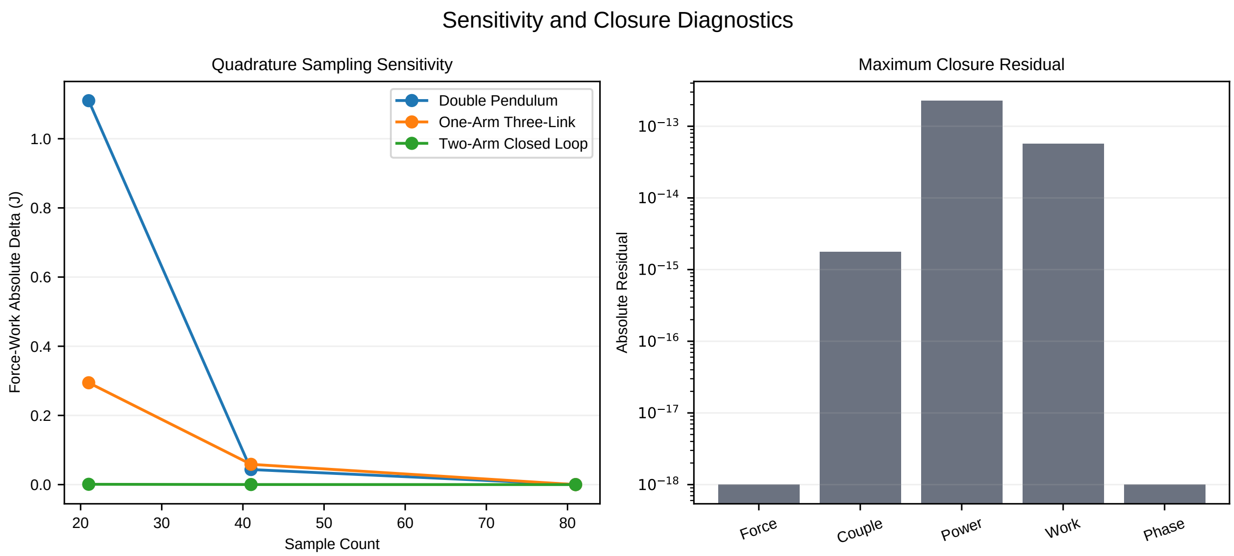

Figure 4.6: Quadrature Sensitivity and Additive Closure Diagnostics

4.7 Two Hands Create Observable and Internal Modes

Let $\mathbf{F}_R$ and $\mathbf{F}_L$ be the right- and left-hand forces on the club. The evidence package uses the explicitly declared convention

$$\mathbf{R} = \mathbf{F}_R + \mathbf{F}_L, \qquad \mathbf{F}_d = \frac{\mathbf{F}_R - \mathbf{F}_L}{2}. \tag{4.14}$$

The common mode is the resultant $\mathbf{R}$. About the grip midpoint, the differential mode creates the force couple

$$\mathbf{M}_{F,M} = -\mathbf{d} \times \mathbf{F}_d, \tag{4.15}$$

where $\mathbf{d}$ points from the right-hand contact to the left-hand contact. Two large opposing forces can therefore produce a small net force and a large club moment. Conversely, a large internal squeeze can increase contact loading while contributing no net rigid-club wrench. Neither the net hand force nor the club's rigid-body work identifies that internal demand (Zatsiorsky and Latash 2008).

The redundancy extends to control allocation. A desired equivalent club moment can be produced by the separated hand-force couple, by applied wrist free torques, or by combinations in which those pathways oppose. Equal net club action does not imply equal joint loading, actuator work, co-contraction, or robustness to perturbation. The constrained model can expose these mechanical alternatives, but without muscles, activation dynamics, and a physiological objective it cannot rank them as human effort strategies. One instructed fast two-hand-grasp experiment likewise produced kinematics nearly indistinguishable from single-hand movement while the hand torques and internal squeeze differed substantially (Reinkensmeyer, Lum, and Lehman 1992). That experiment isolated one strategy in several subjects; it demonstrates non-equivalence of kinematics and internal action, not prevalence or optimality in golf.

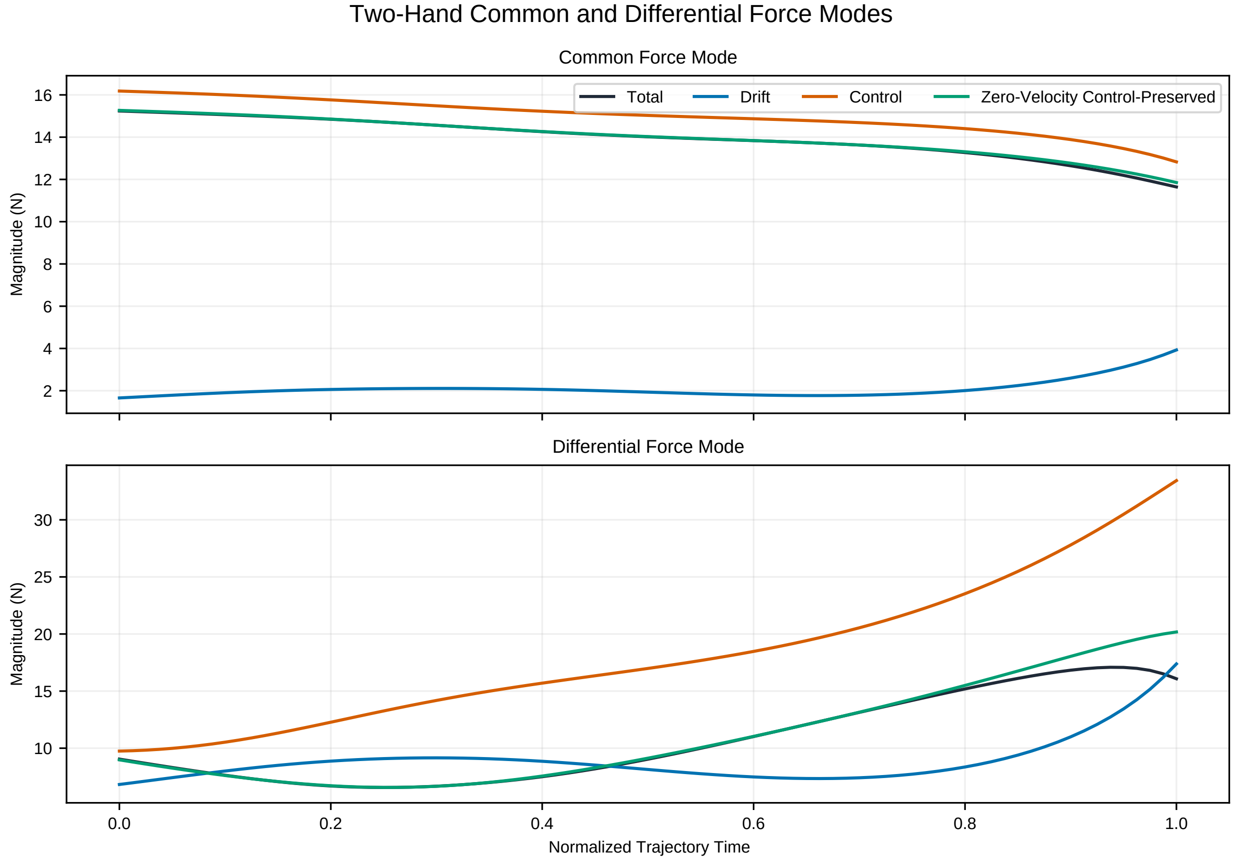

Figure 4.7: Common-Resultant and Differential Two-Hand Force Modes

Figure 4.7 makes the hidden mode visible in the declared local sweep. The common resultant is largely control supplied while the drift contribution remains smaller. The differential-mode magnitudes are larger and diverge late, so the same interval can support a modest net mid-grip force and a substantial separated-contact couple. Magnitudes alone do not identify the sign of that couple; the signed contact vectors and the declared right-minus-left convention are required for that calculation.

4.8 Why an Apparently Counterproductive Control Can Be Useful

Optimal control need not point in the same direction as the instantaneous motion or the net reaction. A control increment may oppose the drift reaction while still improving a later objective through at least four mechanisms:

1. it can retain angular separation and delay distal acceleration;
2. it can rotate the future force vector toward a more useful path projection;
3. it can trade a transient negative actuator work interval for greater later positive force work; and
4. in a closed loop, it can alter the common and differential contact modes without the same change in net club wrench.

Consequently, a negative control force along the path is not automatically a mistake, and a positive drift force is not free propulsion. The achieved state embodies earlier control and energy history. A defensible strategy statement must specify the optimized objective, actuator limits, event definition, and cost of producing that state.

This interpretation is consistent with multijoint reaching evidence in which people exploited or compensated interaction torque differently across the study's speed and load conditions; the authors compared optimal-control costs rather than validating a single force-maximization rule (Vu, Isableu, and Berret 2016). It is supporting upper-limb context, not golf-specific validation or a direct test of the present cost terms.

4.9 Late Reversal and the Preactivation Hypothesis

The archived WSCG result in Section 9 shows a late sign reversal of the force-generated two-hand couple under pointwise zero command. The present closed-loop model makes a related hypothesis testable: an opposed contact mode or wrist command established before that reversal may reduce the size or rate of the command change required when the drift contribution turns favorable. This is a mechanical **prepositioning** or **preloading** hypothesis.

It is not yet evidence of physiological preactivation. That stronger claim requires activation dynamics, electromechanical delay, torque-rate and torque–velocity limits, passive tissue impedance, and a matched physiological cost. It also requires experimental observables capable of separating net club action from individual-hand force and muscle activation. The model can show whether a prior internal-force state changes later wrench attribution; it cannot show that golfers use a neural preactivation strategy or that such a strategy improves performance in humans.

The hypothesis is falsifiable. It would be weakened if the effect disappears under timestep, event-boundary, geometry, and parameter perturbations; if it depends on a rank-deficient contact configuration; if equal-effort actuator models remove the apparent benefit; or if measured two-hand forces and muscle activity do not exhibit the predicted phase relation.

4.9.1 A Bounded Residual-Couple Preview Test

The archived WSCG traces permit one limited part of the hypothesis to be tested without inventing a muscle model. Treat the archived BASE equivalent midpoint couple as a reference, the stitched pointwise ZTCF couple as the reaction available at each achieved state, and their registered DELTA as the required control residual. At the pointwise ZTCF minimum (0.2148 s), the reaction is −19.63 N m while BASE is −22.78 N m. Thus 86.2% of the negative BASE couple at that instant is present in the declared zero-applied-control solve; the required residual is only −3.15 N m. Across the 0.16–0.25 s analysis window, the residual's peak magnitude is 3.18 N m compared with 23.17 N m for BASE.

Those values motivate a narrower signal-allocation hypothesis within this archived decomposition: when drift is recomputed at the achieved state, the additive command target is the residual rather than the net couple. Feeding the entire BASE trace into an additive control channel while also adding the registered drift trace double-counts the same target by construction. This is bookkeeping for the declared split, not a physiological control law. To examine timing, a unit-gain first-order actuator was used solely as a signal model,

$$T_a \dot{C}_a + C_a = C_{\mathrm{cmd}}, \tag{4.16}$$

with the archived BASE and pointwise ZTCF traces held fixed. For the reference $T_a = 30$ ms case, commanding the instantaneous residual produced a late-window tracking RMSE of 1.252 N m. Previewing that same residual by 24 ms reduced the RMSE to 0.531 N m, a 57.6% reduction. By contrast, sending the net BASE couple through the actuator and then adding the drift reaction produced 19.06 N m RMSE. Across assumed time constants from 10 to 50 ms, the best preview ranged from 9 to 35 ms and reduced residual-tracking error by 46.1% to 79.4%.

Figure 4.8 establishes a narrow signal-tracking result: oracle preview can compensate a declared first-order delay when the command targets BASE minus drift. It does not evaluate clubhead speed, muscle activation,

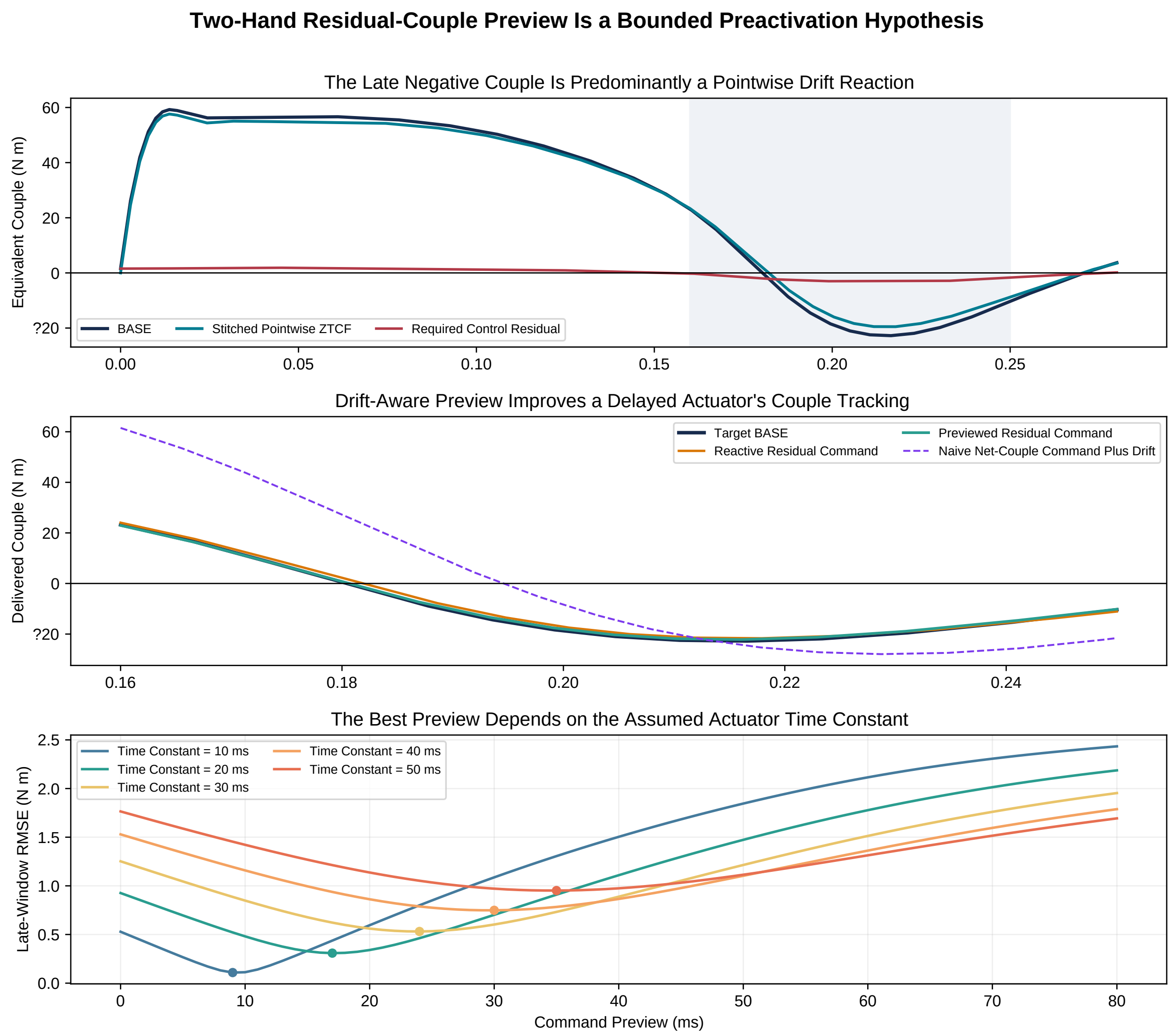

Figure 4.8: Residual-Couple Preview Test for the Archived Two-Hand Model

metabolic cost, or a forward coupled golfer trajectory. The best preview is conditional on the assumed time constant and known future residual; without a causal state estimator or predictor, held-out evaluation, and a forward coupled plant, it is not an implementable controller or a recommended physiological timing value. The study turns anticipation into a reproducible hypothesis with explicit failure conditions rather than presenting preactivation as an observed human mechanism.

4.10 Phase-Resolved Reporting Protocol

Every reference history is partitioned into four nonoverlapping, equal-duration windows whose exact time and sample boundaries are stored with the data. These are named **normalized time quartiles**, not anatomical swing phases. They make the bookkeeping and cross-tier comparisons reproducible, but equal fractions of elapsed time are not assumed to represent equivalent mechanics. When a model or experiment provides independently defined events, a second analysis should replace or supplement these neutral windows with intervals such as:

1. early acceleration and retention;
2. transition toward release;
3. rapid distal acceleration;
4. late drift-reaction reversal; and
5. the final delivery interval.

For every joint and time window, the evidence record stores vector impulse, signed tangent impulse, force work, couple work, total-wrench work, robust shares, cancellation indices, and closure residuals. Dense arrays retain the positive, negative, and absolute tangent-impulse accumulations and the pointwise force, couple, and total-power traces, so peak and sign-specific questions can be recomputed without reconstructing the dynamics. Path length and path-averaged force are reported separately. Total, drift, control, and ZVCF force traces are retained; ZVCF power is not called a realized quantity because its defining velocity is zero. A conclusion is called common across tiers only when its sign and interpretation survive the declared differences in coordinates, mass representation, constraints, and control allocation.

4.11 What the Models Can Establish

The model ladder can establish that a declared fraction of a mechanical reaction, impulse, power, or work is attributable to drift or control within a specified model at a specified state. It can show that drift dominance varies by joint and phase, that a large force may have a weak power projection, and that two-hand internal modes are hidden by the net grip wrench. It can also identify geometries and command allocations that are consistent with late positive transfer.

It cannot convert net force into perceived exertion, muscle activation, metabolic cost, injury risk, or a universal coaching instruction. Those require additional measurements and model layers. The neutral practical implication is therefore diagnostic rather than prescriptive: evaluate how the complete force vector, couple, and interface velocity evolve together, and distinguish the state-dependent reaction from the current command before interpreting a large hand-path force as greater effort.

Chapter 5

Coordinate-Explicit Coriolis, Centripetal, and Gravity Attribution

5.1 Why the Names Need a Contract

The words *Coriolis*, *centripetal*, and *centrifugal* can make a multibody equation sound as though three additional physical agents have appeared. They have not. The physical system still contains applied torques, gravity, damping, constraints, and body-to-body reactions. Coriolis and squared-speed terms are velocity-dependent parts of the same equations after a coordinate system has been chosen. They explain how an achieved configuration and motion redirect the effects of earlier and current loading.

This chapter uses the fixed convention

$$M(q)\ddot{q} + h(q, \dot{q}) + g(q) + d(\dot{q}) = \tau, \tag{5.1}$$

where h is the complete velocity bias. An equation term r_k is reported with its equal-and-opposite generalized **drive** $Q_k = -r_k$. Thus a positive drive accelerates the declared positive coordinate, whereas a positive left-hand-side term resists it. Every figure and data field follows this sign rule.

The first-kind Christoffel symbols are

$$\Gamma_{ijk} = \frac{1}{2}\left(\frac{\partial M_{ij}}{\partial q_k} + \frac{\partial M_{ik}}{\partial q_j} - \frac{\partial M_{jk}}{\partial q_i}\right), \qquad h_i = \sum_{j,k} \Gamma_{ijk}\dot{q}_j\dot{q}_k. \tag{5.2}$$

The registered monomial convention assigns

$$h_i^{\text{sq}} = \sum_j \Gamma_{ijj}\dot{q}_j^2, \qquad h_i^{\text{cor}} = 2\sum_{j<k} \Gamma_{ijk}\dot{q}_j\dot{q}_k. \tag{5.3}$$

The cross-speed terms are called **Coriolis terms** and the squared-speed terms are called **centripetal/centrifugal terms**. Their sum is checked against the provider's independently evaluated h. Any discrepancy is retained as `velocity_residual`; it is never hidden in one of the named sources. The total h is mechanically meaningful within the model, but the cross-versus-squared partition changes under a change of generalized coordinates. A coordinate label is therefore part of every reported result.

5.2 What the Terms Mean in This Pendulum

The double-pendulum study declares q_1 as the absolute arm angle and q_2 as the club angle relative to the arm, so the club's absolute angle is $q_1 + q_2$. Let $K = m_2 l_1 l_{c2}$ be the inertial coupling coefficient. For this coordinate choice, the velocity terms reduce to

$$h^{\text{cor}} = \begin{bmatrix} -2K\sin(q_2)\dot{q}_1\dot{q}_2 \\ 0 \end{bmatrix}, \qquad h^{\text{sq}} = \begin{bmatrix} -K\sin(q_2)\dot{q}_2^2 \\ K\sin(q_2)\dot{q}_1^2 \end{bmatrix}. \tag{5.4}$$

This form gives the names operational meaning:

1. The Coriolis cross term exists only while both the arm and the relative wrist angle are moving. If either rate is zero, it vanishes. Its sign also changes with link geometry through $\sin(q_2)$ and with either rate.
2. The squared-speed terms remain when only one rate is nonzero. The $\dot{q}_1^2$ term is the generalized wrist-coordinate consequence of carrying the distal mass around the proximal pivot; the $\dot{q}_2^2$ term is its reciprocal contribution to the proximal equation.
3. In an inertial free-body diagram, **centripetal** denotes the inward force required to bend a mass trajectory. **Centrifugal** is the outward inertial interpretation used in a rotating frame or generalized-coordinate balance. These are two descriptions of one interaction, not forces to add together.
4. Gravity is configuration dependent rather than speed dependent. Its drive is $-g(q)$ under Equation Equation 5.1, and its power can be positive or negative depending on the direction of motion.

The equations do not say that a golfer consciously creates a Coriolis force. Applied moments and external forces create and reshape the state; the linked system's geometry and velocity then determine the velocity-bias terms. In that limited, useful sense, earlier proximal work can be expressed later as a motion-dependent distal drive. The flow is state mediated, not force free.

> **i** Plain-language picture
>
> Imagine swinging a partly folded two-section ruler. Pulling and turning it builds motion. As the hinge opens, the same moving mass must be redirected, so the ruler pushes back through the hinge. The cross-speed part appears only when the whole ruler is turning *and* the hinge is opening. The squared-speed part is the inward-turning demand associated with either rotation by itself. Gravity tilts the balance throughout. These labels help audit the motion; they do not identify which muscle supplied the original energy.

5.3 From a Generalized Drive to Force Along the Hand Path

MacKenzie, McCourt, and Champoux found that signed linear work per metre of hand travel was strongly associated with clubhead speed in their sample (MacKenzie, McCourt, and Champoux 2020). That observable motivates a hand-path projection, but it does not authorize relabeling every generalized term as a measured hand force.

For endpoint position $x_H(q)$ and Jacobian $J_H = \partial x_H / \partial q$, virtual work requires

$$Q_k = J_H^T F_{H,k} + r_k, \tag{5.5}$$

where $F_{H,k}$ is the minimum-norm force-only equivalent and r_k is the unreconstructed generalized residual. Both are reported. The wrist point in this fixed-hub model depends only on q_1:

$$J_H = \begin{bmatrix} l_1 \cos q_1 & 0 \\ l_1 \sin q_1 & 0 \end{bmatrix}. \tag{5.6}$$

Its rank is one. A two-coordinate generalized drive containing a wrist couple therefore cannot be represented exactly by a single planar force at that point. The contract reports `rank_deficient_force_only` and the residual in N m. The mapped force is useful for a declared along-path comparison, while the residual prevents that comparison from masquerading as a complete grip wrench.

When hand speed exceeds the numerical threshold, the achieved path tangent is

$$e_t = \frac{\dot{x}_H}{\|\dot{x}_H\|}, \qquad F_{\|,k} = F_{H,k} \cdot e_t. \tag{5.7}$$

Zero-speed samples have no tangent and remain undefined. Trajectory integration uses only intervals whose two endpoints have a defined tangent, and publishes valid duration divided by total duration.

5.4 Impulse, Power, and Energy Answer Different Questions

For each source k, the implementation reports

$$I_{\|,k} = \int F_{\|,k}\, dt, \qquad I_{|\||,k} = \int |F_{\|,k}|\, dt,$$

$$P_{q,k} = Q_k^T \dot{q}, \qquad W_{q,k} = \int P_{q,k}\, dt. \tag{5.8}$$

Signed impulse measures directional accumulation; absolute impulse measures how much action occurred before cancellation. Power measures instantaneous energy rate. Work measures its time integral. A large impulse can do little work if it is nearly normal to velocity, and a shorter high-power interval can do substantial work. These quantities must not be substituted for one another.

The generalized work of a Coriolis or squared-speed equation term is a coordinate-explicit kinetic-energy attribution. It is not automatically the energy transferred from arm to club as physical subsystems. That latter claim requires the club free-body balance and wrist reaction-force power developed in Section 3. The two views are complementary: one audits the joint-coordinate equation; the other audits energy crossing a named physical interface.

5.5 Registered Optimization Example

The executable study evaluates a complete, frozen 135-program grid: three shoulder torques (60, 80, and 100 N m), three early wrist-restraining magnitudes (0, 5, and 10 N m), and fifteen drive-onset times from 0.000 to 0.350 s, all followed by a 15 N m wrist drive. Each trajectory is integrated with the ODE reference backend and truncated at the first club-vertical crossing inside the registered delivery zone. Forty-four programs fail that impact gate and are excluded rather than rewarded for additional rotations; 91 qualify.

The primary example maximizes **absolute** Coriolis tangent impulse because the signed values reverse within a swing. A signed companion objective is published so direction and cancellation remain visible. The grid maximum is not a continuous optimal-control solution and not a human technique recommendation.

The two grid-selected programs are:

- **Maximum absolute Coriolis impulse:** shoulder torque 100 N m, early wrist restraint 10 N m, drive onset 0.100 s, absolute/signed Coriolis tangent impulse 13.817/-6.825 N s, and impact speed 46.780 m/s.
- **Maximum clubhead speed:** shoulder torque 100 N m, early wrist restraint 5 N m, drive onset 0.125 s, absolute/signed Coriolis tangent impulse 13.701/-7.033 N s, and impact speed 46.913 m/s.

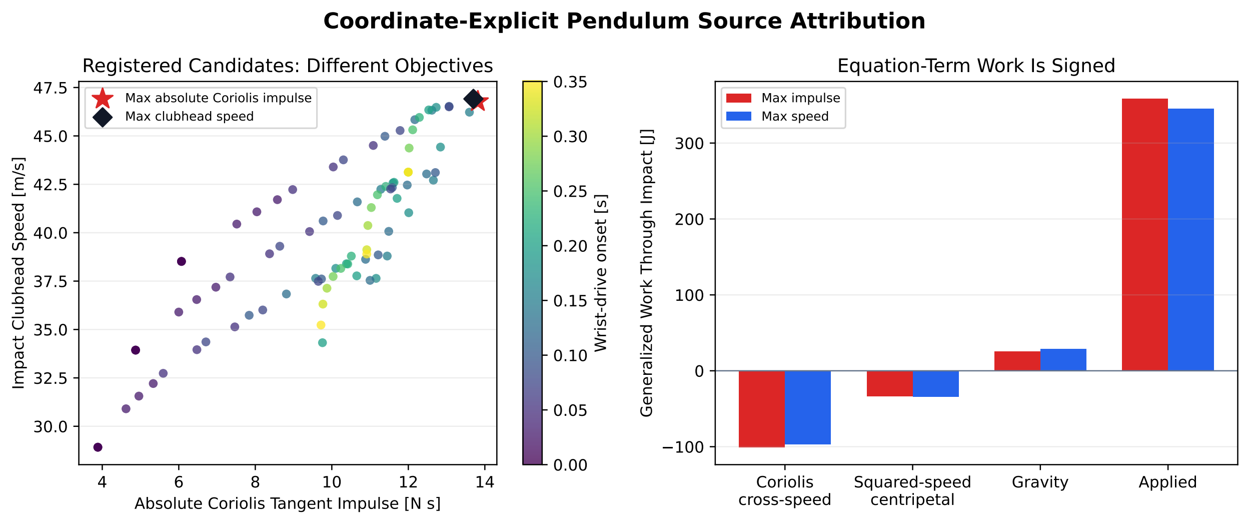

Figure 5.1: The registered search compares absolute Coriolis tangent impulse with impact clubhead speed and signed component work. The two highlighted optima are close but not identical.

For the maximum-impulse program, Coriolis generalized work is -100.69 J, squared-speed work is -33.73 J, gravity work is +25.56 J, and applied-drive work is +358.20 J through impact. The negative Coriolis work does not mean the term was absent: its absolute tangent impulse is the largest in the grid, but its generalized drive opposes the instantaneous generalized velocity on net. That contrast is precisely why impulse and energy-transfer claims are reported separately.

The force-only wrist mapping is rank deficient for every sample. In the two highlighted programs, the maximum retained generalized residual is 54.44 and 52.81 N m, respectively; the hand-path tangent is defined for more than 99.6% of the impact-truncated duration. These diagnostics are part of the result, not footnotes to discard.

5.6 What a Researcher Can Optimize Next

The reusable objective returns the negative signed or absolute component impulse for minimizer-compatible software. A defensible next study can vary a smooth torque history, segment parameters, or event-triggered timing while constraining impact validity, torque, torque rate, joint range, work, peak force, and mapping residual. It should report at least a Pareto surface over

1. clubhead speed or task outcome;
2. signed and absolute Coriolis hand-path impulse;
3. net force-work-per-path-length using the MacKenzie-compatible definition;
4. actuator work and peak applied moment;
5. physical wrist-interface work from the subsystem balance; and
6. robustness on held-out parameter and initial-state distributions.

Optimizing only one named equation term can produce a mechanically extreme trajectory, exploit cancellation, or move work into the actuators. The term is most informative as an explanatory coordinate within a constrained, multi-objective experiment—not as an isolated coaching target.

Chapter 6

Ground-Reaction Drift Attribution

Ground-reaction force (GRF) is the external contact wrench by which the golfer and ground exchange linear and angular momentum. It is measured downstream of the neuromuscular commands, segment interactions, gravity, contact geometry, and inertial motion that jointly determine it. A force-plate trace is therefore neither a direct control signal nor a direct measure of energy transferred to the club. It is a constrained-dynamics observable. A wrench becomes a power quantity only after it is paired with the twist of the same reference point; under an ideal stationary no-slip contact that contact power is zero even though the reaction redirects momentum and changes how internal actuators redistribute energy. This chapter therefore asks the narrower, falsifiable question: **given a declared multibody model and a measured state, how much of its predicted ground-reaction wrench is retained when controllable generalized torques are set to zero?**

The current evidence has two levels. First, a generic constrained-contact solver establishes the algebra and its identifiability conditions. Second, the reference double pendulum provides a deterministic fixed-support benchmark. The latter is a support-reaction analogue, not a human force-plate validation. No bilateral golf force-plate dataset synchronized to whole-body and club kinematics is present in the evidence package, so the human drift fraction remains an open empirical quantity.

6.1 Measurement and Model Boundaries

A six-axis force plate reports an equivalent contact wrench: three force components and three moments about a declared plate origin. The wrench must first be transported to the declared support surface. Under a rigid-ground convention with nonzero vertical force, the two horizontal moment-balance equations then define COP, and transporting the wrench to that COP leaves the vertical free moment. These derived quantities become ill-conditioned as vertical force approaches zero and remain frame-, origin-, surface-height-, and sign-convention dependent. Pressure insoles directly measure local normal pressure rather than the full six-axis wrench; recovering shear force and three-dimensional moments requires an additional model. Joo and colleagues, for example, trained a wavelet neural network against two force plates to predict six-axis reactions from pressure-derived inputs in golf swings from 80 participants; the nonvertical channels were predictions, not direct pressure measurements (Joo, Oh, and Mun 2016).

The golf literature also does not support one universal COP waveform. Ball and Best found two recurring **direction-of-hit** COP clusters among 62 golfers spanning professional through high-handicap levels; the result does not claim that two clusters exhaust two-dimensional COP behavior (Ball and Best 2007). Han and colleagues reported correlations between selected lead- and trail-foot force or moment peaks and maximum clubhead speed in 63 highly skilled men (handicap at most 3) across three club conditions (Han et al. 2019). Worsfold and colleagues measured shoe–natural-turf torque in 24 golfers across handicap, club, and footwear conditions (Worsfold, Smith, and Dyson 2008). A 2026 systematic review retained 24 studies and explicitly called for consistent GRF/COP terminology and methods (Watson et al. 2026). These are sample-specific associations, cluster descriptions, and equipment-condition comparisons, not interventions and not evidence that a particular GRF feature uniquely identifies a biological command.

6.2 Constrained-Reaction Equation

At one state, write the equations of motion as

$$M(q)\ddot{q} + h_0(q) + h_v(q, \dot{q}) = B(q)u + Q_{\text{ext}} + J(q)^{\mathsf{T}}\lambda, \tag{6.1}$$

with acceleration constraint

$$J(q)\ddot{q} + \gamma(q, \dot{q}) = 0. \tag{6.2}$$

Here h_0 is velocity independent, h_v is the term declared to vanish when velocity is zero, u is the declared controllable input, Q_{ext} contains other known applied loads, and λ is the reaction expressed in contact coordinates. Define $A = JM^{-1}J^{\mathsf{T}}$. When M is positive definite, J has full row rank, and A is well conditioned under a declared contact-row scaling,

$$\lambda = A^{-1}\left[JM^{-1}(h_0 + h_v - Bu - Q_{\text{ext}}) - \gamma\right]. \tag{6.3}$$

The implementation uses linear solves, not an explicit inverse. It fails closed when the contact rows are dependent. A pseudoinverse could return one minimum-norm allocation, but that numerical choice would not make the physical left/right allocation identifiable.

Equation 6.3 gives four additive terms:

$$\lambda = \lambda_0 + \lambda_v + \lambda_u + \lambda_e,$$

where

$$\begin{aligned} \lambda_0 &= A^{-1}JM^{-1}h_0, \\ \lambda_v &= A^{-1}(JM^{-1}h_v - \gamma), \\ \lambda_u &= -A^{-1}JM^{-1}Bu, \\ \lambda_e &= -A^{-1}JM^{-1}Q_{\text{ext}}. \end{aligned} \tag{6.4}$$

This is an attribution under a stated model, not a causal identification from force-plate data alone. Modeling errors in M, J, segment inertias, marker kinematics, filtering, or external loads can contribute to residual forces and moments that are not biological controls. Sturdy and colleagues optimized OpenSim residual-reduction tracking weights in running simulations, while Werling and colleagues jointly adjusted inertial parameters and kinematics in an automated motion-processing pipeline (Sturdy, Silverman, and Pickle 2022; Werling et al. 2023). Those methods document and reduce dynamic inconsistency; neither makes the residual a direct measurement of unmodeled muscle action or validates the present golf decomposition.

6.3 Ground-Reaction ZTCF and ZVCF

The ground-reaction zero-torque counterfactual (ZTCF) sets $u = 0$ at the achieved $(q, \dot{q})$ while retaining declared non-control external loads:

$$\lambda_{\text{ZTCF}} = \lambda_0 + \lambda_v + \lambda_e.$$

For an autonomous holonomic constraint, with $h_v(q, 0) = 0$ and $\gamma(q, 0) = 0$, the ground-reaction zero-velocity counterfactual (ZVCF) evaluates the same configuration with both velocity and declared applied control set to zero:

$$\lambda_{\text{ZVCF}} = \lambda_0 + \lambda_e.$$

The formerly labeled quantity $\lambda_0 + \lambda_u + \lambda_e$ is retained as the explicitly named **zero-velocity control-preserved reaction**. This distinction prevents a control-retaining intervention from being mistaken for a zero-control counterfactual.

For a rheonomic contact or any convention in which a velocity-zero constraint bias remains, the reaction must instead be recomputed with that retained term; the displayed shortcut is not valid. Both counterfactuals are **pointwise**. Neither advances a zero-torque or zero-velocity system through time. They also overlap in $\lambda_0 + \lambda_e$; consequently, $\lambda_{\text{ZTCF}} + \lambda_{\text{ZVCF}}$ is generally not the total reaction. The complementary additive split is instead configuration, velocity, control, and other-external reaction in Equation 6.4.

Within the declared split, λ_0 supplies the configuration-dependent support baseline, λ_v can create phase-dependent shear and vertical features through centripetal, Coriolis, and constraint-bias terms, and λ_u captures how applied generalized torques alter the constraint reaction. Similar-looking peaks can arise from different combinations. This is why timing coincidence between a GRF peak and a distal-speed increase does not by itself establish energy transfer through that force peak.

6.4 Fixed-Support Double-Pendulum Benchmark

The first executable case evaluates the shoulder support reaction of the same impact-truncated planar double pendulum used elsewhere in this report. At each of 161 achieved states, the analysis independently evaluates total, ZTCF, ZVCF, and zero-velocity/zero-control support forces. The fixed shoulder is an ideal support; it has no feet, COP, free moment, pelvis, or transverse-plane motion. Its purpose is to test the decomposition before introducing those degrees of freedom.

The additive identities close to 5.7×10^{-14} N for the total split and 1.9×10^{-13} N for the independently evaluated zero-velocity control-preserved identity. Treating ZTCF as a drift-only predictor of the modeled total support reaction gives $R^2 = 0.871$ in the target-horizontal component and $R^2 = 0.814$ in the swing-plane vertical component. These are fixed-prediction coefficients of determination, not squared correlations or fitted-regression results. The corresponding RMSE values are 64.6 N and 89.8 N, with biases of -14.2 N and +71.1 N. The RMSE values are 1.02 and 1.42 times the model's projected planar-weight scale, respectively. The predictor captures substantial waveform variance but fails an absolute-error adequacy screen; R^2 alone would overstate performance.

The total vector impulse is $(22.92, 35.20)$ N s. ZTCF contributes $(17.91, 60.12)$ N s, while control contributes $(5.01, -24.93)$ N s. The vertical result is a clear cancellation case: the passive/configuration-plus- velocity impulse exceeds the total because control opposes it. A "percent of total" ratio would therefore exceed 100% and should not be interpreted as a fraction of biological effort.

6.5 Relation to Common Golf GRF Patterns

The decomposition suggests testable, not prescriptive, interpretations:

1. **Vertical force peaks.** A peak can include configuration support, velocity-dependent vertical acceleration, and input-induced reaction. The declared algebraic velocity-term kill tests what remains after removing the terms that vanish at zero velocity; a physical ZVCF additionally requires the autonomous-constraint condition stated above. Zeroing control tests how much persists without the declared input at the achieved state.

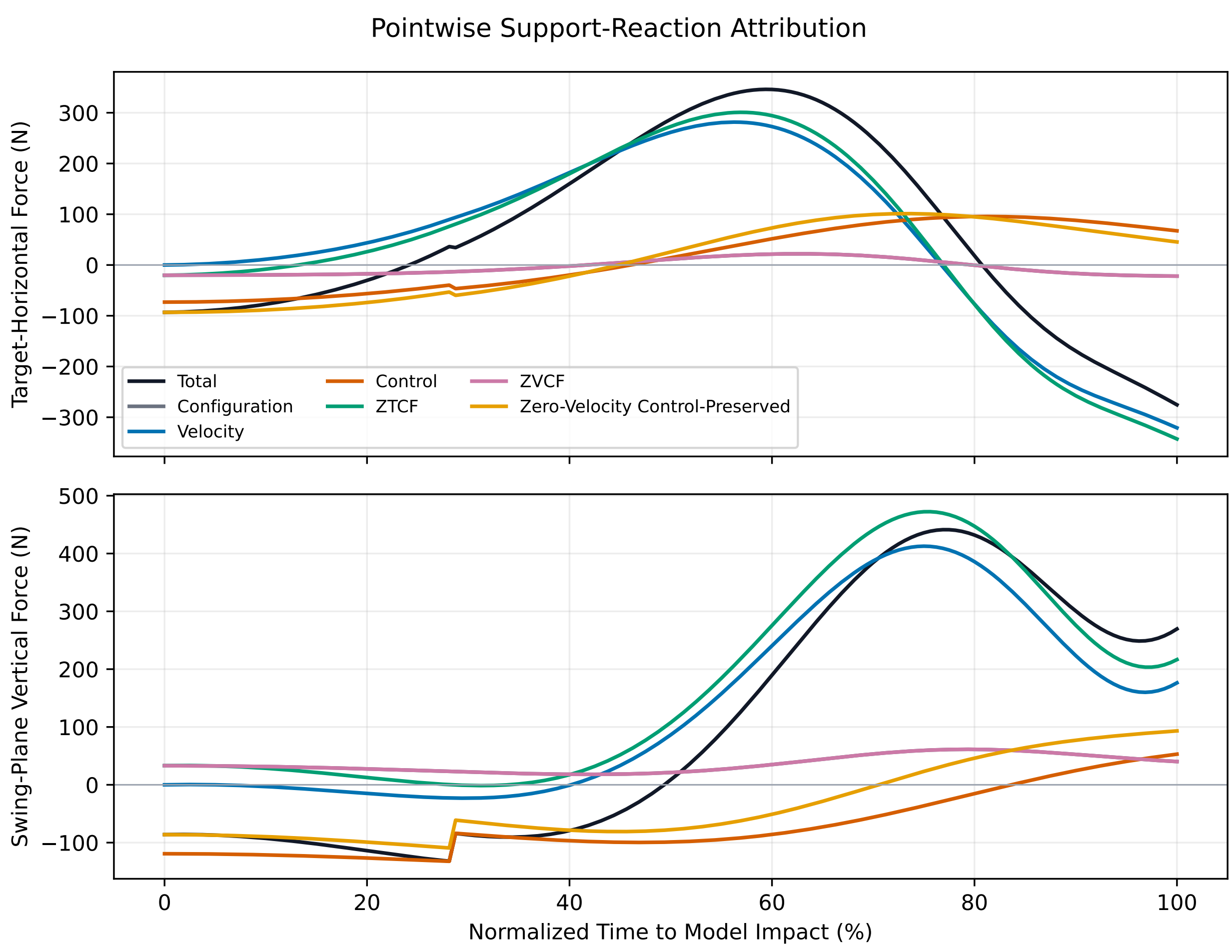

Figure 6.1: Pointwise Support-Reaction Attribution

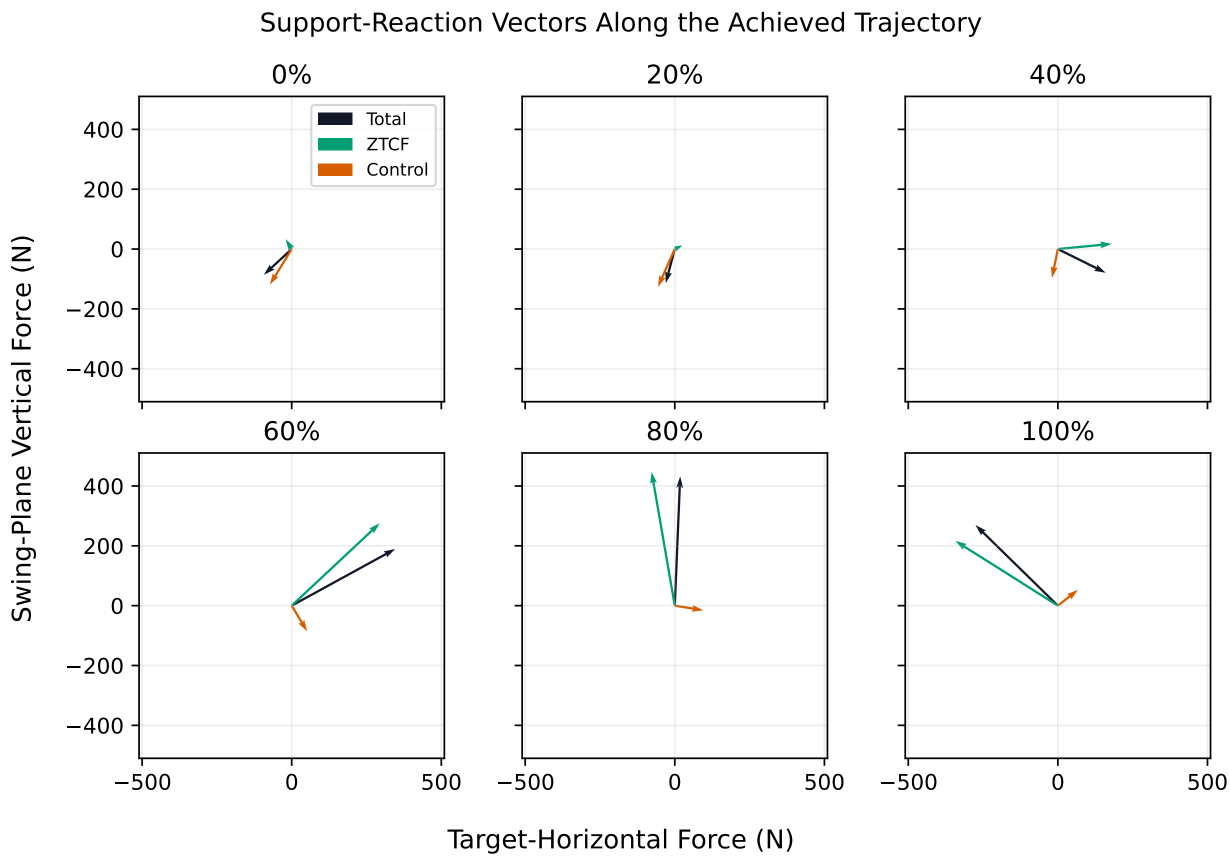

Figure 6.2: Support-Reaction Vectors Along the Achieved Trajectory

2. **Anterior–posterior and medial–lateral shear.** These components are especially sensitive to frame definition, foot contact geometry, and moving-base terms. A resultant whole-body shear prediction does not specify its bilateral allocation.
3. **COP migration.** COP is a ratio derived from force and moment. It cannot be recovered from a planar point support and should not be decomposed by independently dividing component forces and moments. Each counterfactual wrench must first be reconstructed, then mapped to COP with low-force samples masked.
4. **Free moment.** The vertical free moment requires a three-dimensional distributed contact model. It is not present in the planar benchmark. The two-hand negative-couple mechanism elsewhere in this report is analogous in its force-couple geometry, but it is not evidence that a measured foot-ground free moment has the same source.
5. **Pressure transfer.** COP or plantar-pressure migration is not mass transfer and is not identical to energy transfer. Different COP strategies can be viable (Ball and Best 2007).
6. **Net force and center-of-mass motion.** For the complete golfer-plus-club system, net GRF force must close the Newton–Euler identity against total center-of-mass acceleration, gravity, and any other external loads. That is a required consistency check, not a competing empirical theory. The model's additional burden is to predict moments, bilateral allocation, and counterfactual changes without merely reconstructing the measured wrench.

6.6 Human Falsification Protocol

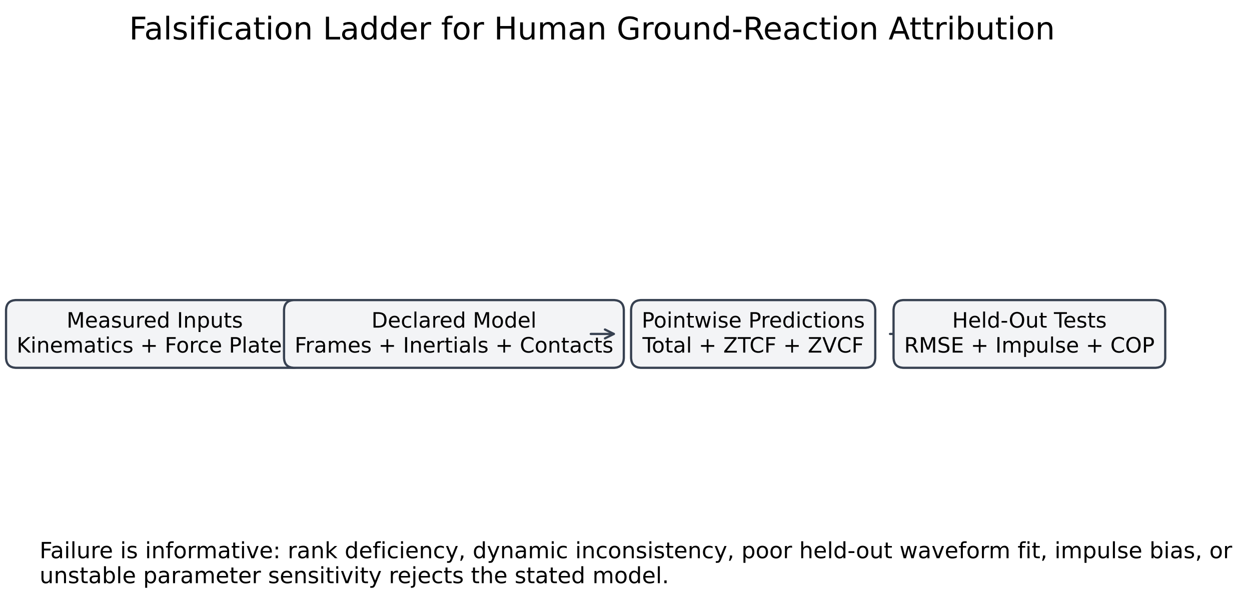

Figure 6.3: Falsification Ladder for Human Ground-Reaction Attribution

A human test requires synchronized bilateral six-axis force plates, whole-body and club kinematics, segment inertial estimates, and declared contact, frame, wrench-origin, and filtering conventions. Model calibration must be confined to training participants. The primary endpoint should be participant-held-out waveform error for each force and moment component, supplemented by vector impulse error, signed bias, peak timing error, COP error during adequately loaded samples, and free-moment error. Randomly splitting time samples or swings from the same participant between training and test sets is not an independent validation.

The following rejection criteria make the framework falsifiable:

- the full modeled wrench does not reproduce measured force and moment within preregistered tolerances;
- residual pelvis forces or moments remain large relative to measured GRF;
- ZTCF/ZVCF shares change qualitatively under plausible inertial, filtering, coordinate, or contact-model perturbations;
- a claimed bilateral attribution is not invariant across equally admissible contact allocations;
- a drift-only model fails held-out component, impulse, or event-timing tests; or
- net modeled force fails the center-of-mass acceleration, gravity, and known- load identity, or the decomposition adds no held-out predictive information for moments, bilateral allocation, or registered counterfactual outcomes.

The machine-readable evidence records the declared frame, scale, component impulses, closure errors, prediction metrics, nonidentifiable quantities, and source hashes. This separates the demonstrated algebra and planar benchmark from the still-unmeasured human hypothesis.

Chapter 7

Proximal Velocity, Geometry, and Drift-Mediated Transfer

7.1 The Question Must Be Posed as a State-Matched Counterfactual

The motivating hypothesis is that releasing while the proximal system is moving rapidly can permit the club to gain speed with less opposing interface work. The subjective description of such motion as a "fling" is not itself an observable. Moreover, the phrase *high shoulder velocity* conflates at least four quantities: thorax angular velocity, shoulder-joint velocity, hand-path velocity, and the angular velocity of the proximal link in a reduced pendulum. This section tests only the last quantity. In the model, $\dot{q}_1$ is the angular velocity of the proximal rigid link about a fixed hub. It is neither measured thorax rotation nor an anatomical shoulder-joint coordinate.

The distinction matters empirically. Horan and Kavanagh measured 14 male professional golfers and reported the largest upper-body peak speed at the thorax together with strong thorax–pelvis coupling; neither the sample nor cross-correlation identifies a causal club-transfer mechanism (Horan and Kavanagh 2012). A systematic review of 92 kinematic studies found substantial methodological variation and insufficient consensus for generalizing many performance results (Bourgain et al. 2022). Choi and Park instrumented an axially divided grip in nine registered professional golfers and reported counteracting hand forces and asymmetric inferred hand kinetics; that result shows why a net club wrench does not uniquely identify its bilateral allocation, but it is not a direct six-axis measurement at each hand (Choi and Park 2020). The present result is therefore a model-level map from achieved state to instantaneous acceleration, interface-force, and power contributions. It is not a human causal result or a coaching rule.

At a fixed configuration q and applied torque u, the implementation uses the sign-explicit equations

$$M(q)\ddot{q} + b(q, \dot{q}) = Bu, \qquad \ddot{q}_{\text{drift}} = -M^{-1}b, \qquad \ddot{q}_{\text{control}} = M^{-1}Bu, \qquad \ddot{q} = \ddot{q}_{\text{drift}} + \ddot{q}_{\text{control}},$$

where the drift term is evaluated at the achieved state with the modeled controls zeroed. Here b contains the model's velocity-dependent, gravity, and damping terms. It does **not** mean passive human motion. The planar wrist- interface force on the club is reconstructed from the same pointwise acceleration split; dotting each force with the wrist-point velocity gives its interface power. Acceleration, force, and power must close componentwise before a sample is admitted.

7.2 Three Velocity-Matching Rules

Changing $\dot{q}_1$ alone is not a unique intervention because the distal angular rate may be expressed either relative to the proximal link or in the laboratory frame. We therefore evaluate three declared counterfactual families:

1. **Preserve Relative Club Rate:** hold $\dot{q}_2$ fixed while changing $\dot{q}_1$. This co-transports the club's absolute angular rate with the proximal link while leaving the relative coordinate rate fixed.
2. **Preserve Absolute Club Rate:** hold $\dot{q}_1 + \dot{q}_2$ fixed while changing $\dot{q}_1$. This changes the relative rate and asks whether proximal speed alone improves the transfer when distal laboratory-frame angular rate is matched.
3. **Preserve Total Kinetic Energy:** hold $T = \frac{1}{2}\dot{q}^\top M(q)\dot{q}$ fixed. For each feasible proximal rate, solve the mass-matrix quadratic for the relative club rate and select the branch continuous with the reference state. This removes instantaneous stored kinetic energy as an explanation, but not the prior work used to create the state.

At five samples from one registered reference trajectory, nine proximal rates are evaluated for each rate-matching rule. The grid is centered on the achieved proximal rate and adds offsets from -75% through +75% of $\max(|\dot{q}_{1,\mathrm{ref}}|, 4\ \mathrm{rad\,s^{-1}})$, so every family contains its reference state and the zero-rate transition sample remains testable. The labels Transition, Early Downswing, Mid-Downswing, Delivery and Release, and Pre-Impact refer to 0%, 15%, 40%, 70%, and 95% of this model's time to club-vertical crossing; except for the endpoint definitions, they are not human event detections. Configuration, torque command, model parameters, and gravity are held fixed within a family. The energy-matched family spans the feasible reference branch at each nonzero-energy phase. Transition begins at zero velocity, for which the only zero-kinetic-energy velocity state is the zero vector; its energy-matched dose is therefore non-identifiable and explicitly omitted. The first two rules change kinetic energy. All three are local state-field sensitivity sweeps, not trajectory optimizations.

7.3 Phase-Resolved Results

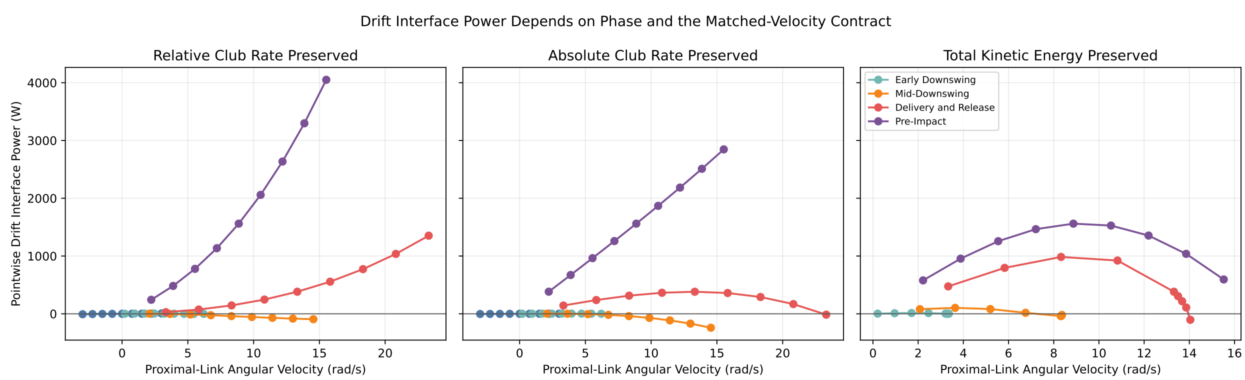

Figure 7.1: Drift interface power across proximal angular-velocity sweeps. Each panel states the velocity-matching rule; the large late-swing benefit is not invariant to that rule.

The result rejects a phase-independent benefit. Under relative-rate matching, the least-squares slope of drift interface power with proximal rate is +1.97 W/(rad/s) at transition, -0.80 in early downswing, -8.25 in mid-downswing, +65.06 in delivery, and +283.74 before impact. Under absolute-rate matching, the corresponding slopes are +0.84, +0.09, -18.78, -5.96, and +184.58 W/(rad/s). These slopes describe the declared finite ranges and are not derivatives at the reference state. The associated linear-fit R^2 values range from 0.028 to 0.999; in particular, the early absolute-rate and delivery absolute-rate slopes summarize strongly nonlinear responses poorly. Reference-centered three-point slopes are therefore reported separately; the delivery absolute-rate value is -0.92 W/(rad/s), versus -5.96 W/(rad/s) over the full range. The largest positive endpoint change survives both matching rules only in the pre-impact state. Delivery remains strongly positive when relative club rate is preserved but has a negative endpoint change when absolute club rate is preserved.

The energy-matched result is more adverse to a monotonic rule. Its drift-power slope is -1.77 W/(rad/s) in early downswing, -22.98 in mid-downswing, -56.71 in delivery, and +5.70 before impact. None of the four energy-matched curves is monotonic. Before impact, the fitted R^2 is only 0.005 and the endpoint change is +15.72 W, compared with +3807.53 W when relative club rate—and thus stored energy—is allowed to co-vary. The maximum kinetic-energy residual across 36 energy-matched states is 5.7×10^{-14} J. This does not prove that proximal speed is harmful; it shows that the largest apparent benefit is not invariant to stored-energy control.

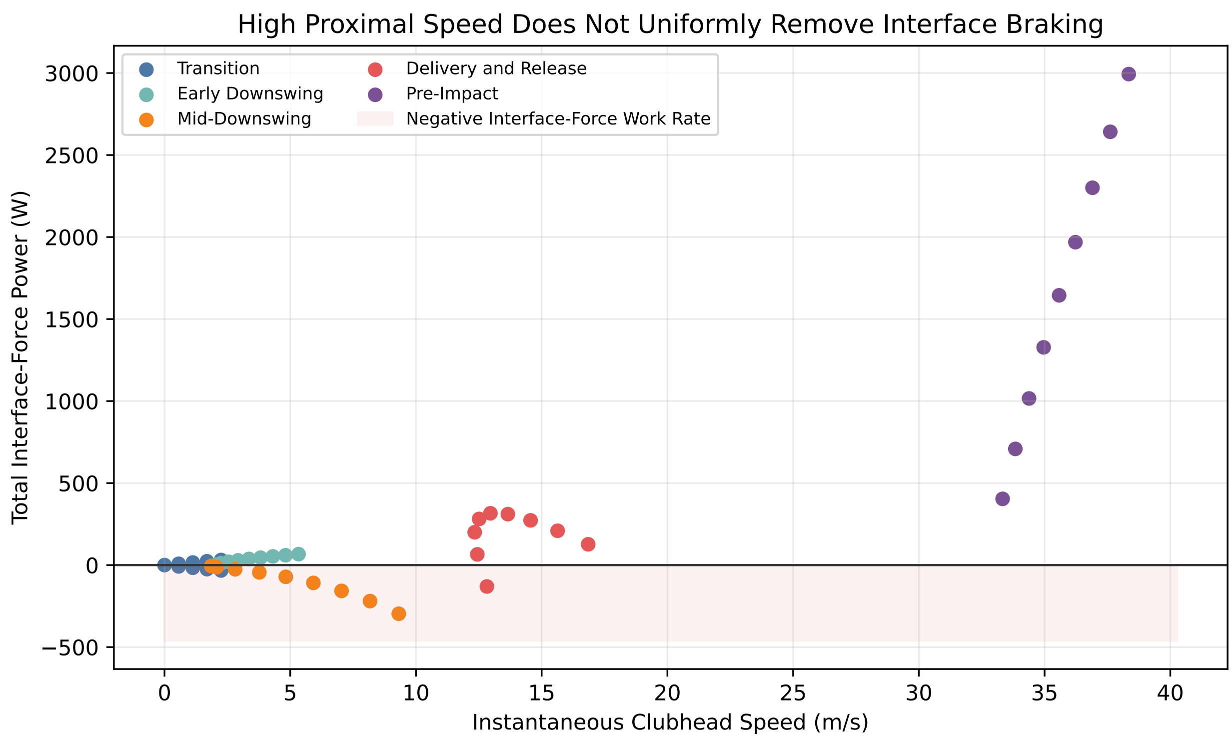

Figure 7.2: Negative interface power across phase and velocity-matching rule. Shading marks states in which the modeled wrist reaction removes mechanical energy from the club at that instant.

The braking map supplies the sharper test of the motivating hypothesis. Higher proximal velocity does not uniformly reduce braking. Mid-downswing contains the strongest opposing region: minimum pointwise grip power reaches −148.8 W under relative-rate matching and −296.5 W under absolute-rate matching. In delivery, relative-rate matching contains no negative grip-power sample, whereas absolute-rate matching reaches −130.2 W. The apparent "clean fling" is therefore a relationship among phase, configuration, sweep range, and relative motion, not a consequence of proximal speed in isolation. Across the transition sweep, the newly included negative proximal-rate states also reach -37.1 W and -32.8 W under the two matching rules.

7.4 Proximal Acceleration as a Separate Intervention

Velocity and acceleration are not interchangeable. A third pointwise study holds configuration, velocity, model parameters, gravity, and distal actuator torque fixed, then solves the proximal actuator torque required to impose each of nine proximal accelerations at each of the five phases. Every row therefore has the same state and instantaneous kinetic energy within its phase, but not the same actuator torque, instantaneous power, accumulated work, or prior reachability. Target-acceleration residual is below 5.7×10^{-14} rad/s² and force closure is exact at stored precision.

At transition, grip velocity is zero, so every acceleration target has zero instantaneous interface power; this is a geometric null, not an absence of required torque. Across early, mid, delivery, and pre-impact phases,

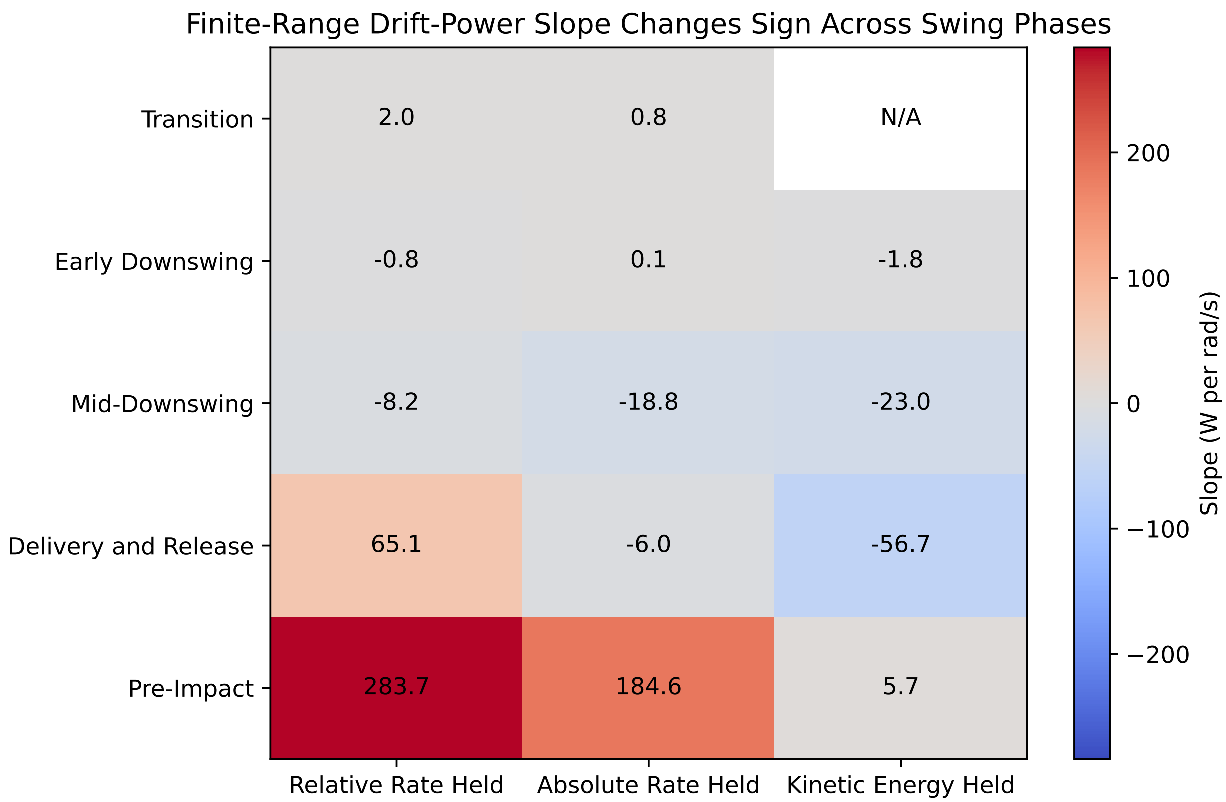

Figure 7.3: Signed finite-range slope of drift interface power with proximal angular velocity. Positive cells indicate that faster proximal motion increases drift-mediated interface power within the declared local sweep.

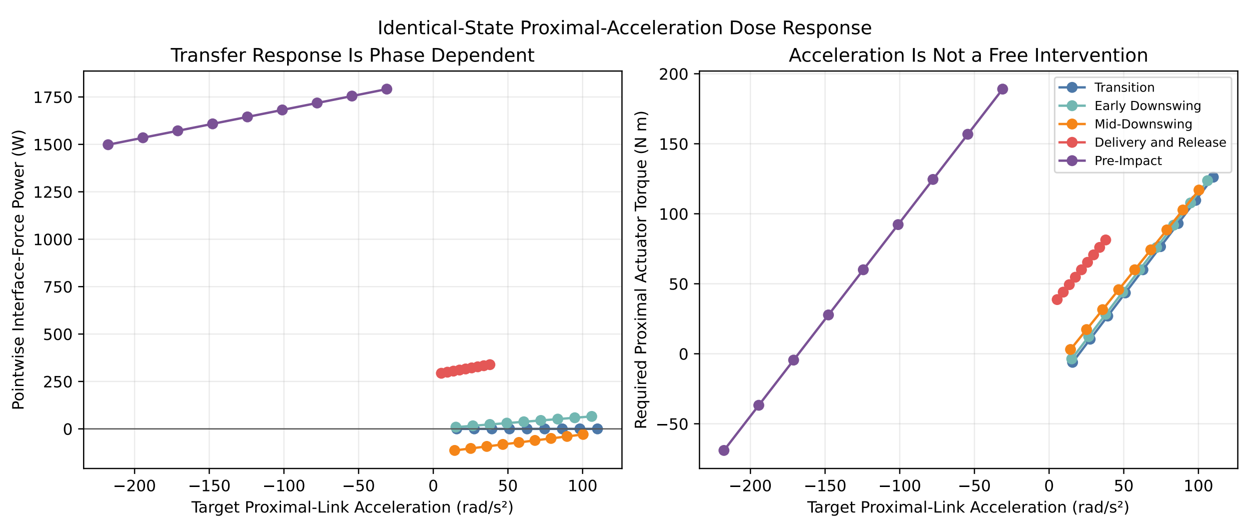

Figure 7.4: Identical-state proximal-acceleration interventions. The left panel reports interface-force power; the right exposes the proximal torque needed to impose the acceleration.

interface- power slopes are +0.62, +0.98, +1.40, and +1.57 W per rad/s². That result does not imply that continued proximal acceleration always accelerates the club. The club-angular-acceleration response slope is +0.116, +0.573, and +0.619 in the first three nonzero phases but reverses to -0.287 before impact. In that pre-impact state, the proximal torque required across the dose ranges from -69 to +189 N m and proximal actuator power from -612 to +1677 W. Increasing proximal acceleration can therefore raise interface power while reducing the club's instantaneous angular acceleration and changing actuator/load cost. Only a forward, work- and load-matched intervention can determine whether that pointwise response improves delivery.

7.5 Trajectory-Level Strategy Search

The pointwise sweep does not show whether a control program can reach a favorable state. A second experiment therefore varies three trajectory-level decisions: the time at which the 60 N m proximal drive is reduced (0.12, 0.18, 0.24, or 0.30 s), the post-cut proximal torque (0, 30, or 60 N m), and the wrist release time (0.10, 0.14, 0.18, 0.22, or 0.26 s). Every program uses a 10 N m opposing wrist command before release and a 15 N m drive afterward. All 60 attempted programs are retained; only 26 cross club vertical inside the registered delivery window.

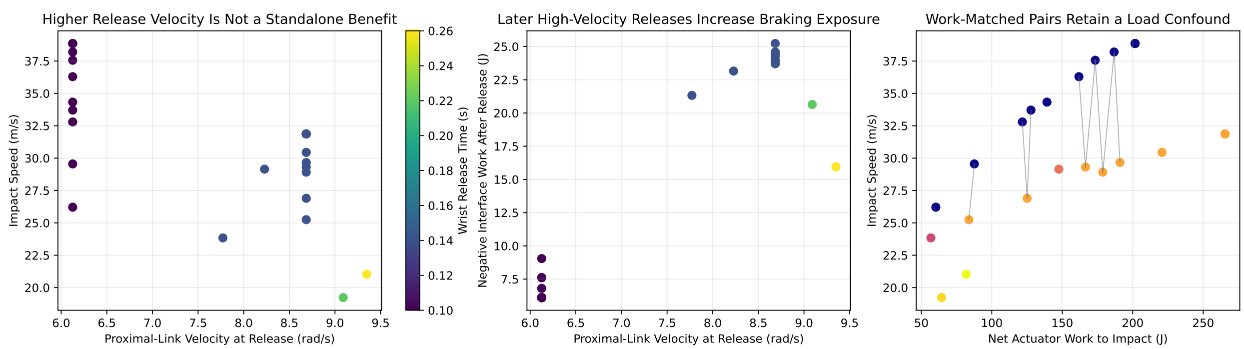

Figure 7.5: Release-state proximal velocity against impact speed and negative interface work, followed by impact speed against net actuator work, for every valid- impact trajectory. Color denotes release time in the first two panels; gray connectors identify the approximate work-matched pairs in the third.

Within this finite grid, the motivating model hypothesis does not survive as a standalone rule. Proximal-link velocity at release correlates with lower impact speed ($r = -0.692$) and greater post-release negative grip work ($r = +0.943$) among the valid trials. In a descriptive standardized regression that also includes release time, proximal-drive cut time, and post-cut proximal torque, the release-velocity coefficient remains negative ($\beta = -0.514$). The 26-row design has rank 5 for five coefficients including the intercept and condition number 3.51, but no sampling-based uncertainty interval is meaningful for this deterministic grid. This is not a causal estimate: release velocity and timing are mechanically coupled, the grid is small, and conditioning on valid impact creates selection. It nevertheless supplies a model counterexample to the claim that waiting for the modeled proximal link to attain a larger angular velocity is sufficient to improve transfer.

The forward ledger now integrates proximal and distal actuator power from the start of motion through impact. Eight sampled program pairs differ by 2.56 rad/s in release-state proximal rate while matching both net and positive actuator work within 5%. In all eight, the higher-rate member is slower by 4.31–9.28 m/s. These pairs are reused, not independent, and no pair also matches peak interface force within 10%; peak-force differences are 34–46%. This is an adverse model counterexample under approximate work matching, not a load-matched causal estimate or a human optimum.

7.5.1 Joint Work- and Load-Matched Forward Screen

The load confound is testable rather than merely acknowledged. A follow-on finite factorial fixes both proximal-drive cut and wrist-release time at 0.14 s, then crosses six early proximal torques, four post-cut proximal torques, three opposing wrist torques, and three post-release wrist torques. All 216 attempts remain in the record; 148 satisfy the same club-vertical impact definition. Candidate pairs must differ by at least 1.5 rad/s in proximal rate at release while matching net actuator work and positive actuator work within 5% and peak modeled interface force within 10%.

The primary screen contains 109 admissible candidate pairs. To prevent one trajectory from being counted repeatedly, a frozen greedy rule selects 46 disjoint pairs, ordered first by the sum of the three relative mismatches and then by larger rate separation. The higher-rate member is faster in 20 pairs and slower in 26. Its speed difference ranges from -3.85 to +1.45 m/s, with a mean of -0.13 m/s. Thus, load matching removes the uniformly adverse result of the earlier eight reused work-only pairs, but it does not reveal a monotonic benefit. It exposes a mixed response: rate is one state coordinate within a coupled control and geometry history.

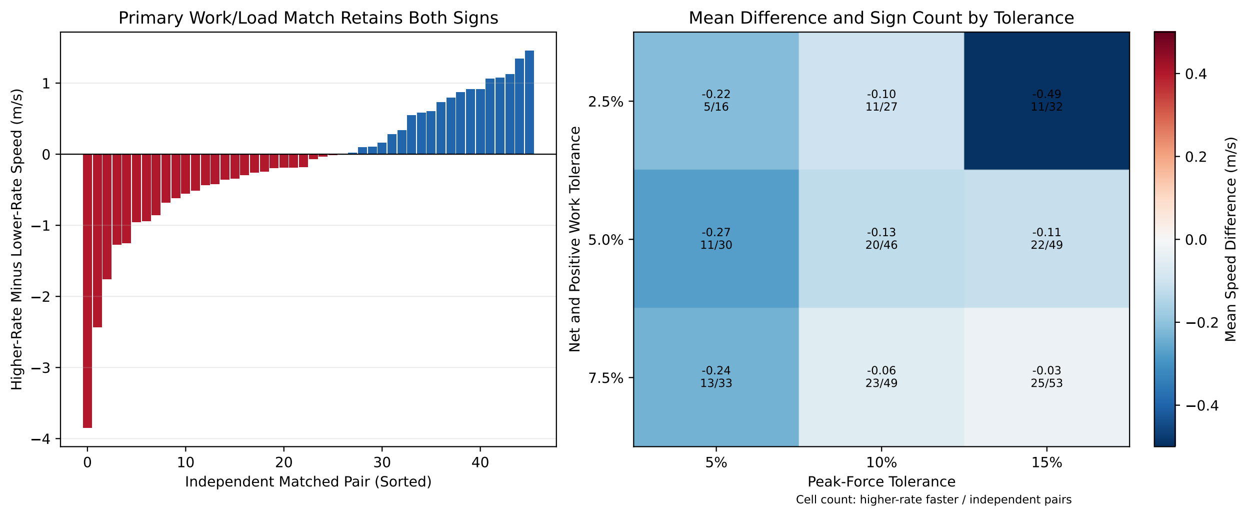

Figure 7.6: Independent primary matches retain favorable and adverse higher-rate outcomes. The sensitivity panel reports the mean higher-minus-lower rate speed difference and the number of favorable pairs over all independent pairs in each tolerance cell.

Work Tolerance	Load Tolerance	Independent Pairs	Higher Rate Faster	Higher Rate Slower	Mean Speed Difference (m/s)
2.5%	5%	16	5	11	-0.216
2.5%	10%	27	11	16	-0.105
2.5%	15%	32	11	21	-0.493
5%	5%	30	11	19	-0.274
5%	10%	46	20	26	-0.127
5%	15%	49	22	27	-0.115
7.5%	5%	33	13	20	-0.235
7.5%	10%	49	23	26	-0.060
7.5%	15%	53	25	28	-0.029

Every tolerance cell retains both signs, and every cell has more slower than faster higher-rate members. This sign mixture is the important result; the small negative means are not estimates of a human effect. Programs can differ in several actuator commands, greedy matching is not a globally optimal assignment, and valid-impact conditioning remains a selection. A decisive next test must independently intervene on the achieved rate or acceleration, match the full delivery state and work/load ledgers, and repeat the contrast in spatial, subject-scaled, and held-out human tiers.

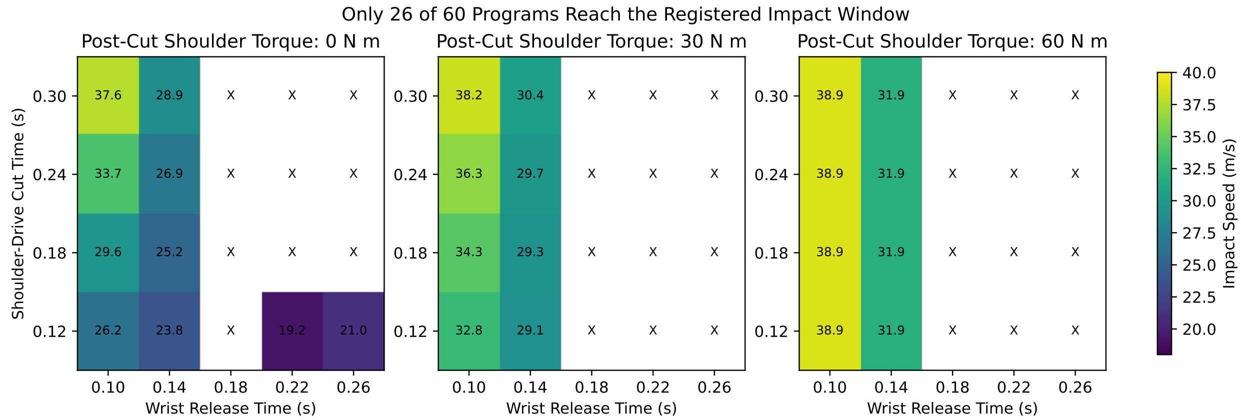

Figure 7.7: Registered impact speed across the complete timing grid. An X denotes a program that fails to reach club vertical inside the declared delivery window.

The highest-speed valid program releases at 0.10 s, retains the full 60 N m proximal drive, and reaches 38.85 m/s. Its post-release interface-force work is 127.21 J, decomposed into 132.08 J drift and -4.87 J control, with 6.11 J of negative interface work and a 315.39 N peak net planar wrist-interface force. That value is neither hand's anatomical grip force. The exact work-closure residual is 2.1×10^{-14} J. Re-evaluating this fixed program at 0.5 ms changes impact speed by 0.00035 m/s, total interface work by 0.0023 J, and peak force by less than 10^{-6} N without changing impact validity. The program was not reselected at the refined step. The large modeled interface load makes clear why speed alone is an incomplete objective.

No single program dominates all registered objectives. Impact speed and peak net interface force are strongly associated within the 26 valid programs ($r = 0.977$). Twenty-one of the 26 are nondominated, so this sparse Pareto screen is weakly discriminating rather than evidence of 21 distinct optimal human strategies. Several nominally different programs are trajectory-equivalent because their proximal-drive cut occurs after impact; they are retained for auditability rather than silently deduplicated. The result is a finite-grid Pareto set, not a unique or continuous optimum.

7.6 Rotating-Base, Bilateral-Hand Mechanism Test

The fixed-hub results above cannot distinguish a moving torso from a proximal pendulum coordinate and cannot recover the two hand reactions independently. The next registered tier therefore introduces seven generalized coordinates: finite-inertia torso rotation, lead- and trail-arm rotation relative to the torso, planar grip-center translation, proximal-club rotation, and distal-shaft rotation relative to the proximal club. Four holonomic constraints close the lead and trail hands onto two club points separated by 0.13 m. The equations are solved as a full-rank KKT system,

$$\begin{bmatrix} M(q) & -J(q)^{\mathsf{T}} \\ J(q) & 0 \end{bmatrix} \begin{bmatrix} \ddot{q} \\ \lambda \end{bmatrix} = \begin{bmatrix} Q_u - b(q, \dot{q}) \\ -\dot{J}(q, \dot{q})\dot{q} \end{bmatrix},$$

where the four multipliers λ are reshaped into two planar hand reactions. Their resultant and force-generated club couple are separately observable. Equal and opposite reactions are applied to the arm and club subsystems. The torso is driven through a declared torque channel, has 4.8 kg m^2 inertia, and is not relabeled from a fixed-hub link. The distal club is joined through an 80 N m/rad torsional spring and 0.6 N m s/rad damper. These values define a mechanism experiment, not identified human parameters.

The implementation rejects nonfinite or nonphysical parameters, rank-deficient constraints, and states outside the closure tolerance. Position and velocity are projected after every step. The bilateral contact-power identity is checked two ways: by summing each reaction dotted with its grip-point velocity and by combining

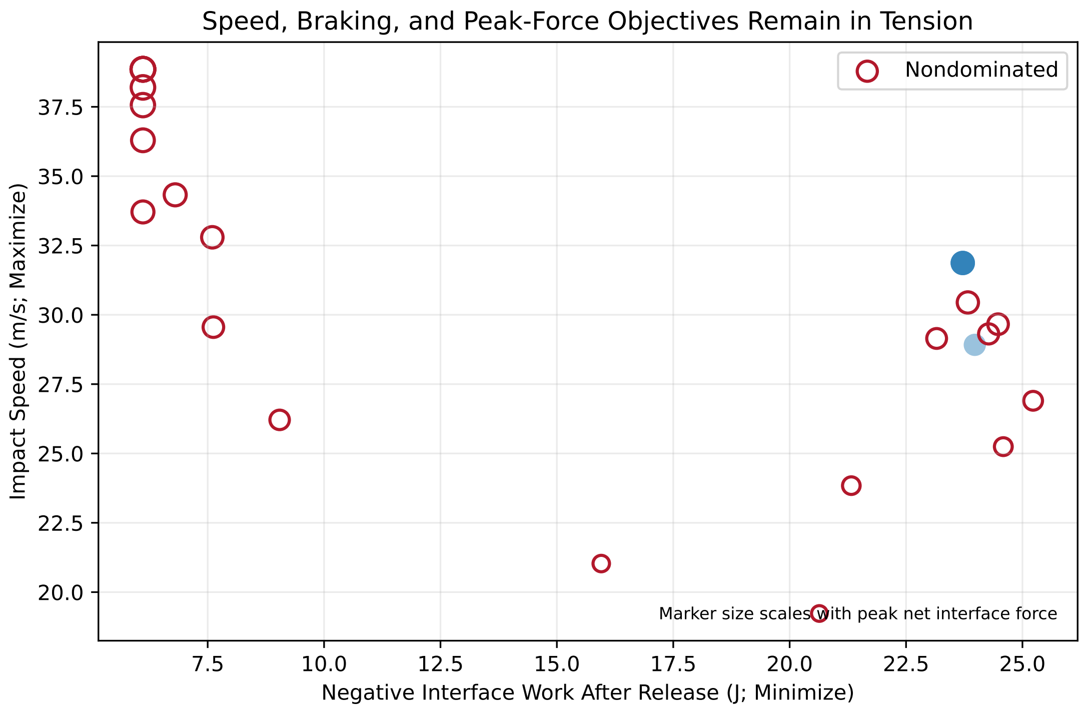

Figure 7.8: Nondominated speed, braking-work, and peak-force outcomes. Open red markers identify programs for which no sampled alternative is at least as good on all three objectives and strictly better on one.

resultant force power at the grip center with force-couple power. The full mechanical-energy change must equal integrated actuator and damping power plus the explicitly recorded projection-energy change. Null and adverse rows remain in the record.

7.6.1 Registered State Matching and Programs

The initial torso rates are 1.5, 3.5, and 5.5 rad/s. Two matching contracts are used. Under **relative-club-rate matching**, initial proximal-club rate is torso rate plus 1 rad/s. Under **absolute-club-rate matching**, proximal-club rate remains 3 rad/s while torso rate changes. Each state is propagated under one of three torso commands: +55 N m, 0 N m, or -55 N m. The bilateral arms receive equal 7 N m commands, and each wrist changes from -3 to +4 N m at 25 ms. The terms accelerating, constant-rate, and decelerating name these declared torso-command windows; the finite-inertia torso rate is an outcome and is not clamped.

Thirteen of the 18 full-resolution rows satisfy the registered envelope. Across valid rows, initial torso rate and delivery speed are positively associated ($r = 0.604$), but initial torso rate and negative grip work are also positively associated ($r = 0.273$). Thus, the model reproduces the apparent speed benefit without reproducing the proposed universal reduction in braking. Under relative-rate matching and positive torso torque, delivery speed rises from 3.78 to 7.44 m/s across the initial-rate grid while negative grip work rises from 0.66 to 1.41 J. Under the zero-torso-torque program, speed rises from 2.00 to 5.97 m/s while negative grip work rises from 0.81 to 2.31 J. These are conditional trajectory differences, not effects of changing one human joint velocity.

The matching contract changes the interpretation. With absolute club rate fixed and positive torso torque, delivery speed rises from 4.10 to 6.20 m/s, whereas negative grip work falls from 0.86 to 0.11 J. This contrast is the central result: rapid base motion can accompany a cleaner modeled transfer when the distal laboratory-frame state is matched, yet it can accompany more opposing work when the relative state is matched. "Release at high torso speed" is therefore under-specified unless club rate, geometry, shaft state, and actuator work are also declared.

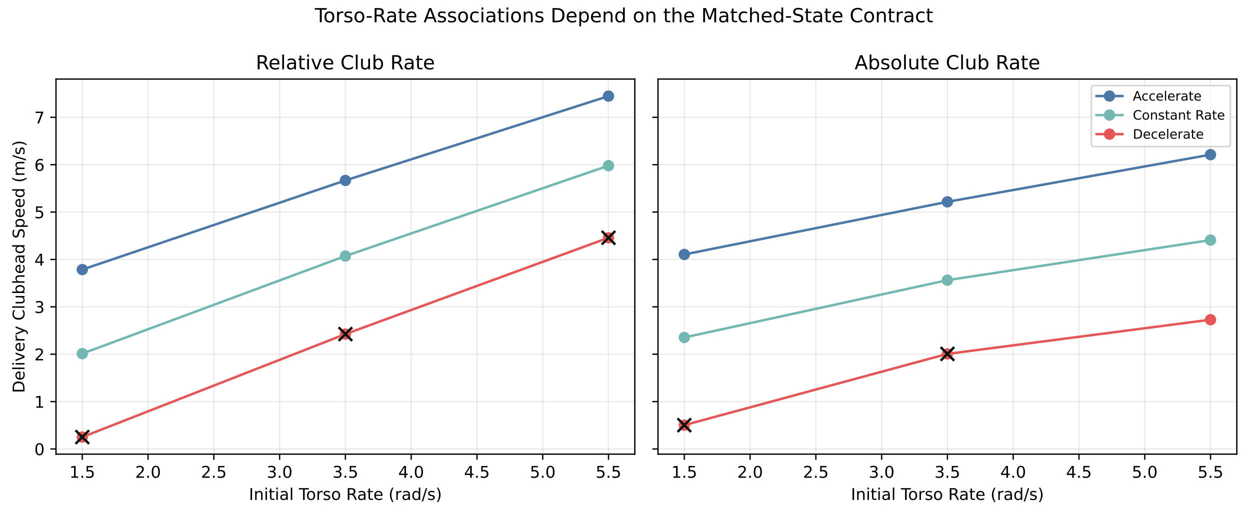

Figure 7.9: Delivery speed across the rotating-base grid. An X identifies a retained row outside the registered 100 N peak-grip-force or 0.08 J work-closure envelope; lines are descriptive connections, not fitted human response curves.

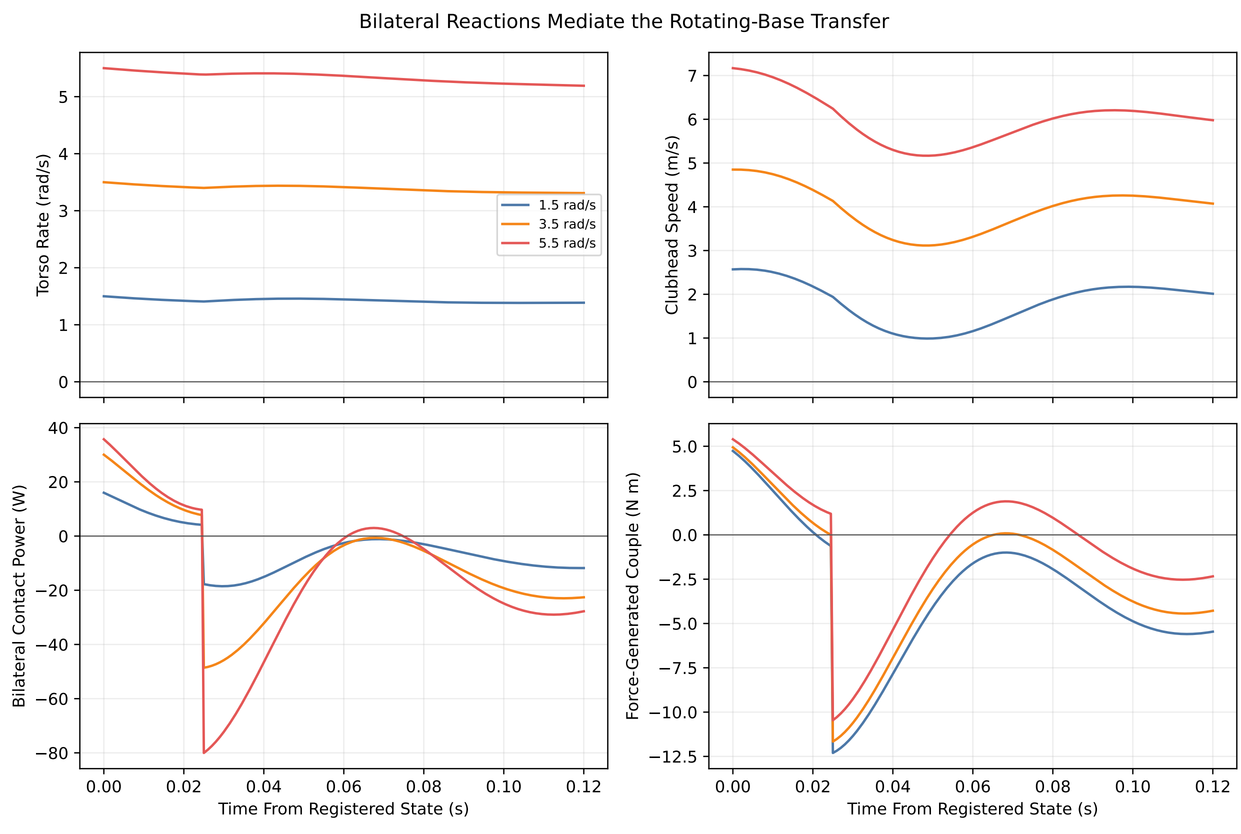

Figure 7.10: Torso rate, delivery speed, bilateral contact power, and force-generated couple for the three initial-rate levels under the relative-rate, zero-torso- torque program. The wrist command changes at 25 ms, producing the visible but auditable discontinuity.

The force-power atlas shows why force magnitude alone cannot define transfer. Positive early contact power becomes negative after the wrist-command change, then briefly returns toward zero before becoming negative again. The force- generated couple changes sign during the same interval. A large reaction can be nearly perpendicular to grip velocity and transmit little power; a smaller reaction aligned against velocity can remove energy. The recorded outcomes therefore include distal-segment kinetic-energy gain, total control work, bilateral wrist work, force-couple work, negative contact work, negative along-path impulse, and peak reaction for every attempted row.

7.6.2 Same-State Killswitches and Geometric Controls

At 30 ms, three counterfactuals branch from numerically identical states and commands: torso torque, both arm torques, or both wrist moments are set to zero while all other channels continue. The maximum pre-branch generalized-state difference is exactly zero at stored precision. Continuing the torso command adds 1.22 m/s to delivery speed relative to its killswitch. Continuing the bilateral arm commands *reduces* delivery speed by 1.36 m/s relative to their killswitch in this program. Continuing the wrist commands adds 1.81 m/s, while its post-branch contact-work difference has the opposite sign from the speed difference. These nonmonotonic results prevent the total gain from being assigned to a single colloquial "fling" mechanism.

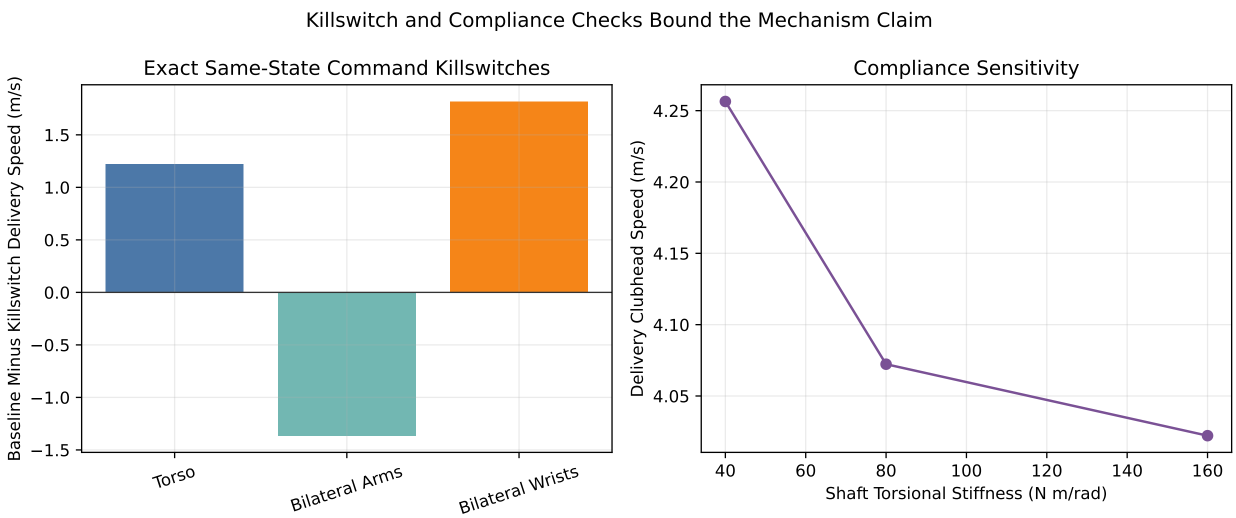

Figure 7.11: Delivery-speed changes under exact same-state command killswitches and shaft- stiffness sensitivity. A positive bar means the continued baseline command finishes faster than the corresponding command-zero branch.

Two geometry controls test the bilateral couple. Coincident grip points make the force-generated couple exactly zero. Reversing only the signed moment arms while holding the solved forces and state fixed reverses the couple from +1.351 to -1.351 N m. The latter is an algebraic sign test, not a dynamically feasible human grip exchange. Shaft stiffnesses of 40, 80, and 160 N m/rad produce delivery speeds of 4.26, 4.06, and 4.03 m/s in the selected reference program. The uncertainty screen also perturbs torso inertia, arm mass, shaft damping, grip spacing, and wrist-release timing. Narrowing grip spacing raises the peak reaction above the registered 100 N ceiling, while an earlier wrist- command change increases speed but also makes contact work more negative. These cases expose a speed–load–braking trade rather than a single optimum.

The supported mechanism claim is consequently limited: in this planar, finite-inertia, closed-loop model, torso-rate history changes bilateral reaction work and delivery speed conditional on matching rule, command history, grip geometry, and shaft parameters. The study does not identify scapular control, anatomical shoulder velocity, safe loading, or a coaching instruction. Only synchronized bilateral grip wrenches and segment kinematics can test whether the same decomposition predicts held-out human swings.

7.7 Candidate Design Hypotheses Stated as Testable Conditions

Within this model tier, the implications are better stated as five testable design hypotheses than as a command to maximize torso speed:

1. **Build Proximal Speed Before the Favorable Geometry.** Additional proximal speed has its largest positive association with drift grip power in the late states. Acceleration history matters because the target velocity must be reached without imposing a compensating distal rate that changes the counterfactual.
2. **Enter Delivery With Compatible Relative Motion.** The delivery result changes sign across the two velocity-matching rules. The proximal link and club must arrive with a relative angular rate that lets the interaction force do positive work; proximal speed alone is insufficient.
3. **Avoid Sustained Negative Interface Power.** The measurable adverse outcome is not a vaguely defined "braking force" but negative interface power and its time integral. A high force perpendicular to hand or club velocity can transmit little power, whereas a smaller force aligned against velocity can remove energy.
4. **Do Not Infer a Useful Release From Drift Acceleration Alone.** A positive state-matched drift acceleration can coexist with adverse interface power or an unfavorable subsequent trajectory. Distal-torque reduction must be evaluated by forward outcomes, not one pointwise term.
5. **Treat Torso Speed as a Candidate State Variable, Not the Objective.** A future human-scaled optimization should treat club delivery speed, opposing work, peak load, face/path, robustness, and anatomical limits as separate registered outcomes. Thorax angular velocity would be one measured state, not an objective justified by the present fixed-hub coordinate.

These conditions distinguish *velocity at transfer* from *continued positive proximal torque*. A proximal segment may be moving rapidly while decelerating. Indeed, outward energy flow can coincide with proximal deceleration, but deceleration itself does not prove transfer: energy may leave through the base, gravity, damping, or an actuator. A trajectory-level study must therefore report proximal actuator power, grip-interface power, club energy change, and external work together.

7.8 Critical Variables for the Two-Hand Extension

The double pendulum cannot decide how two hands should create or resist the club moment. The next mechanically closed tier must preserve the following variables rather than collapsing them into one wrist torque:

- thorax or hub angular velocity and acceleration;
- common-mode hand velocity, which largely transports the grip;
- differential hand velocity and separation, which create a force-generated couple;
- lead- and trail-hand force vectors and their points of application;
- direct wrist moments, separated from the moment of hand forces;
- arm configuration and hand-path curvature;
- club relative angle, relative angular velocity, and shaft deformation;
- bilateral negative work, peak force, constraint residual, and delivery speed.

A sampled two-hand strategy is nondominated only if no sampled alternative raises delivery speed without worsening at least one registered cost. This prevents a large speed gain obtained through excessive grip load, opposing hand work, or an unstable timing boundary from being called optimal. The existing fixed-shoulder two-arm model can test force allocation, the moving-base flexible tier can test translation and shaft response, and the rotating-base tier above tests a finite-inertia planar torso coordinate with bilateral closure. None is an anatomical torso–scapula–arm model. Subject-scaled parameters and synchronized bilateral human measurements remain required before the question can be interpreted as a human torso-velocity strategy.

7.9 Falsification Criteria and Experimental Observables

The high-proximal-velocity hypothesis is weakened or rejected if any of the following occurs in a registered, held-out analysis:

- drift grip power fails to increase with proximal velocity in the declared delivery state;
- the sign changes under small, physiologically plausible perturbations of configuration or parameter estimates;
- negative grip work or peak grip force increases enough to dominate the club-energy gain;
- the effect disappears when the same distal laboratory-frame state is matched;
- a two-hand model attributes the gain to direct wrist work rather than the force-generated interaction term; or
- synchronized human measurements show no within-player association after conditioning on club state, hand path, and phase.

The minimum experimental record is synchronized pelvis and thorax kinematics, upper-arm and hand kinematics, club pose and twist, bilateral six-axis grip wrenches, ground reaction, and launch conditions. Bilateral six-axis hand wrenches would require validated instrumentation or an explicitly identified inverse solution; a net club wrench is insufficient. The preregistered estimands should include phase-resolved grip power, bilateral common/differential-mode power, proximal actuator-power proxies, club kinetic-energy change, and the conditional effect of thorax velocity at matched club state. Because published golf kinematic methods remain heterogeneous (Bourgain et al. 2022), coordinate definitions, filtering, event timing, and reference-point transport must be declared before examining outcomes.

7.10 Reproducibility and Claim Boundary

The committed evidence contains 126 velocity cases (90 across five phase labels and two rate-matching rules, plus 36 energy-matched states across four nonzero-energy phases), 45 identical-state proximal-acceleration cases, all 60 timing-grid programs, and all 216 joint-matching programs. The machine-readable JSON files record every row, phase summary, closure test, invalid-impact attempt, Pareto membership, model-tier statement, falsifier, limitation, and dependency hash; paired NPZ files preserve the numerical arrays. Repeated generation is byte-identical for both JSON and NPZ artifacts. The pointwise generating scripts are `shoulder_velocity_transfer.py`, `run_shoulder_velocity_transfer_study.py`, and `make_shoulder_velocity_transfer_figures.py`. The trajectory scripts are `shoulder_velocity_strategy_search.py`, `run_joint_matched_proximal_rate_study.py`, `run_shoulder_velocity_strategy_study.py`, and `make_shoulder_velocity_strategy_figures.py`.

The supported conclusion is narrow: in the reference fixed-hub planar model, increasing proximal-link angular velocity can markedly increase late drift- mediated interface power when stored energy co-varies, but the effect is phase-, range-, and state-definition-dependent, can reverse earlier, and nearly disappears in the energy-matched pre-impact screen. A separate finite control grid, including approximate actuator-work matches, supplies a counterexample to using release-state proximal rate as a standalone rule. The study does not establish an optimal human thorax velocity, a causal shoulder strategy, a bilateral hand allocation, or a universal instruction to release while rotating rapidly.

Chapter 8

Matched-State Counterfactual Persistence

The previous chapter established an instantaneous result: at a fixed state, zero commanded torque can coexist with substantial wrist reaction force and positive joint-force power. That result does not show how long the behavior persists. This chapter tests persistence by releasing the commanded and zero-torque systems from identical states at multiple downswing phases and integrating both futures over controlled horizons.

8.1 Experimental Contract

Let the source trace provide a state $x_c = [q(t_c), \dot{q}(t_c)]$ at cut time t_c. Two simulations are initialized with exactly that state:

$$x_{\mathrm{cmd}}(0) = x_0(0) = x_c. \tag{8.1}$$

The commanded future continues the declared shoulder and wrist torque program; the killswitch future uses $\tau = 0$ at both joints. The initial acceleration difference is

$$\ddot{q}_{\mathrm{cmd}}(0) - \ddot{q}_0(0) = M(q_c)^{-1}\tau(t_c). \tag{8.2}$$

At the initial instant, the zero-torque acceleration, force, and force power are the pointwise ZTCF quantities. At every later instant, each future is evaluated on its own state. This construction preserves a controlled intervention meaning inside the declared deterministic model:

- pointwise ZTCF attributes acceleration and force at the state already reached;
- the killswitch tests whether the state carries the passive mechanism forward; and
- commanded-minus-killswitch differences quantify the model-conditional consequences of continued declared control over a declared horizon.

The ensemble spans eight cut times from 0.080 to 0.320 s, including 0.099, 0.100, and 0.101 s around the wrist-torque switch; four horizons from 20 to 120 ms; and integration steps of 0.5, 1, and 2 ms. This gives 96 baseline comparisons. Source states are obtained by declared componentwise linear interpolation of the smooth registered trace. Every row records position, velocity, wrist force, wrist-force power, integrated force work, terminal clubhead-speed differences, matched-state error, and initial affine-closure residuals. Commands are sampled at every state time, including the terminal endpoint, so a horizon ending exactly on a torque switch uses the new endpoint command for terminal force and power.

8.2 Why Cut Time and Horizon Matter

A counterfactual effect is not a property of a trajectory in the abstract. It depends on *when* the intervention occurs and *how long* the futures are allowed to diverge. A short early killswitch mostly tests the immediate acceleration change. A long late killswitch also changes geometry, club angular velocity, and the velocity-squared force terms. Figure 8.1 shows this dependence directly.

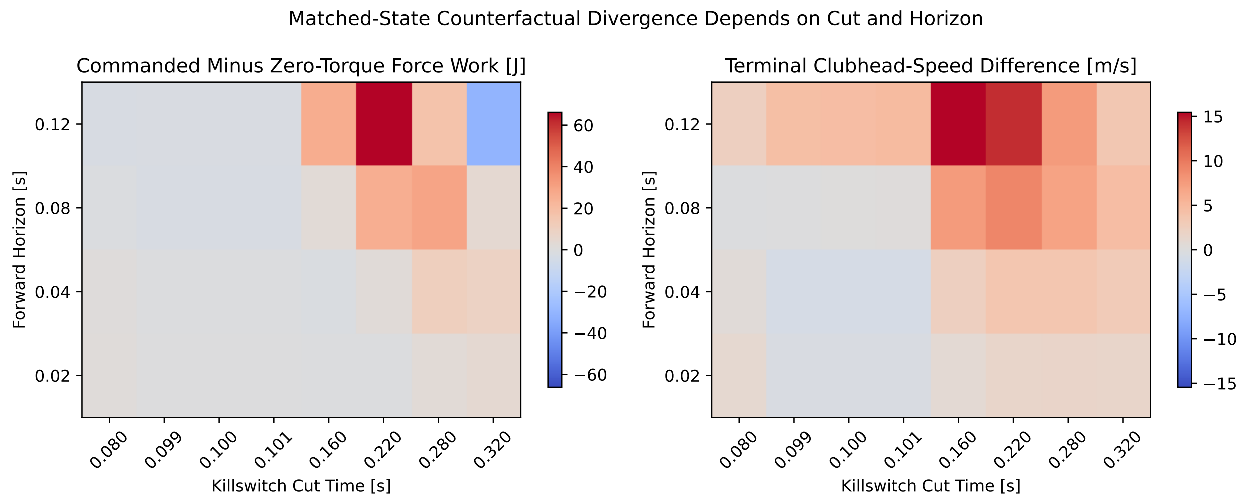

Figure 8.1: Matched-State Counterfactual Divergence by Cut Time and Horizon

At the 1 ms reference step, commanded-minus-zero-torque wrist-force work ranges from -30.88 J for a 0.320 s cut followed for 120 ms to +66.17 J for a 0.220 s cut over the same horizon. The corresponding terminal clubhead-speed differences are +3.42 and +14.20 m/s. A negative force-work difference does not mean the commanded future is globally slower: the wrist moment, gravity, and the state inherited at the cut also contribute to club energy. It means only that, over that horizon, continued control produces less *wrist-force work* than the zero-torque future.

The maps therefore reject a binary interpretation such as “the late swing is passive” or “continued torque is necessary.” Early and middle cuts generally show that continued control creates a rapidly different state and often more clubhead speed. Very late cuts can show less commanded force work because the two futures encounter different orientation and deceleration histories. The mechanism is phase dependent.

8.3 Separation of State, Force, and Power

Figure 8.2 follows three representative cuts for 80 ms. Position and velocity coincide at the vertical dotted line by construction; their accelerations can differ immediately, so their state curves acquire different curvature and then different slopes. Force and power need not coincide even at the cut because force depends on acceleration and power pairs that force with the inherited common point velocity.

The 0.12 s cut occurs soon after the restraint-to-drive transition. Continued wrist drive produces a more open club state, but commanded wrist-force power is initially more negative than in the zero-torque future. At 0.22 s, commanded force and power rise much faster than the killswitch values, producing a large positive work difference. At 0.30 s, both futures initially retain high positive power because both inherit a rapidly moving club; the zero-command force power remains positive for 78 ms on the 1 ms trace. At the 0.22 s cut it remains positive over the full registered 80 ms horizon. These selected cases demonstrate finite-horizon persistence in this model: the zero-torque future does not lose its interaction force at removal, while the two futures separate as their states evolve.

This behavior clarifies the meaning of passive contribution. A passive term can be large because earlier active work created high velocity. Removing torque late does not erase that history. Conversely, observing a large

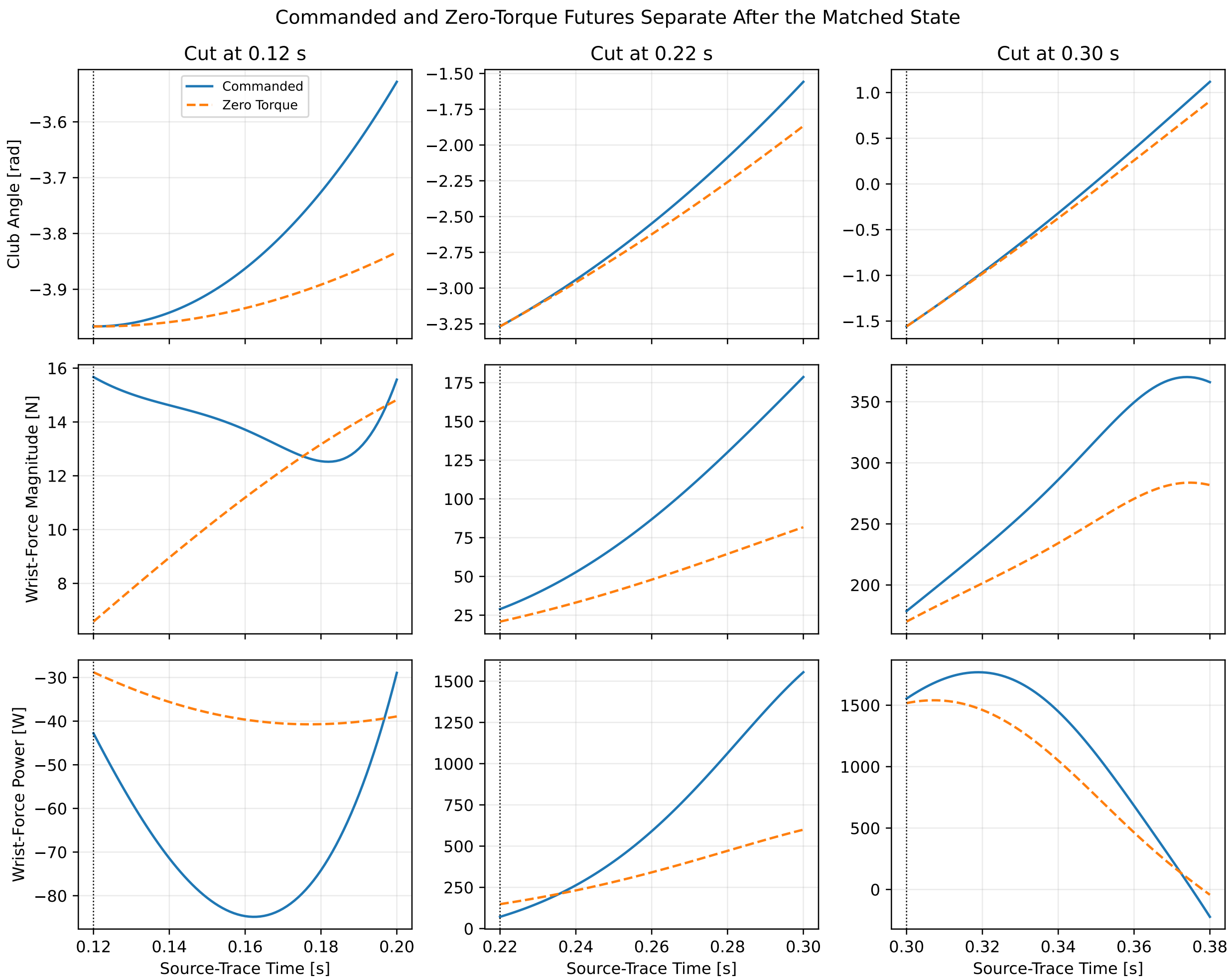

Figure 8.2: Commanded and Zero-Torque State, Force, and Power Futures

zero-torque force at the cut does not show that the same force would persist indefinitely. The matched-state horizon is part of every claim.

8.4 Control Discontinuity Audit

The prescribed wrist torque changes from -10 to +15 $N \cdot m$ at 0.100 s. A pointwise split changes discontinuously at that time because the control vector changes, while position and velocity remain continuous. Three cut times bracket the switch. Over an 80 ms future, commanded-minus-zero-torque force work is -2.83 J at 0.099 s, -2.87 J at 0.100 s, and -2.87 J at 0.101 s; terminal clubhead-speed differences are -0.03, +0.01, and +0.14 m/s. The force-distance metric changes smoothly from 19.98 to 20.85 N.

The close neighboring results show that the ensemble is not dominated by a single-sample numerical impulse. The acceleration changes discontinuously as the idealized step command requires, but RK4 integrates finite state changes, and the adjacent-cut futures remain continuous at the reported scale. A physiological torque-rate model remains preferable for human interpretation; the present audit establishes numerical behavior for the declared open-loop program only.

8.5 Timestep Convergence

The 0.5 ms result is used as the reference. Across all cut-time and horizon combinations, the maximum 1 ms difference is 3.9×10^{-10} rad in terminal angle distance, 1.1×10^{-8} rad/s in terminal velocity distance, 1.1×10^{-7} N in terminal force distance, 0.0174 J in force-work difference, and 4.5×10^{-9} m/s in terminal clubhead-speed difference. The 2 ms step produces larger but still bounded differences: up to 0.0091 rad, 0.0908 rad/s, 0.99 N, 0.356 J, and 0.190 m/s, respectively.

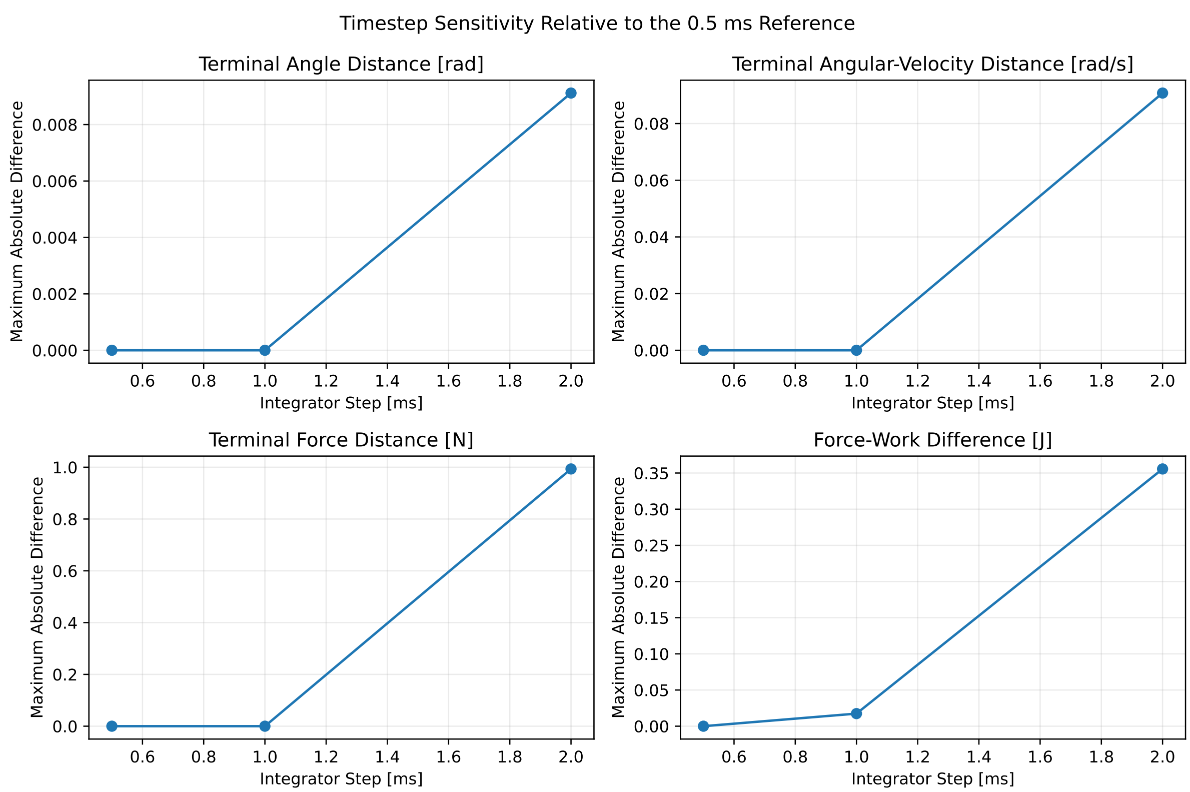

Figure 8.3: Timestep Sensitivity of Matched-State Divergence Metrics

The near-identity of the 0.5 and 1 ms state metrics supports use of the existing 1 ms article grid. Work is slightly more sensitive because it integrates a power difference and because some cases cross the idealized torque step. The 2 ms result is retained as a coarse-step warning rather than hidden by a single convergence number.

8.6 Whole-Model Gravity and Damping Variants

Zero torque does not mean zero generalized forcing. Gravity and viscous damping remain inside the bias vector $b(q, \dot{q})$. To prevent the word *passive* from collapsing these mechanisms into one category, the complete source rollout and 80 ms ensemble are repeated with projected gravity disabled and with both damping coefficients set to zero.

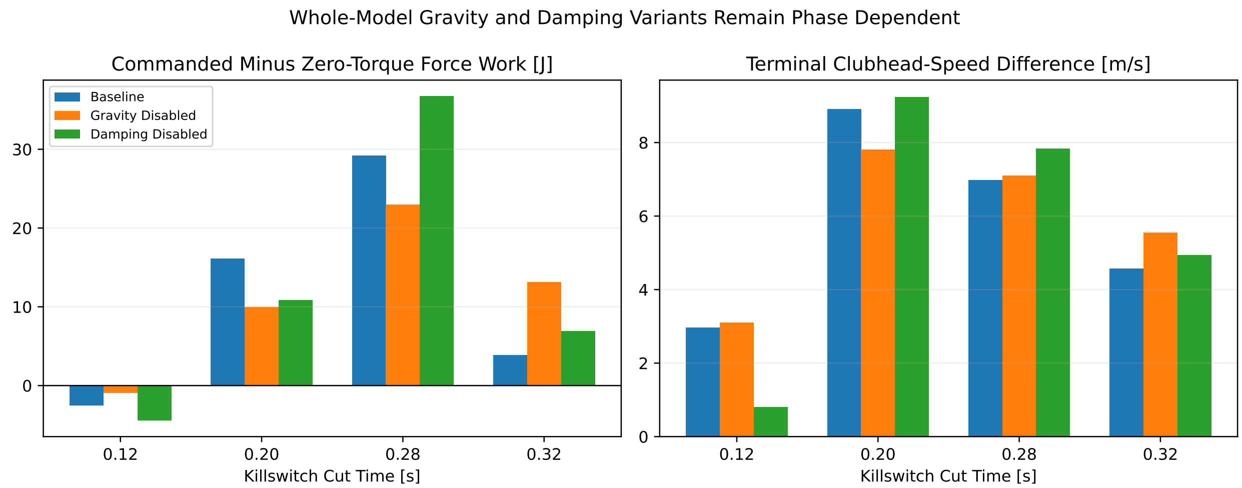

Figure 8.4: Whole-Model Gravity and Damping Variants of the Killswitch Comparison

The scenario variants change magnitudes but do not eliminate phase dependence. At a 0.28 s cut, baseline commanded-minus-zero-torque force work is 29.17 J, versus 22.95 J without gravity and 36.73 J without damping. Terminal clubhead-speed differences remain positive in all three cases. At 0.12 s, force-work differences are negative in all three cases, while the damping-disabled speed difference is much smaller than baseline. These results show that gravity and damping materially shape the counterfactual; neither alone creates the late positive difference.

The variants are not matched-state ablations and are not additive. Each altered model follows a different source trajectory before the cut, so subtracting variant numbers does not produce an orthogonal causal partition. A full mechanism partition would require matched source states with bias subterms selectively disabled inside the same dynamics evaluation. That finer separation is tracked in #8447.

8.7 WSCG BASE/ZTCF/DELTA Convention Check

The registered WSCG chart defines `DELTA = BASE - counterfactual`. Its four stored DELTA series can be reconstructed from the independently cached BASE and counterfactual series after time alignment. Maximum absolute residuals are 0.43 N for lead-hand axial, 1.48 N for lead-hand normal, 0.16 N for trail-hand axial, and 1.54 N for trail-hand normal. The residuals are small relative to the reported force ranges and arise from interpolating the dense BASE cache onto the 55-sample counterfactual grid.

This check establishes sign and subtraction convention, not model parity. The WSCG chart comes from a two-hand flexible-shaft model, while the present killswitch ensemble uses a rigid-shaft single-wrist double pendulum. Numerical agreement between their force magnitudes is neither expected nor claimed. The two-hand reproduction must compare like-for-like states, frames, hand contact points, and equivalent-wrench definitions.

8.8 Counterfactual Conclusions

The ensemble supports a stronger and more precise statement than the original pointwise analysis:

- pointwise ZTCF equals the initial acceleration of the matched-state zero-torque future to numerical tolerance in the same backend;
- zero-torque interaction force and positive force power persist for 78–80 ms in the selected 0.30 and 0.22 s cuts, not as a phase-independent law;
- persistence and commanded-minus-zero-torque differences depend strongly on cut phase and horizon;
- the 1 ms integration step is converged for the reported state, force, work, and speed metrics relative to 0.5 ms; and
- gravity, damping, and the wrist-command discontinuity change quantitative results without explaining away the underlying distinction between instantaneous attribution and a realizable future.

The committed evidence uses schema `matched-state-counterfactual-ensemble-v2`, hashes the complete declared Python and WSCG input closure, retains all 96 baseline comparisons and 12 whole-model variants, and is byte deterministic for both JSON and NPZ artifacts. The results distinguish pointwise attribution from forward intervention for this double pendulum. They do not establish the source of the two-hand negative equivalent couple, a human control strategy, or bilateral hand allocation. Those questions require local hand forces, wrench geometry, and higher-fidelity or measured evidence.

Chapter 9

Two-Hand Wrench Mechanics and Passive Couple Reversal

9.1 The Question Made Testable

The double-pendulum analysis established that a distal segment can receive a large reaction force even when the corresponding joint torque is zero. A two-hand grip adds a second mechanism: the two contact forces can form a substantial *couple* even when their vector sum is comparatively modest. The mechanical question is therefore not simply whether a wrist torque trace turns negative. It is whether the negative action on the club is attributable to commanded free torque, to the moment created by separated hand forces, or to a mixture of both.

The distinction matters because the three statements below are not interchangeable:

1. the resultant hand force is small;
2. the equivalent couple about the grip midpoint is negative; and
3. the golfer actively commands a negative wrist torque.

The first statement concerns translation, the second concerns rotation about a declared point, and only the third is an actuation claim. Two large and nearly opposing hand forces can satisfy the first two statements without satisfying the third. Conversely, a commanded free torque can be present even when the force-generated moment is zero.

This chapter tests the distinction against the archived output tables behind the WSCG presentation (Olson 2024). It does not digitize a picture. It reconstructs the force system from the stored contact positions, global hand forces, and free torques at all 2,801 time samples. The analysis is executable through the linked `run_two_hand_wscg_analysis.py`, and its mechanics are isolated in the backend-independent `two_hand_wrench.py`.

9.2 Source Cases and Evidentiary Boundary

The archived simulation supplies three synchronized tables:

- **BASE** is the commanded model solution;
- **ZTCF** evaluates the reactions after commanded joint torques and the designated damping terms are set to zero at each achieved BASE state; and
- **DELTA** is the stored operational difference, BASE minus ZTCF.

The ZTCF table is an instantaneous attribution evaluated on an exported state that matches BASE to the cache precision: maximum contact-position, contact-velocity, and clubhead-speed differences are 1.85×10^{-7}

m, 8.93×10^{-6} m/s, and 3.67×10^{-5} mph, respectively. Those residuals are registered rather than rounded to exact zero. It is not a single torque-free forward swing. This distinction is the same one developed in Section 8: a pointwise counterfactual can identify which part of the acceleration or reaction is present without current command, but it cannot by itself state how long that behavior would persist after commands were removed. Accordingly, the present result uses *passive* in the narrow actuation sense: the ZTCF contact moment exists while the evaluated command torques are exactly zero. It does not mean that the state was reached without earlier active work.

The binary input tables, portable CSV caches, and three executable export and analysis sources are registered by nine SHA-256 records. The tables are exported to ordinary CSV by `export_two_hand_wscg_tables.m`. The exported cache makes the audit usable without MATLAB; the MATLAB function exists to prove where every column came from. The original MAT files and source presentations remain unchanged. Because these are project-originated model records, agreement with them is a reproduction of the author's prior simulation, not independent empirical validation.

9.3 Frames, Directions, and Signs

The archived right-handed model labels the left wrist as the lead contact and the right wrist as the trail contact. In this chapter:

- $\mathbf{r}_L$ and $\mathbf{r}_T$ are the lead- and trail-contact positions;
- $\mathbf{F}_L$ and $\mathbf{F}_T$ are forces exerted **by the wrists on the club**;
- τ_L and τ_T are free torques exerted on the club;
- O is the grip midpoint; and
- positive moment follows the right-hand rule about the model's $+z$ axis.

The local $+x$ axis points from the lead contact toward the trail contact. The fixed model-plane normal is

$$\mathbf{e}_z = \frac{1}{\sqrt{2}}(0, -1, 1), \tag{9.1}$$

and $\mathbf{e}_y = \mathbf{e}_z \times \mathbf{e}_x$. Projection of the stored global forces onto this basis reproduces the stored local axial and normal components to a maximum 1.05 N cache discrepancy across BASE, ZTCF, and DELTA. The maximum out-of-plane hand-force component is 1.78 N; the largest case-level ratio to the in-plane peak is 0.215%. Thus the archived result is numerically near-planar under this declared tolerance even though its vectors are stored in three coordinates.

Changing any one of force direction, hand labeling, axis direction, or moment sign reverses part of the interpretation. Those conventions are therefore data, not cosmetic plotting choices. They are written into the machine-readable provenance record and tested.

9.4 Reduction of Two Contacts to an Equivalent Wrench

About an arbitrary reference point O, the two-hand action reduces to

$$\mathbf{R} = \mathbf{F}_L + \mathbf{F}_T, \tag{9.2}$$

and

$$\mathbf{M}_O = (\mathbf{r}_L - \mathbf{r}_O) \times \mathbf{F}_L + (\mathbf{r}_T - \mathbf{r}_O) \times \mathbf{F}_T + \tau_L + \tau_T. \tag{9.3}$$

The scalar planar couple is $C_O = \mathbf{M}_O \cdot \mathbf{e}_z$. This is the quantity called the equivalent midpoint couple when O is the grip midpoint. The first two terms in Equation 9.3 are the **contact-force moment**; the last two are the **applied free torque**. Their sum, rather than either contribution alone, is the equivalent couple.

9.4.1 What Is and Is Not Reference Invariant

A useful correction is necessary here. The physical force system is invariant under a change of bookkeeping point, but the reported moment number generally is not. If the reference is moved from A to B,

$$\mathbf{M}_B = \mathbf{M}_A - (\mathbf{r}_B - \mathbf{r}_A) \times \mathbf{R}. \tag{9.4}$$

Only a pure couple ($\mathbf{R} = 0$) has the same moment about every point. A nonzero two-hand resultant requires the transport term in Equation 9.4. Thus an audit should demand *wrench equivalence under reference transport*, not invariance of the scalar midpoint moment. The test suite evaluates Equation 9.4 directly and also verifies invariance to a rigid translation and co-rotation of the complete force system.

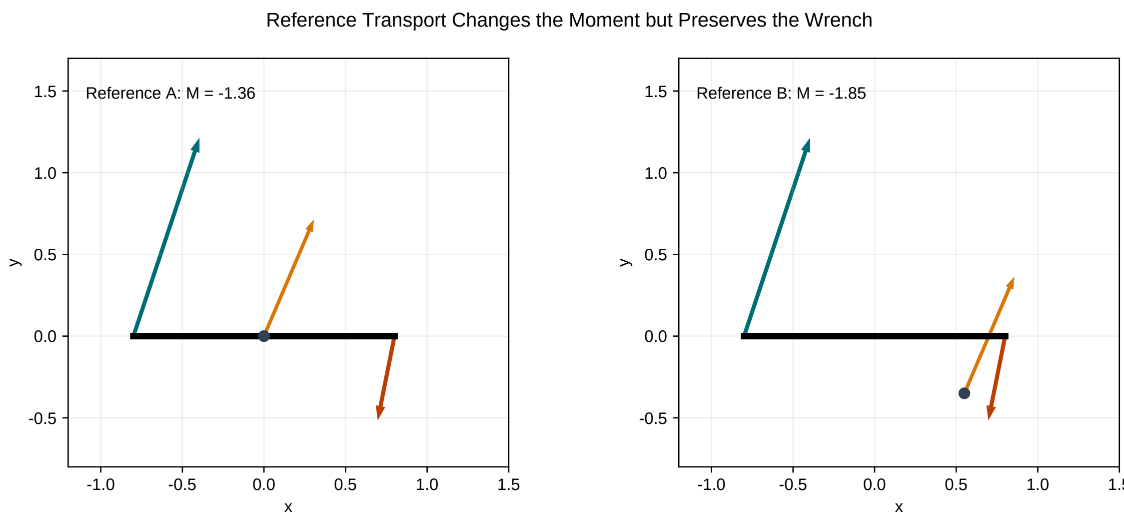

Figure 9.1: Reference Transport Changes the Moment but Preserves the Wrench

Figure 9.1 illustrates the distinction. The resultant arrow is unchanged, while its associated moment changes exactly enough to preserve the action of the original two forces. This prevents a common error: comparing couples calculated about different grip points as if they were the same physical observable.

9.5 Common and Opposed Force Modes

Let the grip midpoint be $\mathbf{r}_M = (\mathbf{r}_L + \mathbf{r}_T)/2$, define the contact-separation vector $\mathbf{d} = \mathbf{r}_T - \mathbf{r}_L$, and introduce common and differential force modes,

$$\mathbf{F}_c = \frac{\mathbf{F}_L + \mathbf{F}_T}{2}, \qquad \mathbf{F}_d = \frac{\mathbf{F}_L - \mathbf{F}_T}{2}. \tag{9.5}$$

Then $\mathbf{R} = 2\mathbf{F}_c$, while the force-generated midpoint moment is

$$\mathbf{M}_{F,M} = -\mathbf{d} \times \mathbf{F}_d. \tag{9.6}$$

Equation 9.6 is the central two-hand mechanism. The common mode controls the resultant. The differential, or opposed, mode controls the couple. A large $\|\mathbf{F}_d\|$ may therefore be nearly invisible in $\|\mathbf{R}\|$.

If $\mathbf{d} = s\mathbf{e}_x$, only the differential normal component contributes to the planar force moment:

$$C_{F,M} = -sF_{d,y}. \tag{9.7}$$

Axial forces can be very large without directly producing a midpoint moment when their lines of action remain collinear with the grip. They still matter to constraint loading, deformation, and power. Normal-force imbalance, contact separation, and their signed relative orientation set the moment.

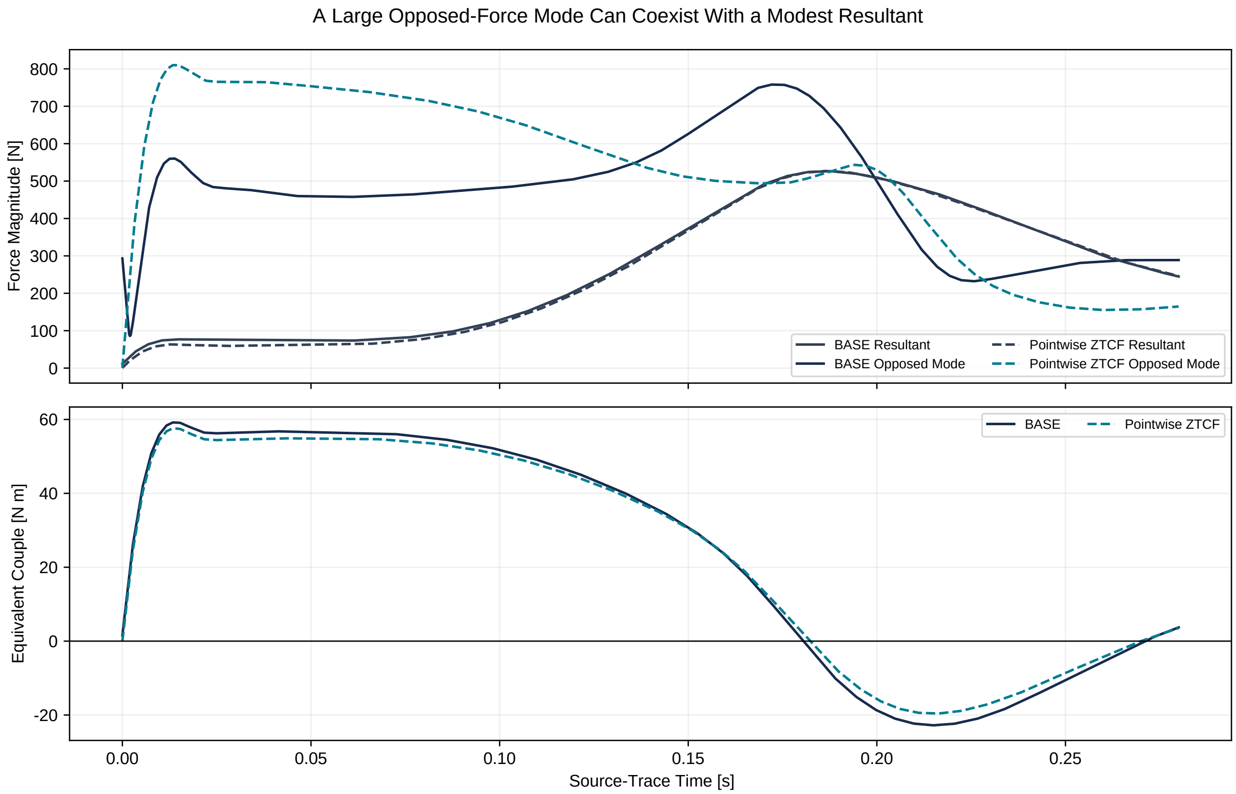

Figure 9.2: A Large Opposed-Force Mode Can Coexist With a Modest Resultant

In Figure 9.2, the opposed mode greatly exceeds the resultant over much of the early and middle trace. BASE and ZTCF resultants are nearly coincident, while their opposed modes differ more visibly. This is why a net-force plot alone cannot diagnose the rotational action of a two-hand grip.

9.6 Which Bilateral Forces Are Identifiable?

The common/differential decomposition also exposes a measurement limitation. Let the stacked point-force vector be $\mathbf{f} = [\mathbf{F}_L^T, \mathbf{F}_T^T]^T$. About a declared reference O, the measured net club wrench is the linear map

$$\begin{bmatrix} \mathbf{R} \\ \mathbf{M}_O \end{bmatrix} = \underbrace{\begin{bmatrix} \mathbf{I} & \mathbf{I} \\ [\mathbf{r}_L - \mathbf{r}_O]_\times & [\mathbf{r}_T - \mathbf{r}_O]_\times \end{bmatrix}}_{\mathbf{A}_F} \begin{bmatrix} \mathbf{F}_L \\ \mathbf{F}_T \end{bmatrix}, \tag{9.8}$$

where $[\mathbf{r}]_\times \mathbf{F} = \mathbf{r} \times \mathbf{F}$. For two distinct point contacts, $\mathbf{A}_F$ has rank five rather than six. Its one-dimensional right null space is

$$\mathbf{n}_F = \frac{1}{\sqrt{2}} \begin{bmatrix} \hat{\mathbf{d}} \\ -\hat{\mathbf{d}} \end{bmatrix}, \qquad \hat{\mathbf{d}} = \frac{\mathbf{r}_T - \mathbf{r}_L}{\|\mathbf{r}_T - \mathbf{r}_L\|}. \tag{9.9}$$

Thus equal and opposite forces directed along the contact-separation axis produce neither a net force nor a net moment. They can preload the grip, change contact pressure, and alter tissue or shaft states while remaining exactly invisible in the net club wrench. This is a structural result, not a statement that such loading is beneficial, intentional, or present in a golfer. It also shows why club motion, inverse dynamics, or a single net-wrench sensor cannot by itself distinguish a lead-arm push from an opposing trail-arm pull.

The left-null counterpart is equally useful: point forces alone cannot create a free moment parallel to **d** about the grip midpoint. Such a measured long-axis moment requires a free hand torque, a non-point contact distribution, or model discrepancy. Perpendicular differential forces remain observable through their couple, with force-to-moment gain proportional to grip span.

If each hand is instead allowed an independent six-axis wrench, the input has twelve components and the net-wrench map has rank six and nullity six. A net club wrench therefore identifies even less of the *allocation*: infinitely many bilateral force/free-moment combinations produce the same resultant wrench. One independent internal axial-force scalar raises the point-force map to full column rank six, but it does not resolve the full six-axis bilateral problem. Direct allocation requires bilateral measurements or additional assumptions that must themselves be calibrated and tested. Instrumented-grip studies show feasible measurement precedents (Koike 2016; Choi and Park 2020), but the available public reports are not a governed participant-level data deposit for the frozen human protocol.

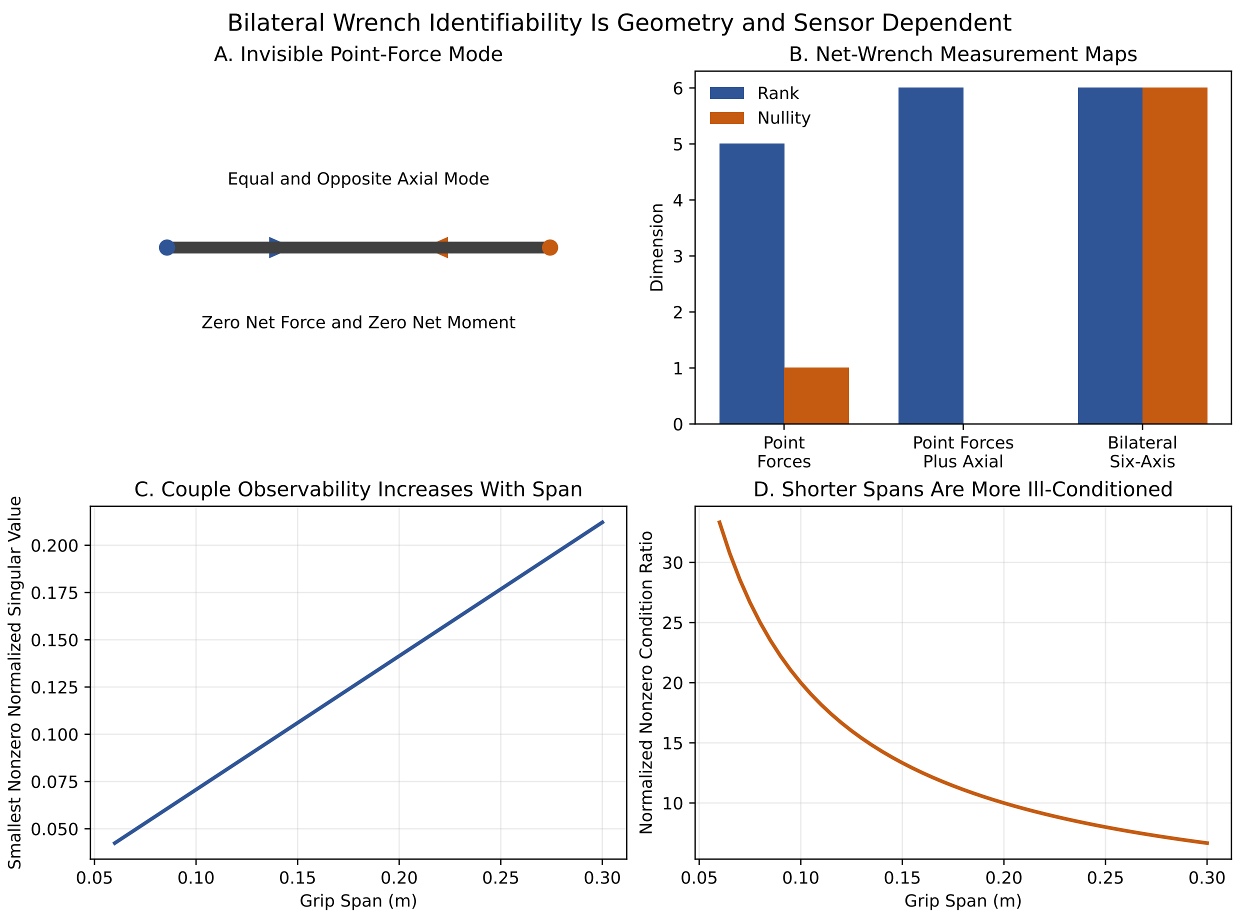

Figure 9.3: Bilateral Wrench Identifiability Is Geometry and Sensor Dependent

Figure 9.3 reports the executable audit. The point- force map is rank five with nullity one; adding the axial scalar gives rank six; and the full bilateral-wrench map is rank six with nullity six. A 0.06–0.30 m declared grip-span sweep preserves rank while increasing the smallest nonzero singular value and reducing the nonzero condition ratio. Because force and moment have different units, the plotted audit uses explicit SI numerical scaling (1 N for force and 1 N m for moment); its condition ratio is therefore measurement-scale dependent, while rank and nullity are not. Three consistent proper rotations preserve the singular values to within 2.3×10^{-16}.

This closes only an instantaneous linear structural-identifiability question. It does not establish practical identifiability under noise, identify wrist, arm, scapular, or muscle commands, or validate a human strategy. Those stronger questions require synchronized bilateral six-axis grip wrenches, contact-state or pressure measurements, kinematics, and participant-held-out evaluation. The machine-readable result and figure are regenerated by `run_bilateral_wrench_identifiability_study.py`.

9.6.1 Trajectory-Level Synthetic Sensor Qualification

The structural result supplies a necessary measurement contract, but not a device specification. A deterministic 301-sample, 32-trial synthetic qualification therefore propagates time-varying bilateral point forces through the same map under declared channel noise, normalized cross-talk, calibration error, and contact-center migration. Force channels use a 100 N normalization, moment channels use 10 N m, and the added internal-axial channel uses 100 N. These scales and perturbation levels are study inputs, not measurements from a particular instrument.

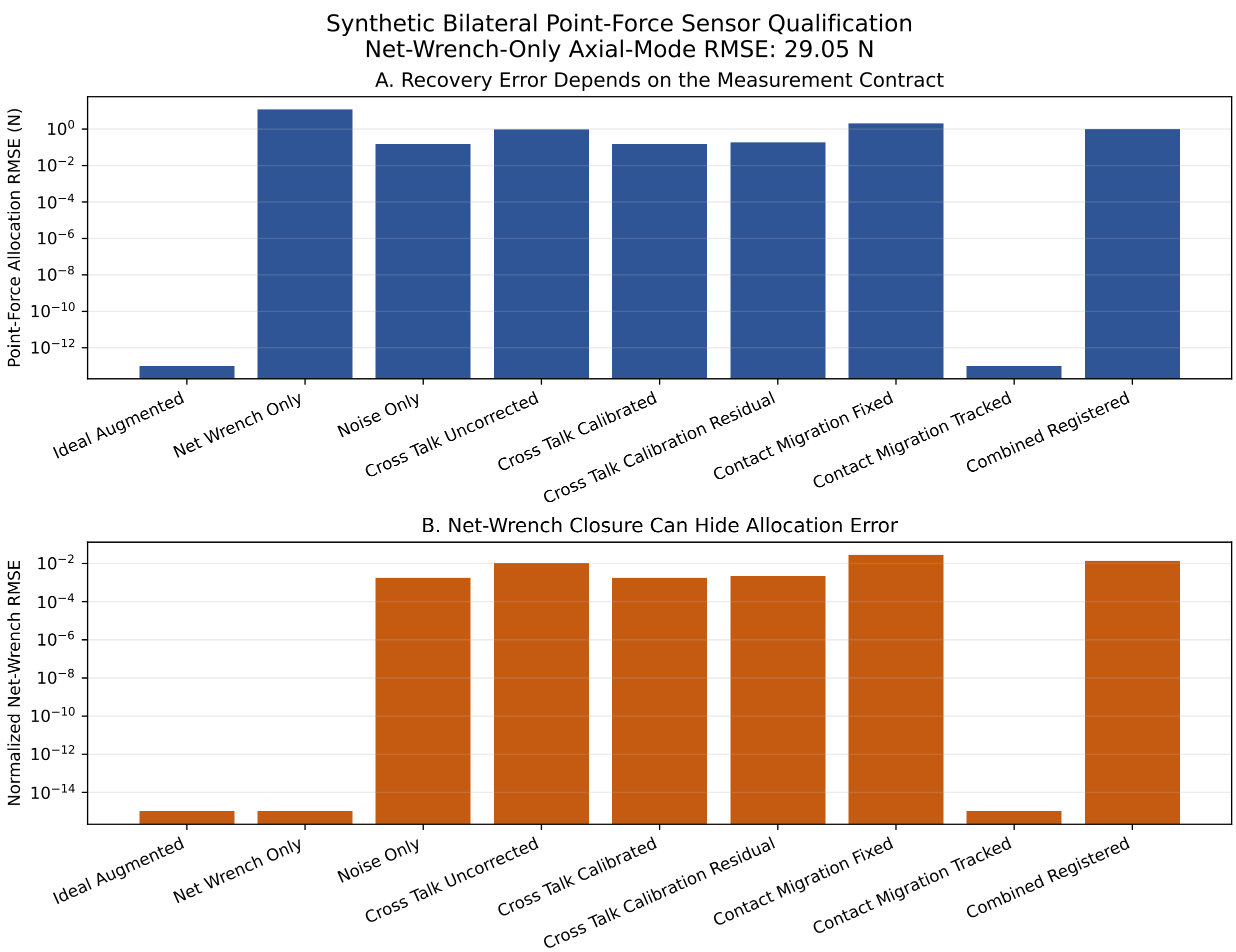

Figure 9.4: Synthetic Bilateral Point-Force Sensor Qualification

Figure 9.4 demonstrates why net-wrench closure is an insufficient acceptance test. The net-wrench-only estimator reproduces the resultant wrench to numerical precision while retaining 11.86 N bilateral allocation RMSE, 45.01 N allocation 95th-percentile error, and 29.05 N error in the invisible axial mode. Adding an independently measured axial scalar reduces the ideal allocation error to numerical precision. Under the registered combined synthetic condition, allocation RMSE is 1.02 N, its 95th percentile is 3.87 N, normalized net-wrench RMSE is 0.0142, and axial-mode RMSE is 0.351 N.

The separated controls localize two practical failure paths. One percent normalized cross-talk produces 0.942 N allocation RMSE when uncorrected and 0.153 N when its matrix is exactly calibrated; a ten-percent residual error in that cross-talk calibration raises the result to 0.179 N. Eight millimetres of declared contact-center migration produces 2.025 N allocation RMSE when the estimator holds nominal contacts fixed, whereas exact contact tracking restores numerical closure. These values qualify the executable synthetic estimator only. They do not constitute sensor calibration, uncertainty bounds for a future device, or evidence about a golfer.

The qualification remains restricted to bilateral point forces. It excludes free hand moments, distributed contact, grip compliance, shaft deformation, skin and tissue dynamics, anatomical source attribution, and human performance. A full bilateral six-axis system still requires traceable load calibration, cross-talk and drift characterization, time-varying contact registration, synchronization, and participant-held-out validation. The machine-readable cases and figure are regenerated by `run_bilateral_wrench_sensor_qualification.py`.

9.7 Reconstruction and Verification Methods

Each of the 2,801 samples is evaluated by the same sequence:

1. read the two contact positions, forces, free torques, velocities, midpoint, and stored equivalent wrench;
2. compute the resultant with Equation 9.2;
3. compute the midpoint contact-force moment and add the free torques with Equation 9.3;
4. project global quantities onto the declared local axes;
5. locate every sign crossing by linear interpolation inside its adjacent 0.1 ms sample bracket; and
6. repeat the crossing estimate after downsampling by factors through 20, using every possible sample offset.

The reconstruction tolerances are absolute and deliberately much tighter than the signal magnitudes. Across BASE, ZTCF, and DELTA, the largest resultant residual is 1.1×10^{-12} N. The largest global couple residual is 0.057 N $\cdot$ m, or less than 0.1% of the approximately 59 N $\cdot$ m peak. BASE minus ZTCF minus DELTA closes to 1.2×10^{-13} N $\cdot$ m for the local equivalent couple.

The small nonzero couple reconstruction residual is consistent with archived table interpolation and coordinate-transform precision. It is not used to infer a physical torque. The test limit is 0.1 N $\cdot$ m, more than an order of magnitude above floating-point noise but far below the negative-couple peak.

9.8 Results: Where the Negative Couple Comes From

Figure 9.5 provides the decisive decomposition. In BASE, the equivalent couple reaches a minimum of -22.79 N $\cdot$ m at 0.2151 s. At that instant, -18.60 N $\cdot$ m comes from separated contact forces and -4.22 N $\cdot$ m comes from applied free torque. In pointwise ZTCF, both individual command-torque columns and kill damping are zero, yet the equivalent couple reaches -19.63 N $\cdot$ m at 0.2148 s. The reconstructed free-torque contribution there is below 3.1×10^{-13} N $\cdot$ m. The reconstructed free torque agrees with the sum of the two command columns to the same bound; the negative couple is therefore entirely a contact-force moment to the resolution of the archive. Checking each command separately is essential because checking only their net could hide equal and opposite nonzero commands.

At the time of the BASE minimum, the ZTCF couple retains 86.1% of the BASE magnitude. DELTA is exact by construction, but its peak negative couple is only -3.18 N $\cdot$ m. These comparisons support a narrow conclusion: *within the achieved states of this model, most of the late negative midpoint couple does not require instantaneous commanded wrist torque.*

They do not support the stronger claim that wrist torque is irrelevant. Active torques helped create the state history on which ZTCF is evaluated, and BASE free torque contributes measurably to the total. Nor do they prove the same partition in a human swing.

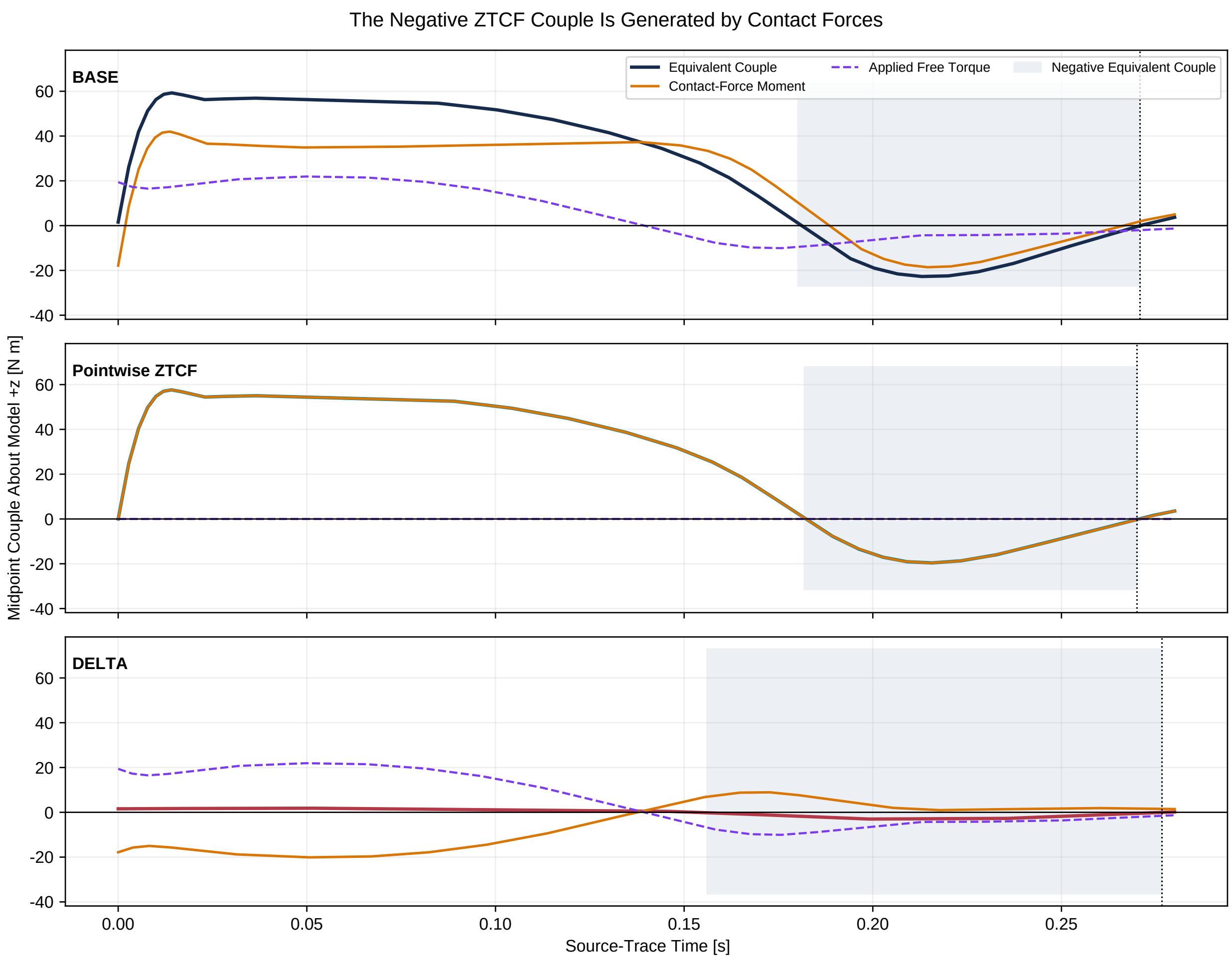

Figure 9.5: The Negative ZTCF Couple Is Generated by Contact Forces

9.8.1 Timing of the Two Sign Changes

All three cases contain an early positive-to-negative crossing and a later negative-to-positive crossing. For BASE, the negative interval begins at 0.180172 s and ends at 0.270824 s. For ZTCF, it begins at 0.181894 s and ends at 0.270016 s. Thus the late BASE and ZTCF reversals differ by 0.808 ms. Their crossing-to-crossing negative intervals last 90.652 and 88.122 ms, respectively.

The archived sample interval is 0.1 ms. After downsampling to effective steps as large as 2 ms and repeating every phase offset, the largest shift in the late crossing is 7.95 microseconds for BASE and 7.41 microseconds for ZTCF. This demonstrates interpolation and sampling stability for the stored smooth curves. It is not a new Simscape solver-tolerance study; changing solver, constraint stabilization, or shaft discretization remains a separate model sensitivity question.

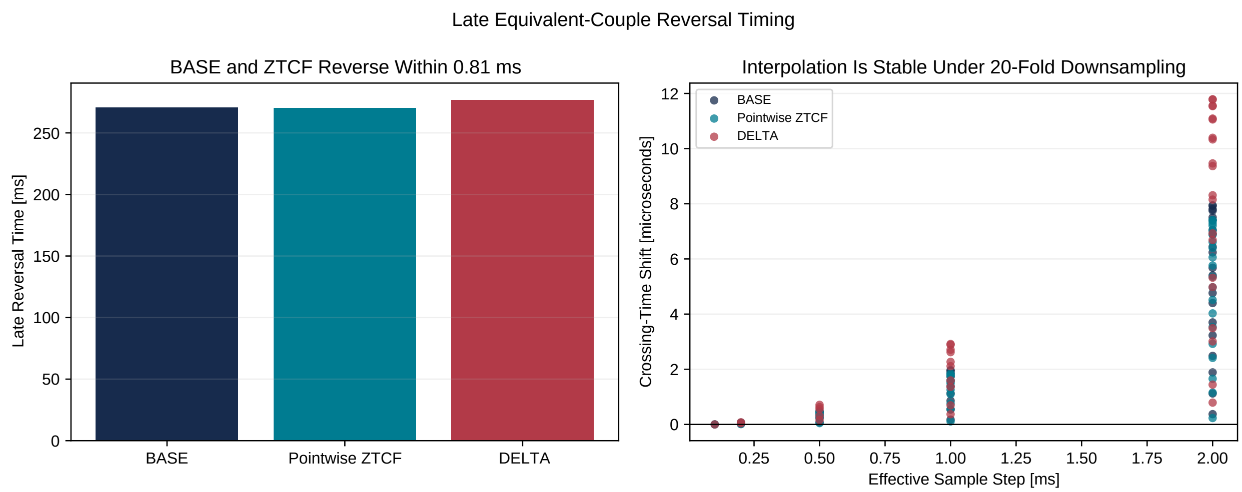

Figure 9.6: Late Equivalent-Couple Reversal Timing

The DELTA late crossing occurs later, at 0.276634 s. Treating the DELTA crossing as the onset of the passive mechanism would therefore be incorrect. DELTA asks how BASE differs from the pointwise zero-command reaction. The ZTCF curve itself is the relevant evidence for a moment that remains without current command.

9.9 Local Force Geometry Through the Downswing

The local force histories in Figure 9.7 expose the mechanism hidden by the resultant. Near the ZTCF minimum, the lead and trail normal forces are +249.8 N and -266.2 N. Their opposition makes the differential normal mode large and negative under Equation 9.7. At the same instant, the lead and trail axial forces are -497.5 N and +30.4 N. Those axial loads influence the resultant and internal loading, but their direct midpoint moment is suppressed by the small perpendicular lever arm.

The sign evolution is geometric. A force does not carry an intrinsic "accelerating" or "decelerating" label. Its moment depends on the cross product between its lever arm and direction, while its power depends on its dot product with contact velocity. During the downswing, both the grip direction and the contact-force directions rotate. The same anatomical hand can therefore move from one moment quadrant to another without an abrupt change in force magnitude.

Figure 9.8 shows six global poses. The view is three-dimensional because the archive stores global vectors in three coordinates, while the nearly equal global y and z coordinates reveal the declared oblique model plane. The force arrows change relative to the short grip segment: the visual transition from positive couple, through the negative minimum, and back through the late reversal is a cross-product change, not evidence of an invisible command.

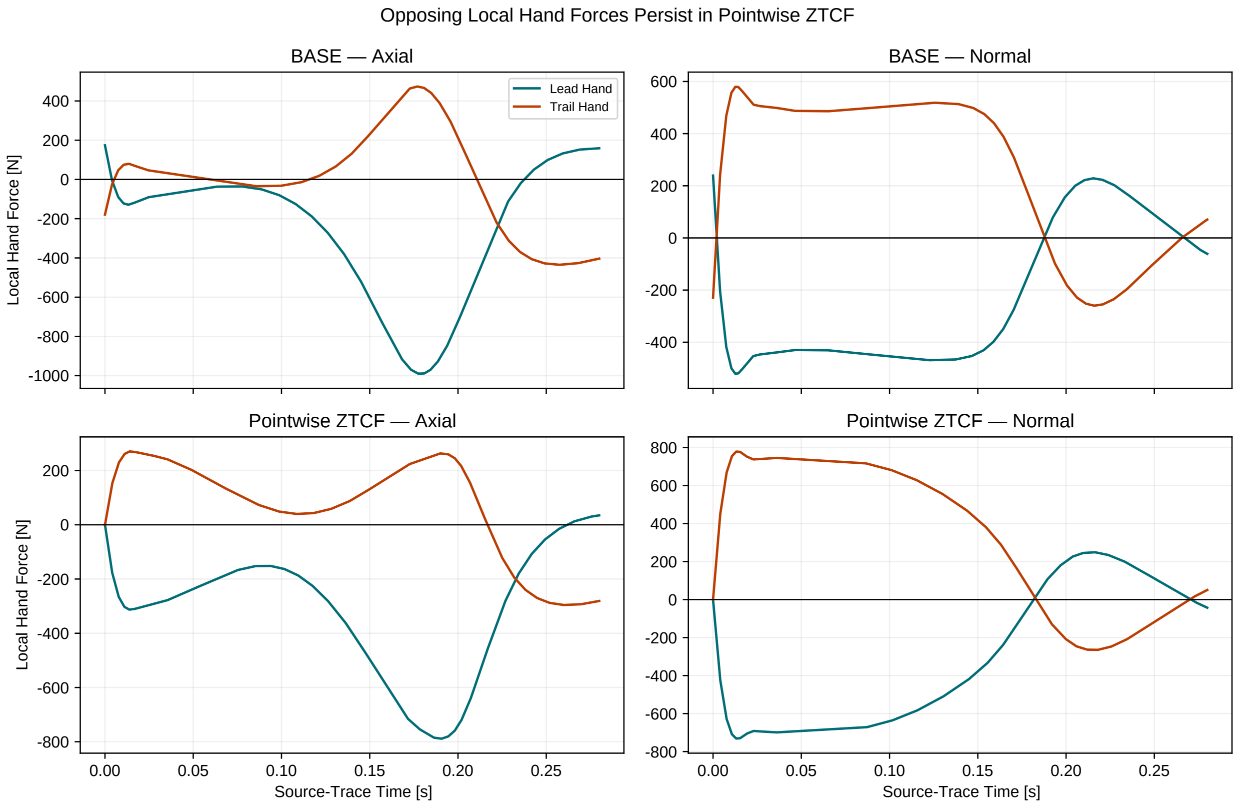

Figure 9.7: Opposing Local Hand Forces Persist in Pointwise ZTCF

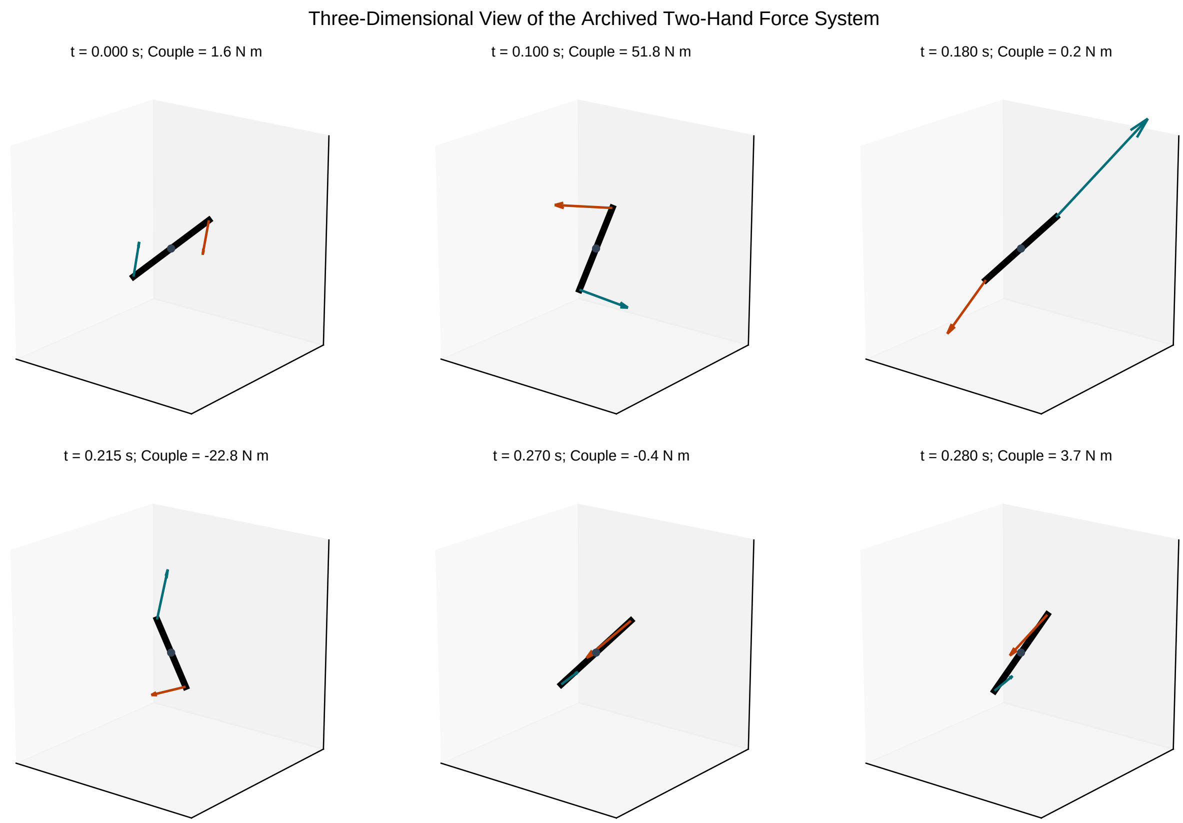

Figure 9.8: Three-Dimensional View of the Archived Two-Hand Force System

9.10 Geometry Counterfactuals

The force-generated couple can be perturbed without changing the force values. At the peak-negative ZTCF sample, two deterministic counterfactuals were applied:

1. scale both contact offsets from the midpoint while holding their directions and forces fixed; and
2. rotate the grip/contact offsets within the model plane while holding the global force directions fixed.

The first experiment produces an exactly linear response, as required by Equation 9.7. Doubling the separation doubles the contact-force moment; collapsing the contacts to one point removes it. This is a mechanics identity, not a recommendation to alter grip width without regard to anatomy or control.

The second experiment produces the expected sinusoidal orientation gate. At some relative orientations the same forces create a positive moment; at others they create a negative one. When the contacts and forces are rigidly co-rotated together, the moment is invariant to 1.5×10^{-14} N · m. Therefore global pose alone does not set the sign. The sign is controlled by the *relative* orientation of the contact-separation vector and differential force.

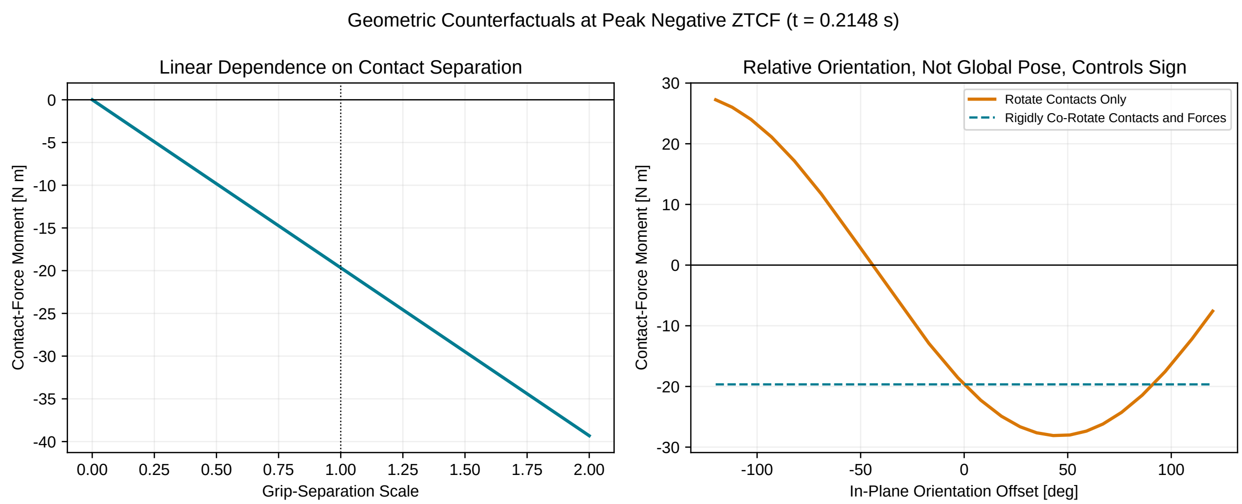

Figure 9.9: Geometric Counterfactuals at Peak Negative ZTCF

The practical implication is a constraint on strategy language. "Create more negative torque" is under-specified. A controller can change the moment by changing contact separation, force opposition, force direction relative to the grip, or a true applied free torque. Those routes have different effects on joint loading, net force, power, and robustness. They must not be collapsed into one scalar cue.

9.11 Couple Sign, Power, and Clubhead Speed

Moment sign is not energy-transfer sign. For a rigid body reduced at midpoint M, wrench power would be

$$P = \mathbf{R} \cdot \mathbf{v}_M + C_M \omega. \tag{9.10}$$

The archived model contains two distinct moving contacts. An exact two-point force-power identity is therefore more informative. With $\Delta\mathbf{v} = \mathbf{v}_T - \mathbf{v}_L$ and $\Delta\mathbf{F} = (\mathbf{F}_T - \mathbf{F}_L)/2$,

$$P_F = \mathbf{F}_L \cdot \mathbf{v}_L + \mathbf{F}_T \cdot \mathbf{v}_T = \mathbf{R} \cdot \mathbf{v}_M + \Delta\mathbf{F} \cdot \Delta\mathbf{v}. \tag{9.11}$$

The relative-velocity term can be separated into rigid rotation and a small contact-deformation remainder. The implemented identity closes internally within 2.0×10^{-11} W. It is not an exact reproduction of the archive's separately stored linear-power columns: the maximum ZTCF discrepancy is 72.8 W. That discrepancy is retained as an evidence limit rather than silently treating the source power as a ground truth. In ZTCF, the maximum magnitude of the relative-contact remainder is only 0.188 W, compared with reconstructed contact-force power peaks above 4 kW; the grip-contact kinematics are effectively rigid for this calculation.

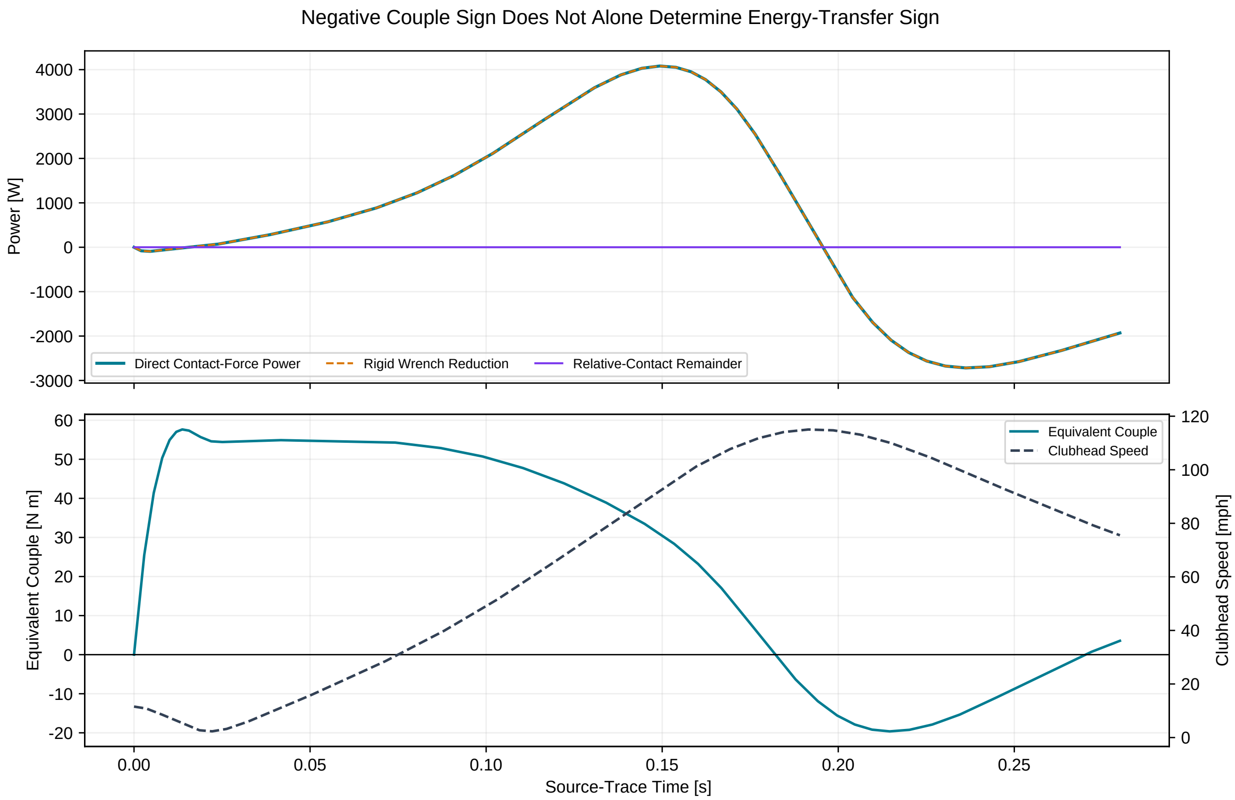

Figure 9.10: Negative Couple Sign Does Not Alone Determine Energy-Transfer Sign

At the ZTCF negative-couple minimum, the reconstructed grip angular velocity is 36.21 rad/s and the reconstructed contact-force power is -2.08 kW. Clubhead speed is already about 110.0 mph, close to the archived 115.1 mph maximum at 0.1933 s. Across the interpolated 88.122 ms negative-couple interval, reconstructed contact-force power is negative at 84.95% of the interval samples and integrates to -149.42 J. The archived linear-power columns retain the same sign throughout those samples and integrate to -149.45 J despite their larger pointwise discrepancy elsewhere. In this particular trace, the negative zero-command couple is principally associated with late redirection and deceleration after peak speed, not with a direct positive-power boost to the club.

That finding sharpens, rather than rejects, the proposed mechanism. A zero-command negative couple can arise from state-dependent dynamics and constraint geometry without being the source of positive club work. This archive does not isolate momentum from every other state-dependent term. Any strategic value would therefore be an indirect hypothesis involving the high-speed state, orientation, and active opposition to the late reaction. Whether it improves impact delivery requires an optimization with impact timing, face orientation, actuator limits, and shaft stress—not inspection of the torque sign alone.

9.12 Mechanistic Interpretation by Phase

The archived trace can be read in four phases without assigning intent to the model:

Positive-Couple Formation (0–0.180 s). The two-hand force system initially creates a positive midpoint couple. Both BASE and ZTCF rise rapidly, showing that constraint reactions dominate even before the sign reversal.

Passive Negative-Couple Entry (approximately 0.180 s). BASE and ZTCF cross zero within 1.7 ms of one another. The similarity of their force-generated moments indicates that the sign transition is largely encoded in the achieved positions and velocities rather than the instantaneous wrist command.

Peak Negative Reaction (approximately 0.215 s). Opposed normal forces form the dominant negative couple while clubhead speed is near its maximum. BASE free torque augments the negative action by about 4.2 N · m, but ZTCF demonstrates that the larger contact-force contribution remains with command removed.

Late Recovery and Reversal (approximately 0.270 s). Relative geometry and contact forces evolve until the couple returns positive. BASE and ZTCF reverse at nearly the same time; DELTA reverses later and should not be mistaken for the passive timing signal.

This phase description is mechanical, not anatomical. The model does not resolve muscle coordination, grip-pressure distributions, tendon elasticity, or neural control. It identifies a candidate force-system pathway that future measurements can attempt to confirm or falsify.

9.13 Implications for Speed-Creation Strategy

The present evidence supports constraints on a strategy rather than a universal instruction:

- **Build the state before judging the late reaction.** ZTCF is large because earlier motion has created large velocities and a particular geometry.
- **Track differential normal force, not net force alone.** The opposed mode is the direct geometric source of the two-hand couple.
- **Separate modeled speed production from impact management.** In this trace, positive club power precedes the late negative-couple interval, while the interval itself is predominantly negative in reconstructed contact-force power. That ordering does not identify which actuator or force pathway caused the earlier speed gain.
- **Test rather than prescribe reaction opposition.** Adding positive command solely to cancel the modeled negative couple could change loading, impact orientation, or both. Whether opposition helps is a registered optimization hypothesis, not a technique recommendation from this single trajectory.
- **Constrain the endpoint.** A credible optimization must evaluate clubhead speed at impact together with face/path orientation, grip loads, shaft stress, actuator work, and sensitivity to timing errors.

This framework rejects two simple slogans: neither "negative torque creates speed" nor "negative torque wastes speed" is generally valid. Power, timing, and endpoint constraints decide the effect.

9.14 Limitations and Falsification Tests

The strongest current result is internal: the archived model's negative ZTCF couple reconstructs from separated contact forces with zero current command. Several limitations bound external interpretation:

- ZTCF is pointwise along the commanded state history, not a forward two-hand killswitch rollout. Its exported contact state matches BASE only to the registered cache precision, with maximum position, velocity, and clubhead- speed residuals of 1.85×10^{-7} m, 8.93×10^{-6} m/s, and 3.67×10^{-5} mph.
- The source is one deterministic planar simulation and one parameter set.
- The model uses idealized wrist contacts and does not resolve pressure across the hands or grip.
- Shaft and grip compliance are present in the source architecture but have not yet been separated by matched rigid/flexible reruns.
- Downsampling verifies interpolation stability, not solver-tolerance or constraint-stabilization independence.
- The reconstructed two-contact force-power identity closes internally, but the archived ZTCF linear-power columns differ by as much as 72.8 W. Agreement of interval sign and work does not erase that pointwise

source discrepancy.

- No synchronized human hand-force and full-body kinematic data are used.

The mechanism would be materially weakened if a like-for-like rerun showed any of the following: the ZTCF negative couple disappears under solver refinement; the sign is caused by a frame or action-reaction error; rigid/flexible variants reverse the attribution; a forward killswitch leaves the negative region too quickly to matter; or measured human contact forces fail to exhibit the predicted differential-normal pattern.

The next model layer should therefore separate gravity, momentum-dependent terms, damping, and shaft elasticity while preserving the same wrench and power contracts. Higher-order and human-data studies should retain the distinction between resultant force, force-generated moment, free torque, and power. That shared vocabulary is the main reusable product of the present analysis.

Chapter 10

Forward Constrained Two-Hand Dynamics

10.1 Purpose and Evidential Scope

The preceding two-hand analysis established that separated contact forces can produce a club couple even when their resultant is small. It also reconstructed the archived WSCG zero-command solution point by point along a commanded state history (Olson 2024). That calculation answers an instantaneous question: what acceleration and constraint force would the model produce if the applied commands were removed at this state? It does not answer whether the resulting negative couple survives after the state begins to evolve under zero command.

This chapter supplies that missing forward test. Two planar two-link arms grasp a club with two independent point constraints. The club translates and rotates; the arm and club coordinates evolve under the constrained equations of motion. At a declared late-downswing state, all six applied joint torques are set to zero and a new trajectory is integrated from the *exact same* generalized position and velocity. The resulting branch is therefore a test of dynamic persistence, not a stitched collection of same-state counterfactuals.

The scope is deliberately narrow. The calculation establishes mechanical feasibility in a planar rigid-body model. It is not a fit to a golfer, contains no muscle model, does not identify neural intent, and does not prove that a human golfer uses the modeled strategy. Redundant two-hand tasks generally do not permit biological effort to be inferred uniquely from the net wrench (Reinkensmeyer, Lum, and Lehman 1992; Zatsiorsky and Latash 2008). The more defensible result is that a negative late force-generated club couple can persist without continued command in a nonsingular forward constrained model.

10.2 Coordinates, Geometry, and Closure

The generalized coordinate vector is

$$q = \begin{bmatrix}\theta_{Rs} & \theta_{Re} & \theta_{Ls} & \theta_{Le} & x_c & y_c & \phi_c\end{bmatrix}^{\mathsf{T}}, \tag{10.1}$$

where the four arm angles describe right and left shoulder–elbow chains and (x_c, y_c, ϕ_c) describe the floating club. Angles are measured in the declared planar frame, with x along the target-line coordinate and y upward. For a segment angle α, the direction and angular derivative are

$$d(\alpha) = \begin{bmatrix}\sin\alpha \\ -\cos\alpha\end{bmatrix}, \qquad d_{,\alpha}(\alpha) = \begin{bmatrix}\cos\alpha \\ \sin\alpha\end{bmatrix}. \tag{10.2}$$

The right and left hand positions follow from the corresponding two-link chains. The club grip points are

$$r_{g,R} = r_c + a_R d(\phi_c), \qquad r_{g,L} = r_c + a_L d(\phi_c), \tag{10.3}$$

with $a_R = +0.065$ m and $a_L = -0.065$ m in the reference case. The four holonomic constraints are

$$C(q) = \begin{bmatrix} r_{h,R}(q) - r_{g,R}(q) \\ r_{h,L}(q) - r_{g,L}(q) \end{bmatrix} = 0, \qquad J(q) = \frac{\partial C}{\partial q}. \tag{10.4}$$

The model has seven coordinates and four independent scalar constraints, leaving three admissible instantaneous degrees of freedom. Every accepted sample must retain rank $J = 4$. A rank-deficient Jacobian, a singular Schur complement, or a constraint residual above the declared limit causes the solver to fail closed; a least-squares fallback is not used. This is important because a numerically convenient force allocation at a singular grasp would not be evidence for a physically identified two-hand couple.

10.3 Constrained Equations of Motion

The mass matrix is assembled from center-of-mass translational Jacobians and segment angular Jacobians. Gravity and the velocity-dependent bias are kept explicit. This follows standard rigid-body dynamics accounting (Featherstone 2008) while retaining the small model's auditable analytical structure. At each state, the acceleration and constraint multiplier solve

$$\begin{bmatrix} M(q) & -J(q)^\top \\ J(q) & 0 \end{bmatrix} \begin{bmatrix} \ddot{q} \\ \lambda \end{bmatrix} = \begin{bmatrix} Q(u) - h(q, \dot{q}) \\ -\dot{J}(q, \dot{q})\dot{q} \end{bmatrix}. \tag{10.5}$$

Here $h = c + g$ contains Coriolis/centrifugal and gravitational terms. With the implemented sign convention, the force exerted by the hands on the club is $F_{h \to c} = -\lambda$ after reshaping the four multipliers into two planar forces. The residuals of both rows of Equation 10.5 are stored for every sample.

The primary acceleration-constraint bias $\dot{J}(q, \dot{q})\dot{q}$ is evaluated from the exact centripetal terms of both arms and both club grip offsets. It is not obtained by numerically differentiating J inside the KKT solve. An independent five-point centered directional derivative agrees within 1.04×10^{-9} m/s² over the reference trajectory, below the registered 10^{-7} m/s² tolerance.

The applied generalized force is not a six-entry vector copied directly into the seven coordinates. Wrist torque is an internal action–reaction pair: a positive wrist torque acts positively on the club and negatively on the two arm coordinates that contribute to the corresponding forearm angle. Thus,

$$Q(u) = \begin{bmatrix} u_{Rs} - u_{Rw} \\ u_{Re} - u_{Rw} \\ u_{Ls} - u_{Lw} \\ u_{Le} - u_{Lw} \\ 0 \\ 0 \\ u_{Rw} + u_{Lw} \end{bmatrix}. \tag{10.6}$$

This mapping prevents the directly applied wrist torque from being silently counted as a contact-force couple.

10.4 Forward Integration and Numerical Audit

The reference trajectory is integrated for 0.400 s with a 0.25 ms step. A velocity-Verlet update is paired with mass-metric position and velocity projection. For a position residual C, the local correction is

$$\delta q = M^{-1} J^\top \left(J M^{-1} J^\top \right)^{-1} C, \qquad q \leftarrow q - \delta q. \tag{10.7}$$

The projection is iterated to the declared tolerance. Velocity is projected onto $J\dot{q} = 0$ with the same mass metric. Projection correction and its numerical energy change are recorded separately. They are numerical stabilization diagnostics and are **not** reclassified as physical work.

The initial club center is $(0, -0.50)$ m, the club angle is 0.16 rad, and the arm angles are obtained by inverse kinematics on specified elbow branches. The initial generalized velocity is zero. The open-loop command is a smooth test input, not an inferred human torque history:

Applied Torque	Command Over $0 \le t \le 0.4$ s (N m)
Right Shoulder	$18 + 4t/0.4$
Right Elbow	$7 - 1.5t/0.4$
Right Wrist	$-3 + 2t/0.4$
Left Shoulder	$16 + 3t/0.4$
Left Elbow	$6 - t/0.4$
Left Wrist	$2 - t/0.4$

The commands create a repeatable state history through which mechanism interventions can be compared. They are not optimized for clubhead speed and are not presented as normative technique. More complete forward golf models have shown why joint-torque timing, body motion, and objective definition must be treated together (MacKenzie and Sprigings 2009; Balzerson, Banerjee, and McPhee 2016).

10.5 Registered Observables

The force-generated couple about the declared club center is

$$M_F = (r_{g,R} - r_c) \times F_R + (r_{g,L} - r_c) \times F_L. \tag{10.8}$$

The direct wrist contribution is stored separately as $M_w = u_{Rw} + u_{Lw}$. The total rotational action on the club is therefore $M_F + M_w$ before any other modeled external moment. This distinction is the central test: $M_F < 0$ cannot be attributed algebraically to a negative applied wrist torque because M_F is computed only from the two constraint forces.

The contact forces are also transformed into common and differential modes,

$$R = F_R + F_L, \qquad D = \tfrac{1}{2}(F_R - F_L). \tag{10.9}$$

The resultant R controls club translation. The differential mode D becomes rotationally effective through the signed grip moment arms. Large opposing forces can therefore produce a substantial couple with a modest resultant, as is familiar in multifinger prehension (Zatsiorsky and Latash 2008).

Finally, contact power is evaluated both pointwise and through the reduced wrench identity:

$$P_{contact} = F_R \cdot v_{g,R} + F_L \cdot v_{g,L} = R \cdot v_c + M_F \omega_c. \tag{10.10}$$

The two forms agree to 6.68×10^{-13} W in the reference run. Couple sign alone still does not determine energy transfer: rotational power also depends on club angular velocity, while the resultant contributes translational power. This is consistent with standard joint-force and segment-power bookkeeping (Winter 2009).

10.6 Counterfactual and Negative-Control Design

Four intervention families expose the result to contradiction.

1. **Matched-State Torque Killswitch.** At 0.200 s, the achieved q and $\dot{q}$ are copied bit for bit into a new forward trajectory and all six commands are set to zero for 50 ms. Additional branches start at 0.180, 0.190, 0.210, 0.220, and 0.240 s.
2. **Zero Contact Moment Arm.** Both grip offsets are set to zero and a new constraint-consistent initial state is constructed. If Equation 10.8 is implemented correctly, the force-generated couple must vanish even though nonzero contact forces may remain.
3. **Timestep Refinement.** The 0.400 s baseline is repeated at 2.0, 1.0, and 0.5 ms. The sign-reversal time and minimum couple must remain stable while the work–energy residual contracts.
4. **Projection Sensitivity.** The position-projection tolerance is changed from 10^{-8} to 10^{-10} m at a fixed 1.0 ms step. A mechanism that depends materially on stabilization tolerance is rejected.

These are mechanistic interventions. They are stronger than visual similarity between two curves because each has a declared null consequence and an observable failure mode.

10.7 Results

10.7.1 Force-Generated Couple Reversal

The baseline force-generated couple first becomes negative at 0.19825 s and reaches −32.85 N m over the recorded interval. The direct wrist torque ranges only from −1.0 to 0 N m and is excluded from that force-generated series. The late negative value is therefore not a relabeled wrist command.

At the 0.200 s cut, the inherited force-generated couple is −2.57 N m. With all applied commands removed, it remains negative throughout the 50 ms branch and reaches −7.43 N m. The commanded continuation becomes more negative, reaching approximately −13 N m over the same horizon, but that difference is not the central claim. The decisive observation is that the negative force-generated couple does not collapse to zero when command is removed.

The branch ensemble also limits the interpretation. A branch at 0.180 s begins before reversal and crosses negative at 0.185 s. Branches initiated from 0.190 through 0.220 s remain negative for the full 50 ms window. The 0.240 s branch remains negative for 37.25 ms before changing sign. Zero-command persistence is therefore state dependent and finite; it is not an invariant property of the club or grip.

10.7.2 Geometric Mechanism

Figure 10.2 displays the actual hand-on-club force vectors with one common scale. Between 0.180 and 0.240 s, the club and arm geometry change the signed moment arms and the tangential components of the two forces. The couple reversal is generated by that evolving vector geometry, not by force magnitude alone. At 0.300 s the force directions and club orientation have changed again, illustrating why a static instruction such as “pull harder” cannot specify the sign of M_F.

The zero-moment-arm intervention makes the geometric requirement explicit. When both grip points coincide with the club center, the maximum absolute force-generated couple is exactly 0 N m to machine representation. Contact force alone is insufficient; a nonzero signed lever arm and a transverse force component are jointly necessary.

10.7.3 Solver Closure and Convergence

The reference trajectory retains constraint rank four. The maximum position constraint residual is 9.51×10^{-11} m, the maximum velocity residual is 5.03×10^{-15} m/s, the KKT residual is below 4.41×10^{-13}, and the acceleration-constraint residual is below 2.57×10^{-13}. Complete two-sided ideal-constraint power, $\lambda^{\mathsf{T}} J\dot{q}$, remains below 1.27×10^{-12} W; this is distinct from the one-sided contact power delivered to the club. Over

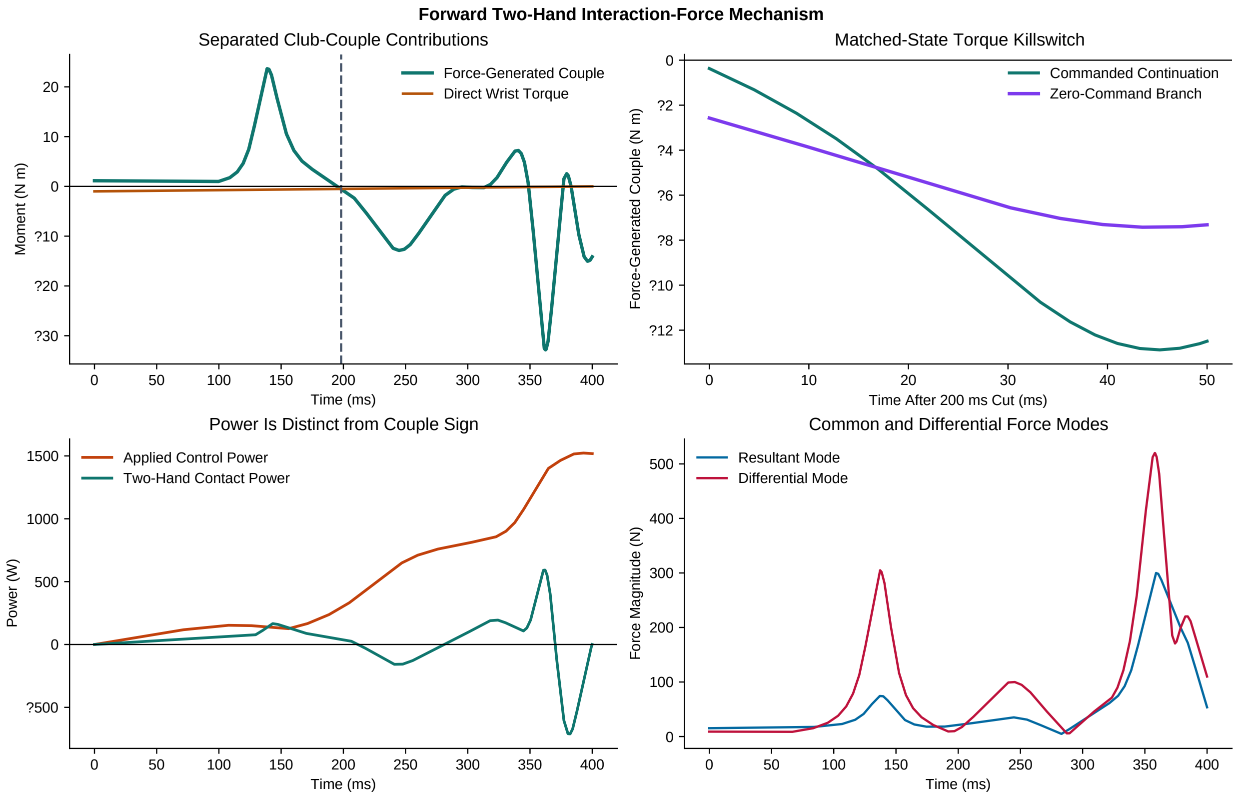

Figure 10.1: Forward Two-Hand Interaction-Force Mechanism. The force-generated couple is separated from direct wrist torque (upper left). A zero-command branch starts from the exact 200 ms state and retains a negative couple for the full 50 ms window (upper right). Contact power and common/differential force modes show why moment sign, power sign, and force magnitude are different observables.

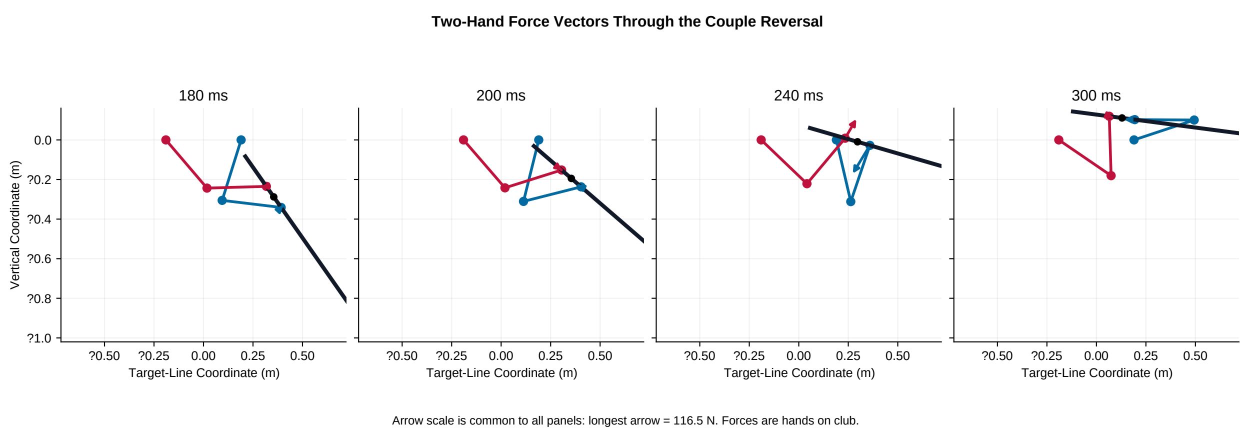

Figure 10.2: Two-Hand Force Vectors Through the Couple Reversal. Blue and red arrows are the right- and left-hand forces on the club; all panels use the same force scale. Black denotes the floating club, colored links denote the two arms, and the black point is the declared club center.

the 0.400 s interval, mechanical energy rises by 203.714 J and integrated applied-control work is 203.618 J, leaving a 0.096 J numerical work–energy residual at the 0.25 ms reporting step.

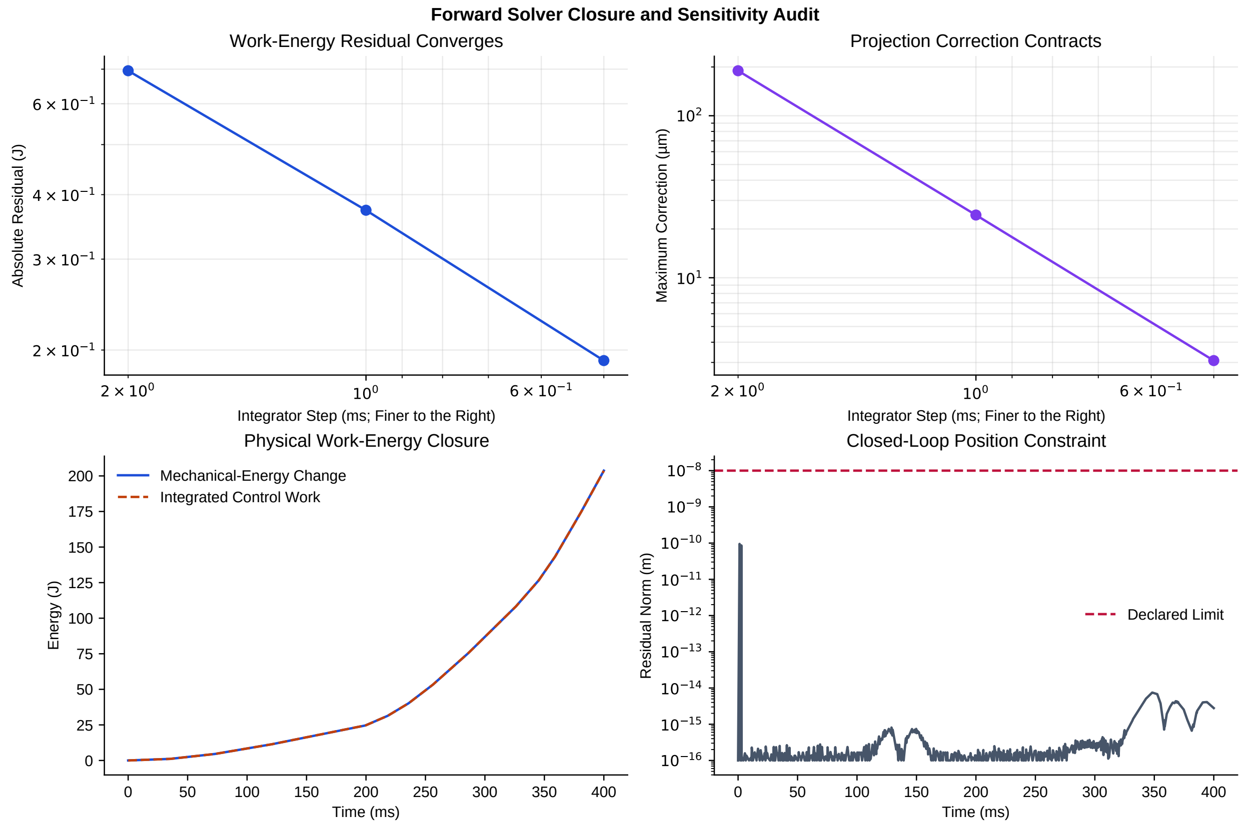

Figure 10.3: Forward Solver Closure and Sensitivity Audit. Work–energy residual and maximum projection correction contract under timestep refinement (top). Integrated control work overlays the mechanical-energy change, while the closed-loop position residual remains below its declared limit (bottom).

The work–energy residual decreases from 0.695 to 0.373 to 0.191 J as the step is refined from 2.0 to 1.0 to 0.5 ms. The maximum projection correction falls from 190 to 24.4 to 3.08 μm over the same sequence. Negative-couple onset is 0.1980, 0.1980, and 0.1985 s, a spread of only 0.5 ms. Tightening the projection tolerance by two orders of magnitude changes the 1.0 ms minimum couple by less than 5×10^{-8} N m and leaves onset unchanged. The reported reversal is therefore resolved relative to both timestep and projection tolerance in this model.

The baseline projections change mechanical energy by -0.778 J in signed sum (0.778 J in absolute sum), with no individual correction larger than 0.00446 J. This cumulative correction is larger than the raw 0.096 J work–energy residual, so the latter is not the complete integration-error budget. The projection-energy diagnostic is negative and converges toward zero with timestep refinement. It is not added to or subtracted from the physical work budget; reporting both prevents numerical stabilization and cancellation from being mistaken for passive energy transfer or exact closure.

10.8 What the Forward Test Establishes

The forward calculation strengthens the archived pointwise result in one specific way: it demonstrates that an achieved state can carry a negative force-generated two-hand couple forward for a finite interval after all applied joint torques are removed. The negative control shows that the effect requires grip geometry, and the convergence studies show that it is not a timestep or projection-tolerance artifact at the declared resolution.

It does **not** establish that the negative couple is wholly passive in a human swing. The baseline state was created by prior applied torques; after the cut, gravity, velocity-dependent interaction terms, and constraint reactions remain. “Passive” here means zero *applied model command after the branch*, not absence of force, momentum, gravity, stored energy, or biological activation. Nor does the model include a moving torso, out-of-plane rotations, compliant wrists, a distributed shaft, hand-contact compliance, or ground reaction pathways.

For strategy, the result supports a conditional mechanical statement rather than a coaching prescription: club acceleration can coexist with a negative hand-force couple when the current state and grip geometry make the coupled reaction favorable. Consequently, maximizing positive wrist torque at every instant is not a necessary condition for increasing distal speed. Whether a specific golfer should reduce, reverse, or maintain wrist torque requires the higher-order moving-base, flexible-shaft, three-dimensional, and human-data tests that follow in the completion program.

Chapter 11

Interactive Proximal–Distal Dynamics Workbench

An open-source interactive workbench accompanies the scripted analyses. It provides PyQt6 and React/Tauri interfaces for the double-pendulum, triple-pendulum, and bilateral golfer models. Both interfaces consume one machine-readable experiment and glossary catalog from the canonical Tools pendulum simulator, so experiment names, hypotheses, falsifiers, limitations, and definitions do not diverge between applications.

The guide exposes six bounded experiments: passive two-link transfer, distal-torque onset, a three-link cascade, the two-hand equivalent-couple mechanism, pointwise versus forward zero-torque counterfactuals, and a parameter-robustness envelope. Each experiment names an observation that would weaken or reject its proposed interpretation. The interfaces expose force and moment vectors, energy and power histories, counterfactual comparisons, and parameter perturbations; hover help and a searchable glossary define the terms at the point of use.

The workbench is not the authority for numerical claims in this document. Interactive states are intentionally exploratory and carry the evidence status `exploratory_model_output`. Publication evidence must be reproduced by the committed scripts, frozen parameters, matched controls, convergence and closure checks, and machine-readable outputs described in Section 28. This separation allows a reader to discover and challenge mechanisms without converting an unrecorded GUI configuration into evidence.

Installation, launch commands, the guided-experiment matrix, and interpretation boundaries are provided in the workbench guide. UpstreamDrift consumes the Tools provider rather than maintaining a second implementation, and its immutable vendor pin identifies the reviewed provider revision.

Chapter 12

Gravity, Momentum, Damping, and Shaft-Flex Contributions

12.1 The Attribution Question

The preceding chapters established two different passive mechanisms. In the double pendulum, interaction forces can accelerate the distal segment at zero instantaneous wrist torque. In the archived two-hand model, separated contact forces can create a negative midpoint couple while the commanded free torques are zero. Neither result identifies the share attributable to gravity, velocity-dependent dynamics, dissipation, or shaft deformation. This chapter separates those terms in one declared, reproducible surrogate and asks four narrow questions:

1. Which terms create the instantaneous distal angular acceleration?
2. Which terms supply external work, dissipate energy, or merely redistribute it?
3. How much does one lumped shaft-flex mode change the matched delivery?
4. Do those conclusions persist when stiffness, damping, torque-cut time, impact window, and integration step are varied?

The analysis is deliberately a mechanism study. It is not a calibrated model of a named shaft, a reconstruction of a human swing, or a validation of the archived Simscape model. The implementation and machine-readable results are available in `flexible_shaft_study.py` and `shaft_contribution_study.json`.

12.2 A Matched Flexible and Rigid Pair

The model is a planar, three-coordinate, point-mass chain. The first coordinate is the arm angle, the second is the wrist-relative club angle, and the third, ϕ_2, is a lumped torsional shaft-deflection coordinate between proximal shaft mass and clubhead mass. The generalized state is

$$\mathbf{q} = (\theta_1, \phi_1, \phi_2)^{\mathsf{T}}. \tag{12.1}$$

The flexible and rigid cases have the same lengths, masses, gravity, joint damping, initial condition, and prescribed shoulder/wrist torque history. The rigid case is the exact coordinate reduction $\phi_2 = \dot{\phi}_2 = 0$, not a separately tuned model. This matched construction isolates the consequence of admitting one elastic degree of freedom.

The reference parameters are intentionally transparent: an 0.75 m arm, 0.45 m proximal shaft, 0.55 m distal shaft, 7.5 kg arm point mass, 0.15 kg proximal shaft point mass, and 0.20 kg distal head point mass. Projected

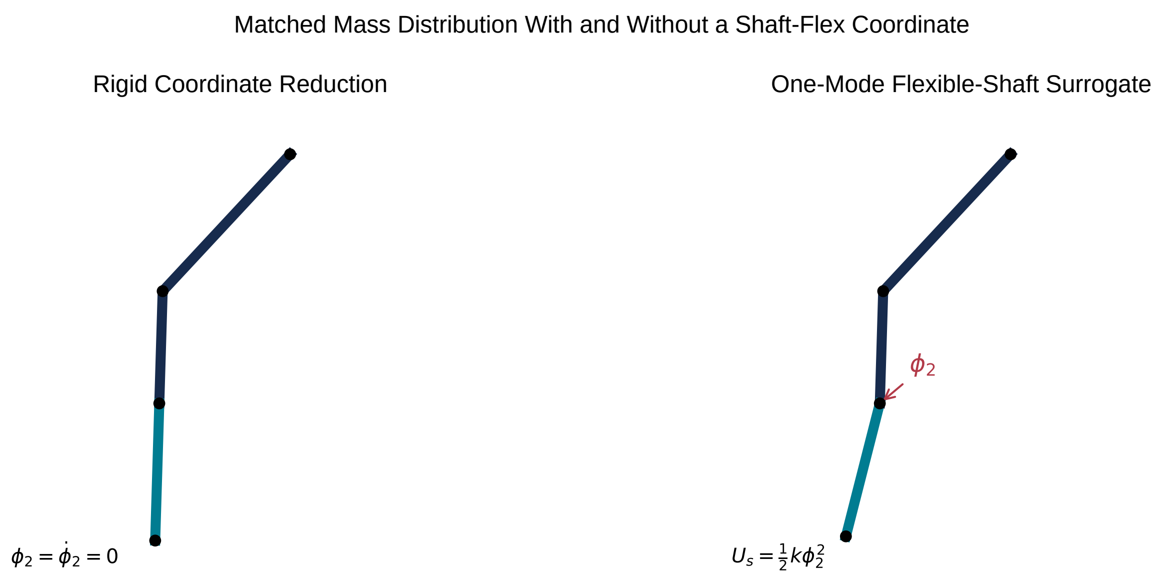

Figure 12.1: Matched Mass Distribution With and Without a Shaft-Flex Coordinate

gravity is 8.033 m/s². The linear shaft mode uses $k_s = 80\ \mathrm{N \cdot m/rad}$ and $c_s = 0.6\ \mathrm{N \cdot m \cdot s/rad}$. These values define the demonstration; they are not presented as a fitted equipment specification.

This point-mass idealization is more restrictive than a distributed Euler– Bernoulli or Timoshenko beam. It omits bending-plane coupling, torsion, frequency-dependent material loss, clubhead inertia, grip compliance, and three-dimensional handle motion. Large deflections in the sensitivity grid therefore identify stress tests of the surrogate, not credible predictions of a real shaft.

12.3 Equation-Level Contribution Accounting

The equations are written as

$$\mathbf{M}(\mathbf{q})\ddot{\mathbf{q}} = \tau_{\mathrm{ctrl}} - \mathbf{C}(\mathbf{q}, \dot{\mathbf{q}}) - \mathbf{G}(\mathbf{q}) + \tau_{\mathrm{joint\,damp}} + \tau_s + \tau_{s,d}, \tag{12.2}$$

where $\mathbf{C}$ contains the velocity-dependent inertial terms. The linear elastic and viscous shaft actions are

$$\tau_s = -k_s \phi_2, \qquad \tau_{s,d} = -c_s \dot{\phi}_2. \tag{12.3}$$

For every right-hand-side term $\mathbf{f}_j$, the corresponding generalized acceleration contribution is

$$\ddot{\mathbf{q}}_j = \mathbf{M}^{-1} \mathbf{f}_j, \qquad \ddot{\mathbf{q}} = \sum_j \ddot{\mathbf{q}}_j. \tag{12.4}$$

This is an exact algebraic decomposition at each state. It avoids assigning physical meaning to a single off-diagonal mass-matrix entry without accounting for the full coupled solve. In the tested trace, reconstructed and directly solved accelerations agree to floating-point precision.

Figure 12.2 shows the contributions to the absolute distal angular acceleration. The shaft-elastic term can be locally large because the reduced distal inertia is small. That statement concerns acceleration, not energy creation. A large instantaneous acceleration contribution can reverse sign later and perform nearly zero net work.

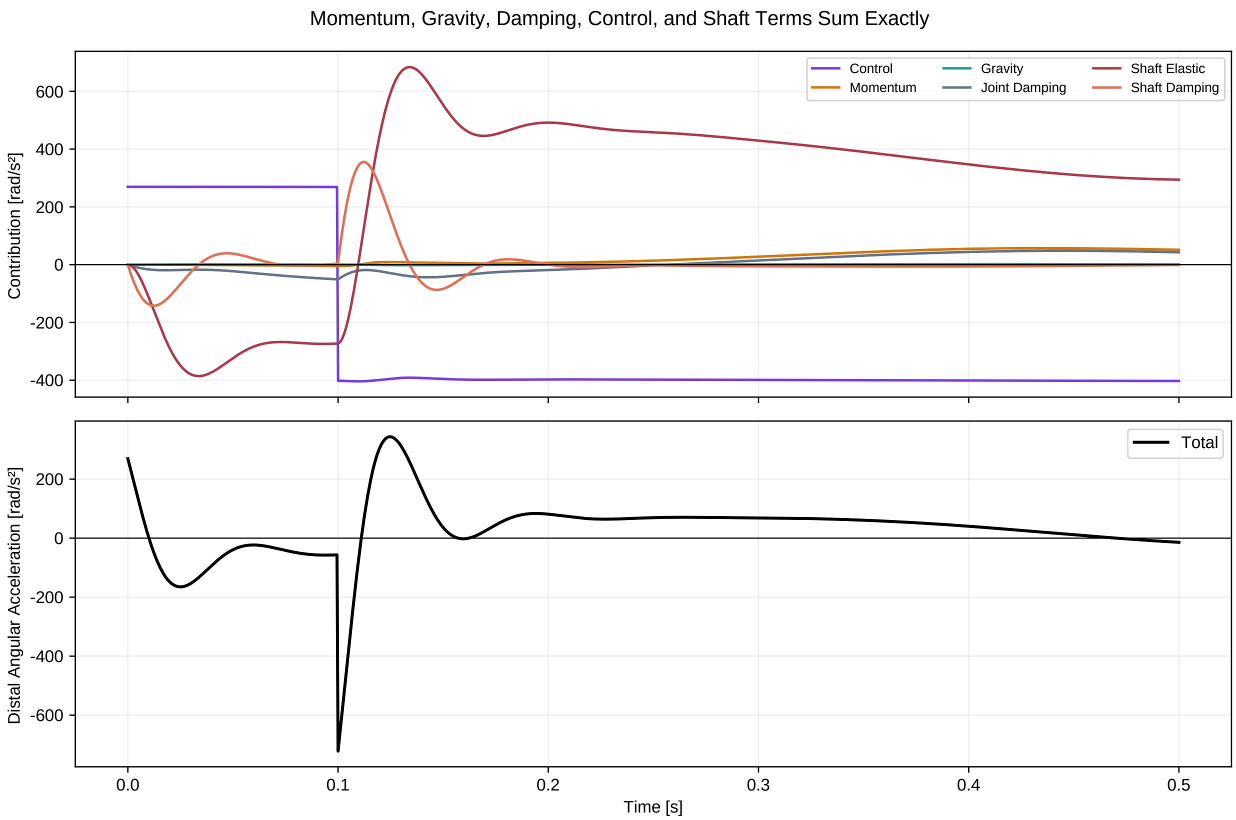

Figure 12.2: Momentum, Gravity, Damping, Control, and Shaft Terms Sum Exactly

12.3.1 Momentum Is Not an External Energy Source

For diagnostic symmetry, the analysis records the generalized quantity $(-\mathbf{C})^\mathsf{T}\dot{\mathbf{q}}$ and its time integral. In the reference trace that signed integral is 8.52 J. It must not be interpreted as 8.52 J of external work. The Coriolis/centrifugal vector arises from the coordinate representation of internal inertial coupling; it redistributes kinetic energy among generalized coordinates while the complete kinetic-energy derivative retains the required mass-matrix terms. Only boundary actuation, conservative potential changes, and declared dissipative processes enter the total energy balance below.

The same caution applies to labels such as "centrifugal power." A coordinate projection is useful for attribution, but it is not a new reservoir. The mechanism is exchange through coupled geometry and constraint forces. Numerically, the Christoffel-form identity $\dot{\mathbf{q}}^\mathsf{T}\mathbf{C} = \frac{1}{2}\dot{\mathbf{q}}^\mathsf{T}\dot{\mathbf{M}}\dot{\mathbf{q}}$ closes within 3.6×10^{-7} W throughout the reference trace using a centered directional derivative of $\mathbf{M}$. This is the missing mass-matrix-rate term that prevents the 8.52 J coordinate integral from being treated as external work.

12.4 Shaft Interface Force, Moment, and Power

The internal shaft interface transmits a planar force $\mathbf{F}_s$ and a moment $M_s = \tau_s + \tau_{s,d}$. The power delivered across the interface is the sum of force power and moment power, evaluated with consistent action, velocity, and sign conventions. The internal force performs equal and opposite power at the common joint point. The opposed couples act at different angular velocities, so their two-body sum is $M_s(\omega_d - \omega_p) = M_s\dot{\phi}_2$: it changes shaft storage and dissipates energy rather than cancelling. The recorded port arrays retain both sides of this identity.

At the reference delivery crossing, the model predicts 56.34 N of interface force, -3.58° of shaft flex, +5.00 N · m of elastic moment, and -0.083 N · m of viscous moment. The positive elastic moment is especially important when this chapter is compared with Section 9: it cannot explain the archived -19.63 N · m pointwise two-hand midpoint couple. The two quantities belong to different models, reference points, and physical mechanisms.

At the nearest stored 0.5 ms delivery sample, the distal-side interface force power is 32.09 W and couple power is 74.60 W. The two-sided joint power is only 0.682 W because most of those distal-side terms are balanced by opposite work on the proximal link; the remainder is the instantaneous elastic/damping relative-coordinate power. A one-sided 106.69 W interface delivery must therefore not be reported as net creation of whole-system energy.

12.5 Closed Work–Energy Accounting

The stored shaft energy is

$$U_s = \tfrac{1}{2}k_s\phi_2^2, \tag{12.5}$$

and the complete mechanical energy is

$$E = T + V_g + U_s. \tag{12.6}$$

Because gravity and the shaft spring are included in E, the external and dissipative balance is

$$\frac{dE}{dt} = \tau_{\text{ctrl}}^\mathsf{T}\dot{\mathbf{q}} + \tau_{\text{joint damp}}^\mathsf{T}\dot{\mathbf{q}} - c_s\dot{\phi}_2^2. \tag{12.7}$$

The shaft spring is absent from the right side because it stores and returns energy. Its signed generalized-power integral equals the negative change in strain energy, apart from numerical integration error; it is not a loss term.

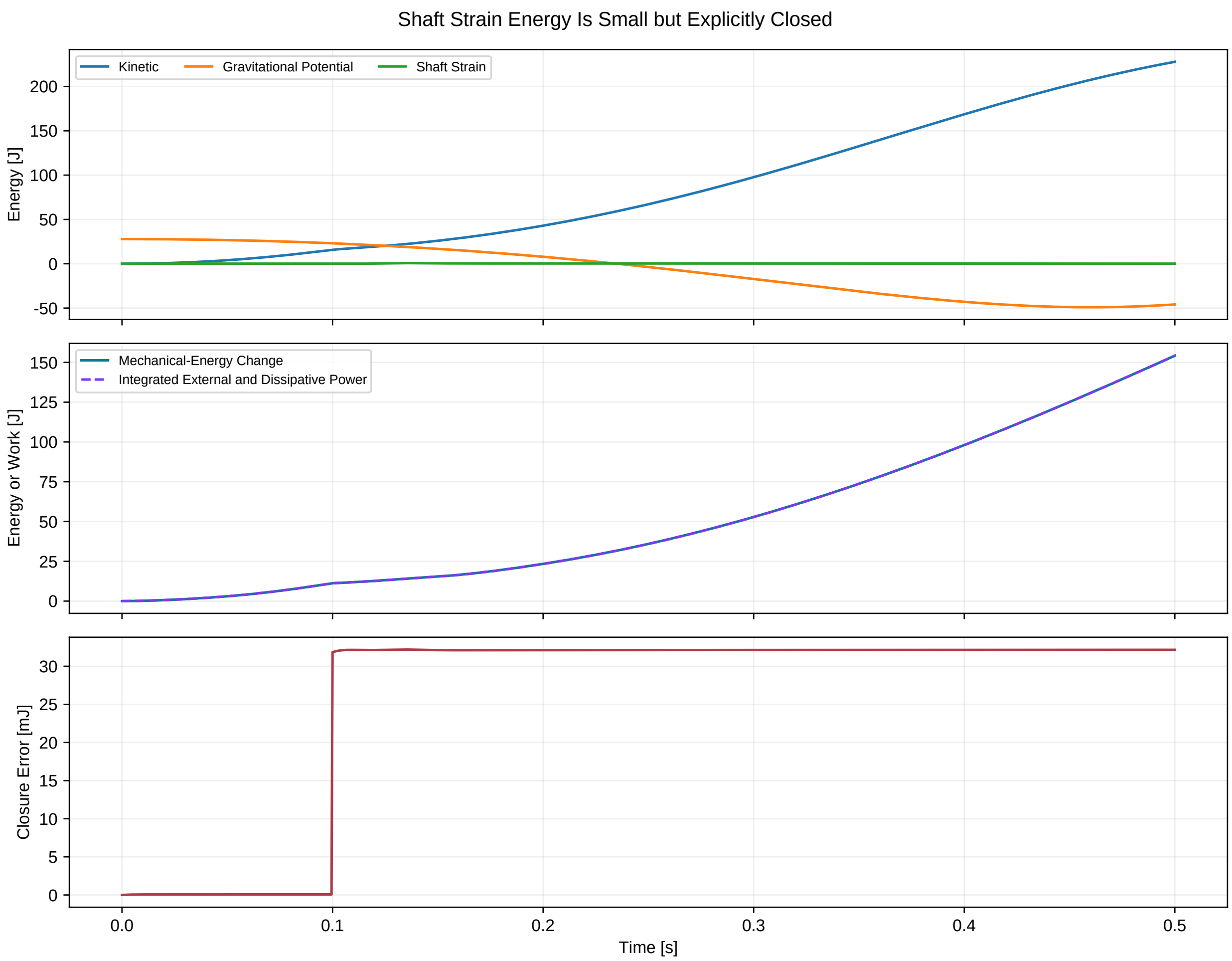

Figure 12.3: Shaft Strain Energy Is Small but Explicitly Closed

The reference run receives 164.38 J of control work. Joint damping removes 9.21 J and shaft damping removes 0.97 J. Peak shaft strain energy is 0.720 J, compared with 227.88 J peak kinetic energy. The maximum accumulated closure error is 0.0322 J, approximately 0.02% of control work. Away from the piecewise-command switch, the root-mean-square differential residual is 0.0092 W. This closure is a numerical consistency result, not validation of the assumed physical parameters.

12.6 Reference Delivery: Flexibility Changes Timing Modestly

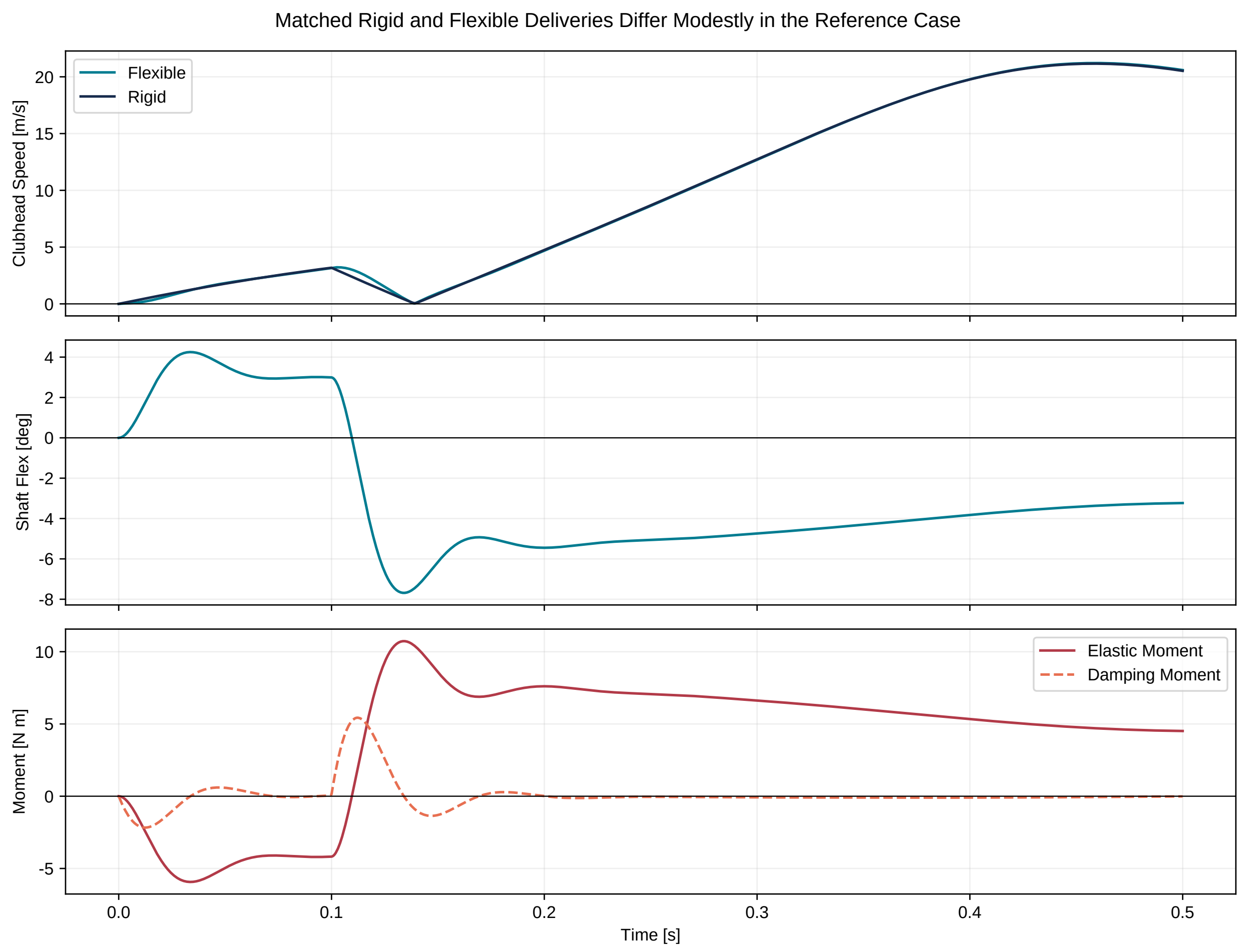

Figure 12.4: Matched Rigid and Flexible Deliveries Differ Modestly in the Reference Case

Clubhead velocity is evaluated analytically from the generalized state rather than by differentiating stored positions. The flexible reference reaches the declared delivery crossing at 0.42725 s with 20.799 m/s clubhead speed. The matched rigid reduction reaches it 2.73 ms earlier at 20.691 m/s. The flexible-minus-rigid difference is therefore +0.108 m/s, or approximately 0.52% of the rigid value. Peak speeds are 21.213 and 21.160 m/s, respectively. A second-order difference of stored tip positions differs from the analytic velocity by at most 0.00134 m/s in the flexible trace and 0.00915 m/s in the rigid trace; it is retained as a numerical audit, not the published velocity authority.

This result supports a restrained conclusion. The admitted elastic coordinate changes local forces, angular accelerations, pose, and delivery timing, but the reference speed effect is small. It does not support a general assertion that shaft recoil is either negligible or a primary source of clubhead speed. Different stiffness, damping, actuation, geometry, and endpoint definitions can change the result.

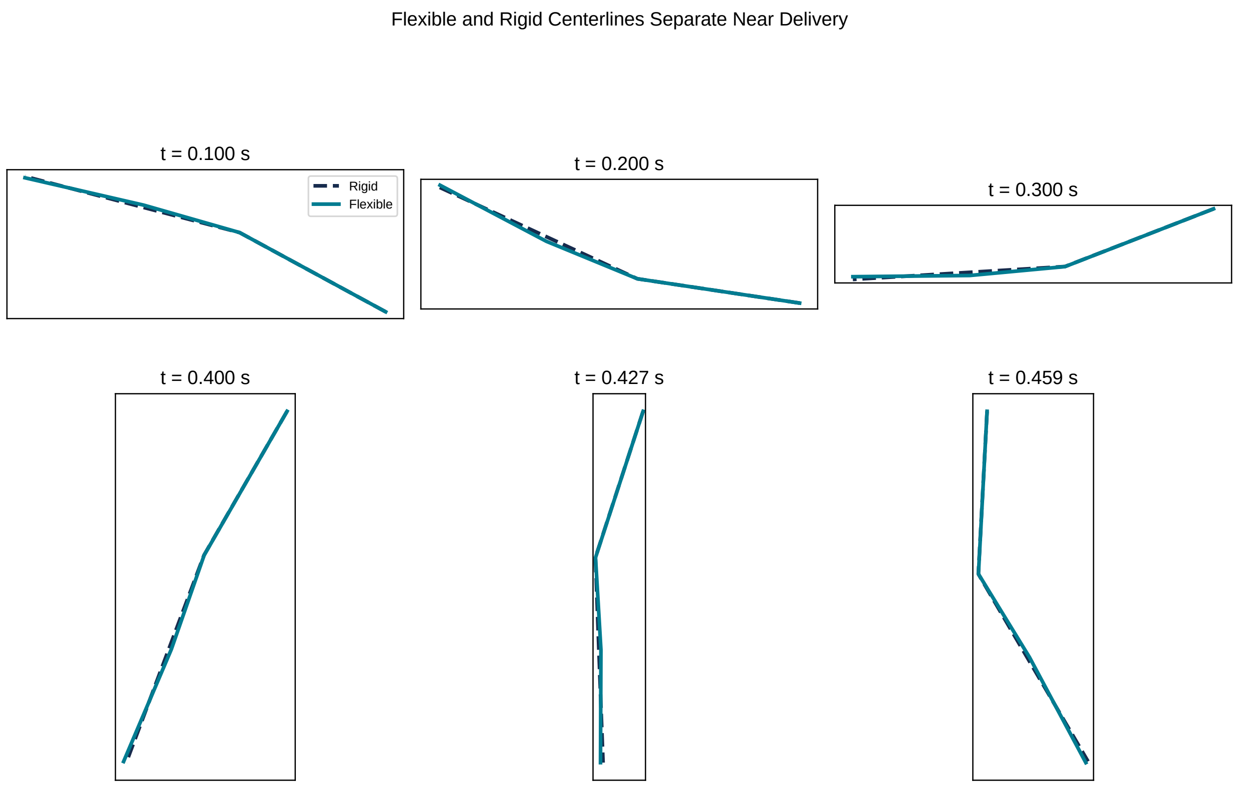

Figure 12.5: Flexible and Rigid Centerlines Separate Near Delivery

The centerline overlays in Figure 12.5 show why endpoint timing matters. Small angular differences accumulate into a visible distal-position change as the chain extends. Comparing speeds at a common clock time, a common configuration crossing, or the maximum within a time window answers different questions.

12.7 Physics Ablations

Removing projected gravity lowers reference delivery speed from 20.799 to 16.035 m/s and delays the crossing to 0.458 s. Removing the declared joint damping raises it to 22.969 m/s and delays the crossing to 0.435 s. Removing shaft damping produces 20.508 m/s at 0.428 s, increases impact flex to -5.66°, and raises peak stored strain energy from 0.720 to 2.805 J.

These are controlled ablations, not estimates of causal shares in a human swing. Turning off one term changes the subsequent state and hence every other state-dependent term. The comparison nevertheless establishes an important scale result for this model: gravity and joint damping alter the delivered speed more than the matched reference flex-versus-rigid change.

12.8 Robustness Across Stiffness, Damping, and Torque-Cut Time

The sensitivity study evaluates 120 combinations of six stiffnesses (10–320 $\mathrm{N \cdot m/rad}$), four damping values (0–1.2 $\mathrm{N \cdot m \cdot s/rad}$), and five command histories (no cut or cuts at 0.12, 0.18, 0.24, and 0.30 s). An extended 0.75 s horizon is used so that every declared case reaches its first delivery crossing.

The two heatmaps are a declared two-dimensional slice at the reference shaft damping of 0.6 $\mathrm{N \cdot m \cdot s/rad}$; they do not marginalize over the other three damping levels. The quantitative attribution below uses all 120 combinations in the full factorial grid.

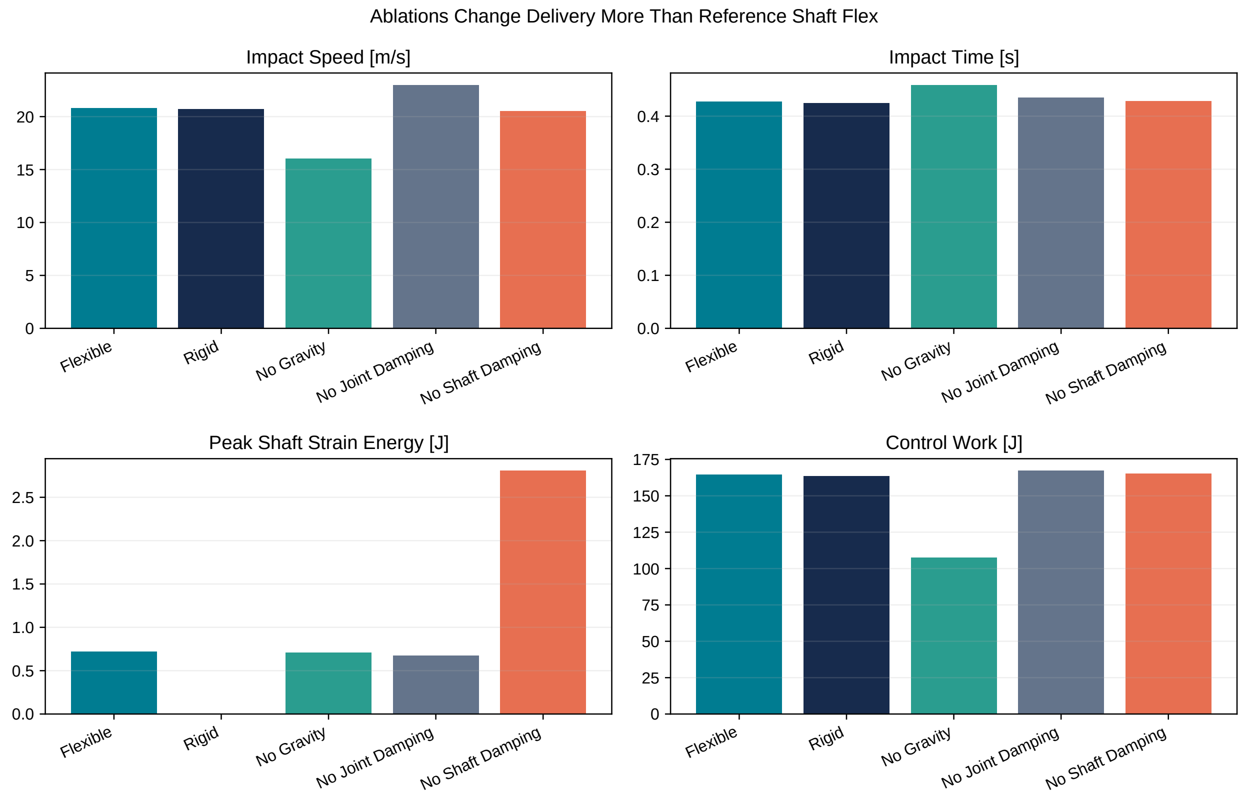

Figure 12.6: Ablations Change Delivery More Than Reference Shaft Flex

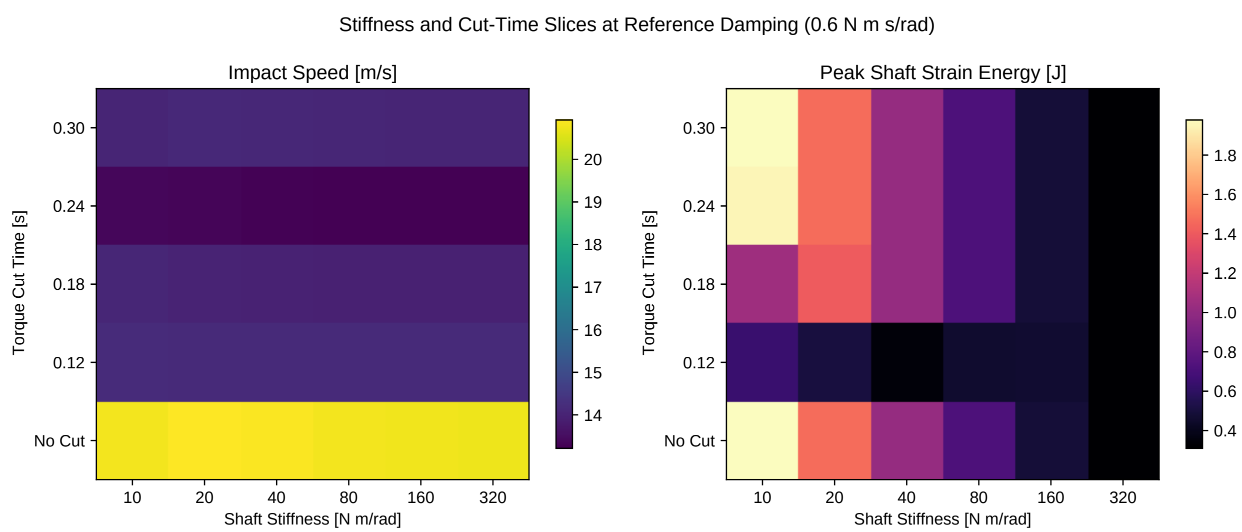

Figure 12.7: Stiffness and Torque-Cut-Time Slices at Reference Damping

Across the full grid, delivery speed spans 12.99–22.65 m/s and crossing time spans 0.425–0.719 s. Peak strain energy spans 0.161–18.05 J. In a descriptive main-effect sum-of-squares decomposition of this balanced deterministic grid, torque-cut time accounts for 99.14% of delivery-speed variation, while stiffness and damping account for 0.140% and 0.083%, respectively. For peak strain energy, the corresponding main-effect fractions are 23.78% for stiffness, 27.06% for damping, and 2.62% for cut time; 46.54% remains in interactions and other nonadditive structure. These are grid descriptors, not sampling uncertainty or human causal shares. They demonstrate why equipment-only comparisons are incomplete when actuation history is not matched.

The full grid also includes impact flex from -42.9° to +11.1°. Those extreme values violate the small-deflection premise implicit in a one-mode linear torsional surrogate. They are retained as transparent stress-test results, not interpreted as physically realizable shaft shapes. A distributed-beam model with calibrated material and boundary properties is required before making equipment-design claims.

12.9 Impact Window and Numerical Resolution

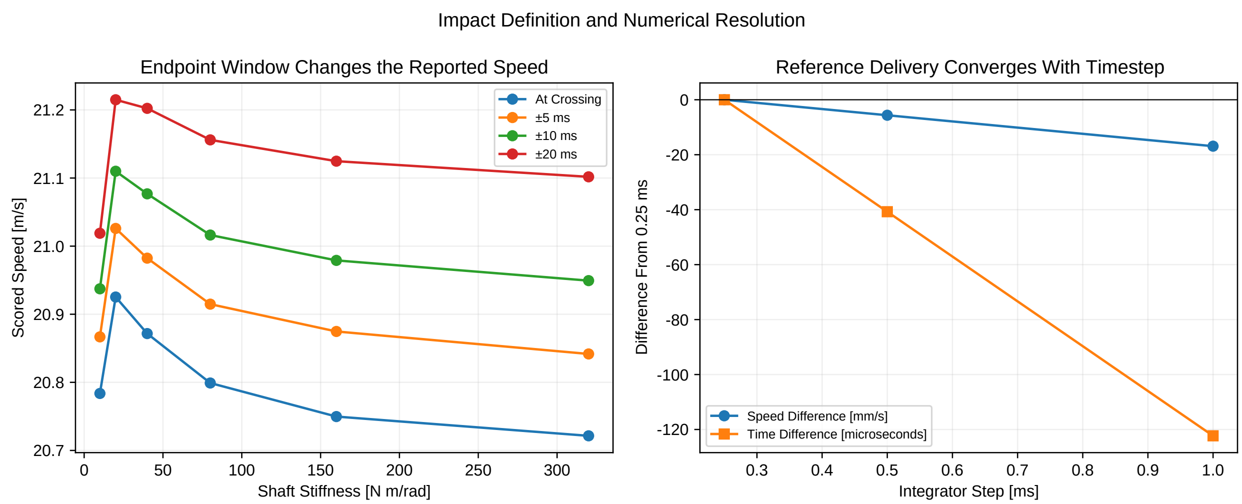

Figure 12.8: Impact Definition and Numerical Resolution

The left panel of Figure 12.8 reports speed at the first configuration crossing and maxima within ±5, ±10, and ±20 ms. For the reference case, the values are 20.799, 20.915, 21.016, and 21.156 m/s. The window is therefore part of the estimand, not a plotting preference.

Halving the reference 0.5 ms step to 0.25 ms changes crossing speed by 5.6 mm/s and crossing time by 41 microseconds. Doubling it to 1 ms changes speed by 11.3 mm/s and time by 82 microseconds. The maximum energy-closure error scales from 0.0161 J at 0.25 ms to 0.0647 J at 1 ms, consistent with a converging fixed-step calculation around a piecewise command.

12.10 Implications for Late-Downswing Strategy

Three strategy-relevant hypotheses are motivated by the declared comparisons.

First, transfer is geometric and state dependent. Momentum coupling can create large distal acceleration without being an external energy source. Its useful effect depends on link orientation, angular velocities, and the direction of the constraint force relative to distal velocity.

Second, elastic storage is a timing mechanism. A spring can temporarily retain energy, alter configuration, and return energy later, but the net benefit is not the peak strain-energy value. The relevant comparison is a matched endpoint under matched actuation, with damping and timing included.

Third, "negative torque" requires an identified object and reference point. In the WSCG two-hand audit, the late negative midpoint couple is a force-generated grip wrench. In this flexible surrogate, the reference shaft elastic moment at delivery is positive. Conflating these signs would erase the distinction between handle-contact geometry and shaft recoil.

Accordingly, the model defines a testable optimization hypothesis rather than a prescription: among trajectories satisfying the same endpoint, loading, and actuation constraints, those with late positive distal-side interface work and less dissipative work may deliver greater clubhead speed. Whether a golfer should actively restrain, release, or oppose a joint at a particular instant cannot be inferred from segment-speed order, one-sided interface power, or torque sign alone. It requires two-sided joint power, interface wrench, state history, a declared outcome window, and governed human evidence.

12.11 Falsification and Next Model Requirements

The present explanation would be weakened if a higher-fidelity model with matched mass distribution and actuation showed any of the following:

- the contribution sum fails after independent equation implementation;
- work–energy closure requires an unmodeled energy source;
- the flex-versus-rigid result reverses under small, physically calibrated parameter changes rather than only under broad stress tests;
- measured handle forces and shaft deformation cannot reproduce the predicted sign and timing of interface power; or
- a distributed shaft and two-hand closed-loop model attributes the archived negative couple primarily to an applied free torque rather than separated contact forces.

The next step is therefore not to add realism indiscriminately. It is to add degrees of freedom in an auditable sequence: moving hub, closed two-arm loop, distributed shaft, three-dimensional rotation, and finally data-constrained parameters. At each step, the rigid/flexible reduction, force/moment balance, work–energy closure, and endpoint definition should remain explicit.

Chapter 13

Coupled Base Motion and Club Compliance

13.1 Why the Mechanisms Must Be Coupled

The preceding forward two-hand experiment establishes that separated contact forces can create a late negative club couple after all commanded joint torques are set to zero. The shaft study separately establishes that elastic storage, viscous loss, and interaction forces can be closed in a forward model. Those results do not by themselves establish that the negative-couple mechanism survives when the shoulder base moves and the club flexes. Prescribing a mobile hub after solving a fixed-base trajectory cannot answer that question because base acceleration then changes reactions without being changed by them. Likewise, attaching a flexible point-mass chain to a single arm does not test whether two-hand differential forces survive the added compliance.

This chapter therefore evaluates one coupled system in which base translation, arm motion, grip reactions, proximal-club rotation, and shaft deflection are all simultaneous forward-dynamics outputs. The implementation, complete traces, and portable evidence record are available in `moving_base_flexible_club.py`, `run_moving_base_flexible_study.py`, and `moving_base_flexible_study.json`.

The question is deliberately narrow: does the registered planar mechanism remain mechanically possible after these two omitted degrees of freedom are admitted? The experiment does not calibrate a golfer, identify muscle forces, or predict the effect of a named shaft.

13.2 Coordinates and Geometry

The generalized coordinate vector is

$$\mathbf{q} = (\theta_R, \phi_R, \theta_L, \phi_L, x_b, y_b, x_g, y_g, \alpha, \beta)^{\mathsf{T}}, \tag{13.1}$$

where (x_b, y_b) translates a finite-mass shoulder base, (x_g, y_g) is the proximal club's grip-center position, α is its absolute angle, and β is the distal-club angle relative to α. Each arm uses an absolute upper-arm angle θ and a relative elbow angle ϕ. The distal angle is therefore $\alpha + \beta$.

For the planar direction and tangent operators

$$\mathbf{e}(\gamma) = \begin{bmatrix} \sin\gamma \\ -\cos\gamma \end{bmatrix}, \qquad \mathbf{t}(\gamma) = \frac{\partial \mathbf{e}}{\partial \gamma} = \begin{bmatrix} \cos\gamma \\ \sin\gamma \end{bmatrix}, \tag{13.2}$$

the right-hand position, for example, is

$$\mathbf{r}_{h,R} = \mathbf{r}_b + \mathbf{s}_R + L_u \mathbf{e}(\theta_R) + L_f \mathbf{e}(\theta_R + \phi_R), \tag{13.3}$$

and the corresponding grip point is

$$\mathbf{r}_{g,R} = \mathbf{r}_g + d_R \mathbf{e}(\alpha). \tag{13.4}$$

The four holonomic constraints are

$$\Phi(\mathbf{q}) = \begin{bmatrix} \mathbf{r}_{h,R} - \mathbf{r}_{g,R} \\ \mathbf{r}_{h,L} - \mathbf{r}_{g,L} \end{bmatrix} = \mathbf{0}, \qquad \mathbf{J} = \frac{\partial \Phi}{\partial \mathbf{q}}. \tag{13.5}$$

This construction leaves six feasible degrees of freedom at regular configurations. The two contact-force vectors are solved Lagrange multipliers; they are not allocated after the motion is known.

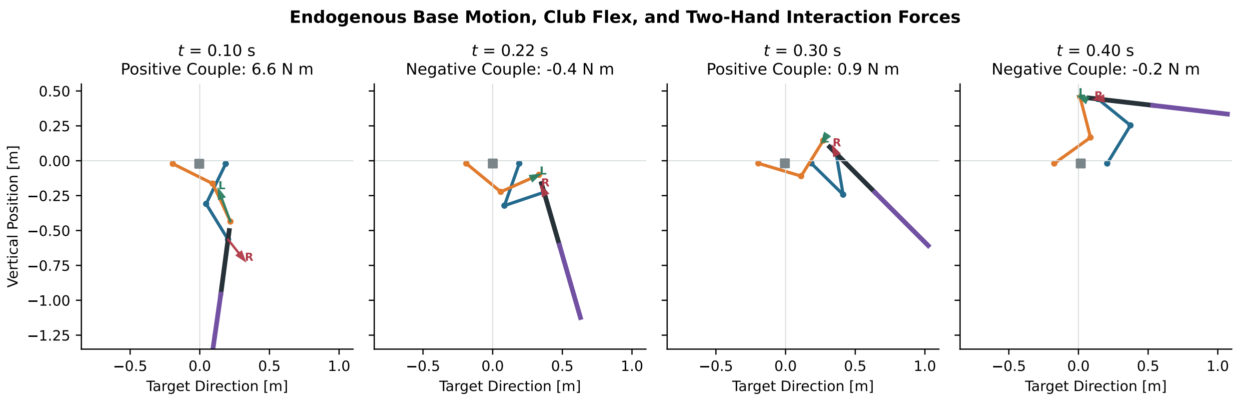

Figure 13.1: Endogenous Base Motion, Club Flex, and Two-Hand Interaction Forces

Figure 13.1 shows four states from the same forward trajectory. The square is the translating base, the black and purple segments are the proximal and distal club, and the arrows are the independently solved forces on the club. The force-generated couple becomes negative when the weighted tangential projections of the two arrows reverse; neither force norm nor shaft curvature alone determines that sign.

13.3 Inertia, Convective Terms, and the KKT Solve

The mass matrix is assembled from each center-of-mass Jacobian $\mathbf{J}_i$ and angular-velocity map $\mathbf{H}_i$:

$$\mathbf{M}(\mathbf{q}) = \sum_i m_i \mathbf{J}_i^{\mathsf{T}} \mathbf{J}_i + \sum_i I_i \mathbf{H}_i^{\mathsf{T}} \mathbf{H}_i. \tag{13.6}$$

This includes translation–rotation coupling between the base and both arms, and between the grip center and both club segments. The convective vector is formed from the exact centripetal accelerations of each center of mass. For a segment contribution $L\mathbf{e}(\gamma)$, that acceleration is $-L\dot{\gamma}^2\mathbf{e}(\gamma)$. This direct Jacobian construction avoids a finite-difference mass-matrix derivative in the primary dynamics.

The acceleration-constraint bias $\dot{\mathbf{J}}\dot{\mathbf{q}}$ is likewise evaluated from the exact centripetal terms of the two arms and grip offsets, not by differentiating $\mathbf{J}$ in the solver. An independent centered directional derivative of $\mathbf{J}$ agrees within 6.28×10^{-8} m/s² over the reference trace under a registered 10^{-7} m/s² audit tolerance.

The base is connected to the world by an isotropic linear spring and damper; the shaft mode has its own torsional spring and damper:

$$\mathbf{Q}_b = -k_b \mathbf{r}_b - c_b \dot{\mathbf{r}}_b, \qquad Q_\beta = -k_s \beta - c_s \dot{\beta}. \tag{13.7}$$

These values define a transparent mechanism experiment. The reference values are $m_b = 35$ kg, $k_b = 24{,}000$ N/m, $c_b = 500$ N · s/m, $k_s = 80$ N · m/rad, and $c_s = 0.6$ N · m · s/rad. They are not fitted torso or shaft properties.

At every step, the acceleration and contact multipliers solve

$$\begin{bmatrix} \mathbf{M} & -\mathbf{J}^{\mathsf{T}} \\ \mathbf{J} & \mathbf{0} \end{bmatrix} \begin{bmatrix} \ddot{\mathbf{q}} \\ \lambda \end{bmatrix} = \begin{bmatrix} \mathbf{Q}_{\text{control}} + \mathbf{Q}_{\text{damp}} - \mathbf{h} - \nabla V \\ -\dot{\mathbf{J}}\dot{\mathbf{q}} \end{bmatrix}. \tag{13.8}$$

The solver fails closed if the mass matrix is not positive definite, the four-row constraint Jacobian loses rank, or either KKT residual exceeds its declared tolerance. Velocity-Verlet integration is followed by mass-metric configuration and velocity projection. Projection corrections and their energy changes remain explicit numerical diagnostics rather than hidden stabilization work.

13.4 Separating Grip and Shaft Moments

The force-generated couple about the grip center is

$$M_F = (\mathbf{r}_{g,R} - \mathbf{r}_g) \times \mathbf{F}_R + (\mathbf{r}_{g,L} - \mathbf{r}_g) \times \mathbf{F}_L. \tag{13.9}$$

Direct wrist torque is reported separately as $M_W = \tau_{w,R} + \tau_{w,L}$. The internal shaft moment is also separate:

$$M_s = -k_s \beta - c_s \dot{\beta}. \tag{13.10}$$

M_s is internal to the whole club, whereas $M_F + M_W$ is the external grip couple on it. Combining them into a single curve would obscure both the system boundary and the mechanism.

The two-point contact power closes against the wrench transported to the grip center:

$$\mathbf{F}_R \cdot \mathbf{v}_R + \mathbf{F}_L \cdot \mathbf{v}_L = (\mathbf{F}_R + \mathbf{F}_L) \cdot \mathbf{v}_g + M_F \dot{\alpha}. \tag{13.11}$$

The maximum discrepancy is 1.28×10^{-13} W in the reference trace. This identity is important because a negative couple need not imply negative net contact power: resultant force power can offset or exceed couple power.

13.5 Whole-System Energy Balance

The mechanical energy contains kinetic energy of the base, four arm segments, and two club segments; gravitational potential; base-spring energy; and shaft strain energy:

$$E = T + V_g + \tfrac{1}{2} k_b \|\mathbf{r}_b\|^2 + \tfrac{1}{2} k_s \beta^2. \tag{13.12}$$

Ideal constraints perform zero net work on the complete system: the executable audit evaluates $\lambda^{\mathsf{T}} \mathbf{J} \dot{\mathbf{q}}$ at every stored state, and its maximum absolute residual is 2.65×10^{-13} W. This is the complete two-sided action–reaction power, not the one-sided power delivered to the club. The remaining balance is

$$\frac{dE}{dt} = \mathbf{Q}_{\text{control}}^{\mathsf{T}}\dot{\mathbf{q}} - c_b\|\dot{\mathbf{r}}_b\|^2 - c_s\dot{\beta}^2 - c_j\sum_{k=1}^{4}\dot{q}_k^2. \tag{13.13}$$

Over 0.4 s, the reference run gains 91.521 J of mechanical energy from 111.133 J of applied work and -19.624 J of declared dissipation. The absolute work–energy residual is 0.0130 J. It falls monotonically from 0.0483 J at a 2 ms step to 0.0254 J at 1 ms and 0.0130 J at 0.5 ms. The maximum position projection falls from 69.2 μm to 8.87 μm and then 1.12 μm over the same refinement. Constraint rank remains four; the maximum position, velocity, KKT, and acceleration-constraint residuals are respectively 7.47×10^{-11} m, 2.42×10^{-15} m/s, 2.05×10^{-13}, and 1.77×10^{-13}.

The reference projections change mechanical energy by -0.0758 J in signed sum (0.0758 J in absolute sum), with no individual correction larger than 0.000439 J. That cumulative correction is larger than the raw 0.0130 J work–energy residual, so both quantities are retained; the residual alone must not be read as the complete integration-error budget.

13.6 Coupled Reference Response

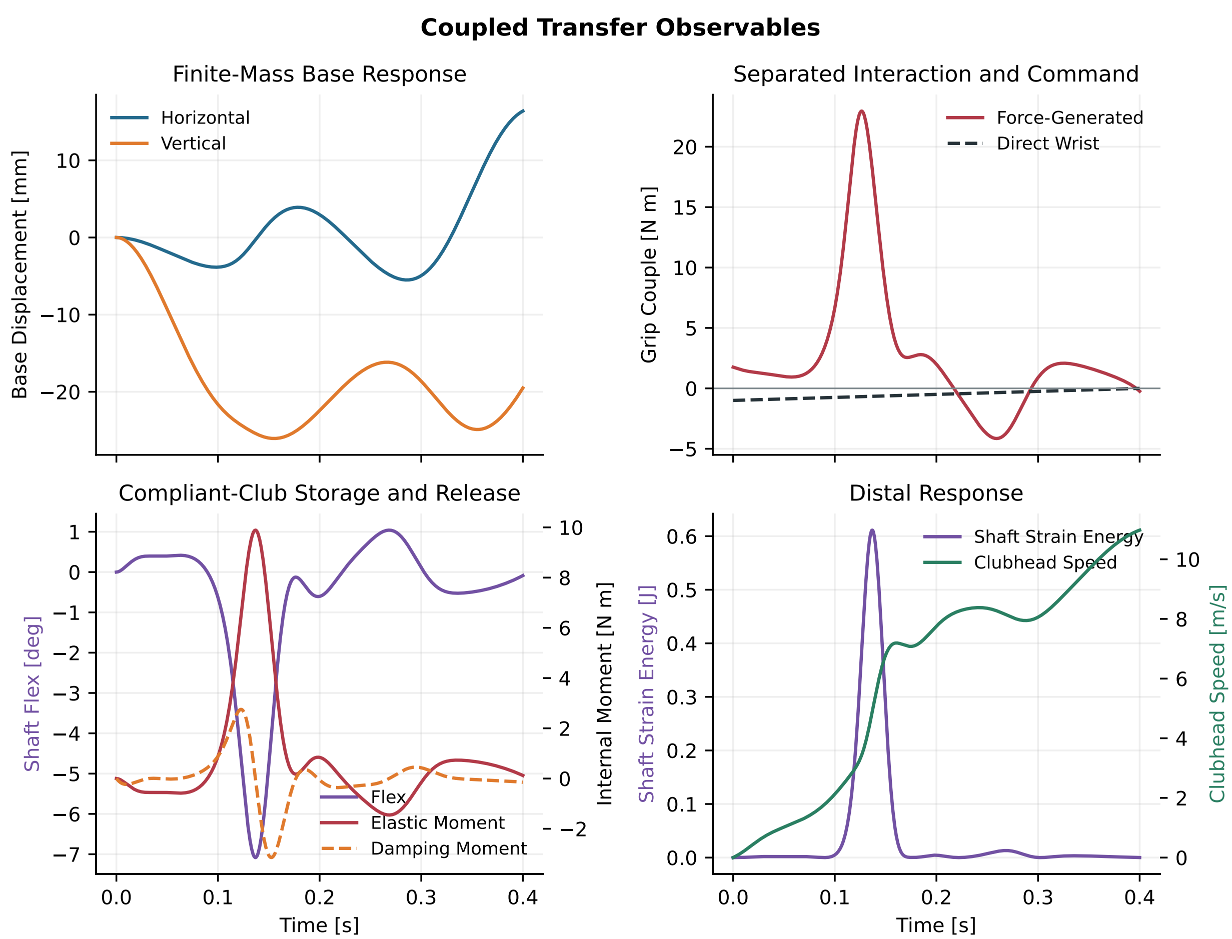

Figure 13.2: Coupled Transfer Observables

The base moves by at most 26.9 mm and the shaft coordinate reaches 7.08° in absolute value, so neither added coordinate is dormant. Peak shaft strain energy is 0.611 J and peak clubhead speed is 10.98 m/s. These values are model outputs under the declared loads, not equipment or performance predictions.

The force-generated grip couple spans -4.15 to +22.95 N · m and first crosses negative at 0.2175 s. By contrast, the direct wrist torque spans -1 to 0 N · m. The negative force-couple interval therefore cannot be relabeled as the direct wrist command. The shaft elastic moment reaches 9.89 N · m in absolute value and the damping moment reaches 3.15 N · m, but both remain separately identified at their internal interface.

13.7 Same-State Intervention and Geometric Negative Control

At exactly 0.200 s, the commanded trajectory is branched without changing any of its ten coordinates or velocities. All six joint commands are then set to zero for 50 ms. The branch begins with a force-generated couple of -0.675 N · m, reaches -2.17 N · m, and remains negative for the full recorded interval. Its work–energy residual is 0.00266 J; the energy loss is accounted for by the declared damping terms.

The force couple changes discontinuously at the intervention even though the coordinates and velocities do not. This is expected: contact multipliers are algebraic dynamics outputs, so removing generalized force at the same state changes the reactions required to satisfy the acceleration constraints.

This intervention does not establish that muscles are passive. It establishes that, after the coupled state has been created, continued applied torque is not mathematically necessary for the modeled negative grip couple over that interval. The contact reactions still depend on inertia, gravity, base restoring forces, shaft elasticity, and damping.

The geometric negative control sets both grip offsets to zero while retaining two independent hand constraints. Equation 13.9 then predicts $M_F = 0$ for any finite contact forces. The executed trace returns zero to machine precision. This rules out a solver sign convention or contact-force magnitude alone as the source of the reported couple.

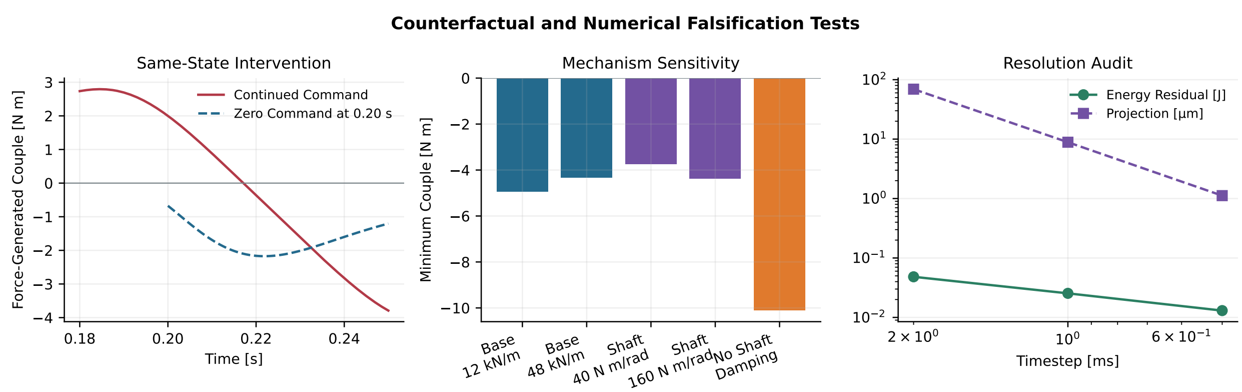

Figure 13.3: Counterfactual and Numerical Falsification Tests

13.8 Mechanism Sensitivity

The registered sensitivity cases vary one parameter while retaining the same initial configuration and open-loop command. Halving base stiffness to 12 kN/m increases maximum base displacement to 49.6 mm and moves the first negative crossing to 0.211 s; doubling it to 48 kN/m reduces displacement to 15.9 mm and yields a 0.217 s crossing. Both retain a negative minimum couple.

Changing shaft stiffness from 40 to 160 N · m/rad changes peak flex from 11.26° to 3.98° and peak strain energy from 0.773 to 0.386 J. The negative-couple minimum changes from -3.73 to -4.38 N · m. Removing shaft damping increases flex to 9.38°, stored energy to 1.072 J, and peak clubhead speed to 13.05 m/s; it advances the first negative crossing to 0.160 s and deepens the minimum couple to -10.09 N · m. All sensitivity cases now use the same 0.5 ms step as the reference, so parameter effects are not mixed with a coarser integrator.

These cases demonstrate local transport of the mechanism, not global robustness. The parameter range is too small to represent population or equipment uncertainty, and the open-loop command is not reoptimized after a parameter change. The appropriate next step is a registered ensemble with identifiability and uncertainty bounds, developed after the spatial model so that planar parameter compensation is not mistaken for physical certainty.

13.9 What This Tier Supports and What It Does Not

Three findings now survive the move from a rigid fixed-base model to this coupled tier:

1. separated hand-force moment arms can generate a late negative club couple;
2. the couple can persist for a finite interval after a same-state command removal; and
3. force/couple power, whole-system energy, constraints, and numerical projection can be closed simultaneously while base motion and shaft flex evolve endogenously.

The result would be contradicted at this tier if the sign reversal disappeared, the zero-command branch became immediately nonnegative, coincident grip points retained a force couple, base or flex motion had to be prescribed, wrench power failed its identity, or the finding changed under timestep refinement. None of those registered failure conditions occurs in the executed study.

The model still omits base rotation, legs and ground reactions, anatomical joints, out-of-plane motion, distributed beam modes, contact compliance, activation dynamics, and measured parameter distributions. It also cannot identify biological effort from constraint forces. Consequently, this chapter supports a planar mechanism-feasibility statement only. The next fidelity gate is a spatial full-body experiment that preserves the same wrench, intervention, energy, and discrepancy observables in two independent dynamics engines.

Chapter 14

Arm–Wrist Torque Allocation and Transmission Preload

14.1 The Hypothesis Requires Two Separate Tests

A club can receive a moment from direct wrist moments, from the moment of two separated hand forces about the club reference point, or from both. Those mechanisms are mechanically distinguishable even when their net club moment is identical. They are not, however, uniquely recoverable from club kinematics alone. The central comparison in this section therefore holds the club-level task fixed and varies only the modeled actuator allocation.

The word *slack* presents a different problem. It can refer to a contact gap, series-elastic extension, low tangent stiffness, delayed force development, or simply low activation. Those conditions are not interchangeable. The second experiment therefore declares one operational definition: a rotational dead zone followed by a linear series stiffness and first-order torque development. It asks what that element predicts during a change in actuator roles. It does not claim that the wrist, grip, or shoulder girdle is literally a backlash joint.

This separation is essential. If two complete swings are assigned different kinematics, a difference in club speed cannot identify whether allocation, preload, geometry, or the changed trajectory caused the result. Here the allocation comparison is same-state and task-matched; the transmission comparison uses the same post-transition net torque target. The implementation and evidence are available in `torque_allocation_preload.py`, `torque_allocation_preload_study.json`, and the corresponding `NPZ trace archive`.

14.2 Physiological Evidence and Its Limits

Scapular electromyography in 15 competitive male golfers reported trail-side levator scapulae, rhomboid, and trapezius activity during takeaway; lead-side trapezius and rhomboid activity during the forward swing; and high trail-side serratus anterior activity during the forward swing (Jobe, Perry, and Pink 1995). This is compatible with phase-dependent shoulder-girdle coordination. It does not establish the direction of either hand force, a bilateral grip couple, or a unique mapping from scapular activation to club moment.

The wrist evidence is likewise informative but non-identifying. In 15 subelite male golfers, extensor carpi ulnaris activity differed by side and swing phase, yet downswing activation was not significantly related to the reported clubhead kinematics (Robinson et al. 2023). A three-dimensional kinetic study found that wrist action and hand trajectory were important to the simulated swing, but its individual-subject results do not resolve a universal actuator allocation (Nesbit 2005a). A systematic review covering 92 golf-kinematics studies found substantial methodological heterogeneity and contradictory results (Bourgain et al. 2022). These sources motivate measurement; they do not prove either extreme strategy.

Direct bilateral measurement is necessary because closed-chain inverse dynamics does not uniquely allocate forces between two hands. Instrumented grip studies have demonstrated that this ambiguity can be reduced with strain gauges or a six-axis grip sensor (Koike 2016; Choi and Park 2020). The present model therefore reports hand-force requirements as predictions to test, not as measured biological loads.

14.3 Matched-Task Allocation

At a fixed configuration $\mathbf{q}$ and velocity $\dot{\mathbf{q}}$, the KKT system from Section 10 is affine in generalized control. Define the control-only club angular acceleration as

$$\ddot{\alpha}_C(\mathbf{u}) = \ddot{\alpha}(\mathbf{q}, \dot{\mathbf{q}}, \mathbf{u}) - \ddot{\alpha}(\mathbf{q}, \dot{\mathbf{q}}, \mathbf{0}). \tag{14.1}$$

Two actuator subspaces are evaluated. The *proximal* subspace contains the four shoulder and elbow generalized torques and sets both direct wrist moments to zero. The *wrist* subspace contains the two direct wrist moments and sets the four proximal torques to zero. Within each subspace, the minimum Euclidean-norm control is selected subject to the same target $I_C\ddot{\alpha}_C = 8$ N m. This is a reproducible mathematical allocation; the proximal subspace must not be relabeled as a measured scapular strategy.

Convex mixtures of the two task-normalized controls generate an allocation fraction from zero (proximal-only) to one (wrist-only). Because the KKT solve is linear in same-state control, every mixture retains the task. Across 19 club angles and 21 allocation fractions, the maximum task error is 5.33×10^{-15} N m. The direct wrist moment plus the moment generated by the two-hand force couple closes to the same net moment within 4.44×10^{-15} N m.

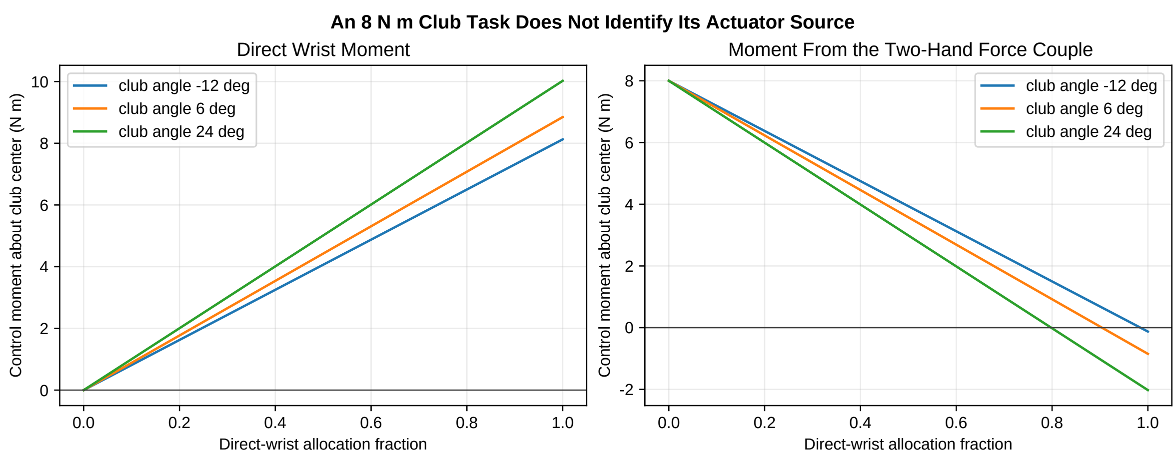

Figure 14.1: The Same Net Club-Moment Task Can Be Divided Between Direct Wrist Moment and a Two-Hand Force Couple

The task match does not make the internal demands equivalent. Across the declared geometry, RMS modeled hand force spans 7.58–91.51 N and the generalized-torque norm spans 5.74–25.45 N m. For these particular unweighted metrics, intermediate-to-wrist-dominant allocations minimize hand force, while wrist-dominant allocations minimize generalized-torque norm. The minimizing fraction changes with club geometry.

This result rejects two shortcuts. First, a measured net club moment does not identify whether the arms or wrists supplied it. Second, a single scalar `effort` cannot select the best allocation without declared weights for hand force, joint torque, work, stability, discomfort, accuracy, and robustness. The model supports an allocation surface, not universal technique advice.

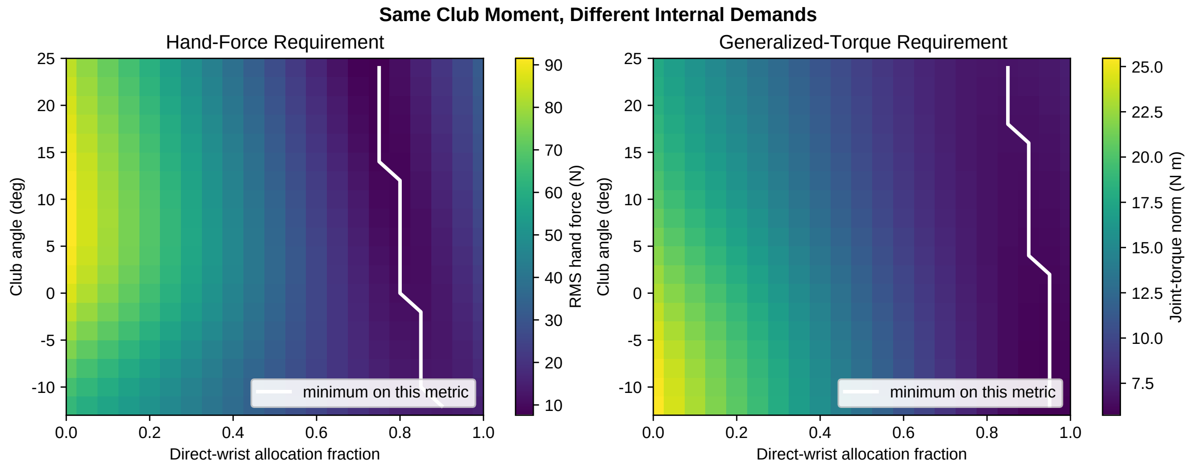

Figure 14.2: Modeled Demand Minima Vary With Geometry and Objective

14.4 A Falsifiable Definition of Slack

For each actuator channel i, desired torque is converted to an equilibrium deflection x_i^* through a dead zone δ_i and stiffness k_i:

$$x_i^* = \operatorname{sgn}(\tau_i^*)\left(\delta_i + \frac{|\tau_i^*|}{k_i}\right), \qquad \dot{x}_i = \frac{x_i^* - x_i}{T_i}, \tag{14.2}$$

$$\tau_i(x_i) = k_i \operatorname{sgn}(x_i)\max(|x_i| - \delta_i, 0). \tag{14.3}$$

The declared numerical experiment uses $k = 600$ N m rad^{-1}, $\delta = 0.012$ rad, and $T = 18$ ms for both abstract channels. These are synthetic sensitivity parameters, not identified tissue or grip properties. An interval with $|x_i| \leq \delta_i$ is the only condition called `zero transmission` here.

Two matched net-torque programs are compared. In the *persistent-direction* program, the arm channel remains positive and the wrist channel remains negative across the transition, with net torque changing from 6 to 10 N m. In the *role-reversal* program, the arm channel changes from -4 to +16 N m while the wrist channel changes from +10 to -6 N m, preserving the same pre- and post-transition net targets. Each is evaluated from its pre-transition loaded equilibrium and from a relaxed zero-deflection state.

A separate history test removes the loaded-equilibrium initialization. Both channels start from zero deflection, experience their preparation commands for 180 ms, and then cross the transition without resetting deflection or transmitted torque. Only the desired commands change at $t = 0$. This operational preparation interval is not a simulated anatomical backswing; it is a direct test that the declared internal state can be generated by finite prior loading and carried continuously into the post-transition interval.

From the loaded state, the persistent-direction program has no zero-transmission interval and a net torque-error impulse of 0.0717 N m s. The role-reversal program spends 11.5 ms and 22.0 ms in zero transmission for the arm and wrist channels, respectively, and its error impulse is 0.1954 N m s. These are zero-valued sample-occupancy estimates on a 0.1 ms grid; unresolved entry and exit locations bound them to 11.4–11.6 ms and 21.9–22.1 ms. A relaxed start produces an error impulse of 0.2011 N m s for either program. Thus preload improves continuity for a fixed desired program, while a sign reversal can discard that advantage under this particular dead-zone model.

The finite-history test reproduces those post-transition values without state reinitialization: the persistent-direction program again has zero gap in both channels and a 0.0717 N m s error impulse, while complete role reversal produces 11.5 ms and 22.0 ms gaps and a 0.1954 N m s impulse. Equality with the loaded

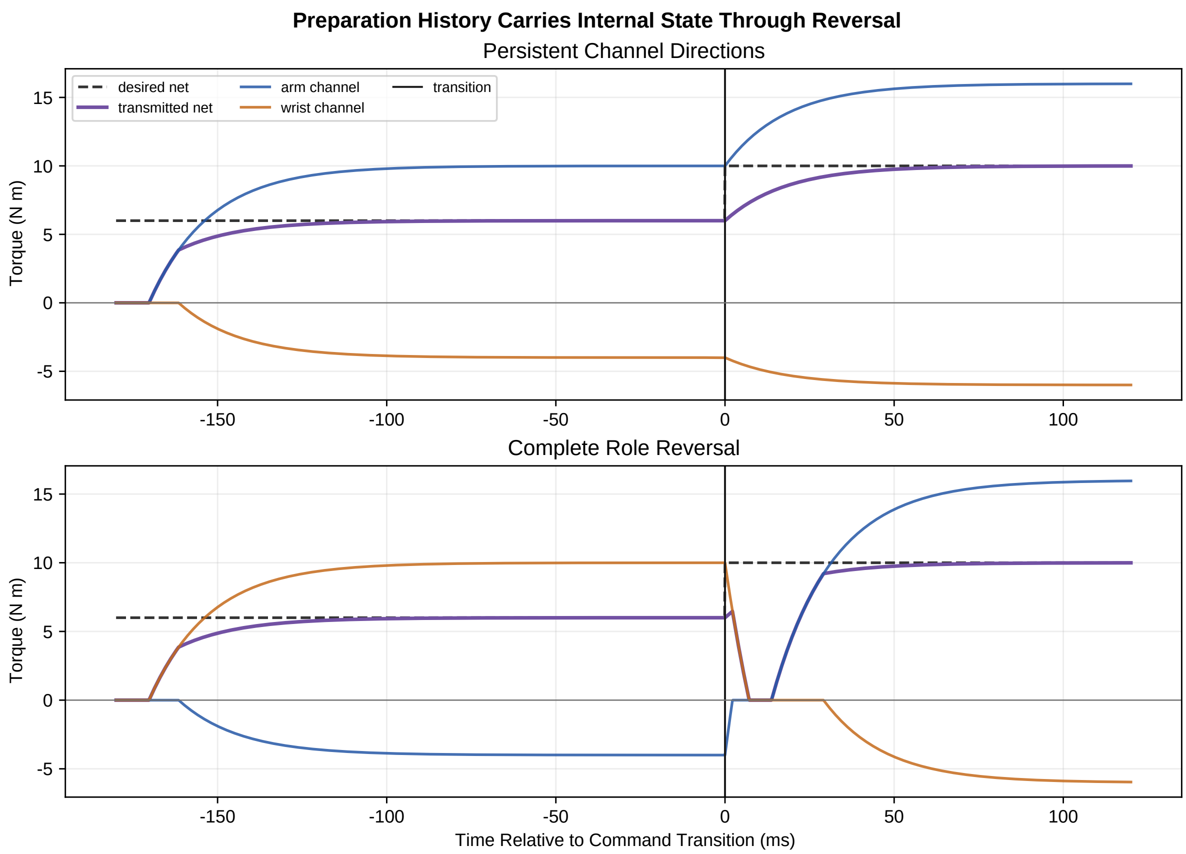

Figure 14.3: Continuous Preparation History and Command Transition

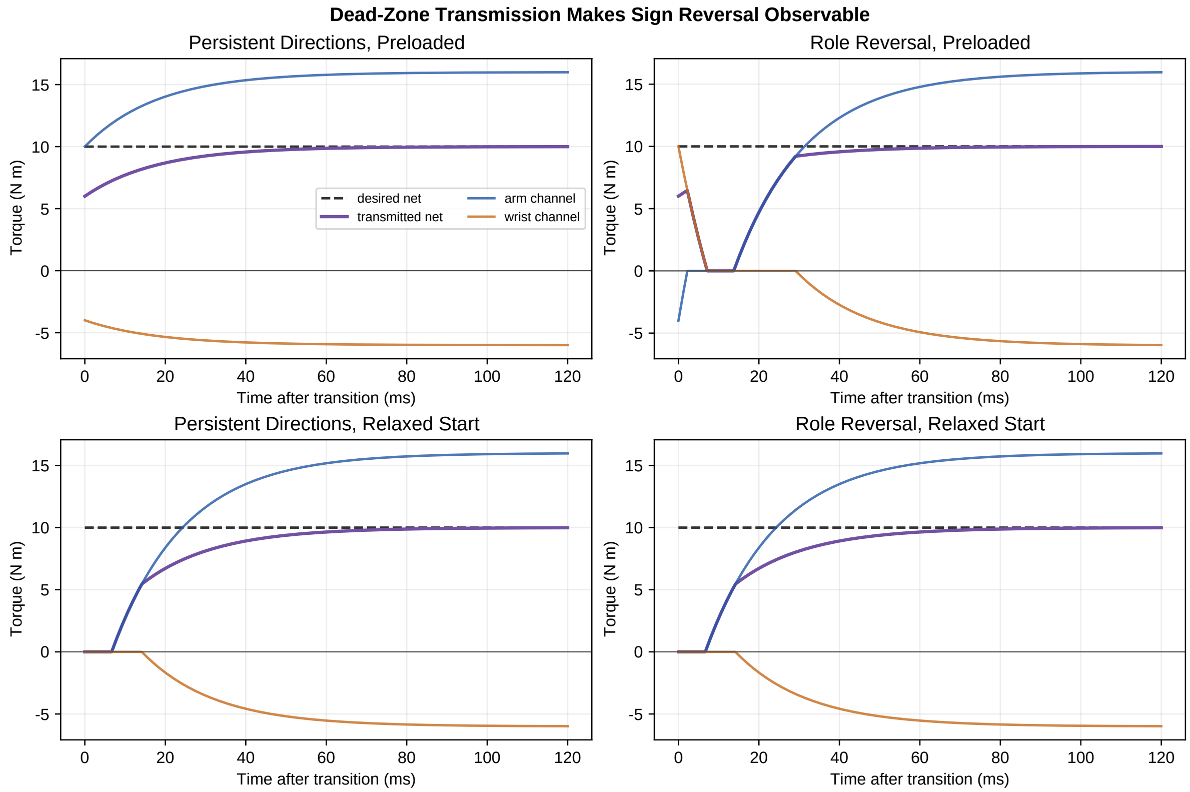

Figure 14.4: Transmission Continuity for Persistent-Direction and Role-Reversal Programs

initialization is expected after ten declared time constants of preparation; the new evidence establishes state continuity, not a new physiological result.

The interpretation is conditional. Biological series elasticity normally stores and returns energy rather than acting as backlash, and short-range muscle stiffness can increase with activation (Araz et al. 2023; De Groote, Allen, and Ting 2017). Series compliance can also delay force rise (Luo, Cooke, and Pate 1994; Mayfield, Cresswell, and Lichtwark 2016), while co-contraction can improve task-relevant stiffness at an energetic cost (Berret et al. 2024). Consequently, neither zero compliance nor maximum co-contraction is presumed optimal. Useful compliance can filter impact, store energy, and permit coordination; unwanted gaps or low tangent stiffness can impair rapid torque transmission. The distinction must be measured.

Across the registered four-dead-zone by three-time-constant grid, an explicit 10^{-10} N m s equivalence tolerance classifies all three zero-dead-zone cases as equivalent, all nine positive-dead-zone cases as favoring persistent direction, and none as favoring complete role reversal. This is a structural result of the chosen backlash-like law: when its defining dead zone is removed, the modeled advantage disappears. The grid does not establish that biological transmission contains such a dead zone or that the sampled parameters span a human population.

14.5 Critical Comparison of the Two Extremes

Question	Persistent Arm Drive With Wrist Resistance	Wrist-to-Arm Role Reversal
Club-level task	Can match the same net moment	Can match the same net moment

Question	Persistent Arm Drive With Wrist Resistance	Wrist-to-Arm Role Reversal
Transmission continuity in the declared dead-zone model	Favored when each channel remains loaded in the same direction	Penalized when both channels cross zero
Possible coordination benefit	Reuses a directionally persistent proximal command	Separates preparation and delivery roles
Principal modeled cost	May require larger hand forces or proximal generalized torques, depending on geometry	May require reversal delay and transient torque error
Physiological evidence	Scapular phase activity is compatible but non-identifying	Wrist phase activity is compatible but non-identifying
Main falsifier	Measured bilateral forces show no predicted couple or preload continuity	Measured reversal occurs without force/stiffness gap and yields equal or better robustness

The persistent-direction strategy therefore has a clear conditional advantage: if the relevant biological transmission behaves like the declared dead-zone element, retaining load direction can preserve immediate torque transmission. It is not established as universally superior. The wrist-led preparation may reduce proximal loading, exploit elastic storage, or improve accuracy in a participant-specific system; the current model does not price those outcomes.

14.6 Measurements That Can Refute the Interpretation

The experimental protocol in Section 20 should add the following preregistered observables:

1. bilateral six-axis grip wrenches and grip-pressure distribution, transformed to a declared club reference point;
2. wrist moments from a closed-chain inverse-dynamics solve constrained by the measured internal grip wrench;
3. ultrasound or validated musculotendon-length proxies where feasible, plus perturbation-based or system-identification estimates of tangent stiffness;
4. surface EMG for forearm, shoulder, and scapular muscles, interpreted as activation timing rather than joint torque;
5. transition-aligned force-development delay, zero-force duration, torque-error impulse, club angular acceleration, shaft strain, and launch outcomes; and
6. participant-held-out comparisons of the two extremes and intermediate allocations, with no universal optimum asserted from group means alone.

The interpretation is falsified if the same club task does not show the predicted allocation-dependent hand forces, if inferred channel reversal does not produce a measurable transmission delay under a documented gap or low stiffness, or if any claimed performance advantage disappears on participant holdout. Observing scapular or wrist EMG timing alone is insufficient.

Chapter 15

Distributed-Shaft Reference and Modal Reduction

15.1 Structural Question and Evidence Boundary

The coupled model in Section 13 admits one linear torsional flex coordinate. That coordinate is sufficient to test whether stored elastic energy can coexist with the two-hand negative-couple mechanism, but it cannot represent a distributed bending field or decide when higher shaft modes matter. This section therefore compares a one-mode reduction with a higher-order Euler–Bernoulli reference assembled by the repository's shared finite-element shaft implementation. The exact analysis and evidence are in `shaft_beam_reference.py`, `run_shaft_beam_reference.py`, and `shaft_beam_reference.json`.

This is a structural verification experiment, not an equipment calibration. The modal observations used for identification are generated from a declared synthetic truth. No measured shaft frequencies, EI profile, clubhead inertia, or human loading data enter the result.

15.2 Distributed Beam and Tip Inertia

Each tapered beam element carries transverse displacement and section rotation at both nodes. Its standard consistent mass and bending-stiffness matrices are assembled into M_b and K_b, the butt displacement and rotation are clamped, and declared clubhead translation and rotary inertia are added at the free-end degrees of freedom. The generalized eigenproblem is

$$\mathbf{K}_b \phi_i = \omega_i^2 \mathbf{M}_b \phi_i, \qquad \phi_i^\mathsf{T} \mathbf{M}_b \phi_j = \delta_{ij}. \tag{15.1}$$

The reference shaft is 1.0 m long with a 15.0 mm butt diameter, 8.5 mm tip diameter, 1.0 mm wall, 1,600 kg/m^3 density, 112 GPa elastic modulus, 0.205 kg tip mass, and 4.8×10^{-4} kg m^2 tip rotary inertia. These values define the synthetic test article only. Twenty-four elements form the executed reference; comparison against 48 elements changes the first three frequencies by at most 0.0896%. The converged first three frequencies are 5.240, 62.931, and 137.909 Hz.

15.3 Synthetic Identification and Uncertainty

Two parameters—the elastic modulus and clubhead mass—are identified from the first two synthetic modal frequencies. Optimization occurs in log-parameter space to enforce positivity. With an assumed independent frequency uncertainty of 0.05 Hz, local covariance is propagated from the residual Jacobian. The fit recovers

112.000 GPa and 0.2050 kg with a maximum modal residual of 9.94×10^{-9} Hz. The corresponding assumed-noise 95% intervals are 111.651–112.350 GPa and 0.1970–0.2133 kg.

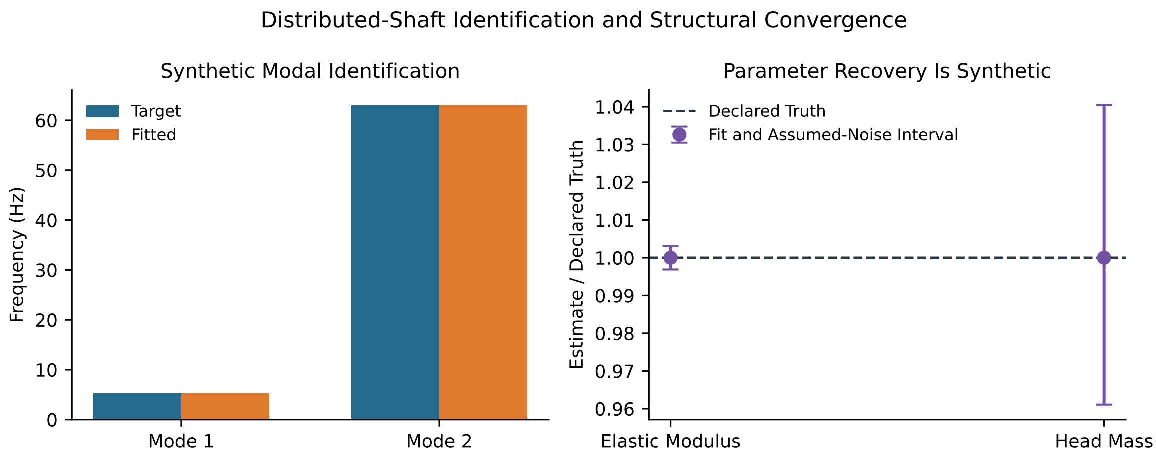

Figure 15.1: Synthetic Identification and Beam Convergence

Figure 15.1 verifies that the inference path can recover an identifiable synthetic truth. It does not show that real equipment follows the uniform-modulus, axisymmetric, Euler–Bernoulli assumptions. Practical equipment identification still requires measured modal frequencies, boundary conditions, mass properties, and their uncertainties.

15.4 Matched Reduced and Higher-Order Responses

The mass-normalized modal coordinates satisfy

$$\ddot{\eta}_i + 2\zeta\omega_i\dot{\eta}_i + \omega_i^2\eta_i = \phi_i^{\mathsf{T}}\mathbf{f}(t), \tag{15.2}$$

with a damping ratio of 0.018. The reduced model retains only the first mode. The higher-order reference retains six modes. Both receive exactly the same load history and use fixed-step fourth-order Runge–Kutta integration at 12.5 μs. A slow 80 ms tip-force pulse probes first-mode behavior; a short 4 ms tip-force-and-moment pulse deliberately introduces higher-frequency content.

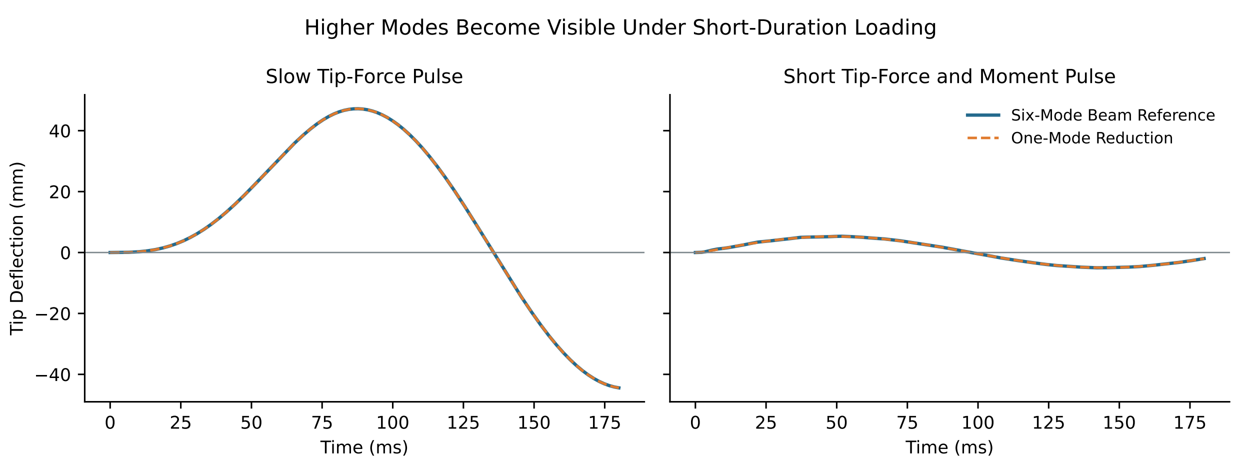

Figure 15.2: Reduced and Higher-Order Tip Responses

Under the slow pulse, the tip-deflection RMS discrepancy is 0.000687 mm. Under the short pulse it grows to 0.0413 mm, sixty times larger, even though the peak values remain close (5.287 mm reduced and 5.339 mm reference). Peak-only agreement therefore conceals a structural discrepancy in the response history. The one-mode model is a useful low-frequency surrogate, not a general replacement for the distributed beam.

15.5 Work–Energy Closure and Remaining Coupling Gate

For either modal truncation,

$$E = \tfrac{1}{2}\sum_i(\dot{\eta}_i^2 + \omega_i^2\eta_i^2), \qquad \dot{E} = P_{\text{tip}} - \sum_i 2\zeta\omega_i\dot{\eta}_i^2. \tag{15.3}$$

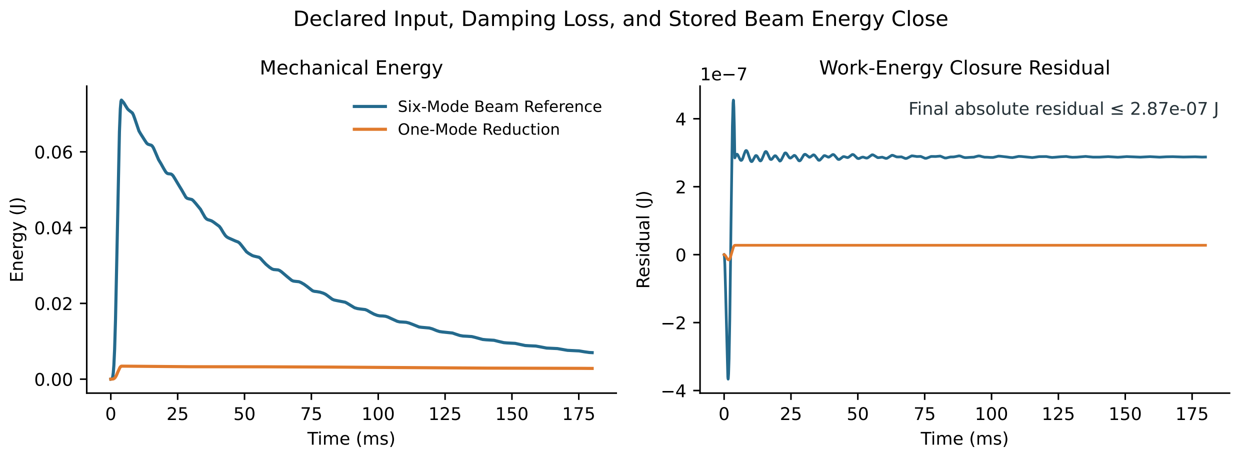

Figure 15.3: Beam Input, Damping, and Energy Closure

The maximum absolute integrated work–energy residual is 2.87×10^{-7} J for the six-mode reference and 2.77×10^{-8} J for the one-mode reduction. This closes the isolated beam comparison and makes damping loss explicit.

The isolated experiment narrows, but does not itself close, the structural coupling gap. Section 16 next inserts the transported modes into the moving-base, two-hand KKT solve and repeats the contact, constraint, and whole-system energy interventions. Equipment-specific language remains prohibited until measured modal, damping, inertia, and boundary-condition data are supplied.

Chapter 16

Forward Coupling of a Distributed Modal Shaft

16.1 Question, Scope, and Claim Boundary

The isolated beam experiment in Section 15 established that a one-mode reduction can conceal excitation-dependent response history. It did not establish whether the two-hand force-couple mechanism survives when the distributed shaft participates in the same forward dynamics as the moving base, arms, grips, and clubhead. This section closes that specific numerical gate. Finite-element-derived bending modes are inserted directly into the planar constrained solve from Section 13; the grip forces, modal coordinates, base motion, and clubhead motion are simultaneous outputs of one KKT system.

The implementation, deterministic study, and machine-readable result are available in `moving_base_modal_shaft.py`, `run_moving_base_modal_shaft_study.py`, and `moving_base_modal_shaft_study.json`. The corresponding trace archive is `moving_base_modal_shaft_study.npz`.

This remains a synthetic mechanism experiment. The shaft bending rigidity is four times the isolated structural reference (implemented as 448 GPa with the reference geometry). That multiplier was intended to keep the declared drive inside a conservative small-deflection screen, but the executed baseline still fails that screen as shown below. It is a numerical stress-test choice, not a material, commercial-shaft, or equipment-calibration claim. No measured EI profile, damping, grip compliance, hand force, body segment, or launch data enter the calculation.

16.2 Coupled Coordinates and Distributed Inertia

The generalized coordinate vector is

$$\mathbf{q} = [\theta_R, \phi_R, \theta_L, \phi_L, x_B, y_B, x_G, y_G, \alpha, \eta_1, \dots, \eta_n]^\mathsf{T}, \tag{16.1}$$

where the first four angles describe the two planar arms, (x_B, y_B) is the finite-mass translating base, (x_G, y_G, α) describes the club root, and η_i are mass-normalized shaft bending coordinates. At shaft station s,

$$\mathbf{r}(s, \mathbf{q}) = \mathbf{r}_G + s\,\mathbf{e}(\alpha) + \left[\sum_{i=1}^{n} \Phi_i(s)\eta_i\right] \mathbf{n}(\alpha). \tag{16.2}$$

The finite-element mode shapes from Equation 15.1 are evaluated by Hermite interpolation at Gaussian quadrature stations. Distributed shaft mass, clubhead translation mass, and clubhead rotary inertia then contribute through their exact point Jacobians,

$$\mathbf{M}_s(\mathbf{q}) = \int_0^L \rho A(s)\mathbf{J}(s,\mathbf{q})^\mathsf{T}\mathbf{J}(s,\mathbf{q})\,ds + m_h\mathbf{J}_h^\mathsf{T}\mathbf{J}_h + I_h\mathbf{J}_\omega^\mathsf{T}\mathbf{J}_\omega. \tag{16.3}$$

This construction retains rigid–modal inertial coupling. It is not a beam response calculated after a rigid-club trajectory has already been prescribed. The transported quadrature basis reproduces the first three finite-element frequencies to a maximum relative discrepancy of 1.09×10^{-5} and the modal mass matrix differs from identity by at most 2.22×10^{-16}. For the declared four-times-EI case, those frequencies are 10.480, 125.891, and 276.066 Hz.

16.3 Constraint Forces, Couples, and Power

Both hand endpoints remain constrained to separated grip points. With four holonomic constraints $\mathbf{c}(\mathbf{q}) = \mathbf{0}$, the acceleration and reaction multipliers are obtained without a rank-deficient fallback:

$$\begin{bmatrix} \mathbf{M}(\mathbf{q}) & -\mathbf{J}_c^\mathsf{T} \\ \mathbf{J}_c & \mathbf{0} \end{bmatrix} \begin{bmatrix} \ddot{\mathbf{q}} \\ \lambda \end{bmatrix} = \begin{bmatrix} \mathbf{Q} - \mathbf{h}(\mathbf{q}, \dot{\mathbf{q}}) \\ -\dot{\mathbf{J}}_c\dot{\mathbf{q}} \end{bmatrix}. \tag{16.4}$$

The two solved forces on the club are $\mathbf{F}_R$ and $\mathbf{F}_L$. Their force-generated grip couple about the club-root reference is

$$M_F = (\mathbf{r}_R - \mathbf{r}_G) \times \mathbf{F}_R + (\mathbf{r}_L - \mathbf{r}_G) \times \mathbf{F}_L. \tag{16.5}$$

This quantity remains separate from the directly commanded wrist moment and from the internal elastic generalized forces. The contact-power identity is checked at every sample in both equivalent forms,

$$\mathbf{F}_R \cdot \mathbf{v}_R + \mathbf{F}_L \cdot \mathbf{v}_L = (\mathbf{F}_R + \mathbf{F}_L) \cdot \mathbf{v}_G + M_F\dot{\alpha}. \tag{16.6}$$

The maximum discrepancy is 1.71×10^{-13} W in the baseline and 1.42×10^{-13} W after the intervention. Position, velocity, acceleration, and KKT residuals are also recorded rather than inferred from visual agreement.

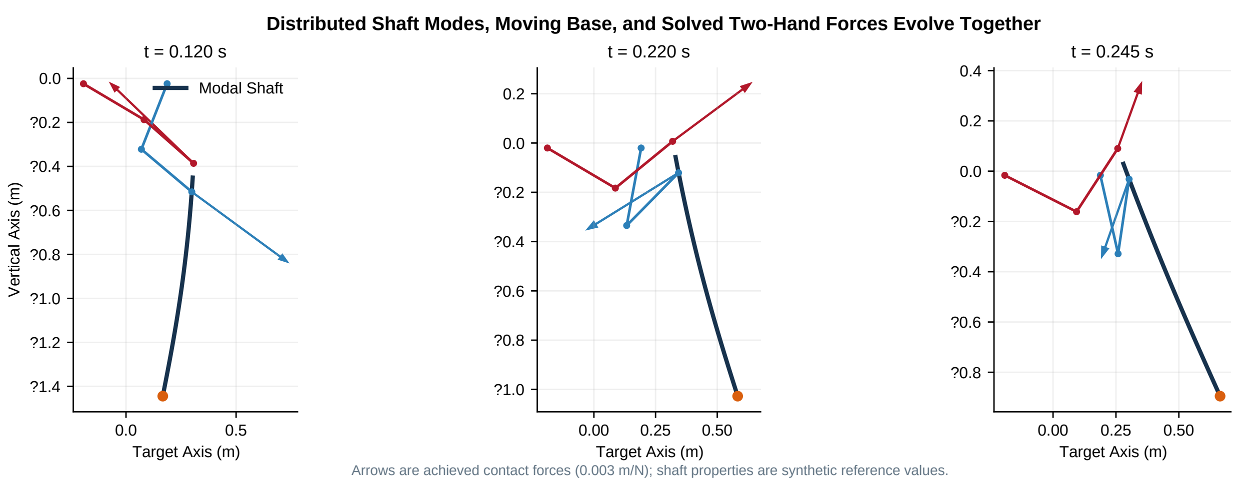

Figure 16.1: Forward Geometry, Distributed Shaft, and Achieved Grip Forces

Figure 16.1 shows three states from the integrated trajectory. The arrows are the achieved constraint forces, not specified loads. Their directions change with the arm–grip geometry while the modal centerline, base, and clubhead evolve in the same solve. Arrow length uses one common display scale; force interpretation still requires the registered reference point and power variables.

16.4 Model-Use Screen and Baseline Closure

Linear Euler–Bernoulli kinematics are inappropriate if the numerical case is allowed to bend without a declared range-of-use guard. This study therefore preregisters the screening rule

$$\max_t |w(L,t)|/L < 0.05. \tag{16.7}$$

The observed maximum is 0.13476, so the current baseline **fails** this preregistered screen. The coupled run is retained as an explicit out-of-domain stress test, not as quantitatively valid small-deflection beam evidence. The 5% value is a conservative model-use screen for this resource, not a universal theorem about beam validity. Torsion, shear deformation, geometric nonlinearity, impact, and material anisotropy remain absent.

At a 0.50 ms step, the base moves by at most 26.70 mm, the modal tip deflection reaches 134.76 mm, and the first three modal coordinates all depart from zero. Peak shaft strain energy is 2.123 J and peak clubhead speed is 7.356 m/s. The force-generated couple spans -21.60 to 28.87 N m. Mechanical energy changes by 39.482 J while integrated applied and dissipative work is 39.464 J, leaving a 0.0174 J absolute residual. These are numerical observations for an out-of-screen synthetic stress test, not estimates of golfer or equipment performance.

16.5 Excitation-Dependent Mode Truncation

One-, three-, and six-mode systems are integrated from identical initial states under two resolved inputs. A smooth drive represents the low-frequency case; a 2 ms wrist-moment pulse deliberately excites higher frequencies. The six-mode result is the within-model comparison reference, not experimental truth.

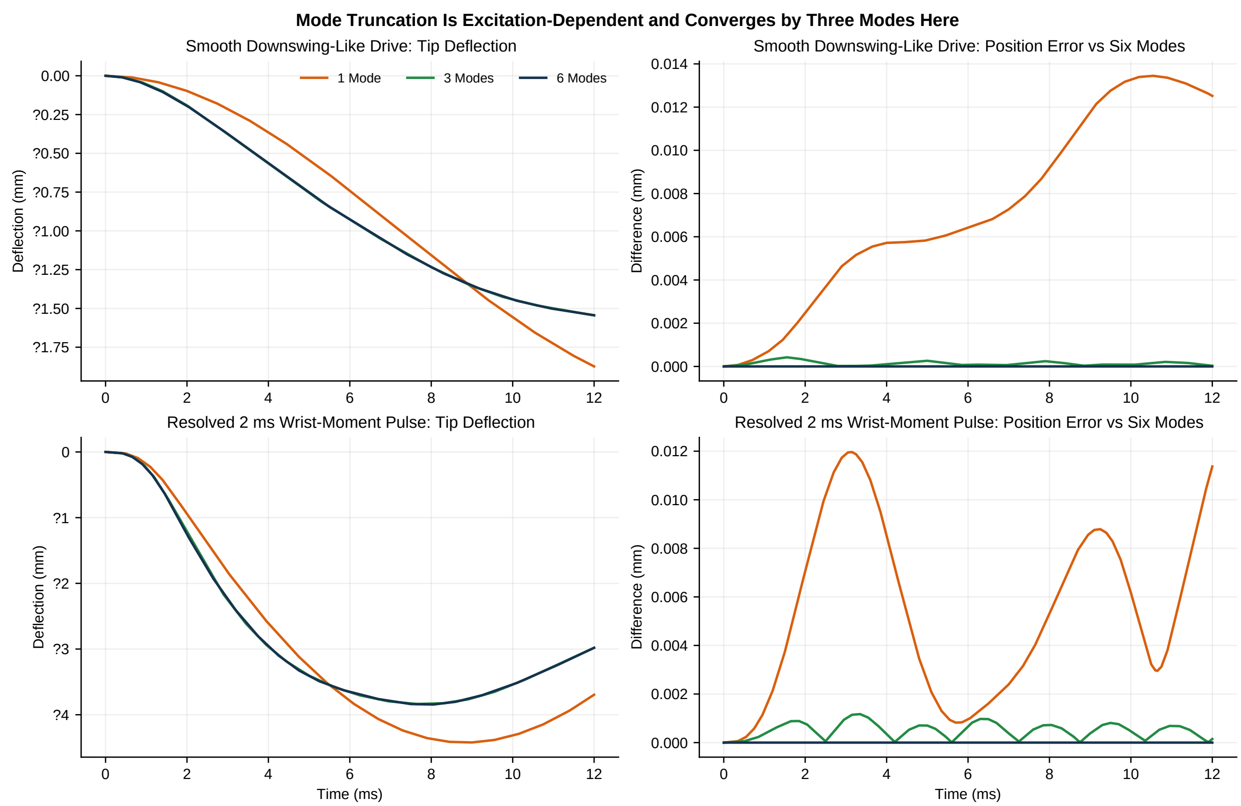

Figure 16.2: Mode-Truncation Response Under Smooth and Short Inputs

For the smooth drive, the one-mode tip-deflection RMS discrepancy relative to six modes is 0.160 mm and its maximum clubhead-position discrepancy is 13.45 μm. Retaining three modes reduces those values to 0.00186 mm and 0.422 μm. Under the short pulse, the one-mode deflection discrepancy grows to 0.484 mm, 3.03 times its smooth-input value, while the three-mode discrepancy is 0.00755 mm and its maximum clubhead-position discrepancy is 1.184 μm. Figure 16.2 therefore supports a conditional statement: three modes are converged for the two declared excitations and timestep, whereas a single-mode approximation is input-dependent. It does not establish that three modes suffice for impact or arbitrary loading.

16.6 Same-State Zero-Command Intervention

At 0.220 s, the complete state $(\mathbf{q}, \dot{\mathbf{q}})$ is copied exactly and all shoulder, elbow, and wrist commands are set to zero. The branch is then integrated for 30 ms. Because the branch shares its cut state bit for bit, any subsequent difference from a zero-inertia or relabeled-load construction cannot be attributed to a changed initial condition.

The force-generated couple is already negative at the cut and remains negative for 25.5 ms of the branch, reaching -21.17 N m. This is a statement about the continued constrained motion of the declared model after command removal; it is not evidence that biological muscles are inactive. The branch continues to contain inertia, gravity, base restoring forces, joint damping, modal elasticity, and shaft damping.

Two exact geometry controls bound the interpretation. Moving both grip moment arms to the same reference point makes the force-generated couple identically zero while retaining the achieved force records. Reversing the registered moment arms reverses the couple with zero residual. Thus the negative sign is not a force-magnitude label: it depends on the cross products in Equation 16.5.

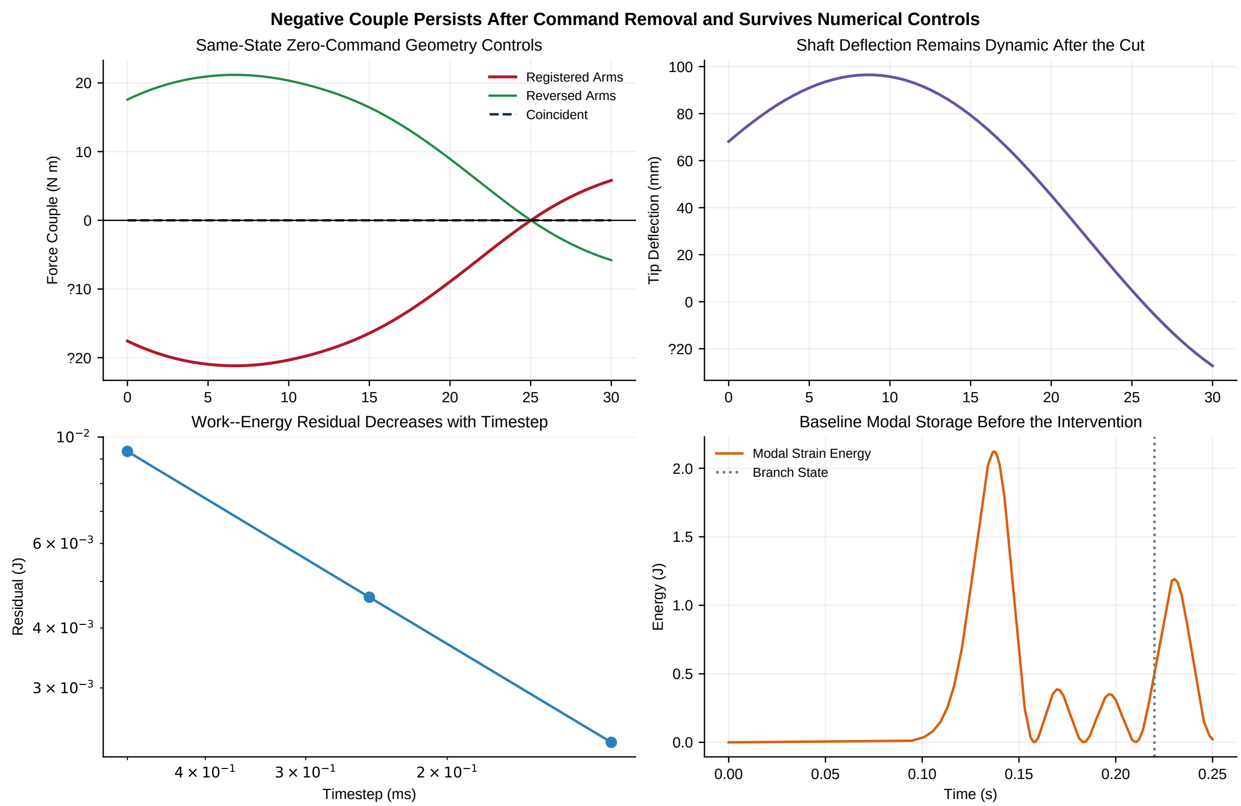

Figure 16.3: Same-State Killswitch, Geometry Controls, and Numerical Closure

The intervention is repeated at 0.50, 0.25, and 0.125 ms. The absolute work–energy residual decreases monotonically from 0.00934 to 0.00464 to 0.00231 J, while the negative interval converges from 25.50 to 25.25 to 25.125 ms and the minimum couple from -21.17 to -21.19 N m. This separates a persistent mechanism result from a fixed-step artifact without claiming zero numerical error.

16.7 Falsifiers and Remaining Inference Gaps

The coupled distributed-shaft result would fail its declared claim if any of the following occurred: transported modes did not reproduce the finite-element frequencies; higher modes remained numerically inert under the resolved pulse; the negative interval disappeared with timestep refinement; the coincident or reversed moment-arm controls failed; the 5% deflection screen failed; or the constraint, contact-power, and work–energy residuals ceased to close.

The 5% screen does fail in the current synthetic planar baseline, so the quantitative small-deflection claim is rejected for this run. The remaining supported claim is narrower: the finite-element-derived modal coordinates can be coupled into the moving-base two-hand forward solve while preserving the registered negative-couple intervention, geometry controls, and numerical identities, but the resulting amplitudes cannot be interpreted as a valid linear-beam equipment prediction. Equipment calibration, anatomical arms, base rotation, three-dimensional shaft bending and torsion, compliant tissue, impact, muscle coordination, optimal control, human strategy, and coaching benefit remain untested. Those omissions define the next model tiers; they are not conclusions supplied by this one.

Chapter 17

Spatial Full-Body Common-State Dynamics

The preceding forward models establish a planar mechanism under increasing coupling, but a planar result cannot answer whether the same wrench geometry survives out-of-plane motion or whether it is an artifact of one dynamics implementation. This chapter executes a spatial comparison at identical achieved states. It uses one immutable reduced full-body model definition in two independent formulations: native MuJoCo inverse dynamics and a Lagrange–Christoffel implementation assembled directly from body Jacobians (Todorov, Erez, and Tassa 2012; Featherstone 2008).

This is a deliberately bounded test. It is a real three-dimensional dynamics calculation, not a rotation of planar vectors. The body and club move about all three world axes; the club has three translational and three rotational coordinates; and the hand forces include out-of-plane components. The two formulations evaluate exactly the same position, velocity, acceleration, inertias, gravity, and applied action–reaction loads. That common-state design isolates dynamics implementation from trajectory divergence; it does not test whether the two implementations would integrate to the same later state.

The hand loads are prescribed. Therefore the experiment can test spatial wrench transport, geometry interventions, and inverse-dynamics equivalence. It cannot establish that the loads would emerge passively from compliant two-hand contact. That distinction controls every claim below.

17.1 Why a Common Model Is Necessary

Names such as "full body" or "humanoid" do not establish model equivalence. The available native engine artifacts differ in joint count, floating-base representation, lower-body topology, club attachment, and treatment of the second hand. Comparing their force histories directly would mix at least four effects:

1. numerical implementation;
2. coordinate and frame conventions;
3. structural model differences; and
4. distinct initial conditions or inputs.

No tolerance can make that comparison causal. The present experiment instead defines one study-specific tree and generates the MuJoCo representation from the same in-memory specification consumed by the independent analytical formulation. A SHA-256 digest of the canonical joint, inertia, attachment, and interface-index record is stored for both implementations. The two recorded hashes must be identical before an outcome is evaluated. This is a content-integrity check on the shared generator, not evidence of independent model transcription.

This common model is a reduced full-body model rather than a subject-specific anatomical reconstruction.

It contains pelvis and lower-body mass, a spatial torso, bilateral three-axis shoulders, elbows, wrists, and a separately moving club. Twenty generalized coordinates comprise 14 body coordinates and six club coordinates. Thirty-two spherical inertia elements include explicit small carrier inertias for otherwise massless compound-joint frames. Those carrier masses are present in both formulations and are part of the model hash; they are not an engine-specific numerical patch.

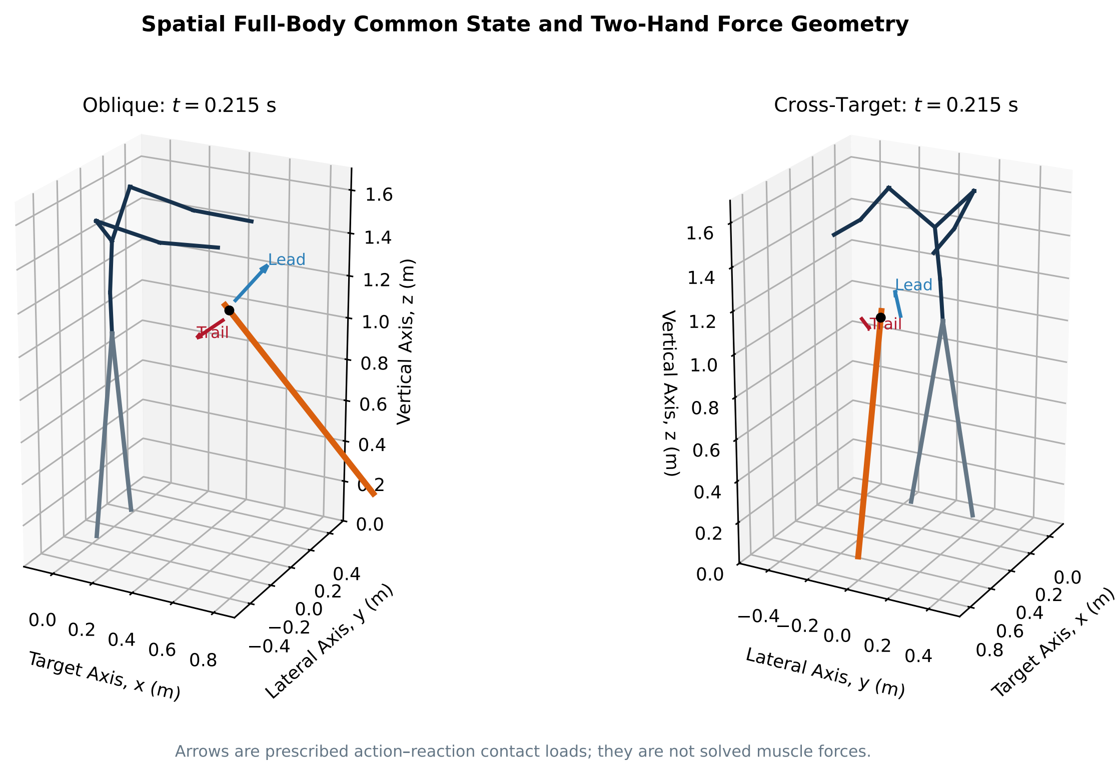

Figure 17.1: Spatial Full-Body Common State and Two-Hand Force Geometry

Figure 17.1 shows the achieved state at 0.215 s from two views. The lateral club displacement spans 35.0 mm over the registered window, and the model axes have rank three. The blue and red arrows are the lead- and trail-hand forces on the club. They are prescribed contact loads, not estimates of muscle force or measured human hand force.

17.2 Shared Spatial Dynamics Definition

Let the generalized state be

$$\mathbf{q} = \begin{bmatrix}\mathbf{q}_B & \mathbf{r}_C & \eta_C\end{bmatrix}^{\mathsf{T}}, \tag{17.1}$$

where $\mathbf{q}_B \in \mathbb{R}^{14}$ contains the reduced body coordinates, $\mathbf{r}_C \in \mathbb{R}^3$ is club-frame translation, and $\eta_C \in \mathbb{R}^3$ is the ordered club rotation coordinate. Every joint is a scalar revolute or prismatic coordinate. This avoids hiding a quaternion/Euler remapping inside the engine comparison.

For body b with mass m_b, world rotation $\mathbf{R}_b$, isotropic local inertia $\mathbf{I}_b$, linear COM Jacobian $\mathbf{J}_{v,b}$, and angular Jacobian $\mathbf{J}_{\omega,b}$, the analytical mass matrix is

$$\mathbf{M}(\mathbf{q}) = \sum_b \left(m_b \mathbf{J}_{v,b}^{\mathsf{T}} \mathbf{J}_{v,b} + \mathbf{J}_{\omega,b}^{\mathsf{T}} \mathbf{R}_b \mathbf{I}_b \mathbf{R}_b^{\mathsf{T}} \mathbf{J}_{\omega,b}\right). \tag{17.2}$$

The independent bias calculation uses

$$\mathbf{h}(\mathbf{q}, \dot{\mathbf{q}}) = \dot{\mathbf{M}}\dot{\mathbf{q}} - \frac{1}{2}\nabla_{\mathbf{q}}\left(\dot{\mathbf{q}}^{\mathsf{T}}\mathbf{M}\dot{\mathbf{q}}\right) + \nabla_{\mathbf{q}}V, \tag{17.3}$$

with centered finite differences of the mass matrix and an analytical gravity gradient. MuJoCo independently compiles the same tree and evaluates its native inverse dynamics. Both outputs are normalized to the same required-action convention,

$$\tau_{\text{required}} = \mathbf{M}\ddot{\mathbf{q}} + \mathbf{h} - \mathbf{Q}_{\text{contact}}. \tag{17.4}$$

This normalization matters. MuJoCo's inverse-dynamics output reports inertial plus bias generalized force; applied generalized loads are not subtracted from that field automatically. The first implementation audit exposed a 26% apparent discrepancy when the two sides used different external-load conventions. Applying Equation 17.4 explicitly reduced the maximum relative discrepancy to 2.14×10^{-11}. The preregistered 5% relative and 0.75 generalized-force absolute bounds were not changed.

As an adversarial control, omitting that normalization produces a 26.3% maximum relative mismatch. Separate component audits compare the native and analytical mass matrices to 2.49×10^{-14} absolute (1.33×10^{-15} relative) and the bias vectors to 1.25×10^{-9} absolute (4.05×10^{-11} relative). Thus the final agreement is not explained by cancellation between erroneous mass and bias terms. These component checks still share the same generated tree and do not constitute an independent anatomical-model validation.

17.3 Two-Hand Wrench and Action–Reaction Contract

At the declared club reference O, the lead and trail forces produce

$$\mathbf{F}_O = \mathbf{F}_L + \mathbf{F}_T, \qquad \mathbf{M}_O = (\mathbf{r}_L - \mathbf{r}_O) \times \mathbf{F}_L + (\mathbf{r}_T - \mathbf{r}_O) \times \mathbf{F}_T. \tag{17.5}$$

The complete wrench is $\mathcal{W}_C = [\mathbf{F}_O^{\mathsf{T}}, \mathbf{M}_O^{\mathsf{T}}]^{\mathsf{T}}$. The equal and opposite body-side wrench is $\mathcal{W}_B = -\mathcal{W}_C$. For a compatible contact twist $\mathcal{V} = [\mathbf{v}_O^{\mathsf{T}}, \omega^{\mathsf{T}}]^{\mathsf{T}}$,

$$\mathcal{W}_C^{\mathsf{T}}\mathcal{V} + \mathcal{W}_B^{\mathsf{T}}\mathcal{V} = 0. \tag{17.6}$$

The recorded maximum residual in Equation 17.6 is zero to stored precision. This checks the common virtual-work convention. It does not assert no work at a slipping or compliant biological contact, because the two sides would then have different point velocities and contact storage or dissipation would require its own state.

An independent point-force calculation agrees with generalized external-load power within 2.67×10^{-15} W. Transporting the club wrench and twist to an offset reference point preserves scalar power within 8.88×10^{-16} W. These audits expose sign, Jacobian, and reference-point errors that the equal-and-opposite construction alone could conceal.

The force-generated scalar club couple is the moment projection on the local club axis $\hat{\mathbf{e}}_C$,

$$M_F = \hat{\mathbf{e}}_C^{\mathsf{T}}\mathbf{M}_O. \tag{17.7}$$

No direct club torque command is applied. This keeps direct couple and force-generated couple separate, but prescribed force is still an external input. "Zero direct torque" is therefore not synonymous with "passively generated contact force."

17.4 Registered Interventions and Tolerances

Three interventions are evaluated at the same achieved state and with the same force histories:

- **Registered Geometry:** maintain the declared 0.18 m signed separation of lead and trail contact points;
- **Reversed Moment Arm:** reverse the signed contact separation without changing either force vector; and
- **Coincident Hands:** set both force application points to the same reference, which analytically requires the force-generated couple to be zero.

The preferred result is not used to select a tolerance. Before inspecting the event-window outcome, the numerical region was fixed at 0.75 absolute generalized-force units, 5% relative error, and 4 ms intervention-grid alignment error. Because both formulations receive one registered load history, this last quantity checks input alignment; it is not a second event detector. The analytical derivative was evaluated with 2×10^{-6} and 10^{-6} coordinate steps. Their maximum generalized-force difference is 1.47×10^{-9}, far below the predeclared absolute region.

The experiment is falsified at this tier if any of the following occurs:

1. the two implementations use different model hashes;
2. the same-state inverse-dynamics residual exceeds either registered bound;
3. complete action–reaction wrench power does not close;
4. reversing the moment arm fails to reverse the force-generated couple;
5. coincident force application points retain a finite force couple; or
6. the purported spatial trajectory has no out-of-plane motion;
7. mass-matrix or bias-force agreement fails when audited separately; or
8. generalized point-force power or wrench-reference transport fails to close.

17.5 Executed Results

Figure 17.2 overlays three representative generalized actions. The curves are visually indistinguishable. Across all 20 coordinates and 61 event-aligned states, the maximum absolute discrepancy is 1.25×10^{-9} and the maximum relative discrepancy is 2.14×10^{-11}. The registered intervention-grid alignment error is zero by construction and is reported separately from the dynamics residual. This result supports implementation equivalence for the declared common model and same-state inverse-dynamics observable.

The separate component and virtual-work audits above narrow that conclusion to the mass, bias, external-load, and reference-transport pathways actually tested; they do not validate forward contact, tissue mechanics, or human anatomy.

It does not show that arbitrary MuJoCo and analytical humanoid models agree. The equivalence depends on the identical model digest, joint order, spherical inertias, gravity vector, state, and generalized external-load convention. Changing any of those inputs creates a new experiment and requires a new tolerance record.

The registered geometry reaches a minimum force-generated couple of $-4.32\ \mathrm{N \cdot m}$ and first becomes negative at 0.172 s. Reversing only the signed moment arm yields an equal positive response; the maximum sign-reversal residual is $8.88 \times 10^{-16}\ \mathrm{N \cdot m}$. Collapsing the contact separation makes the force-generated couple exactly zero while retaining the total force history. These results reject force magnitude alone as an explanation of the couple sign in this model.

The intervention is intentionally stronger than a visual pose comparison. It holds force vectors and achieved state fixed while changing only the geometric lever arm. Consequently, the sign response is attributable to Equation 17.5 within the declared model. It is not attributable to a change in force norm, event timing, solver state, or reference-frame rotation.

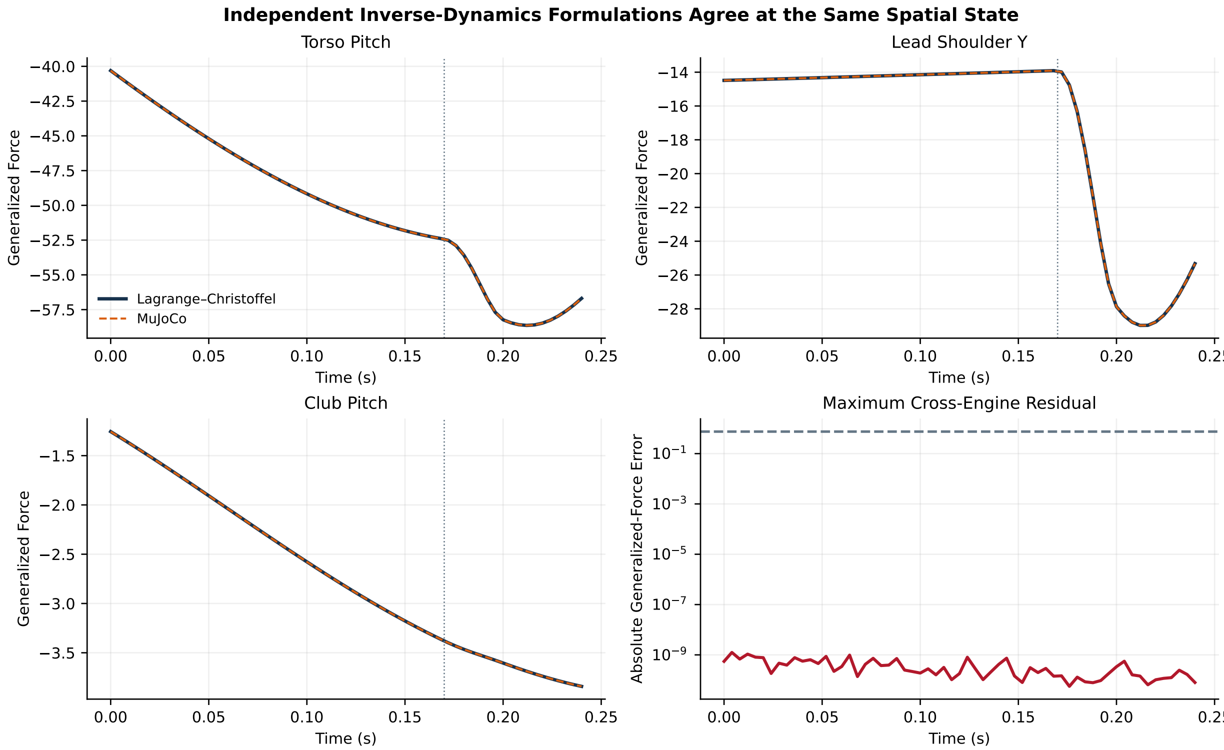

Figure 17.2: Independent Inverse-Dynamics Formulations Agree at the Same Spatial State

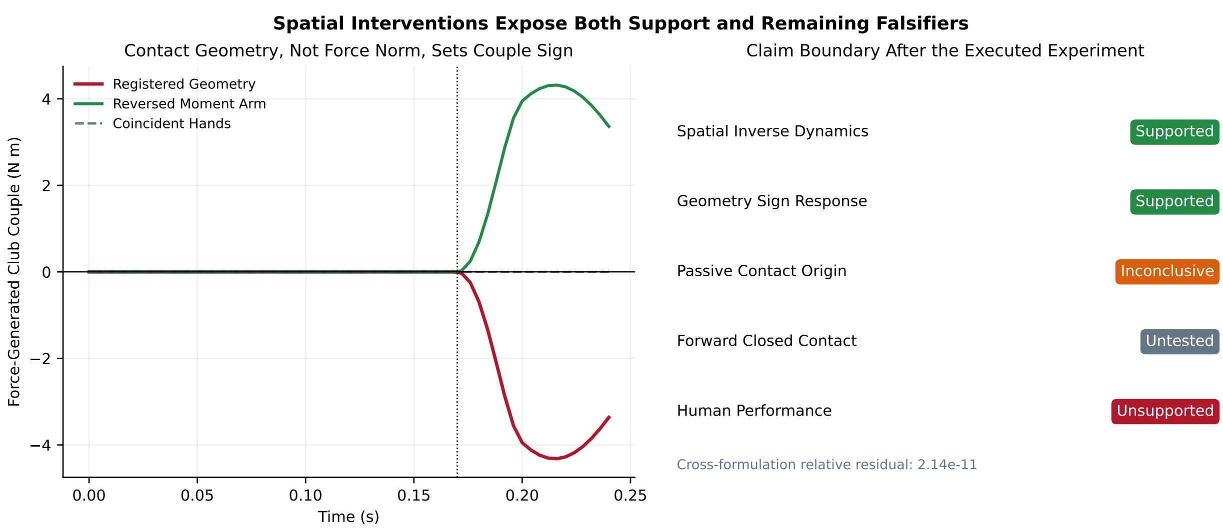

Figure 17.3: Spatial Interventions Expose Both Support and Remaining Falsifiers

17.6 Subject-Scaled Contact-Closure Audit

The common-state result still leaves a more basic geometric question: do the anatomical hand points occupy the declared club-contact points? A constraint Jacobian can have full row rank even when the points it would constrain are far apart. Treating rank as proof of feasible two-hand contact would therefore hide a model-structure failure.

A deterministic atlas scales the same 20-coordinate tree with the repository's canonical de Leva anthropometric estimator. It uses female and male regression tables at statures of 1.55, 1.75, and 1.95 m, with mass fixed by a declared 24 kg/m^2 design rule. These six profiles are engineering design points, not participants or a population sample. Each is evaluated at 61 prescribed states and grip spans of 0.12, 0.18, and 0.24 m. The audit records the two anatomical hand-to-grip distances, the 6×20 bilateral point-constraint Jacobian and its singular values, the two-point force-to-wrench rank, and the regional generalized loads.

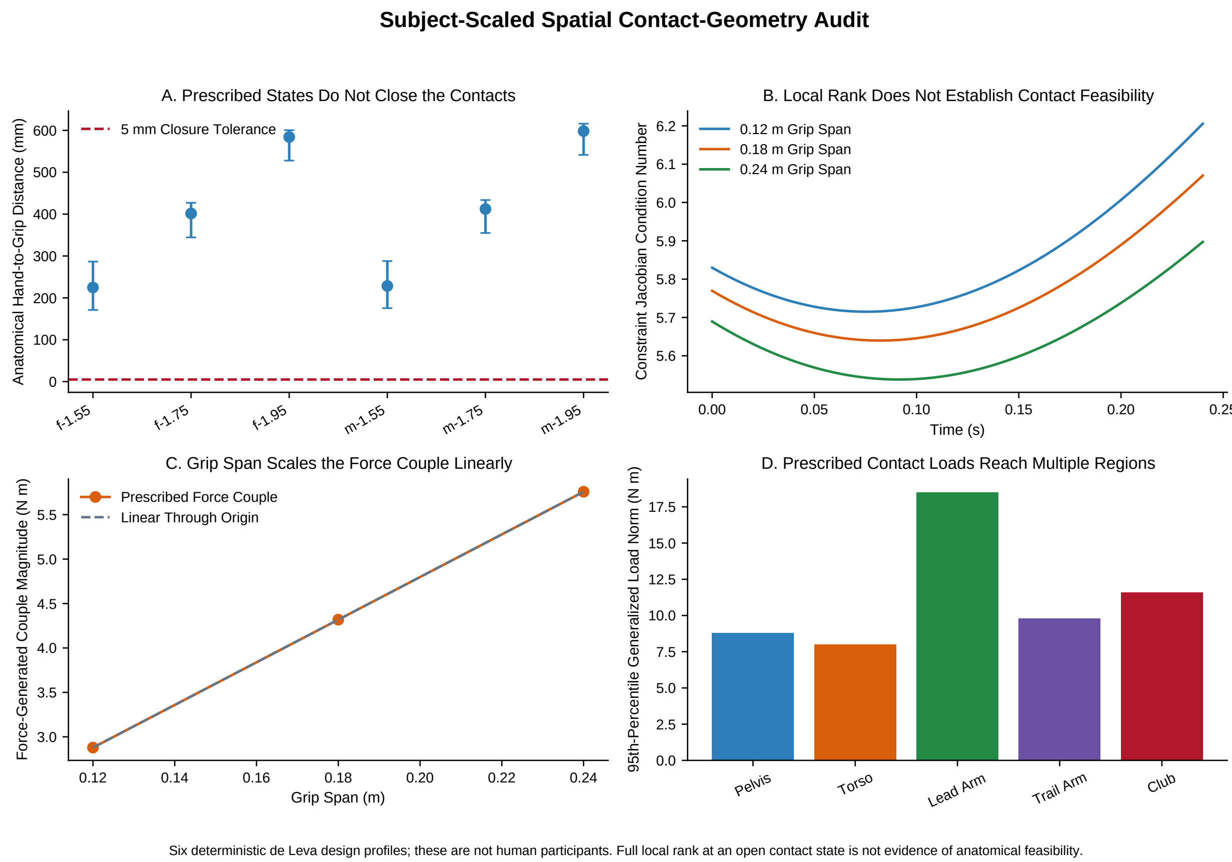

Figure 17.4: Subject-Scaled Spatial Contact-Geometry Audit

The adverse result is unambiguous. Anatomical hand points miss the declared grip points by 0.171–0.616 m across the atlas, with a median miss of 0.405 m; none is within the preregistered 5 mm closure tolerance. At the same open states, however, every local bilateral constraint Jacobian has rank six and condition number 5.35–6.40. Thus the rank calculation answers whether six local closure directions are independently available, not whether the prescribed configuration already satisfies those closures.

The point-force measurement map retains rank five and one invisible axial push–pull mode at every grip span. Adding the independently measured internal axial scalar raises the augmented map to rank six. The prescribed force-generated couple scales exactly with grip span to stored precision. These positive algebraic controls do not rescue anatomical feasibility; they show that measurement rank, local kinematic rank, contact closure, and forward contact dynamics are four distinct gates.

17.6.1 Closed-Contact Inverse-Kinematics Gate

The next registered rung solves rather than prescribes the body and arm coordinates. For each of the six profiles, three grip spans, and 13 samples from 0.00 through 0.24 s, a bounded least-squares solve holds all six club coordinates at their prescribed values and adjusts the 14 pelvis, torso, shoulder, elbow, and wrist coordinates. Bilateral point errors are the primary residual; a weak reference-posture term selects one solution from the underdetermined family. An unreachable 2.0 m grip span is retained as an adverse control and correctly fails the closure gate.

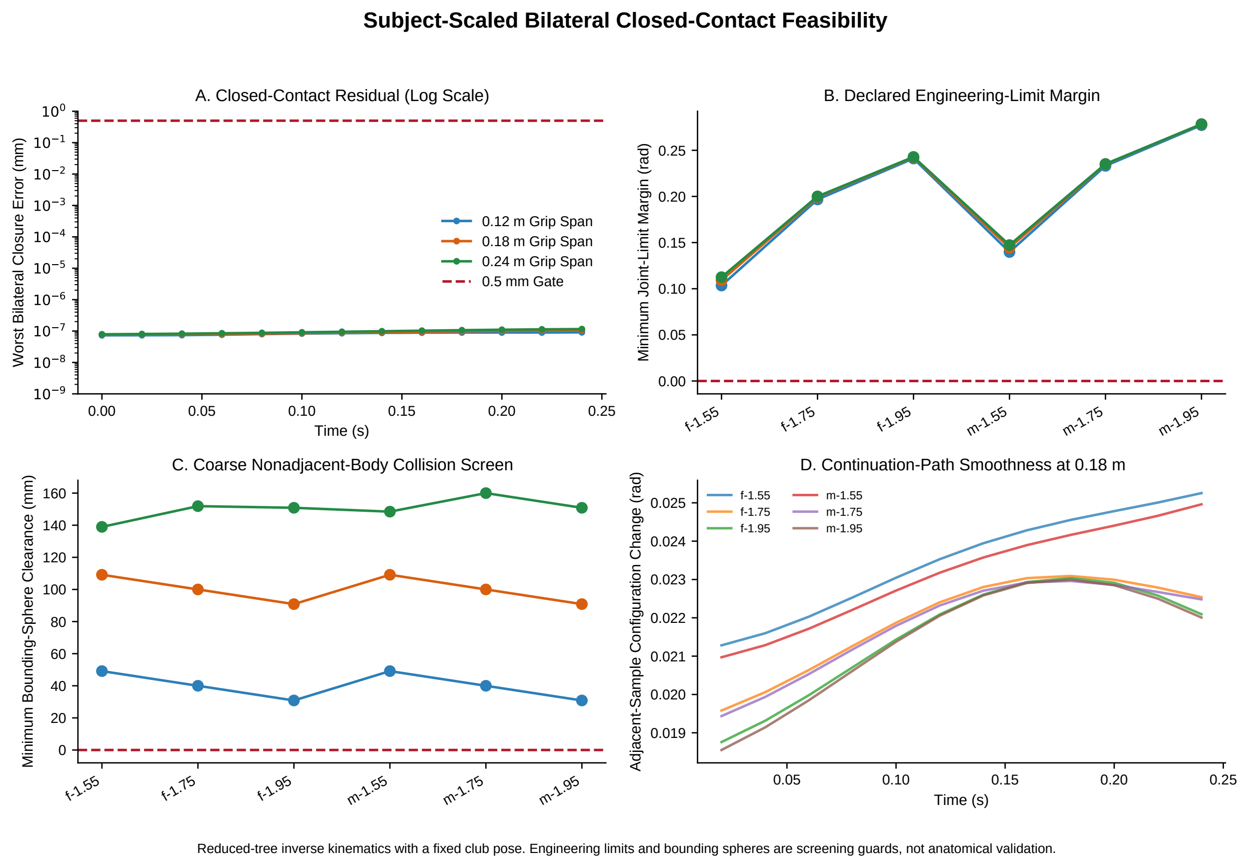

Figure 17.5: Subject-Scaled Bilateral Closed-Contact Feasibility

All 234 registered samples close both contacts. The largest bilateral error is 1.16×10^{-10} m, every achieved constraint Jacobian retains rank six, and the maximum adjacent-sample change across the 20 ms continuation grid is 0.0256 rad. The smallest margin to the declared reduced-model joint bounds is 0.103 rad, and the smallest nonexempt bounding-sphere clearance is 30.9 mm. The result therefore rejects the earlier prescribed trajectories without showing that the grip geometry itself is unreachable in this reduced tree.

Those favorable checks remain a necessary-condition result. The broad bounds are engineering guards, not measured clinical ranges. Bounding spheres omit mesh-level anatomy; connected segments and intended hand–grip contacts are exempt. The tree has no explicit scapular glide, forearm pronation–supination, multi-axis wrist, fingers, or distributed tissue contact. Inverse kinematics supplies neither force nor work and cannot test passivity, timing demand, self-correction, proximal-speed benefit, or any class of slack.

17.6.2 Closed-State Forward-Contact Initialization Gate

The closed configurations now enter the independently authored MuJoCo and Pinocchio contact solvers through one engine-neutral state contract. For each of the 234 profile–span–phase states, a constant rigid transformation places the club reference at the canonical center and aligns its initial orientation with the canonical axes. Positions are rotated and translated; linear and angular velocities are rotated without subtracting the club velocity, so the map changes coordinates rather than changing inertial motion. The two local grip offsets remain $(0, \pm s/2, -0.03)$ m.

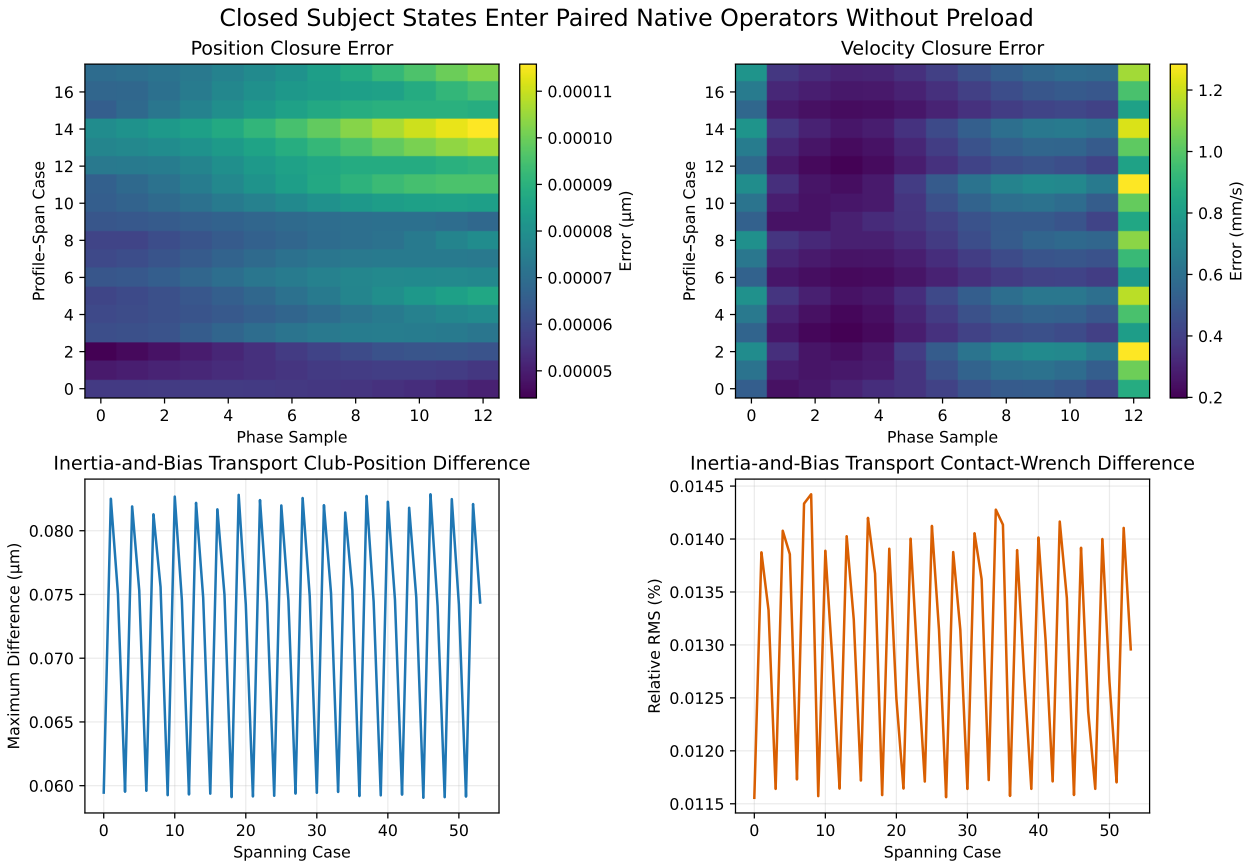

Figure 17.6: Closed Subject States Enter Paired Native Operators Without Preload

All 234 position mappings retain the source closure, with a maximum error of 1.16×10^{-10} m. Velocities estimated by second-order finite differences along each closed inverse-kinematics path close to 1.29 mm/s at worst, below the preregistered 5 mm/s mapping tolerance. Every mapped state has a distinct SHA-256 digest. Exact closure produces zero Kelvin–Voigt preload; the 1 mm constitutive perturbation preserves action–reaction and produces nonpositive damping power.

A spanning subset advances all six profiles, all three grip spans, and early, middle, and late phases through both native inertia-and-bias operators under the shared projected-contact and semi-implicit-update formulation: 54 shared initial states and 108 trajectories. Every operator pair reports the same initial-state digest and passes the existing trajectory, wrench, and normalized-energy comparison gates over the preregistered 4 ms initialization audit. The largest transport club-position difference is 0.083 μm, the largest relative contact-wrench RMS difference is 0.0145%, and the largest normalized-energy difference is 2.19×10^{-7}.

This is an initialization and short-horizon numerical-transport result, not a subject-scaled forward golfer. The forward tier still replaces the articulated arms with finite-mass hand carriages after initialization; its hand mass is profile-scaled, but its club, contact stiffness, damping, and driver remain declared engineering values. The result therefore removes an executable gap between closed geometry and compliant contact without establishing calibrated equipment, anatomical dynamics, tissue loading, passive late-downswing transfer, delivery benefit, or a human strategy. The next falsifier is a full-horizon articulated solve with typed contact loss, calibrated grip and shaft compliance, refinement, adverse-load, null, and reversal controls.

17.6.2.1 Inertia-and-Bias Transport Validity Horizon and Adverse-Load Map

The 4 ms result establishes initialization transport but leaves its persistence unmeasured. A preregistered extension therefore advances the same six profiles, three grip spans, and early, middle, and late closed states to 4, 10, 25, and 50 ms. Ten branches retain the nominal model; halve or double contact stiffness, contact damping, represented hand mass, or timestep one factor at a time; or remove the grounded driver from the first integration step. Both native rigid-body operators receive identical state and parameter records, projected-contact loads, and project-authored updates. Failed, unstable, and non-finite cases would remain typed outcomes rather than being removed.

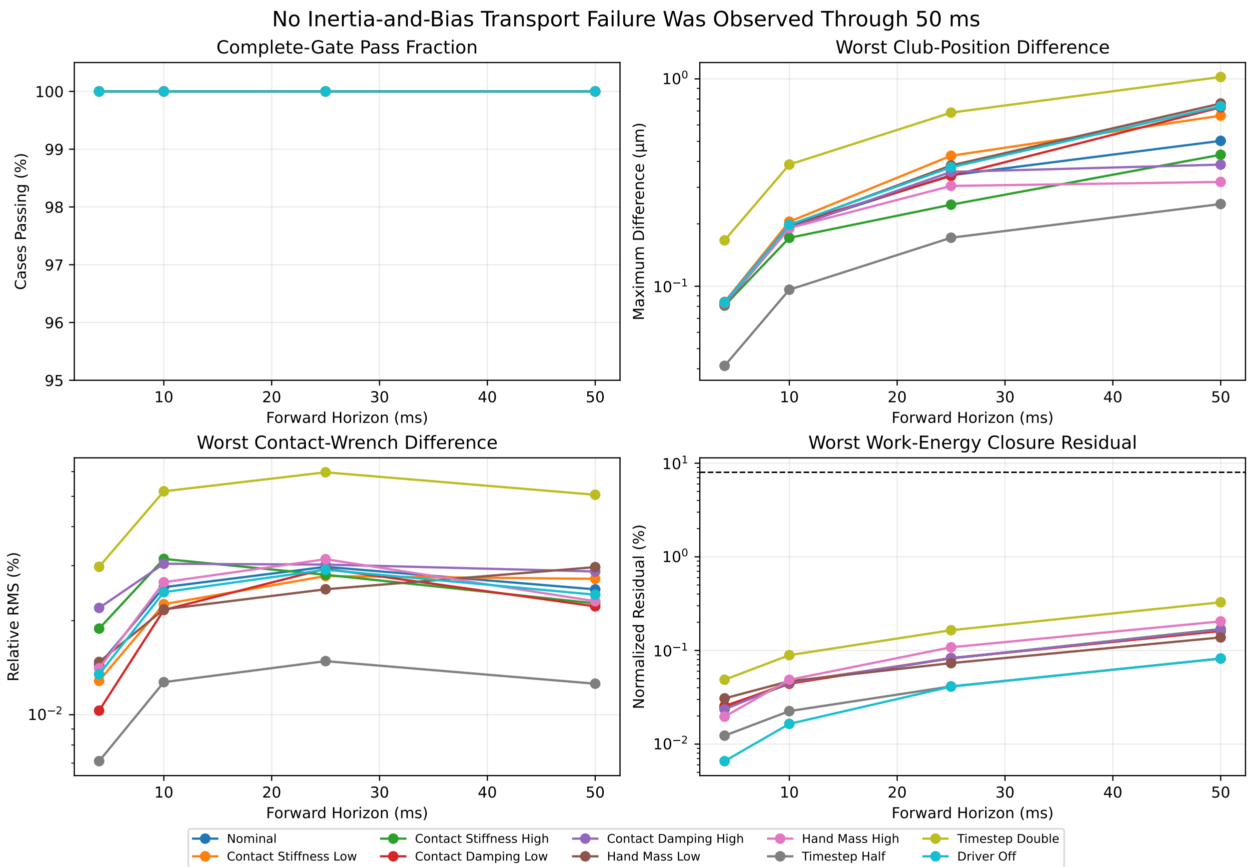

Figure 17.7: Inertia-and-Bias Transport Validity Horizon and Adverse-Load Map

All 2,160 profile–span–phase–variant–horizon cases pass the existing trajectory, contact-wrench, and normalized-energy discrepancy gates together with an 8% work–energy closure gate. At 50 ms, the worst nominal club-position difference is 0.503 μm, the worst nominal relative contact-wrench RMS difference is 0.0252%, and the worst nominal normalized-energy difference is 3.20×10^{-6}. Across every adverse and null branch, the largest club-position difference is 1.02 μm, the largest relative wrench RMS is 0.0506%, and the largest normalized work–energy closure residual is 0.327%. Halving the timestep reduces the worst closure residual from 0.164% to 0.0818%, whereas doubling it raises the value to 0.327%, supplying the expected first-order refinement direction without retuning a threshold.

No first-failure horizon is observed inside the registered 50 ms interval. That is a right-censored engineering result, not permission to extrapolate to the remaining downswing or impact. The carriages, rigid club, engineering contact law, and prescribed driver still omit articulated arms and scapulae, distributed grip and shaft properties, contact loss, ground coupling, and calibrated equipment. The study strengthens the reduced inertia-and-bias transport reference. The articulated tier reproduces its power, energy, refinement, and operator-transport logic only through 5 ms, not the full 50 ms interval. Neither result establishes anatomy, passive human transfer, timing economy, slack benefit, or coaching strategy.

17.6.2.2 Native Articulated Inertia Qualification

The reduced forward-contact result cannot be promoted merely by replacing the hand carriages with a more detailed drawing. Before adding compliant contact, the two native engines must first agree on the inertia and gravity operators of the subject-scaled articulated tree itself. The next common-state gate therefore uses all 234 closed configurations: six engineering profiles, three grip spans, and 13 continuation samples. Each model retains the 20-coordinate pelvis, torso, bilateral three-axis shoulder, elbow, wrist, and six-coordinate rigid-club tree. Segment lengths and masses remain de Leva-derived engineering design points; each spherical body inertia is declared as $2mr^2/5$.

MuJoCo independently evaluates its full mass matrix, bias force, and inverse dynamics with `mj_fullM`, `qfrc_bias`, and `mj_inverse`. Robotics Pinocchio builds the same scalar-joint tree and evaluates `crba`, `nonLinearEffects`, and `rnea`. Velocities and accelerations are second-order finite differences of the closed 13-sample paths. Because both engines receive the same achieved state rather than advancing a trajectory, this isolates model assembly and native dynamics conventions from contact-law and integrator divergence.

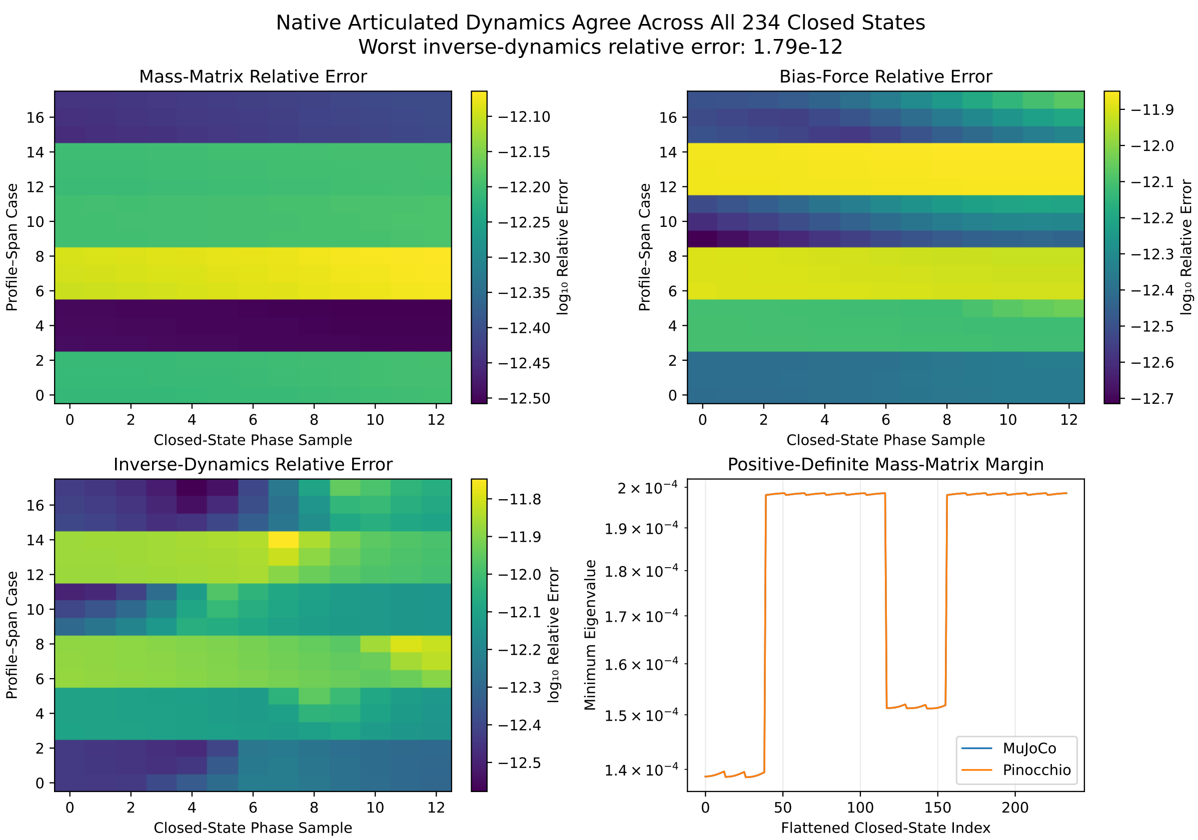

Figure 17.8: Native Articulated Dynamics Across All Closed States

All 234 states pass the preregistered mass-matrix, bias-force, inverse-dynamics, symmetry, and positive-definiteness gates. The largest relative mass-matrix error is 8.62×10^{-13}, the largest relative bias error is 1.41×10^{-12}, and the largest relative inverse-dynamics error is 1.79×10^{-12}. The largest symmetry residual is zero at stored precision, and the smallest native mass-matrix eigenvalue is 1.386×10^{-4}.

An independent release requalification audited the storage contract behind these results. Pinocchio's CRBA operator guarantees the upper triangle of the returned mass matrix, so the project adapter now copies that triangle into independent storage and mirrors it explicitly before any solve or comparison. The six directly affected evidence families were then regenerated twice from clean snapshots in a single-worker Linux environment with MuJoCo 3.8.0 and robotics Pinocchio 3.8.0. All JSON records, every typed NPZ member, all eleven vector figures, and the reconciled claim registry reproduced exactly. A new semantic gate also detected and repaired two stale reciprocal review links; the reconciliation changed no claim statement, classification, or adjudication outcome. The machine-readable requalification report records the execution identity, distribution hashes, thread limits, artifact hashes, array schemas, and inference boundary. This is reproducibility and internal-consistency evidence, not human or anatomical validation.

This closes an engine-transport question, not the articulated-contact question. The common-state comparison applies no bilateral contact, advances no forward trajectory, and adds no scapulothoracic glide, forearm pronation–supination, multi-axis wrist, fingers, distributed grip, flexible shaft, ground contact, or muscle model. Consequently it cannot establish anatomical validity, passive human transfer, timing demand, slack benefit, or a coaching strategy. It provides a qualified inertial foundation for the next forward-contact falsifier.

17.6.2.3 Independent Manufactured-Solution and Conservation Controls

Cross-engine agreement alone can remain circular if both reported paths call the same operator, and an inverse-dynamics residual is vacuous if the applied torque is checked against the equation that defined it. The articulated verification tier therefore assigns three distinct authorities. The manufactured generalized torque is defined by the analytical Lagrange–Christoffel implementation; MuJoCo evaluates the same state with `mj_inverse`; and robotics Pinocchio evaluates it with `rnea`. An explicit killswitch adds 10 N · m to the MuJoCo result and must make the gate fail.

For the registered closed state, the maximum relative discrepancies are 3.09×10^{-11} for Lagrange–MuJoCo, 3.07×10^{-11} for Lagrange–Pinocchio, and 3.54×10^{-13} for MuJoCo–Pinocchio. These small but nonzero values replace a former self-comparison that was zero by definition. Semi-implicit Euler is evaluated at 2.0, 1.0, and 0.5 ms; adjacent three-level Richardson estimates are 1.0011 and 1.0007, inside the registered first-order interval of 0.9–1.1.

Momentum is assessed in a separate gravity-free, zero-torque rollout. Because the pelvis branch is world-supported, exciting it would introduce support reactions and make total momentum an invalid invariant. The conservation control therefore excites only the genuinely free-floating club subtree. Over 10 ms, relative drift is 1.01×10^{-6} for linear momentum, 1.51×10^{-6} for angular momentum, and 8.67×10^{-7} for kinetic energy. These are measured integration errors rather than stored constants.

The constrained control coordinates pelvis yaw with the three club translations so that one declared lead-hand-to-grip point constraint is satisfied throughout the manufactured trajectory. The imposed three-component multiplier is then recovered independently from each native inverse-dynamics result. This control does not test simultaneous two-hand closure. The maximum relative multiplier, cross-engine multiplier, and equilibrium residuals are 3.39×10^{-13}, 3.25×10^{-13}, and 5.51×10^{-13}, respectively. Position, velocity, and virtual-power residuals are exact zeros for this analytically coordinated trajectory; they are reported as identities, not treated as independent evidence.

The machine-readable record is `articulated_manufactured_solution.json`. These controls verify the declared numerical operators and first-order integration behavior. They do not validate the manufactured motion as a human swing, identify biological torque, or support a coaching prescription.

17.6.2.4 Native Constraint and Integrator Discrepancy Control

The transport comparisons below deliberately share a project-authored contact law and state update. A separate control is required before language about a native constraint solver or integrator is justified. The control starts both branches from the same achieved 20-coordinate closed state, translates the club by 1 mm, applies no active generalized drive, and advances 4 ms at 0.5 and 0.25 ms steps. The first branch implements two MuJoCo `equality/connect` constraints, advances with `mj_step`, and records `qfrc_constraint`. The second branch retains the projected bilateral Kelvin–Voigt point-force law, MuJoCo mass-and-bias transport, and the project-authored semi-implicit update. These operators follow the current MuJoCo constraint and simulation interfaces.

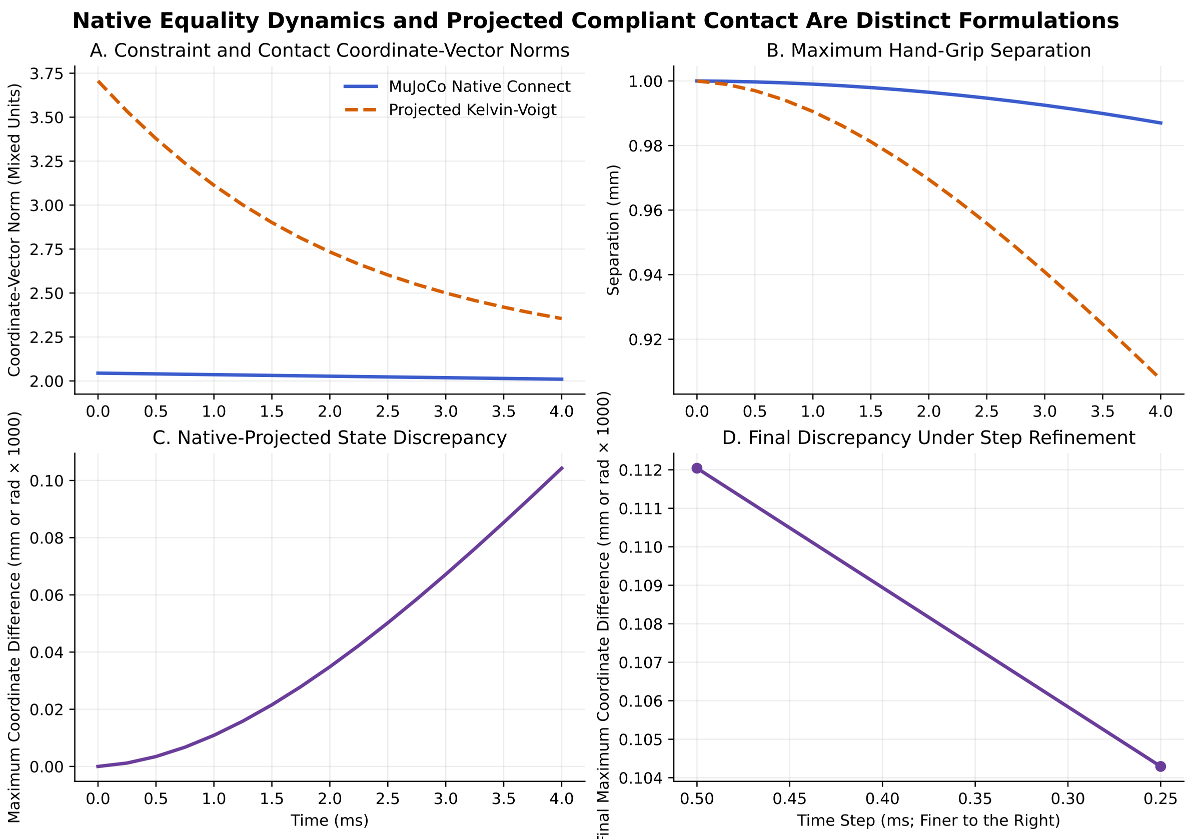

Figure 17.9: Native Equality Dynamics and Projected Compliant Contact Are Distinct Formulations

Both native equalities contribute three scalar rows, so the active native branch exposes at least six constraint rows. Its equality-disabled killswitch returns zero generalized constraint force. At the finer step, the native and projected final hand–grip separations are 0.987 and 0.908 mm, respectively, and their maximum coordinate difference is 1.04×10^{-4} rad in club pitch. The maximum coordinate-vector force norms are 2.045 and 3.706 in mixed generalized units. Those norms are numerical diagnostics only: revolute and prismatic coordinates carry different physical units and the two constraint formulations do not define interchangeable force parameters.

The nonzero discrepancy is the result, not a failed parity target. Applying the same stiffness and damping numerals does not make MuJoCo's regularized equality response physically equivalent to a direct Kelvin–Voigt point-force law. Step refinement reduces the final coordinate discrepancy from 1.12×10^{-4} to 1.04×10^{-4}, so the observed separation is not removed by the tested halving. Two refinement levels do not establish an asymptotic order or continuum limit. This control establishes that a genuine native constraint-and-integrator branch has been executed and that it differs from the projected formulation. It does not validate either contact law, identify anatomical grip mechanics, establish engine equivalence, or support a human-transfer or coaching claim.

17.6.2.5 Articulated Contact Projection and Initial Acceleration

The next gate adds finite bilateral interaction forces without yet advancing a trajectory. At each of the 234 closed states, the club is displaced 1 mm and given 0.05 m/s additional velocity along its world x coordinate. Paired Kelvin–Voigt interfaces with the previously declared 1,800 N/m stiffness and 18 N s/m damping then generate forces from achieved hand–grip displacement and relative velocity. No wrench or direct club actuator is prescribed.

For each hand i, the generalized contact load is

$$Q_c = \sum_i \left(J_{g,i}^{\mathsf{T}} f_i + J_{h,i}^{\mathsf{T}}(-f_i) \right), \tag{17.8}$$

where J_g and J_h are the club-grip and hand-point Jacobians. This form exposes the action–reaction and virtual-power identities directly. MuJoCo and robotics Pinocchio then independently evaluate their native mass and bias operators at the perturbed state and solve $\ddot{q} = M^{-1}(Q_c - h)$. The comparison is therefore an initial-acceleration test of force projection into the qualified articulated tree, not a forward contact simulation.

All 234 states pass. The largest contact force is 2.708 N, the largest zero-preload leakage is 2.08×10^{-7} N, and the largest virtual-power residual is 4.44×10^{-16} W. Damping power is non-positive at every state. Coincident moment arms remove the force couple exactly, reversing both moment arms reverses it exactly, and the largest MuJoCo–Pinocchio generalized initial-acceleration discrepancy is 4.85×10^{-13} relative.

This closes the same-state contact-projection question only. No trajectory is integrated, so contact loss, recovery, numerical stability over time, delivered speed, accumulated work, and late-downswing torque duration remain untested. The interfaces, anatomy, club, and ground pathway remain uncalibrated. It therefore cannot establish passive human transfer, slack benefit, timing economy, or coaching strategy. The next falsifier is bounded integration with contact-loss, adverse-load, refinement, power, and work–energy controls.

17.6.2.6 Bounded Articulated Bilateral-Attachment Forward Dynamics

The forward gate advances eighteen selected closed states spanning all six synthetic profiles, all three grip spans, and three phase samples. Seven registered branches cover nominal parameters, half and double stiffness, half and double damping, reversed initial club velocity, and zero preload. Each branch is advanced for 5 ms at 1.0, 0.5, and 0.25 ms time steps with native MuJoCo and robotics Pinocchio mass and bias operators, producing 756 bounded trajectories. No active joint torque, hand driver, or direct club actuator is applied during the interval.

Each trajectory begins from an achieved closed configuration. The nominal and one-factor branches add the declared 1 mm club displacement and 0.05 m/s club velocity perturbations before evaluating the same two

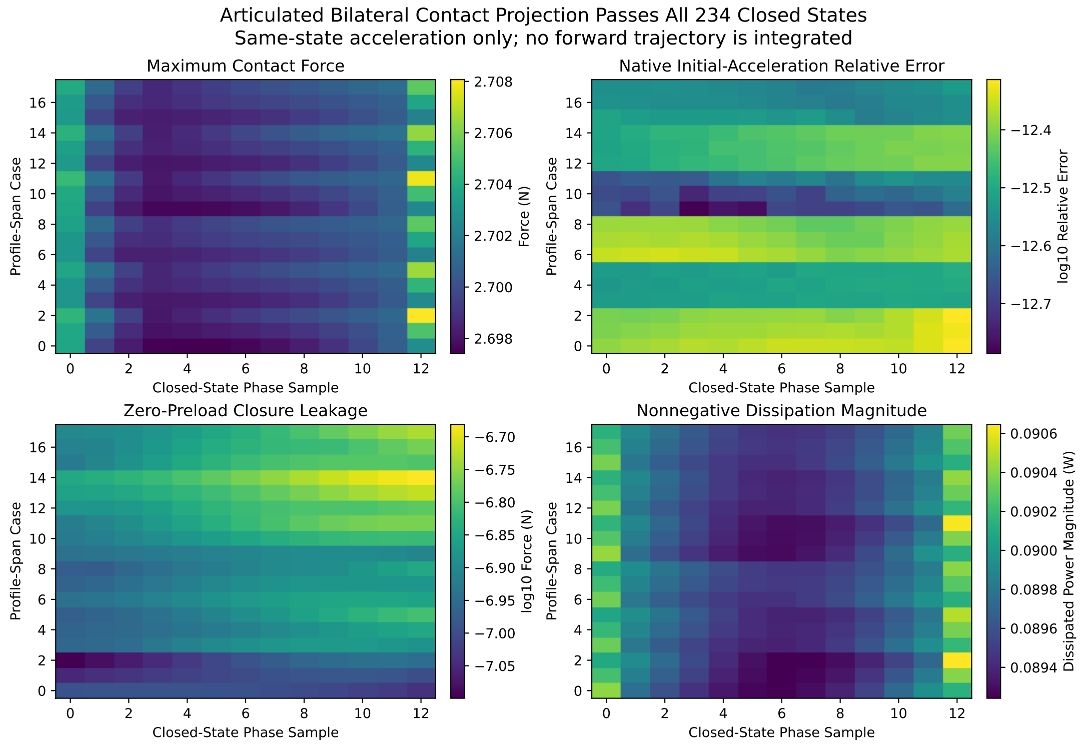

Figure 17.10: Articulated Contact Projection and Initial Acceleration Across All Closed States

bilateral Kelvin–Voigt attachments. These are tensile-and-compressive attachment springs, not unilateral collision contacts. "Retention" therefore means that attachment separation stays below a predeclared 10 mm numerical screening threshold; it does not mean that anatomical grip contact, tissue preload, or slack has been identified.

The mechanical ledger adds native rigid-body kinetic and gravitational potential energy to the two attachment strain energies,

$$E = T + V_g + \sum_i \frac{1}{2} k \|d_i\|^2, \qquad R_E(t) = E(t) - E(0) - \int_0^t P_d \, dt, \tag{17.9}$$

where $P_d \leq 0$ is the declared damping power. Semi-implicit Euler advances the common coordinates, while each engine independently evaluates its mass and bias operators at every step. The registered gates cover the 10 mm attachment threshold, action–reaction virtual power, non-positive damping, normalized work–energy residual below 0.02, monotone refinement with a fine-to-coarse ratio below 0.8, and inertia-and-bias transport trajectory and force-history differences below 10^{-7} relative.

All registered five-millisecond trajectories pass. The largest attachment separation is 1.229 mm and the largest contact force is 17.761 N. The worst normalized work–energy residual decreases from 0.00738 to 0.00170 and then 0.000854 as the step is halved. The largest virtual-power residual is 3.55×10^{-15} W; damping power remains negative; and the largest MuJoCo–Pinocchio inertia-and-bias transport trajectory and force-history discrepancies are 1.53×10^{-14} and 1.34×10^{-11} relative, respectively.

This is a right-censored synthetic result: no registered failure occurs before 5 ms, but persistence later in the downswing or through impact is not tested. The result does not model unilateral slack, distributed grip pressure, shaft bending or torsion, ground coupling, calibrated anatomy, muscle action, or participant-specific control. It therefore cannot establish passive human transfer, timing economy, a benefit of avoiding slack,

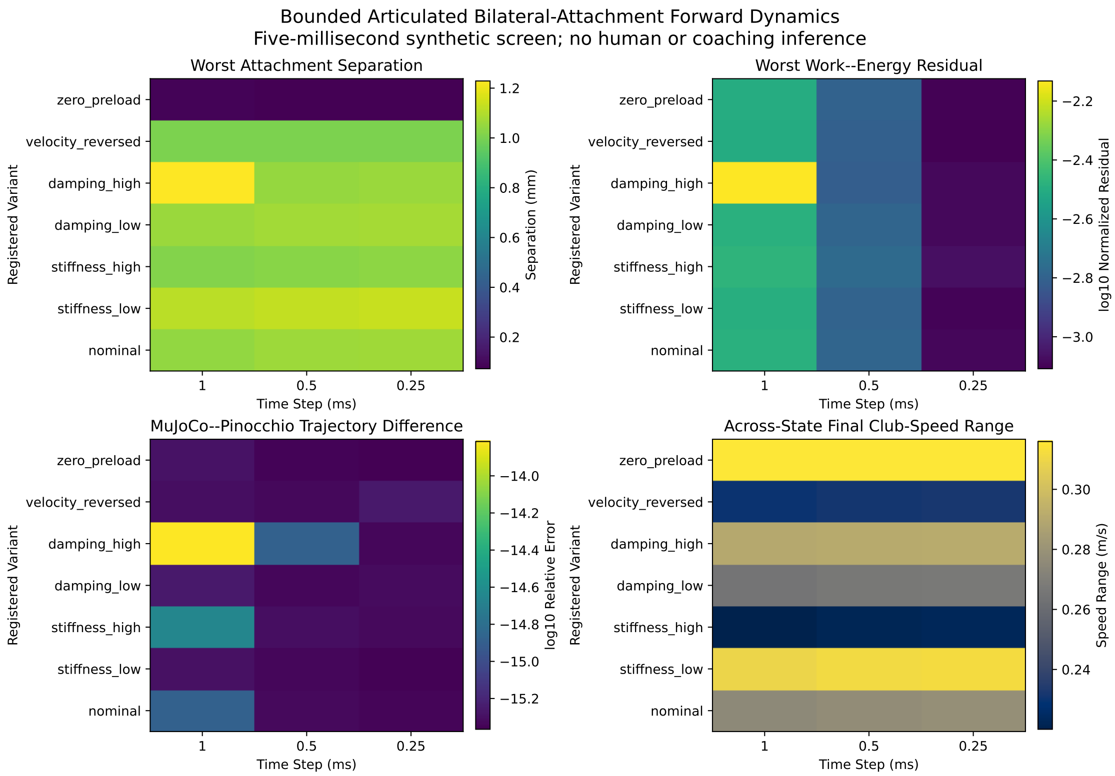

Figure 17.11: Bounded Articulated Bilateral-Attachment Forward Dynamics Across Registered States and Controls

or a coaching strategy. Those questions require longer typed-slack trajectories and the governed bilateral six-axis grip-wrench data identified in the human protocol.

17.6.2.7 Typed Unilateral Slack and Reattachment Falsification

The next gate replaces the ambiguous word *slack* with three explicit passive constitutive classes. The bilateral comparator retains the vector Kelvin–Voigt law above. The tension-only law acts along the instantaneous hand–grip separation direction, and the dead-zone law adds a declared free length s. For separation magnitude r, radial extension $e = \max(r - s, 0)$, radial rate $\dot{e}$, and direction n, the unilateral law is

$$f = \begin{cases} [ke + c\max(\dot{e}, 0)]\, n, & e > 0, \\ 0, & e = 0. \end{cases} \tag{17.10}$$

The loading-only damper is a declared modeling choice: it prevents a damper from creating compressive force during unloading and retains the non-positive dissipation identity $P_d = -c\max(\dot{e}, 0)\dot{e} \le 0$. It is not a tissue model. An open interface transmits exactly zero force, while equal-and-opposite active-interface forces are projected through the same hand and grip Jacobians as the bilateral gate.

The atlas evaluates eighteen articulated states across four law settings (bilateral, tension-only, and 0.5 and 1.5 mm dead zones), two preload controls, and both signs of the initial club-velocity perturbation. The common-displacement control applies 1 mm to every law. The matched-extension control adds the dead-zone width to that displacement, making the initial radial spring energy approximately equal to the bilateral/tension-only value. This distinction prevents a change in preload energy from being silently called a slack effect. Two separate zero-background-velocity probes cross the 1.5 mm boundary in opposite directions; they verify opening and reattachment logic but are not natural-state predictions. Three time steps and two native engines yield 1,944 five-millisecond trajectories.

All numerical and inertia-and-bias transport gates pass. Across the complete atlas, the largest force is 23.643 N, virtual-power residual is 2.13×10^{-14} W, and positive damping-power maximum is zero. The worst normalized work–energy residual decreases from 0.01923 to 0.01097 and then 0.00480 under refinement. Maximum trajectory and force-history differences between MuJoCo and Pinocchio are 1.32×10^{-15} and 1.82×10^{-12} relative, with no active-set parity failure.

The natural-state branches produce no opening or reattachment transition in 5 ms. The 1.5 mm dead-zone/common-displacement branch remains open throughout, whereas the matched-extension branch remains taut; this is direct evidence that law choice and preload matching can reverse the contact classification without changing the articulated state authority. The boundary probes produce 108 opening-cell and 216 reattachment-cell observations, with at most two active-set transitions. These event counts qualify the implementation only.

The result therefore falsifies any claim that a scalar label such as "slack" has a unique model consequence. It does not show that slack is beneficial, necessary, intentional, self-correcting, or less timing-sensitive. Natural events remain right-censored at 5 ms, and the laws have no calibrated tissue, friction, distributed grip pressure, shaft compliance, ground coupling, or human wrench data. Longer distributed-contact trajectories and the governed participant protocol remain necessary before a delivery or coaching inference.

17.6.2.8 Distributed Grip Friction and Contact Events Across Nested Horizons

The next gate isolates contact discretization before admitting shaft or ground degrees of freedom. Each hand receives $N \in \{1, 3, 5\}$ tension fibers across a declared 30 mm grip-axis width. Fiber j has free length $\ell_{0j} = \|d_j(q_0)\|$ at the unperturbed closed state and

$$e_j = \max(\|d_j\| - \ell_{0j}, 0), \qquad k_j = \frac{k_{\text{grip}}}{N}, \qquad c_j = \frac{c_{\text{grip}}}{N}. \tag{17.11}$$

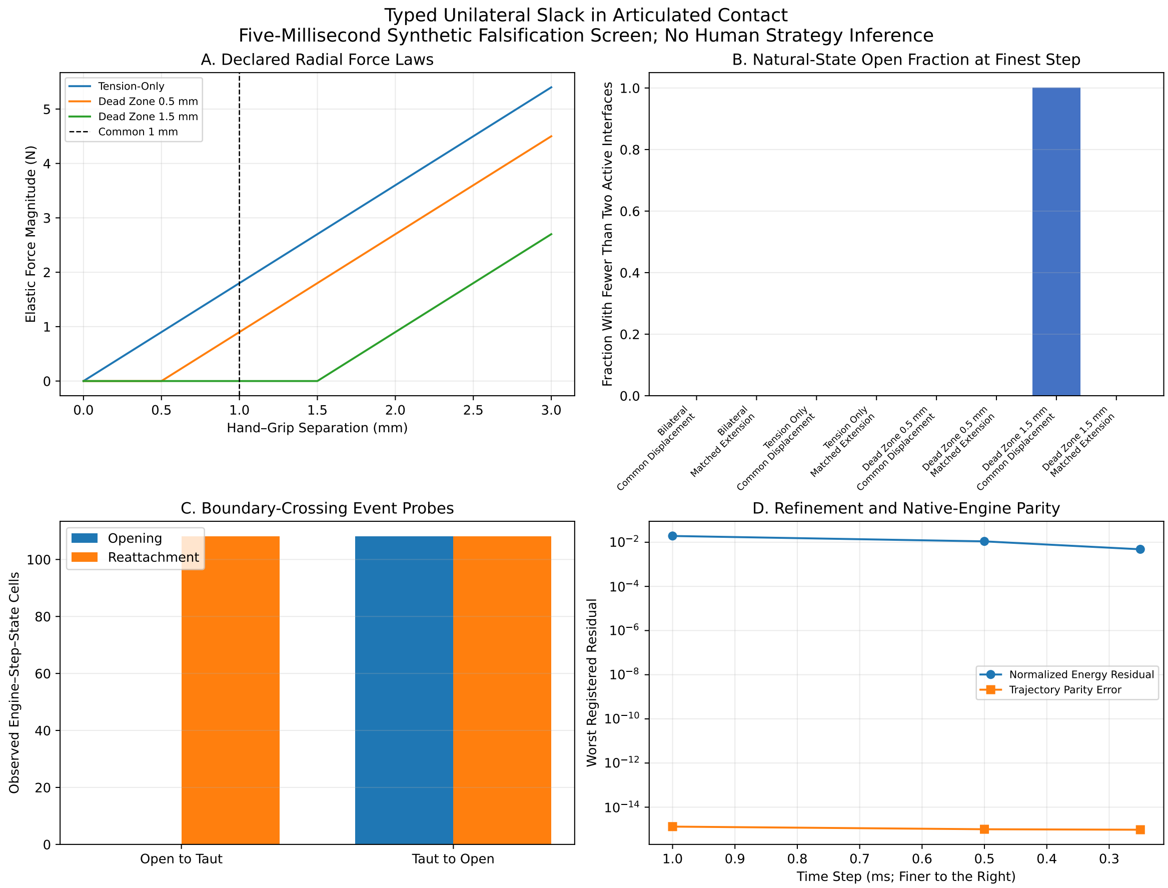

Figure 17.12: Typed Unilateral Slack and Reattachment Across Natural-State and Boundary-Crossing Controls

The frictionless comparator sets $\mu = 0$. The finite comparator uses the equipment-provisional bound $\mu = 0.35$ and a memoryless tangential damper,

$$v_{tj} = v_j - (\hat{d}_j^{\mathsf{T}} v_j)\hat{d}_j, \qquad F_{tj} = \min\Big(\frac{c_t}{N}\|v_{tj}\|, \mu\|F_{nj}\|\Big)\,\frac{v_{tj}}{\|v_{tj}\|}. \tag{17.12}$$

The force on the club follows the relative sliding velocity so that interface power is nonpositive. This is a bounded regularized Coulomb comparator, not a static-friction, bristle, hysteresis, measured-tissue, or perfect-stick law.

An instantaneous perfect-stick control supplies a deliberately different upper bound. For the active fibers, let J_t stack two orthonormal tangential velocity rows per station and let M be the native engine mass matrix. The minimum kinetic-energy change that removes the registered tangential velocity is the mass-metric projection

$$\dot{q}^{+} = \dot{q}^{-} - M^{-1}J_t^{\mathsf{T}}\lambda, \qquad \lambda = (J_t M^{-1} J_t^{\mathsf{T}})^{+} J_t \dot{q}^{-}, \tag{17.13}$$

where $(\cdot)^{+}$ is the Moore–Penrose inverse. The captured kinetic energy is $\Delta K = \frac{1}{2}\dot{q}^{-\mathsf{T}}M\dot{q}^{-} - \frac{1}{2}\dot{q}^{+\mathsf{T}}M\dot{q}^{+} \geq 0$. This is an impulsive, single-state constraint bound. It does not assert that static friction can supply λ, determine subsequent contact evolution, or represent tissue. The numerical implementation factors $M = LL^{\mathsf{T}}$ and applies a rank-revealing singular-value decomposition to $J_t L^{-\mathsf{T}}$. This is algebraically the same mass-metric projection, but it does not form the normal-equation matrix $J_t M^{-1} J_t^{\mathsf{T}}$, whose condition number is squared when distributed station rows are redundant. The registered residual therefore tests the independent constraint row space rather than numerical agreement obtained by relaxing the no-slip tolerance.

Thus station count does not silently multiply total grip stiffness or damping, and finite off-axis reference length does not become hidden preload. Closure residuals below 10^{-8} m are treated as zero; the one-fiber configuration then reproduces the point tension law and its forward trajectory. Every fiber retains equal-and-opposite force, loading-only damping, strain energy, active state, and virtual-power accounting. Replacing all realized application points by their midpoint removes the force couple exactly, while reversing all moment arms reverses it exactly without changing the realized forces.

The atlas selects twelve states spanning four profile–grip cases and three phase samples. The complete registered generalized velocity and the added club perturbation are reversed together. Crossing that control with one-, three-, and five-fiber grips, $\mu \in \{0, 0.35\}$, 1.0 and 0.5 ms steps, and native MuJoCo and Pinocchio produces 576 trajectories. Each trajectory is advanced once to 50 ms and summarized at nested 4, 10, 25, and 50 ms horizons, yielding 2,304 engine–horizon summaries without resetting the state. A separate 24-trajectory dead-zone probe crosses station count, friction bound, step, and engine. No active joint torque, hand driver, or direct club actuation is applied. A separate 144-cell stick projection crosses the twelve states, three station counts, complete velocity reversal, and both native mass matrices.

All registered numerical and native-engine gates pass. The largest station force is 4.021 N and the largest force couple is 0.434 N m. Coincident and reversed-moment-arm residuals are exactly zero; the largest virtual-power residual is 1.44×10^{-15} W and positive damping power is zero. The worst normalized work–energy residual decreases from 0.03346 to 0.01673 when the step is halved. The largest genuine MuJoCo–Pinocchio trajectory and station-force discrepancies are 3.84×10^{-13} and 1.44×10^{-10} relative, respectively, with no nominal or event active-set parity failure. At the fine step, the largest three-to-five-fiber state discrepancy is 0.00300 relative; the one-to-three discrepancy is 0.04188.

The active-set and friction results are structural rather than benefit results. No nominal active-set transition occurs, so natural opening or reattachment remains right-censored through 50 ms. The dead-zone probes record 80 opening and 186 reattachment station events, with at most 21 transitions in one trajectory and exact engine agreement. Those probes begin fully disengaged; they qualify event direction and repeated active-set handling, but not an attached-to-open first-failure experiment. At 50 ms, finite-friction minus frictionless speed differences range from -0.0483 to +0.0462 m/s, with a median of +0.00056 m/s. Mixed signs reject a universal finite-friction speed benefit in this unmatched synthetic matrix.

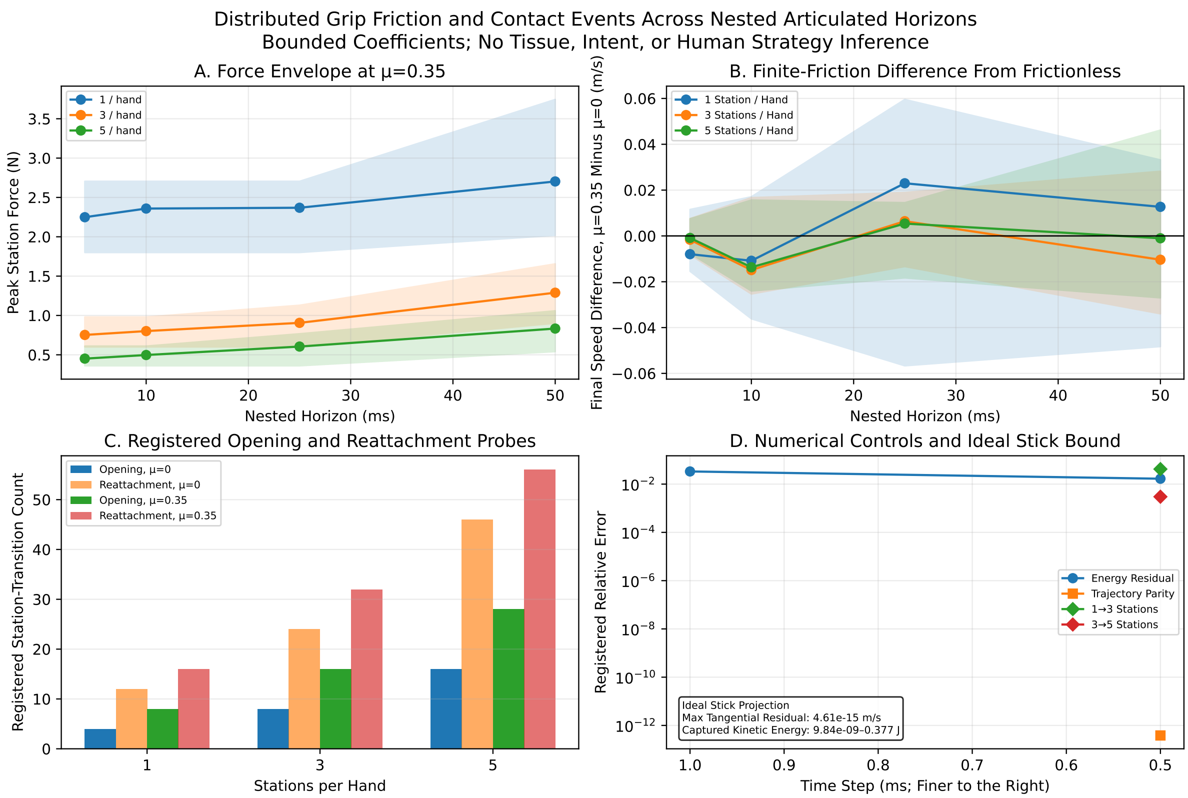

Figure 17.13: Distributed Grip Friction and Contact Events Across Nested Articulated Horizons

The perfect-stick control removes registered active-station tangential velocity to at most 4.61×10^{-15} m/s. The largest genuine MuJoCo–Pinocchio projected-velocity discrepancy is 3.99×10^{-12} relative, with identical active sets. The instantaneous captured kinetic energy ranges from 9.84×10^{-9} to 0.37665 J across the registered matrix. These values bound the kinetic change for an ideal sticking impulse at each sampled state; they are not predictions of realizable grip work or evidence that sticking improves delivery.

The fibers remain memoryless engineering lines rather than calibrated pressure, fingers, tissue, or measured grip mechanics. The club is rigid and the support pathway is unchanged. An attached-to-open event probe, static-friction feasibility and subsequent stick–slip evolution, matched delivery, shaft/ground coupling, and governed human measurements remain required before equipment, timing, or strategy inference.

17.6.2.9 Passive Shaft Bending and Torsion Under Distributed Grip Loading

The next intervention admits shaft compliance while holding the articulated state authority, five-fiber grip law, initial perturbation, and support pathway fixed. The active elastic coordinates are two orthogonal tip-normalized bending deflections and a tip twist,

$$\eta = [\eta_x, \eta_y, \phi]^\mathsf{T}, \qquad \mathcal{M}(q) = \begin{bmatrix} M_r(q) & C_{r\eta}(q) \\ C_{r\eta}^\mathsf{T}(q) & M_\eta \end{bmatrix}. \tag{17.14}$$

Here M_r is assembled independently by native MuJoCo or Pinocchio. $C_{r\eta}$ and M_η are formed from the same shaft and clubhead body linear/angular Jacobians used by the rigid tree, evaluated against the elastic mode velocities. Configuration derivatives of this added mass block supply its Christoffel bias. The passive elastic force is

$$Q_\eta = -K_\eta \eta - D_\eta \dot{\eta}, \qquad U_\eta = \tfrac{1}{2}\eta^\mathsf{T} K_\eta \eta, \qquad P_D = -\dot{\eta}^\mathsf{T} D_\eta \dot{\eta} \le 0. \tag{17.15}$$

A first-order gravitational deflection term is included in the augmented potential. The work–energy ledger therefore contains rigid mechanical energy, rigid–elastic kinetic coupling, shaft strain, deflection gravity, grip strain, grip damping, and shaft damping. There is no shaft actuator, wrist torque, hand driver, or direct club torque. Selecting the rigid branch removes all elastic coordinates and delegates exactly to the previously qualified distributed-grip integrator.

The bending basis is not refitted in this experiment. A hash-checked frozen artifact carries the first mode of the existing 24-element Euler–Bernoulli authority into the lean native-engine runtime. Its frequency is 5.2399 Hz. A tip-normalized stiffness is reconstructed with the articulated shaft/head inertia so that the reduced coordinate retains that frequency. The torsional stiffness follows the compliance integral of the same tapered hollow section, $k_\phi = [\int_0^L (GJ)^{-1}\, ds]^{-1}$ with $G = E/[2(1+\nu)]$ and $\nu = 0.30$, giving 70.1260 Hz. Both modes use a declared damping ratio of 0.018. These are synthetic structural references, not measured properties of a golf shaft. The separate six-mode beam authority also remains decisive: its one-mode RMS discrepancy is 6.87×10^{-7} m under the slow pulse but 4.13×10^{-5} m under the short pulse. High-frequency conclusions therefore cannot inherit first-mode adequacy from the slow-loading result.

The registered atlas crosses twelve articulated states, rigid/bending-only/ torsion-only/coupled shaft branches, two initial club-velocity signs, 0.25 and 0.125 ms steps, and both native engines. The 384 trajectories are each advanced once to 50 ms and summarized at nested 4, 10, 25, and 50 ms horizons. All branches begin at zero elastic displacement and velocity; their initial total-energy range is exactly zero. Two deliberately coarser probes fail the declared linear-domain gate: a 1.0 ms torsion trace at state $(0, 0)$ with the negative velocity sign and a 0.50 ms trace at state $(8, 0)$ with the positive sign. They are retained as excluded negative controls. For the latter state, 0.25, 0.125, and 0.0625 ms maximum absolute work–energy residuals halve from 0.00776 to 0.00390 to 0.00195 J while remaining bounded through 50 ms; the registered matrix uses the first two bounded steps.

All fine-grid numerical and native-engine gates pass. Maximum tip bending is 1.696 mm, maximum twist is 0.001855 rad, and peak shaft strain energy is 3.33×10^{-4} J; every cell remains within the declared 5%

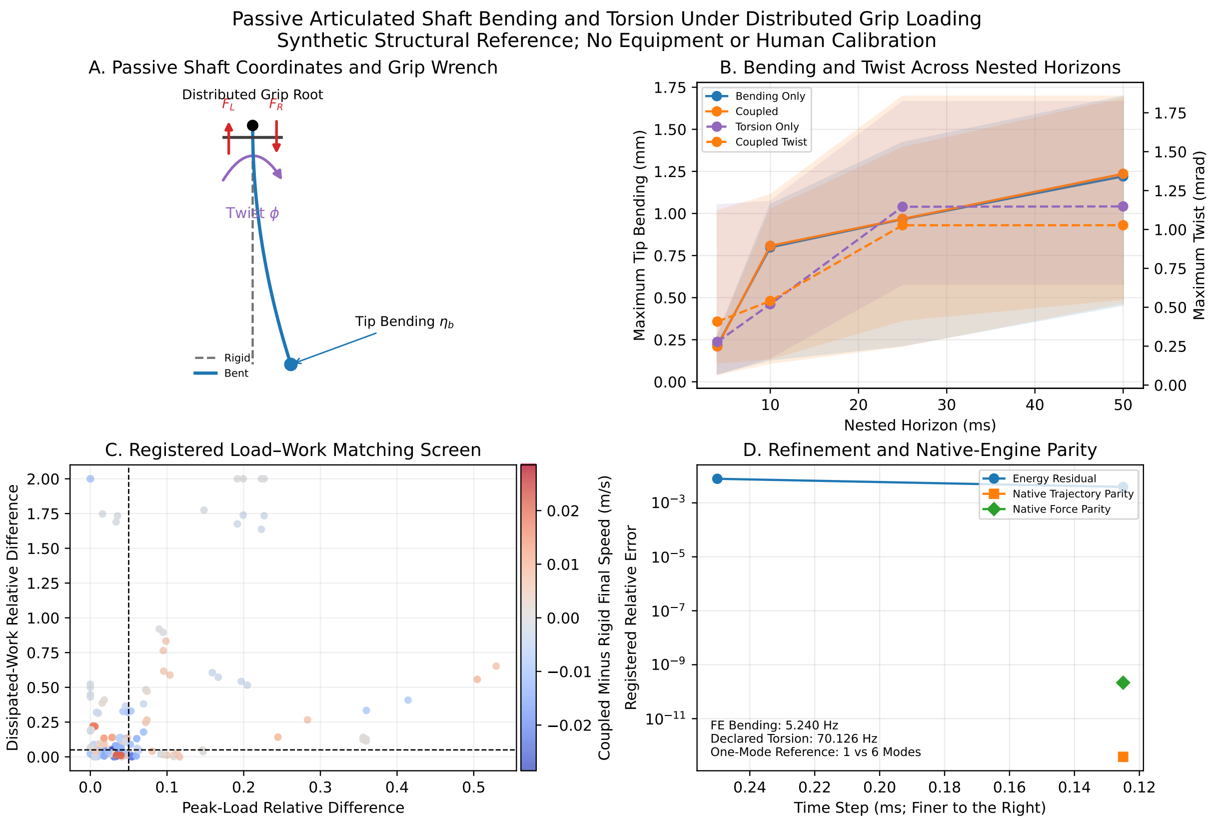

Figure 17.14: Passive Articulated Shaft Bending and Torsion Under Distributed Grip Loading

deflection and 10-degree twist bounds. The largest station force is 1.621 N and the largest grip-force couple is 0.340 N m. The worst normalized work–energy residual decreases from 0.007798 to 0.003900. Maximum MuJoCo–Pinocchio trajectory and station-force errors are 3.84×10^{-13} and 2.15×10^{-10} relative, with no active-set parity failure. Bending, torsion, and both coupled coordinates are independently excited, while their killswitch branches contain only the declared coordinates.

The shaft comparison is intentionally screened against load and work rather than ranked from unmatched speeds. A coupled and rigid cell is called matched only when both peak station load and cumulative dissipated work differ by no more than 5% symmetrically. This admits 126 of 384 possible comparisons. The coupled-minus-rigid final translation-speed difference spans −0.0285 to +0.0212 m/s: 82 matched cells are negative and 44 are positive. Thus passive shaft storage and return can change a delivery proxy in this model, but its sign depends on state, velocity branch, horizon, and load/work selection. The atlas falsifies a universal speed benefit just as directly as it demonstrates a mechanically active elastic pathway. Post-registered matching is descriptive, not randomized or causal, and it does not determine an optimal human shaft or action.

At this shaft-only tier, the contact fibers remain frictionless, memoryless engineering lines with state-registered free lengths, and ground reaction and free moment are absent. Shaft deformation does not establish tissue loading, timing economy, impact performance, or coaching strategy. The finite-base extension below retains the same initial-energy, matched-load/work, killswitch, reversal, power, refinement, and two-engine controls.

17.6.2.10 Articulated Same-State Drift and Contact Attribution

The contact-projection gate establishes that bilateral contact forces enter the articulated equations consistently, but it does not identify how much of the resulting acceleration is associated with configuration-dependent drift, velocity-dependent bias, contact, or applied input. The next registered gate therefore evaluates all four contributions at exactly the same state. With $h(q, \dot{q})$ denoting native bias, Q_c the bilateral contact generalized force, and τ_a the applied generalized input,

$$\begin{aligned}
\ddot{q}_{\text{configuration}} &= M^{-1}[-h(q,0)], \\
\ddot{q}_{\text{velocity}} &= M^{-1}\{-h(q,\dot{q}) + h(q,0)\}, \\
\ddot{q}_{\text{contact}} &= M^{-1}Q_c, \\
\ddot{q}_{\text{active}} &= M^{-1}\tau_a, \\
\ddot{q} &= \sum_i \ddot{q}_i.
\end{aligned} \tag{17.16}$$

The baseline sets $\tau_a = 0$ exactly. “Configuration” is an operational name for $-h(q, 0)$, not a claim that gravity is the only configuration-dependent effect in every formulation. “Velocity” is the finite native bias difference $-[h(q, \dot{q}) - h(q, 0)]$, so it includes all velocity-dependent terms returned by the engine rather than a manually selected Coriolis term. This distinction keeps the decomposition reproducible across the two native operators.

Two complementary signed observables are reported. The mass-metric acceleration projection is

$$s_i^{(a)} = \frac{\ddot{q}_i^{\mathsf{T}} M \ddot{q}}{\ddot{q}^{\mathsf{T}} M \ddot{q}}, \tag{17.17}$$

and the generalized-power contribution is $P_i = Q_i^{\mathsf{T}} \dot{q}$, with a signed power share reported only when the total-power denominator is adequate. These are algebraic projections at one state. They are not fractions of stored energy, impulse, accumulated work, anatomical effort, or clubhead-speed gain. They can be negative or exceed one when contributions cancel; the release therefore also records denominator suppression and cancellation indexes.

The atlas reuses the six synthetic subject profiles, three grip spans, and thirteen closed states per case, for 234 states and twenty generalized coordinates. Each state receives the declared 1 mm club-translation and 0.05 m/s club-velocity perturbation. MuJoCo 3.12.0 and Pinocchio 4.1.0 evaluate the mass, bias, contact, and acceleration operators independently; no forward step is taken. Zero-contact, zero-velocity, gravity-off, coincident/reversed moment-arm, coordinate-rescaling, and deliberately corrupted-force controls are all registered before interpreting the attribution.

All registered gates pass. The maximum acceleration closure residual is 7.65×10^{-13} and the maximum power closure residual is 2.13×10^{-14} W. The worst cross-engine contribution discrepancy is 3.91×10^{-12} relative, while coordinate rescaling changes physical power by at most 1.42×10^{-14} W and a reported share by at most 1.22×10^{-15}. Each pathway killswitch collapses its intended contribution exactly, and the corrupted-force sentinel exceeds its detection floor.

Across both engines, the configuration term supplies 75.5–91.0% of the mass-metric total-acceleration projection, contact supplies 9.41–23.5%, and the velocity-dependent term spans -2.79–1.08%; the active-input contribution is identically zero. The sign of the velocity projection is mixed across the atlas. More importantly, the contact acceleration projection is positive in every state while contact generalized power is negative in every state, spanning -0.2713 to -0.2685 W. Total generalized power is also negative. Thus positive alignment with the total acceleration does not imply positive work, energy transfer, or a speed benefit. The two observables answer different questions and cannot be substituted for one another.

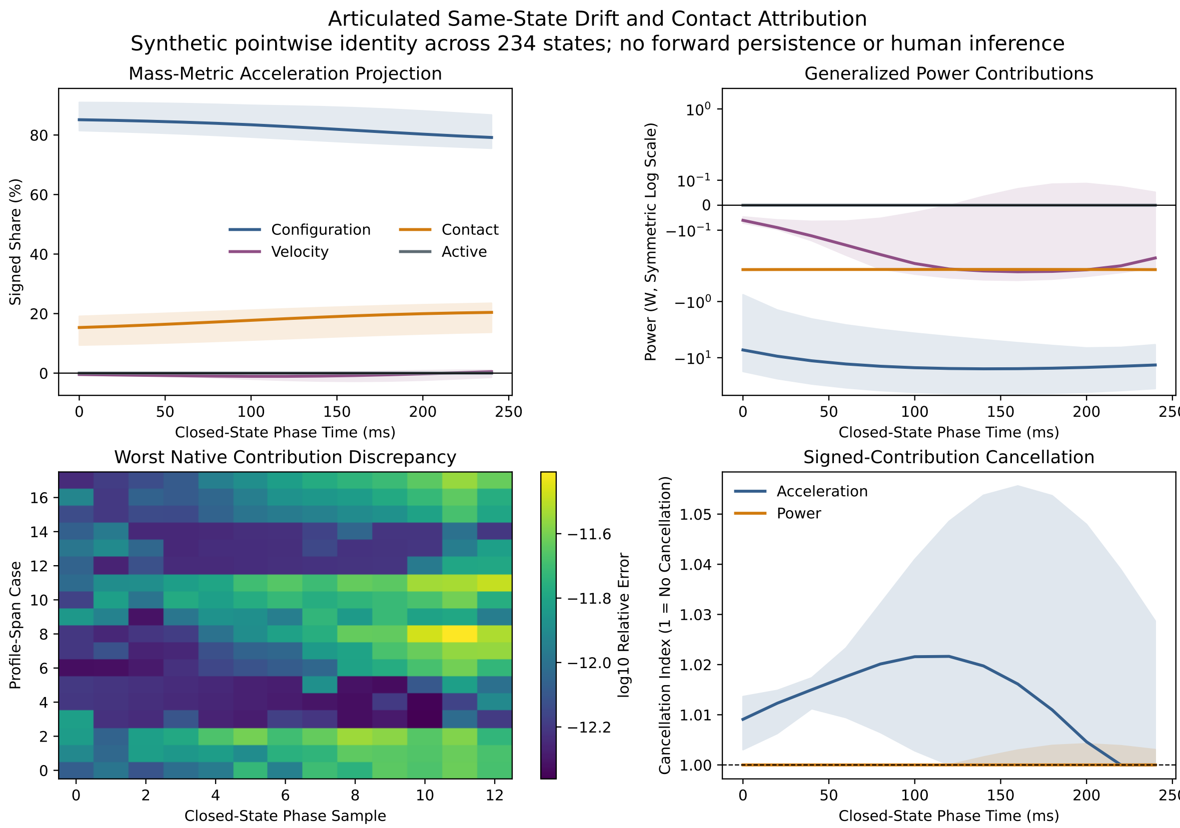

Figure 17.15: Articulated Same-State Drift and Contact Attribution

The machine-readable JSON summary and NPZ arrays retain every state, engine, contribution, denominator, control, and gate. This result is a pointwise synthetic mechanics attribution under an imposed perturbation. It does not establish persistence through contact transitions, accumulated impulse or work, zero-velocity constraint force, biological torque or effort, human transfer, slack management, timing economy, coaching strategy, or safety. The next falsification gate is a matched forward attribution of impulse and work through contact transitions, shaft/base coupling, uncertainty, and adverse loading.

17.6.2.11 Finite Ground Reaction and Intrinsic Free Moment

The finite-base extension supplies that separate transport gate. Three planar coordinates translate the articulated human tree in world x and z and rotate it about world y,

$$b = [x_b, z_b, \theta_b]^\mathsf{T}, \qquad \mathcal{M}_g(q) = \begin{bmatrix} M_{r\eta}(q) & C_{r\eta,b}(q) \\ C_{r\eta,b}^\mathsf{T}(q) & M_b(q) \end{bmatrix}. \tag{17.18}$$

Only the non-club body tree receives this common base transformation. The club remains independently rooted and is connected to the moving hands through the same distributed grip fibers. The cross block is assembled from every non-club body's translational and angular Jacobians. Its configuration derivatives contribute the associated Christoffel bias; base translation and rotation also enter gravity and the distributed-contact Jacobians. Thus the finite base changes inertia, gravity, hand geometry, grip reaction, and power simultaneously rather than adding a prescribed force to a fixed posture.

The synthetic passive support law is

$$Q_b = -K_b b - D_b \dot{b}, \qquad U_b = \tfrac{1}{2} b^\mathsf{T} K_b b, \qquad P_{D,b} = -\dot{b}^\mathsf{T} D_b \dot{b} \le 0. \tag{17.19}$$

Its first two generalized components form the ground-on-body force $F_g = [Q_x, 0, Q_z]^\mathsf{T}$ and the third is the intrinsic free moment $M_y = Q_\theta$. A moment reported about a different reference point is $M_y^{(O)} = M_y + r_z F_x - r_x F_z$. Reversing the declared center-of-pressure reference therefore changes the transported moment but not F_g, M_y, the generalized force, or the trajectory. This distinction prevents a reference-transport term from being misidentified as an additional physical torque.

Four exact pathway selections are retained: fixed base; translation only; intrinsic free moment only; and coupled translation plus free moment. The fixed selection has no base coordinate and delegates bit for bit to the qualified shaft solver. Two independent controls accompany the coupled selection. One removes every shaft elastic coordinate; the other sets horizontal support stiffness and damping to zero while retaining vertical support and intrinsic free moment. The latter is accurately described as removal of modeled horizontal restraint, not as a complete Coulomb-friction or unilateral foot contact model.

Initialization is a model variable rather than an invisible convenience. A natural-zero base gives identical initial total energy across pathway killswitches, but it is not static equilibrium. A gravity-only displacement balances the support law while ignoring grip preload. A conditional nonlinear solve balances ground, grip, and gravity generalized forces in the three base coordinates with posture and club state held fixed. It does not balance the remaining rigid coordinates and therefore is not whole-mechanism equilibrium. The three choices are retained as separate sensitivity branches; the atlas uses natural zero because it is the only exact common-state killswitch comparison.

The preregistered atlas uses the same twelve articulated states, two signed club-velocity perturbations, 0.25 and 0.125 ms steps, and independent native MuJoCo and Pinocchio operators as the shaft study. Each trajectory advances once to 50 ms and is summarized at 4, 10, 25, and 50 ms. The four primary pathways produce 384 trajectories. Rigid-shaft and horizontal-restraint- removed control families add 192. Every cell records grip force and couple, active fibers, ground force, intrinsic and transported moments, support and shaft strain, damping work, base motion, club speed, virtual-power closure, work–energy closure, declared-domain status, and inertia-and-bias transport parity.

The constitutive values are transparent synthetic references: horizontal and vertical stiffnesses are 15 and 30 kN/m; damping values are 400 and 800 N s/m; free-moment stiffness is 900 N m/rad; and rotational damping is 45 N m s/rad. They have not been fitted to a force plate, pressure map, participant, or golf outcome. Consequently this experiment can identify whether the named pathways are mechanically active and whether their effects survive killswitch, reversal, refinement, and matched-load/work screens. It cannot establish that the values represent a golfer, that a pathway is intentionally controlled, or that a speed difference is beneficial.

The 42-trajectory initialization diagnostic passes every active-set and native- engine comparison. Across seven branches and three decreasing steps, all 14 engine-specific work–energy series decrease monotonically at approximately first order. Maximum trajectory and ground-force relative discrepancies are below 2.5×10^{-12} and 1.1×10^{-10}. The initialization sensitivity is material. On the 0.125 ms grid, natural-zero, gravity-only, and conditional-base starts produce peak ground forces of 32.8, 565.5, and 510.3 N and 4 ms club-translation speeds of 0.264, 1.908, and 0.946 m/s. These are transient synthetic responses, not alternative estimates of a human swing. Their separation shows that an unreported preload convention could dominate a short-horizon comparison.

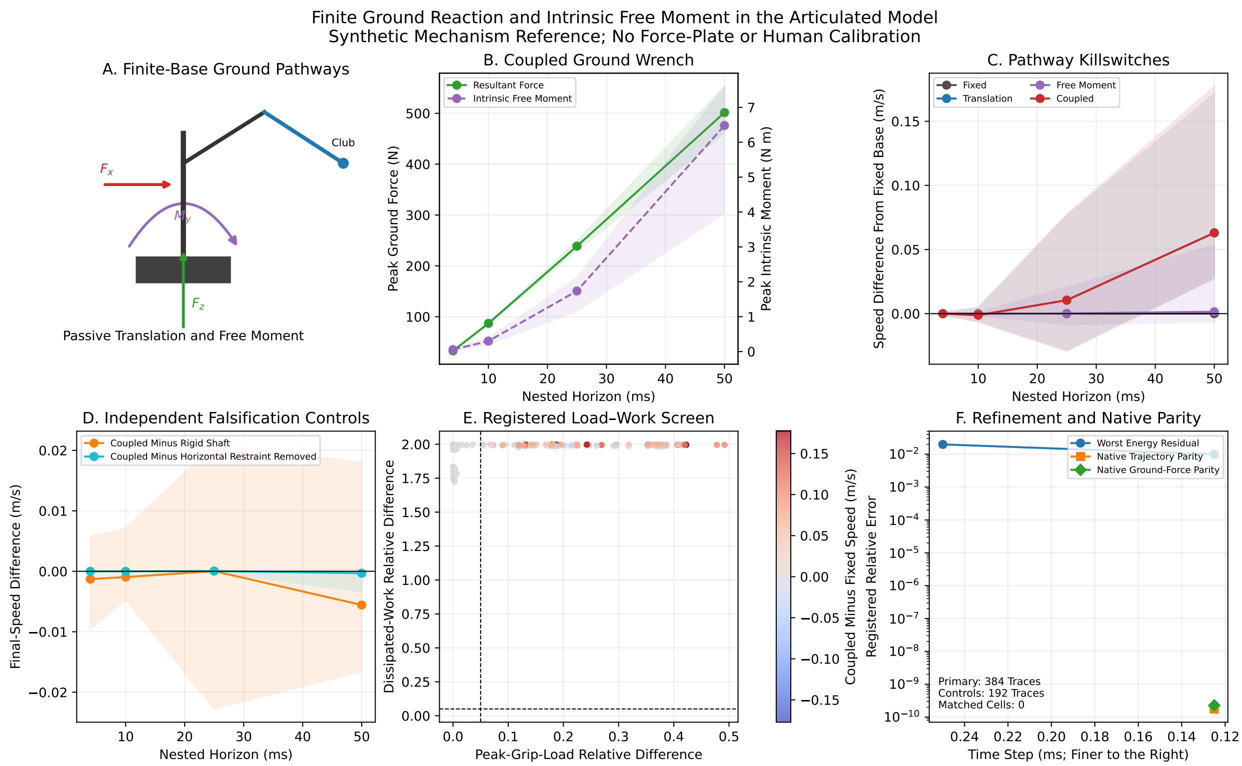

Figure 17.16: Finite Ground Reaction and Intrinsic Free Moment in the Articulated Model

All 576 atlas trajectories remain inside the declared shaft and base domains and pass the numerical and native-engine gates. The worst normalized work– energy residual decreases from 0.01986 at 0.25 ms to 0.00995 at 0.125 ms. Maximum trajectory, grip-force, and ground-force relative discrepancies are 1.77×10^{-10}, 6.41×10^{-10}, and 2.28×10^{-10}, respectively. The largest ground-force resultant is 559.1 N, the largest intrinsic free moment is 14.58 N m, base translation remains below 9.79 mm, and base pitch remains below 0.00548 rad. Maximum shaft bending and twist remain 1.708 mm and 0.001856 rad. These values qualify the declared synthetic computation; they do not calibrate any load magnitude.

The primary load–work screen is adverse. A coupled and fixed cell was preregistered as matched only when both peak grip load and total dissipated work differed by no more than 5%. None of 384 possible comparisons qualifies. The total-work relative difference spans 1.72–2.00 because coupled ground damping contributes a dissipative pathway that fixed base cannot contain; even a 100% tolerance admits no cell. Although every unmatched coupled-minus- fixed 50 ms speed difference is positive on the fine grid, spanning 0.0280– 0.1772 m/s, those values cannot identify a ground-pathway speed effect because the registered work match failed.

A separately labeled post-hoc sensitivity excludes ground damping from the work-matching variable while retaining the peak-grip-load screen. At 5%, 60 cells then qualify: coupled-minus-fixed speed differences include 20 positive and 40 negative values and span -0.00075 to +0.01394 m/s. This alternative cannot replace the primary estimand, but it demonstrates that the sign is not universal once a non-ground dissipation comparison is imposed. Independent controls are likewise mixed at 50 ms: coupled-minus-rigid-shaft differences span -0.0166 to +0.0181 m/s, and coupled-minus-horizontal-restraint-removed differences span -0.00338 to +0.00029 m/s. The finite ground and intrinsic free-moment pathways are mechanically active in this model, but their isolated delivery contribution is not identified by this experiment.

The support is linear and bilateral; it lacks unilateral normal contact, Coulomb friction, segmented feet, measured pressure, and force-plate calibration. The 50 ms horizon excludes impact and most of the downswing. Accordingly Figure 17.16 and its machine-readable evidence support a finite-base software and mechanism qualification with an adverse primary matching result, not a conclusion about ground-use strategy, passive transfer benefit, timing economy, or human clubhead speed.

17.6.3 Paired Scapula-on-Ellipsoid Geometry Screen

The fixed shoulder centers are the next explicit structural intervention. A paired arm-only screen holds the prescribed trunk and club pose fixed and compares the existing fixed centers with four bounded scapular coordinates per side: protraction, elevation, upward rotation, and winging. Protraction and elevation move the shoulder center on a declared thoracic ellipsoid; upward rotation and winging precede the three glenohumeral rotations. The construction is informed by the ellipsoid-constrained OpenSim shoulder complex of Seth et al. (2016), but it is a reduced kinematic surrogate rather than a reproduction of that model.

The screen uses the same six deterministic profiles and three grip spans at 0.00, 0.12, and 0.24 s, yielding 54 paired states. Only the two arms move; the trunk and all six club coordinates remain fixed. The fixed-shoulder problem has eight arm coordinates, whereas the scapular problem has sixteen. The fixed solution is embedded exactly at zero scapular coordinates, so a larger residual in the mobile branch would be a numerical failure rather than a geometric finding.

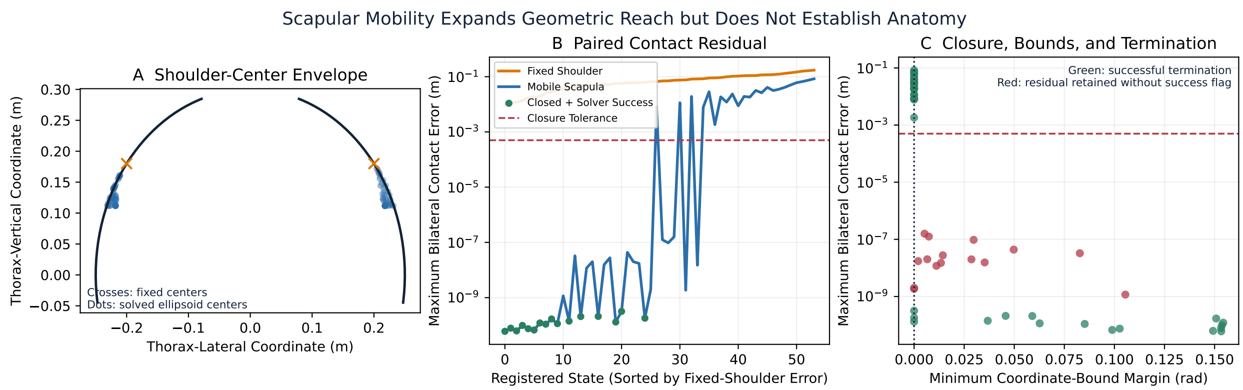

Figure 17.17: Scapular Mobility and Bilateral Contact Geometry

No fixed-shoulder arm-only state reaches the 0.5 mm bilateral tolerance. The mobile-scapula branch reaches that residual in 31 of 54 states, but only 16 of 54 also receive a successful optimizer termination. Twenty-eight states place at least one coordinate on its declared screening bound, and the largest shoulder-center excursion is 0.101 m. The retained 2.0 m adverse grip span still fails, with 0.480 m maximum bilateral error. These counts expose a model-structure effect and a numerical/range boundary; they do not establish that the remaining states are anatomically infeasible.

Both paired contact Jacobians have rank six at every registered state. The fixed branch therefore has a two-dimensional local coordinate null space and the scapular branch has a ten-dimensional null space. Bilateral contact position alone cannot allocate motion uniquely among scapular and glenohumeral coordinates. Adding scapular mobility materially changes the geometric screen while simultaneously increasing allocation non-identifiability.

This result advances the model ladder without identifying a human mechanism. The ellipsoid radii and angular bounds are engineering values, the screen has no subject-specific bone or muscle geometry, and no contact force, power, work, passivity, tissue load, or club-delivery outcome is solved. The decisive next test replaces this surrogate with the independently validated articulated shoulder model, subject-specific anatomy where governed, calibrated grip contact, and paired forward dynamics.

The bounded articulated experiments retain the verified closed-state initialization. Bilateral and typed point-attachment tiers repeat power, work–energy, refinement, adverse-load, event, and engine-parity controls through 5 ms. The distributed extension then preserves total stiffness and damping while advancing one-, three-, and five-fiber tension grips through 50 ms with geometry and station-refinement controls. The separate passive-shaft extension adds first-mode bending and torsion with initial-energy, matched-load/work, refinement, and engine-parity controls; its matched speed differences retain both signs. The finite-base extension now combines those grip and shaft mechanics with planar ground force and intrinsic free moment; its numerical gates pass, but its primary coupled–fixed match is empty. All three tiers still lack calibrated tissue, pressure, friction, unilateral foot contact, and human observations. Only trajectories passing those next gates may test whether drift-mediated transfer reduces timing demand, creates recovery, benefits from slack, or supports a human strategy.

17.7 Falsifiability Gained and Claims Still Open

The executed experiment advances the evidence boundary in three ways.

First, the common spatial wrench is now coupled to a nonplanar reduced full-body inverse-dynamics calculation. The earlier three-dimensional result was only a frame-transformation audit. Here the mass matrix, bias forces, gravity, external generalized loads, and body Jacobians change with a genuine spatial state.

Second, the same model is evaluated through independent algorithms. Agreement therefore tests implementation transport rather than coordinate relabeling. The discovered external-load convention error demonstrates why that test has scientific value: two individually plausible calculations disagreed until the reported estimand was made identical.

Third, the geometry intervention remains exact in the spatial tier. It supports the statement that separated force application points can set club-couple sign independently of total force magnitude.

Four stronger statements remain open:

- **Passive Contact Origin Is Inconclusive.** The hand forces are inputs. A forward compliant two-hand solve must determine whether equivalent loads emerge after a distal command killswitch.
- **Bounded Inertia-and-Bias Transport Does Not Establish Full Contact.** The 5 ms articulated trajectories test divergence, attachment separation, typed unilateral opening and reattachment, power, and energy in two engines. They do not test calibrated distributed grip or shaft mechanics, tissue, friction, late downswing, or impact.
- **Anatomical Magnitude Is Unsupported.** The reduced tree and spherical inertias are not subject-specific anatomy, muscle, or tissue mechanics. The subject-scaled audit shows that its prescribed states do not close the anatomical hands on the declared grip points; the bounded follow-up closes only a reduced tree under engineering-limit and coarse collision screens.
- **Human Strategy Is Unsupported.** No measured trajectory or force record is held out for validation, and no coaching prescription follows from this mechanism experiment.

The next chapter tests the reduced contact mechanism under independent forward integration. Identifiability and uncertainty are then treated before control claims. Parameter compensation can otherwise make a structurally inadequate model reproduce one output while assigning the wrong contribution to contact, base motion, passive tissue, or actuation.

Chapter 18

Spatial Contact With Native Inertia-and-Bias Transport

The common-state experiment in Section 17 asks whether two dynamics formulations return the same generalized action at identical achieved states. It deliberately prescribes the hand forces and removes trajectory divergence. The experiment in this chapter asks the next, stronger question:

> Can a negative force-generated couple arise from the achieved state of a forward compliant two-hand system, persist after its grounded driver is removed, and survive propagation through two independently assembled multibody inertia-and-bias operators?

The answer is affirmative for one declared reduced model. MuJoCo and Pinocchio independently evaluate the mass, bias, gravity, kinematics, and continuous-time acceleration of the same 13-coordinate contract (Todorov, Erez, and Tassa 2012; Carpentier et al. 2019). Neither operator receives a prescribed contact-force history. The project-authored contact law calculates each force from the achieved relative hand–club displacement and velocity, then the same project-authored semi-implicit update advances both branches. The comparison therefore changes the rigid-body operator while holding the contact solver and integrator fixed.

The independence claim is component-specific. MuJoCo and Pinocchio independently supply mass, gravity, rigid-body kinematics, spatial-force mapping, and continuous-time acceleration. They intentionally share the Kelvin–Voigt constitutive law, grounded driver, and semi-implicit state update. Agreement tests articulated inertia-and-bias transport of one declared reduced mechanism across two native dynamics libraries. It does not exercise either library's native contact or constraint solver and is not independent confirmation of the contact law or time integrator.

This result closes the *reduced forward-contact* gate, not the anatomical or human gate. The hand bodies are finite-mass translational carriages, not arms; the grounded driver is not muscle; and the grip parameters are declared rather than identified from measurements. Those boundaries are properties of the experiment, not qualifications added after observing its outcome.

18.1 Model Estimand and Deliberate Reduction

The model contains two finite-mass hand carriages and one free rigid club. The hand positions are $\mathbf{h}_L, \mathbf{h}_T \in \mathbb{R}^3$. The club state is a world position $\mathbf{x}_C$, orientation $\mathbf{R}_C \in SO(3)$, linear velocity $\mathbf{v}_C$, and angular velocity ω_C. Its lead and trail grip offsets, expressed in the club frame, are

$$\rho_L = \begin{bmatrix} -0.080 & 0.015 & 0 \end{bmatrix}^\top \text{ m}, \qquad \rho_T = \begin{bmatrix} 0.080 & -0.015 & 0 \end{bmatrix}^\top \text{ m}. \tag{18.1}$$

The achieved club-side contact positions and velocities are therefore

$$\mathbf{p}_i = \mathbf{x}_C + \mathbf{R}_C \rho_i, \qquad \dot{\mathbf{p}}_i = \mathbf{v}_C + \omega_C \times (\mathbf{R}_C \rho_i). \tag{18.2}$$

The reduction is purposeful. A full arm introduces joint topology, anthropometric estimation, muscle redundancy, and tissue compliance at the same time as contact and engine divergence. The carriage model isolates a narrower estimand: whether finite hand-side inertia and compliant two-point closure can generate the proposed spatial wrench without direct club actuation. A positive result makes an anatomical test worthwhile; it does not substitute for one.

The common record fixes each hand mass at 0.55 kg, club mass at 0.32 kg, principal club inertias at $[0.0012, 0.025, 0.025]$ kg m^2, gravity at -9.81 m/s^2 on the vertical axis, a 0.240 s interval, and a 0.25 ms timestep. The complete JSON-serializable record is hashed before either engine is constructed. Both realized adapters report the same SHA-256 model digest.

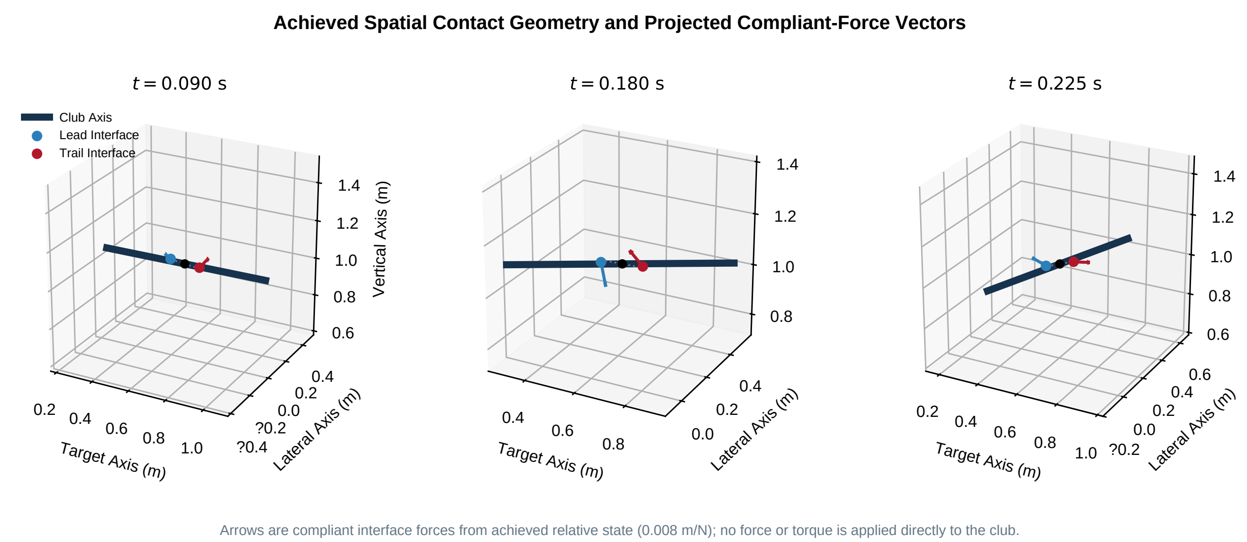

Figure 18.1: Achieved Spatial Contact Geometry and Projected Compliant-Force Vectors

Figure 18.1 shows three achieved MuJoCo states. The blue and red arrows are not prescribed inputs. They are the compliant interface forces obtained from the achieved engine state at each sample. The two engines start from identical hand positions, club position, orientation, and zero velocity.

18.2 Paired Contact and Grounded Driver Contracts

Each interface uses a paired Kelvin–Voigt law,

$$\mathbf{F}_i = k_c(\mathbf{h}_i - \mathbf{p}_i) + c_c(\dot{\mathbf{h}}_i - \dot{\mathbf{p}}_i), \tag{18.3}$$

with $k_c = 1800$ N/m and $c_c = 18$ N s/m. The club receives $+\mathbf{F}_i$ at $\mathbf{p}_i$ and the hand receives $-\mathbf{F}_i$ at $\mathbf{h}_i$. The force-sum residual is therefore an exact runtime invariant rather than an outcome tolerance. The contact storage and dissipation terms are

$$U_{c,i} = \frac{1}{2} k_c \|\mathbf{h}_i - \mathbf{p}_i\|^2, \qquad P_{d,i} = -c_c \|\dot{\mathbf{h}}_i - \dot{\mathbf{p}}_i\|^2. \tag{18.4}$$

The executed record also audits the complete interface-power identity. Across both engines and both branches, pointwise body power plus storage-rate minus dissipation closes within 1.56×10^{-14} W. Mapping the club-side point forces to the reference wrench preserves power within 5.51×10^{-14} W. These checks are independent of the exact equal-and-opposite force sum and expose velocity-frame, moment-arm, and sign errors that force closure alone cannot detect.

A world-referenced trajectory moves the finite hand carriages through a grounded spring–damper driver,

$$\mathbf{G}_i = k_d(\mathbf{h}_i^\star - \mathbf{h}_i) + c_d(\dot{\mathbf{h}}_i^\star - \dot{\mathbf{h}}_i), \tag{18.5}$$

where $k_d = 420$ N/m and $c_d = 24$ N s/m. The declared target contains a downswing-like rotation, translation, changing swing-plane tilt, and a bounded bilateral out-of-plane component. It is a manufactured excitation designed to exercise three-dimensional coupling. It is not a measured hand path.

No force or torque is applied directly to the club. The only club-side generalized load is the transported contact wrench

$$\mathcal{W}_C = \begin{bmatrix} \sum_i \mathbf{F}_i \\ \sum_i (\mathbf{p}_i - \mathbf{x}_C) \times \mathbf{F}_i \end{bmatrix}. \tag{18.6}$$

The equal and opposite driver wrench about the world origin is retained as a reduced ground-pathway reaction proxy. Because the carriages omit legs, pelvis, trunk, and anatomical arms, that proxy is not a prediction of measured ground-reaction force. It answers the bookkeeping question "where does the external reference-driver action close?" and prevents that pathway from being silently omitted.

18.3 Native Dynamics-Operator Realizations

The common experiment executes in two native libraries, both version 3.8.0 in the archived run:

- **MuJoCo.** Two three-axis slide bodies and one free club body are compiled from generated MJCF. World-frame hand and point forces are mapped through `mj_applyFT`; `mj_forward` computes continuous-time acceleration.
- **Pinocchio.** Two `JointModelTranslation` branches and one `JointModelFreeFlyer` branch are assembled programmatically. Equal and opposite forces are transformed into each joint's local spatial-force convention; the articulated-body algorithm computes acceleration.

Both branches use the same project-authored semi-implicit position/velocity update after their native acceleration evaluation. This is a controlled numerical choice, not an assertion that either library's native integrator has been exercised. It removes integration-method variation while retaining independent mass, bias, gravity, kinematics, spatial-force mapping, and continuous-time acceleration implementations. The Pinocchio adapter uses a local-world-aligned velocity at the moving club origin; using a world-origin spatial velocity instead creates an artificial contact-velocity discrepancy. That frame distinction is now covered by the forward trajectory gate.

The comparison evaluates complete trajectories, not just matched states. The declared engineering regions are 3 mm RMS and 9 mm maximum club-position difference, 0.035 rad maximum orientation difference, 10% relative RMS complete-wrench difference, and 8% normalized energy discrepancy. They are algorithmic acceptance regions, not statistical confidence intervals. Exact initial-state equality, action–reaction closure, analytical geometry controls, and timestep refinement provide independent checks that a passing trajectory is meaningful.

18.4 Inertia-and-Bias Transport Results

Figure 18.2 shows that the two shared-update trajectories propagated through separate native rigid-body operators remain close. In the continuing-driver branch:

- club-position RMS difference is 12.75 µm and maximum difference is 37.95 µm;
- maximum orientation difference is 8.94×10^{-8} rad;

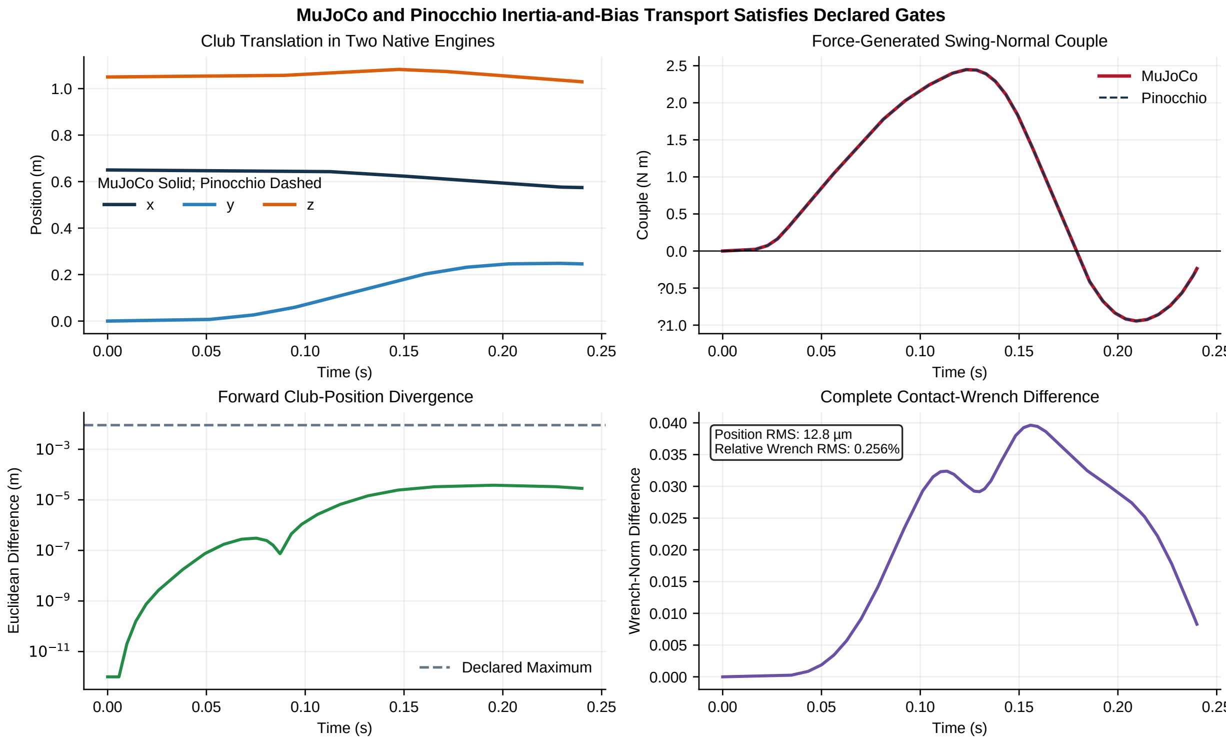

Figure 18.2: MuJoCo and Pinocchio Inertia-and-Bias Transport Satisfies Declared Gates

- relative RMS complete-wrench difference is 0.256%; and
- normalized energy discrepancy is 0.0235%.

In the driver-killswitch branch, the corresponding values are 16.96 µm, 77.89 µm, 9.42×10^{-8} rad, 0.274%, and 0.0461%. Every observed value is well inside its declared region. The result is stronger than the preceding common-state inverse-dynamics comparison because numerical error can now accumulate and feed back into the contact law. It remains narrower than a an independently formulated contact-and-integration comparison because both branches share one reduced contact law and state update.

18.5 Exact Same-State Driver Killswitch

The baseline and intervention branches are bit-identical through $t_k = 0.180$ s. At that sample, the intervention sets $\mathbf{G}_L = \mathbf{G}_T = \mathbf{0}$ for the remainder of the rollout. Contact, gravity, hand inertia, club inertia, and interface storage/dissipation remain active. This intervention removes the complete grounded driver rather than merely setting a named distal torque to zero.

After the killswitch, both engines retain a negative force-generated swing-normal couple for 37.5 ms and reach approximately -0.409 N m. The branch duration is the longest contiguous negative interval after the cut, not a sum of disconnected negative samples. The branch also retains 7.55 degrees of club-axis out-of-plane evolution, a peak club-long-axis rotation rate of 13.59 rad/s, and a peak force-generated long-axis couple of 0.242 N m. These observables are separated deliberately: the negative quantity is a projection of contact moment on the instantaneous swing normal, while long-axis couple and rotation report torsional evolution. Calling either projection “the club torque” without naming its axis would be ambiguous.

The ground-pathway proxy reaches 56.85 N in resultant force and 62.61 N m in moment before the branch. It becomes exactly zero with the driver at the killswitch, while the two compliant interfaces continue to exchange force and moment internally. This separates prior external input from subsequent interaction dynamics. It does not make the pre-killswitch motion unforced or biologically passive.

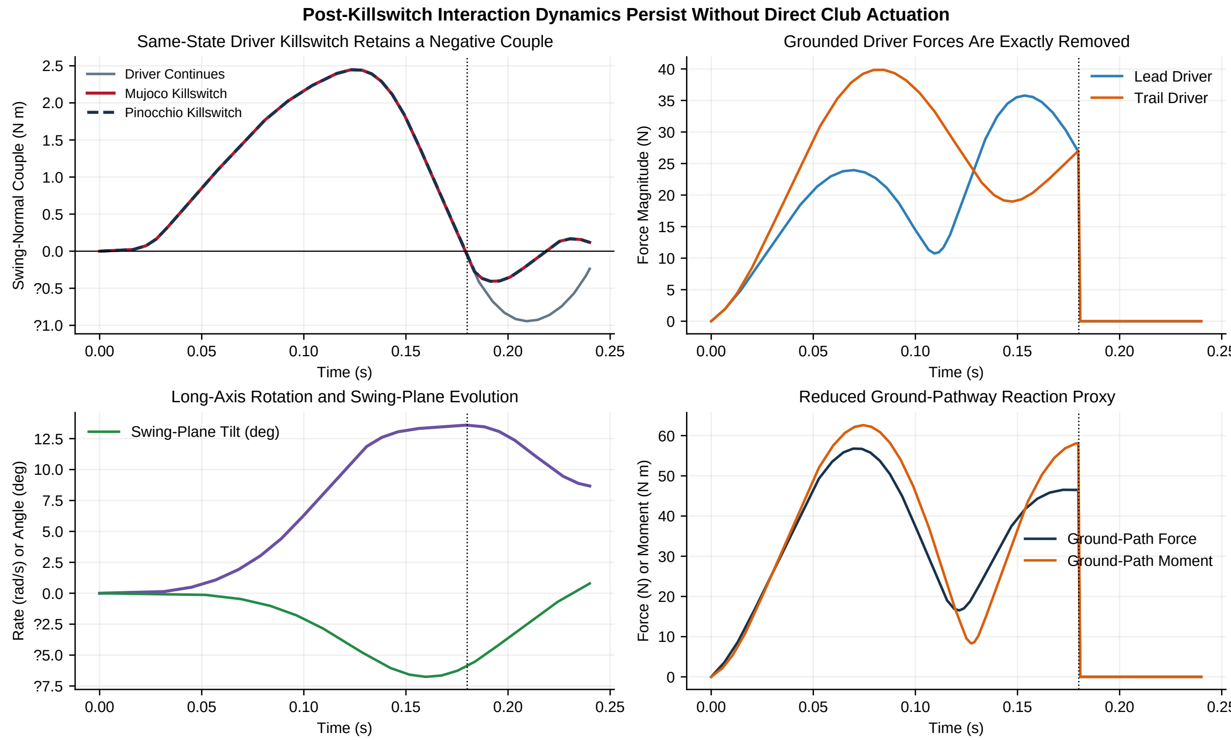

Figure 18.3: Post-Killswitch Interaction Dynamics Persist Without Direct Club Actuation

18.6 Geometry Controls and Work–Energy Closure

Two same-force geometry controls are evaluated without advancing a new trajectory:

1. transport the achieved forces through the club reference, making both moment arms zero; and
2. negate both achieved moment arms while retaining force vectors and state.

The coincident-grip couple is exactly zero at every stored sample. Reversing the arms reverses the swing-normal couple with a maximum residual below 9.2×10^{-16} N m. These controls rule out total force magnitude, integration history, and engine state as explanations for the sign response. Within the declared wrench equation, moment-arm geometry is necessary.

The work–energy residual includes engine-native rigid-body kinetic and potential energy, interface storage, driver power, and contact dissipation. For the MuJoCo killswitch branch its maximum absolute value decreases from 0.0611 to 0.0305 to 0.0153 J as the timestep decreases from 0.50 to 0.25 to 0.125 ms. The monotone approximately first-order reduction is consistent with the shared semi-implicit step. At 0.25 ms, the residual is about 0.55% of the 5.52 J total-energy range. Pinocchio's corresponding maximum is 0.0349 J. The residual is reported rather than normalized away because it is a direct falsifier of the discretized experiment.

18.7 What the Experiment Falsifies

The committed record fails closed if any of these conditions occurs:

1. either imported library lacks its native model and forward-dynamics API;
2. the generated adapters report different common-model digests;
3. baseline or killswitch trajectories exceed a declared inertia-and-bias transport-discrepancy region;
4. contact action–reaction force does not close at each evaluation;
5. the coincident-grip couple is nonzero;

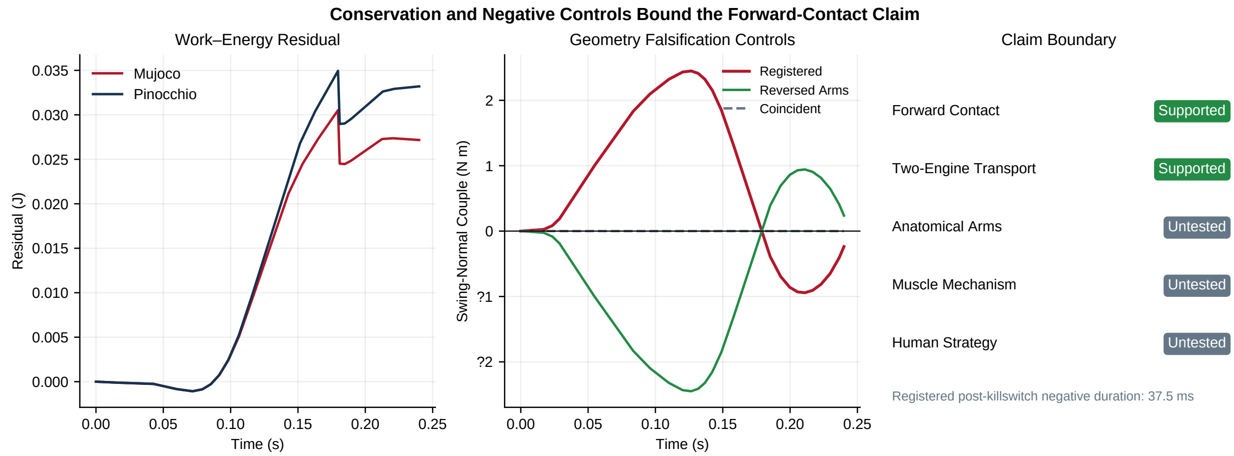

Figure 18.4: Conservation and Negative Controls Bound the Forward-Contact Claim

6. reversed moment arms do not reverse couple sign;
7. baseline and killswitch states differ before the branch sample;
8. the post-killswitch negative interval is shorter than 30 ms; or
9. the work–energy residual fails to decrease under timestep refinement; or
10. interface storage/dissipation power or point-force/wrench power fails to close.

The experiment would therefore reject the stated reduced mechanism if a second native solver does not transport it or if it depends on hidden direct club actuation. Passing those tests does not establish that humans use the mechanism, that the declared stiffness represents tissue, or that a player should seek a particular force pattern.

18.8 Reproduction and Platform Boundary

The evidence is stored in `data/spatial_forward_contact_study.json` and `data/spatial_forward_contact_study.npz`. Reproduction requires the repository's MuJoCo and Pinocchio optional engine dependencies. The native Pinocchio wheel used here executes in the Linux/WSL environment; a package named `pinocchio` on the default Windows Python index can resolve to an unrelated stub and is explicitly rejected by the adapter.

```
python3 -m scripts.research.proximal_distal_energy.run_spatial_forward_contact_study
python3 -m scripts.research.proximal_distal_energy.make_spatial_forward_contact_figures
python3 -m pytest tests/research/test_spatial_forward_contact.py -q
```

The next transport step is not "more confidence" in the carriage model. It is replacement of the carriages with subject-scaled articulated arms and a distributed shaft while preserving the same engine identity, wrench, killswitch, energy, event, and claim-boundary contracts.

Chapter 19

Coupled Uncertainty, Identifiability, and Control

19.1 Questions and Evidential Boundary

The preceding studies isolate feasible transfer mechanisms. They do not imply that a single parameter set is representative, that internal hand forces can be recovered from a net wrench, or that the fastest nominal command is robust. This chapter therefore asks three narrower questions in the coupled moving-base/flexible-club model:

1. Which uncertain inputs are associated with the largest changes in declared delivery observables?
2. Which internal quantities and parameters are identifiable from the chosen observations?
3. Do preselected delayed-actuation programs retain their advantages on an independently generated held-out ensemble?

The answers are model-screening results. Parameter ranges are engineering envelopes, not fitted population distributions; the actuator is a bounded command surrogate, not muscle physiology; and delivery is evaluated at a fixed registered time rather than at a simulated ball collision.

19.2 Registered Coupled Model and Design

Every rollout uses the ten-coordinate forward KKT model of Section 13. Base translation, both two-link arms, four grip constraints, two solved hand reactions, and one compliant shaft mode evolve in the same solve. This matters: uncertainty is propagated through the mechanism and its constraint reactions rather than through a disconnected response surface.

A deterministic Latin hypercube distributes samples across each declared range (McKay, Beckman, and Conover 1979). The global screen contains 24 points (seed 8426). Control programs are compared on a separate six-point training ensemble (seed 8449) and a six-point held-out ensemble (seed 8450). All runs use 0.24 s duration and a 4 ms step. The design varies 12 quantities simultaneously:

Parameter	Range	Interpretation
Anthropometric scale	0.95–1.05	Common arm-length scale
Limb-mass scale	0.90–1.10	Common arm-mass scale
Inertia-distribution scale	0.85–1.15	Segment inertia about its center
Base-mass scale	0.85–1.15	Translating-base inertia
Base-stiffness scale	0.75–1.25	Translational restoring stiffness

Parameter	Range	Interpretation
Joint-damping scale	0.60–1.40	Passive rotary damping
Grip-separation scale	0.85–1.15	Two-hand geometric lever arm
Shaft-stiffness scale	0.70–1.30	Lumped flex stiffness
Shaft-damping scale	0.60–1.40	Lumped flex damping
Activation delay	0.015–0.055 s	Pure command delay
Activation time constant	0.020–0.055 s	First-order command lag
Impedance scale	0.70–1.30	Linear joint-impedance proxy

These ranges were declared before selecting a preferred program. They bound a computational experiment; they do not encode prevalence or correlations in a golfer population.

19.3 Actuator and Outcome Contract

For commanded joint torque $u(t)$, the applied drive uses a delayed target and first-order state a,

$$\dot{a} = \frac{u(t - t_d) - a}{T_a},$$

followed by a torque-rate limit, asymmetric torque–velocity saturation, and a linear impedance term. The delivered torque is therefore history dependent and authority limited. No state is labeled as neural activation, muscle force, tendon force, reflex response, or co-contraction.

The registered outputs are delivery speed at 0.24 s; a planar face/path proxy; peak individual solved hand force; integrated squared delivered joint torque (the *effort proxy*); minimum force-generated grip couple; and peak shaft flex. The effort proxy has units associated with squared torque integrated over time; it is not metabolic or muscular cost. The face/path quantity is a planar orientation proxy, not a three-dimensional clubface measurement.

19.4 Global Sensitivity and Identifiability

Partial rank correlation coefficients (PRCCs) screen monotonic multivariable associations after ranking inputs and outputs and residualizing each variable against the remaining inputs (Marino et al. 2008). PRCC is useful for prioritization, but it is not causal attribution, a variance decomposition, or proof that the response is globally monotonic. With 24 samples for 12 inputs, the estimates are deliberately reported as a compact screening tier rather than precise population sensitivities.

Across the global ensemble, the 5th/median/95th percentiles are 4.005/5.188/ 5.840 m/s for delivery speed, 5.45/8.98/12.14 degrees for the face/path proxy, 140.7/162.3/200.0 N for peak individual hand force, and 66.0/82.0/94.4 for the effort proxy. Peak shaft flex spans 3.36/4.17/5.50 degrees. The signed minimum force couple spans -0.00478/-0.00035/approximately 0 N m in this particular global program; its small magnitude warns against transporting the much larger negative-couple values from different branch protocols without matching state and command.

The largest absolute PRCC is activation delay for delivery speed and effort, activation time constant for face/path error, limb mass for hand force, grip separation for minimum force couple, and shaft stiffness for peak flex. These rankings are hypotheses for larger designs, not settled parameter importance.

A leave-one-sample-out audit sharpens that boundary. Five of the six leading absolute-PRCC identities persist in all 24 omissions. The peak-hand-force leader does not: limb mass leads 12 omissions, activation time constant nine, and activation delay three. Several smaller coefficients also change sign. Thus the stable leaders are reproducible properties of this design, while the hand-force ranking and nonleading signs are especially fragile; none is a confidence interval or population statement.

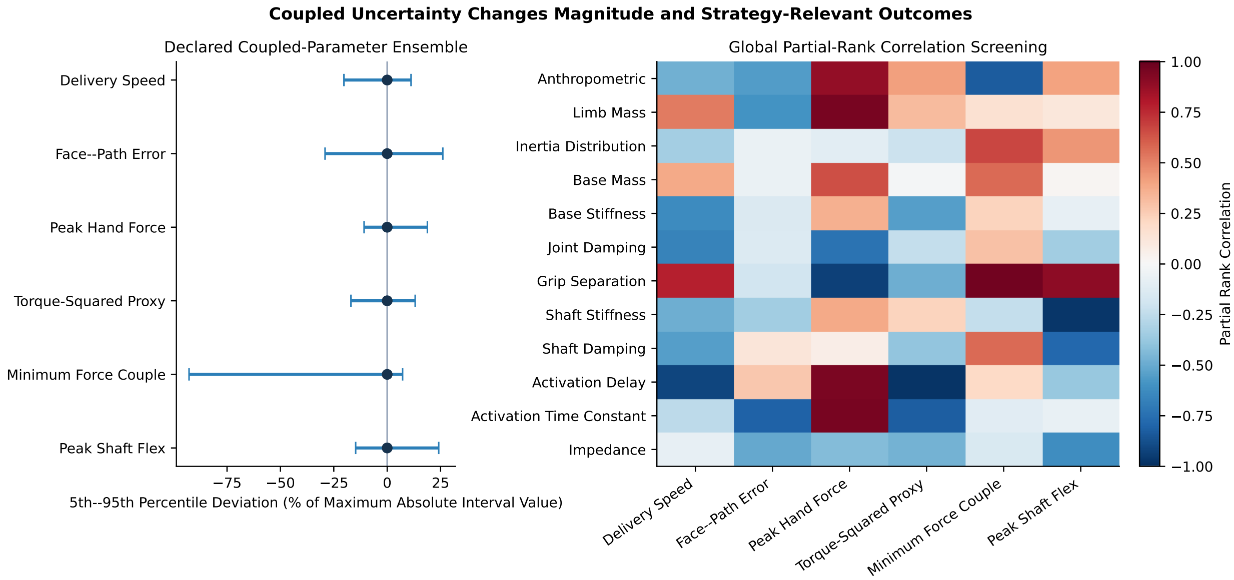

Figure 19.1: Uncertainty Intervals and PRCC Screening. Left: 5th–95th percentile ranges, normalized only for visual comparison. Right: partial rank correlations for the six registered outputs.

Identifiability is assessed separately from sensitivity (Raue et al. 2009). At a single planar instant, the two hand forces contain four scalar components, but their transported net force and scalar couple provide only three independent equations. The wrench map therefore has rank 3 and nullity 1: individual hand forces are structurally non-identifiable from the net planar wrench alone. Independent contact measurements or an additional constitutive assumption are required.

For the 12 uncertain parameters, a standardized sensitivity matrix is formed from the six summary observables. Its six singular values are 1.785, 1.146, 1.039, 0.863, 0.379, and 0.239. The effective rank at the registered 5% rule is six, so the full parameter vector has a nullity lower bound of six under this summary observation set. This is a local practical-identifiability screen, not a profile-likelihood analysis and not proof that every six-parameter subset is estimable. Threshold sensitivity gives rank six at 1%, 5%, and 10% of the largest singular value, but rank five at 20%; the registered conclusion is therefore stable across the first three declared thresholds, not invariant to threshold choice.

19.5 Constraint Rank Is Not Force Identification

The cross-tier constraint audit keeps three right nullspaces separate. The planar closure nullspace contains locally feasible generalized velocities; the two-point-force nullspace contains bilateral force allocations invisible to a net club wrench; and the full two-hand-wrench nullspace contains allocations among twelve inputs that one six-component resultant cannot distinguish. Neither kinematic freedom nor a sensing ambiguity identifies a produced hand force.

At the declared regular planar geometry, the 4×5 closure Jacobian has rank 4 and nullity 1. The constructed alignment with both arm angles zero and grip angle $\pi/2$ has rank 3 and nullity 2. This is an analytical adverse geometry, not a closed anatomical pose. Near the alignment, rank remains 4 while conditioning degrades. Because angular and translational columns have different units, the reported singular values use explicit 1 rad angular and 0.75 m translational coordinate scales; alternative translation scales change the condition number without changing exact rank.

The three-dimensional point-force map has rank 5/nullity 1 for separated contacts and rank 3/nullity 3 for coincident contacts. Its force and moment rows are normalized with a declared 0.10 m length. A 1 micrometre separation remains rank 5 at relative SVD tolerances 10^{-12} and 10^{-8} but is classified rank 3 at 10^{-6}. Thus

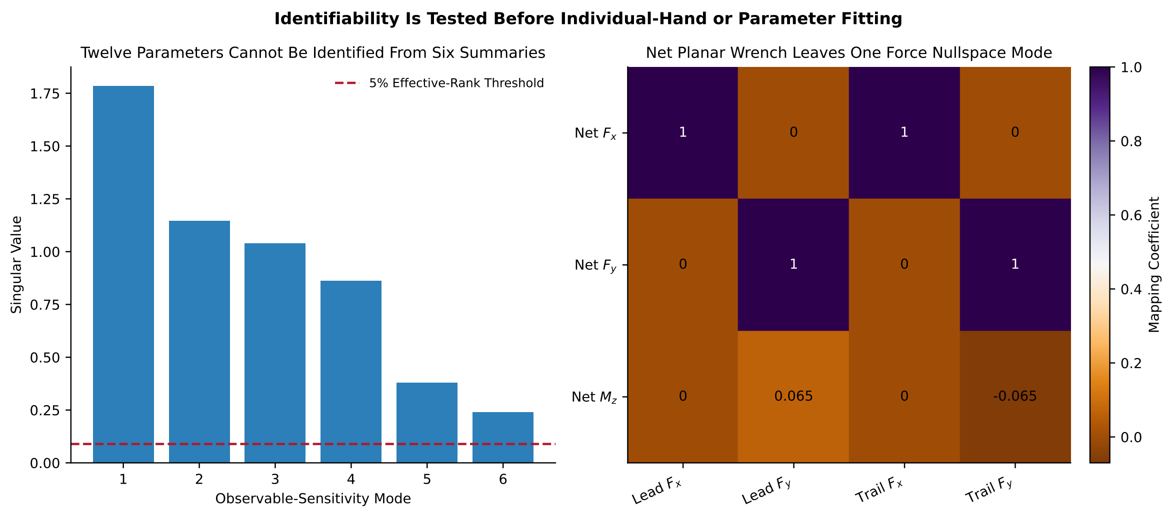

Figure 19.2: Identifiability Audit. The net planar wrench cannot uniquely allocate both hand forces, and six summary observables cannot identify the full 12-parameter vector.

geometry, units, scaling, and tolerance are part of the result rather than incidental solver settings.

The complete contract, source digests, scale alternatives, adverse cases, and reproduction commands are recorded in CONSTRAINT_INTERNAL_FORCE_DIAGNOSTICS.md and `data/constraint_internal_force_diagnostics.json`. These diagnostics do not recover constraint multipliers, establish feasible spatial contact, observe a human internal-force strategy, or support coaching guidance.

19.6 Preselected Programs and Held-Out Evaluation

Eight programs were fixed before comparing results: passive wrist, early drive, late drive, restrain-then-drive, higher impedance, later release, lower drive, and early restrain. Five objectives are retained rather than collapsed prematurely: maximize the 10th-percentile delivery speed; minimize mean face/path error; minimize the 90th-percentile individual-hand force; minimize the effort proxy; and minimize delivery-speed dispersion.

Seven programs are nondominated on the training ensemble; all eight are nondominated on held-out samples. That instability is substantive evidence against a universal optimum: even the poor-speed early-drive program retains a held-out tradeoff in another objective. A balanced equal-range Chebyshev rule selects later release, a speed-priority rule selects early restrain, and a load-priority rule selects higher impedance. These are objective-specific selections, not interchangeable recommendations.

Held-out Pareto membership is itself small-sample sensitive. Across the six leave-one-case-out recalculations, passive wrist, early drive, late drive, and higher impedance remain nondominated six times; restrain-then-drive, lower drive, and early restrain remain five times; later release remains four. The full-sample statement that all eight are nondominated is exact, but it should not be read as a stable estimate of a population Pareto set.

19.7 Bounded Test of Delayed Opposing Command

Hypothesis H4 asks whether a delayed actuator can benefit from an anticipatory opposing command. In the held-out ensemble, early restrain raises the 10th-percentile delivery speed to 4.706 m/s compared with 4.417 m/s for late drive, but worsens mean face/path error from 1.58 to 5.44 degrees. Thus H4 is supported only as a conditional lower-tail speed result for these bounded model schedules. It does not demonstrate human preactivation, neural timing, or a generally superior strategy.

Numerical closure remains materially below the reported effects across all rollouts: the maximum position-

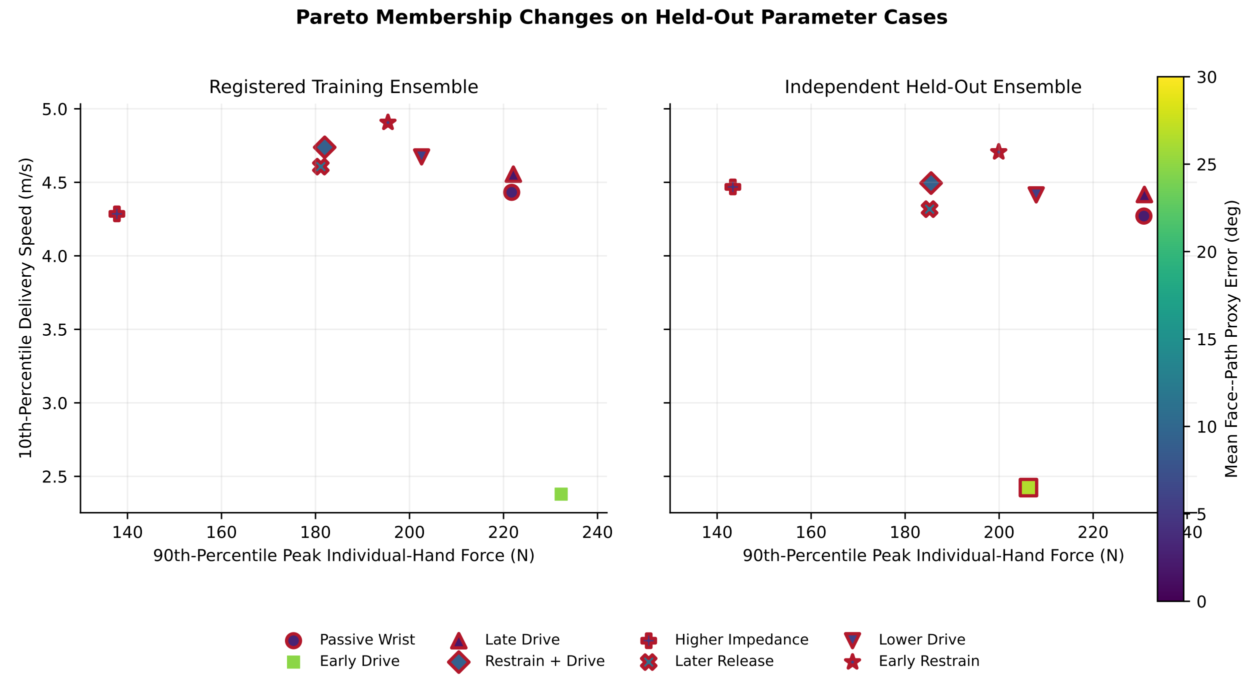

Figure 19.3: Training and Independently Held-Out Pareto Comparisons. Membership changes across ensembles, so no program is promoted as universally optimal.

constraint residual is 9.99×10^{-11} m, velocity-constraint residual 2.40×10^{-15} m/s, KKT residual 1.90×10^{-13}, and contact-power residual 6.40×10^{-14} W.

19.8 Claims, Falsifiers, and Next Measurements

This phase supports four bounded conclusions: coupled uncertainty can change delivery materially; the chosen summaries cannot identify all 12 parameters; net wrench cannot identify individual planar hand forces; and command selection depends on the objective and evaluation ensemble. It does **not** support a universal program, physiological effort inference, human preactivation, or a coaching prescription.

The results would be challenged by a larger registered ensemble that reverses the H4 lower-tail speed ordering, a direct two-hand measurement that uniquely resolves the wrench null mode without extra assumptions, or an independently implemented model in which the declared tradeoffs disappear under the same observables and actuator bounds. The next experimental protocol should measure both hand wrenches, club kinematics, ground reaction, and synchronization uncertainty; estimating all internal forces from club motion alone is not an acceptable substitute.

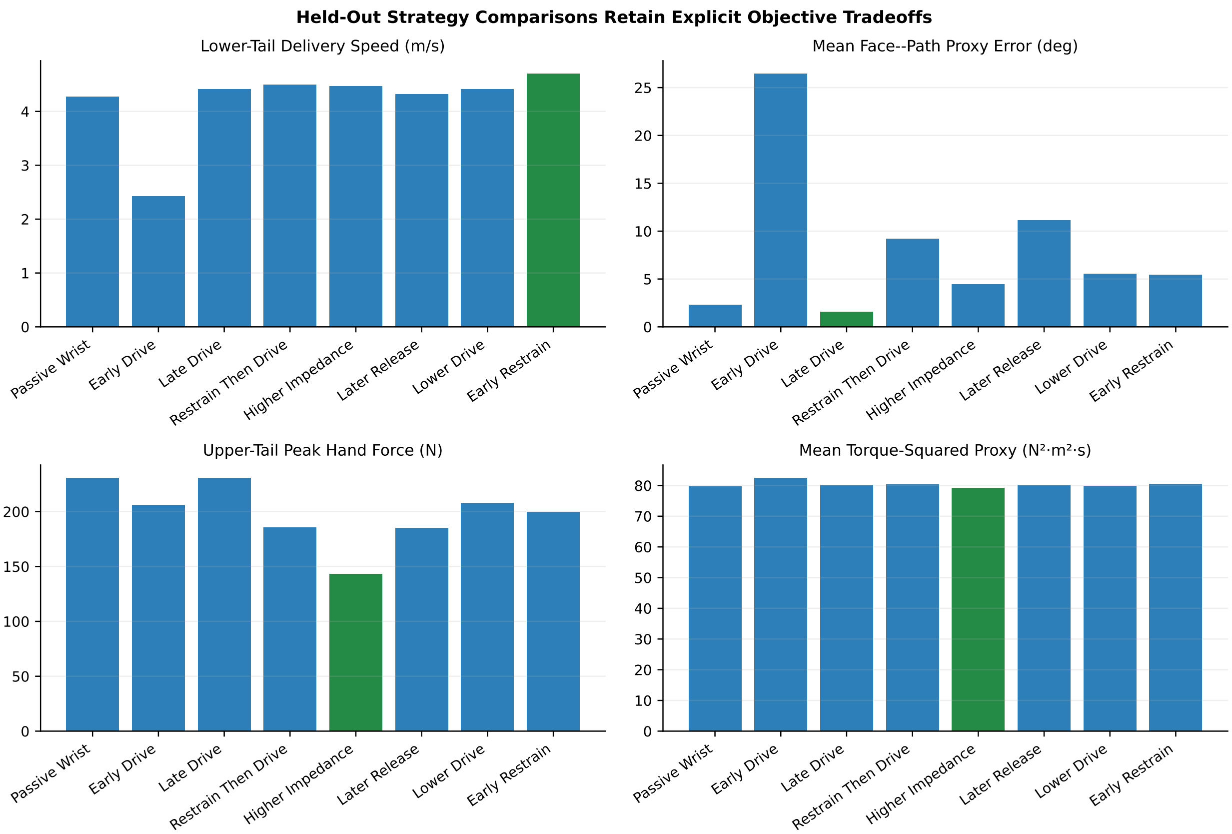

Figure 19.4: Held-Out Strategy Tradeoffs Across Speed, Planar Delivery Error, Hand Load, Effort Proxy, and Dispersion.

Chapter 20

Experimental Falsification Protocol

20.1 Why Readiness Is Not Evidence

Human measurements are the decisive next tier, but an empty data slot must not be filled with model output or an opportunistic dataset lacking the required observables. Protocol `proximal-distal-human-falsification-v1` is frozen before human outcomes are accessed. Its validator qualifies acquisition metadata, modality coverage, provenance, participant splits, and inference boundaries. The committed input is synthetic and the result is explicitly `synthetic_dry_run_only`; all human predictions remain untested.

20.2 Registered Measurements

H1–H3 require synchronized full-body kinematics, bilateral hand wrenches, club kinematics, and ground reaction. H4 additionally requires launch-monitor delivery and surface EMG or an equivalent governed activation measurement. The arm–wrist allocation hypotheses in Section 14 also require grip-pressure distribution, a closed-chain inverse-dynamics estimate conditioned on the measured internal grip wrench, and a preregistered estimate of force-development delay or tangent stiffness. Ultrasound-derived musculotendon length is preferred where feasible. EMG remains an activation timing measure and is not converted directly to joint torque. The protocol fixes SI units, minimum rates, and maximum synchronization uncertainty before outcome access. Hand wrench and ground reaction are sampled at at least 1000 Hz, club motion at at least 500 Hz, and the primary non-launch streams are synchronized within 1–2 ms.

Every stream carries a SHA-256 digest, coordinate frame, reference point, sampling rate, units, synchronization uncertainty, calibration record, and acquisition identity. Governed source data stay outside the public repository. Public evidence contains approved pseudonyms and derived results, never names, contacts, birth dates, medical identifiers, or identities inferred from filename, directory, session, row order, club, or device.

20.3 Fixed Outcomes and Falsifiers

Prediction	Primary Estimand	Falsifier or Inconclusive Condition
EXP-H1	Participant-level late distal drift work	Hierarchical interval enters the negligible region, or reconstruction/residual gates fail
EXP-H2	Event-aligned force–velocity projection and transported wrench power	Sign order is smaller than timing uncertainty or fails reference/frame controls

Prediction	Primary Estimand	Falsifier or Inconclusive Condition
EXP-H3	Negative equivalent club-couple interval after active/passive inventory	Sign is explained by measured active/passive terms or fails filtering/residual sensitivity
EXP-H4	EMG onset–reversal interval and held-out delivery association	Anticipatory interval or held-out association disappears under registered sensitivity
EXP-H5	Bilateral force-couple and direct-wrist allocation under a matched club task	Internal-force pattern does not vary with the assigned allocation or fails wrench closure
EXP-H6	Transition-aligned zero-force duration, tangent stiffness, and torque-error impulse	Inferred channel reversal has no measurable transmission gap, or preload does not improve same-program continuity

EXP-H3 can establish an observational interval, not muscular inactivity. EXP-H4 can establish timing and held-out association, not that a neural strategy caused the outcome.

20.4 Calibration, Filtering, and Residual Gates

The laboratory frame is right-handed and SI-valued. The club-frame transform, wrench reference, functional joint centers, segment inertias, and ground reference are retained. The primary low-pass cutoff is selected before held-out outcomes are opened; residual-analysis and plus/minus 20% cutoff variants are mandatory sensitivities. Event-specific filter tuning is prohibited.

Primary-window force and wrench values are never imputed. Kinematic gaps are limited to 10 ms and reported. Force residual greater than 10% body weight or moment residual greater than 5% body-weight-times-height fails the primary inverse-dynamics gate. Event uncertainty combines device synchronization, resampling, and event localization. A predicted order within that interval is inconclusive.

20.5 Participant-Level Holdout and Hierarchy

The split unit is the participant, never the swing. At least 25% of eligible participants are assigned to the held-out set by governed random allocation before fitting or threshold selection. Repeated swings are nested within participants; participant contrasts, not swing rows, are the primary units. Hierarchical partial pooling reports both within- and between-participant uncertainty. Skill is analyzed only if it is a governed declared variable and is never inferred from performance, session, filename, row order, or club.

20.6 Negative Controls

The experiment retains four controls. Rotating complete wrench/twist pairs or transporting them together to a second reference must preserve power. Shuffled timing within a prespecified noncausal window tests spurious event alignment. Replacing bilateral loads with net wrench must recover the known individual-hand null mode. Model-only sign-reversing geometry interventions remain labeled as model counterfactuals rather than human interventions.

Each outcome is classified as supported, contradicted, inconclusive, or untested. Missing modality, residual failure, ambiguous timing, or unapproved provenance cannot be silently excluded after outcomes are known.

20.7 Executed Dry Run and Open Gate

20.7.1 Torso-Velocity Validation Amendment

The rotating-base study adds a frozen, outcome-blind amendment, `torso-velocity-human-validation-registration-v1`. Its primary null is that measured thorax velocity adds no participant-held-out prediction of distal energy gain after conditioning on release geometry, club angular velocity, bilateral wrist state, shaft state, hand-path velocity and curvature, phase, and measured control-work proxies. A second test estimates the matched high- minus-low thorax-velocity contrast in negative bilateral grip work. The adverse test estimates the corresponding peak-wrench contrast at equal clubhead speed.

All three tests require full-body, club, and ground-reaction measurements plus bilateral six-axis hand wrenches; launch outcome is also required. Registered sensitivities vary filtering, wrench reference and coordinate frame, inverse- dynamics residual threshold, synchronization extremes, shaft-state inclusion, and the participant-level holdout assignment frozen before outcomes. Failure to improve held-out prediction, an interval overlapping the negligible region, increased braking, or increased peak load weakens the proposed strategy. Even a positive held-out result would remain observational and would not establish a causal coaching instruction.

The synthetic record contains two pseudonymous fixture participants separated at participant level and all six modality descriptors. The validator confirms units, hashes, sampling, synchronization, split uniqueness, and absence of identity fields. Deliberate identity, unit, hash, synchronization, split, and governance violations fail closed in tests.

No governed human dataset was available in this phase or found in the subsequent workspace and public-data search recorded in UpstreamDrift #8556. Published instrumented-grip studies by Choi and Park and Koike do not provide a governed participant-level deposit satisfying the synchronized bilateral six-axis grip-wrench contract. Accordingly, EXP-H1 through EXP-H6 remain `untested_no_governed_human_data`. Synthetic traces, digitized figures, and publication-level aggregates are not substitutes. Evaluation begins only after an ethics/oversight reference, consent and reuse basis, private data authority, synchronized streams, calibration records, frozen participant split, and analysis-release authorization pass the same validator. The protocol removes analytical discretion; it does not remove the need for measurements.

Chapter 21

Open-Resource Release and Reviewer Qualification

21.1 Release Contract

The scientific product is distributed as an open research resource rather than as evidence for a software platform. Canonical presets identify reproducible entry points across the analytical, moving-base, two-hand, distributed-shaft, articulated-contact, passive-shaft, finite-ground, uncertainty/control, and experimental-readiness tiers. Preset names preserve the model ladder and never imply that a higher unexecuted tier is available.

The release manifest hashes the report source and PDF, chapter source, linked bibliography, evidence JSON/NPZ/CSV, publication PDF/SVG figures, analysis scripts, evidence schema, data dictionary, citation metadata, and reviewer guide. A separate `CHECKSUMS.sha256` is sorted by path for standard tooling. Validation is read-only and fails on missing or changed bytes, unsafe paths, and malformed records. Updating expected hashes requires a separate explicit write command after analysis, render, and visual gates pass.

21.2 Reviewer Path

The reviewer workbench begins with the claim–evidence–alternative–falsifier matrix, then groups static SVG/PDF figures and downloadable data by model tier. It distinguishes analytical attribution, branched forward counterfactuals, common-state inverse dynamics, uncertainty/control screening, and experimental readiness. This is a deliberately static, link-stable review surface; it does not recompute results in a browser or introduce a second scientific code path.

The data dictionary defines common units, state and wrench fields, power/work terms, residuals, provenance, ensemble partitions, and interpretation boundaries. Citation metadata points to the article and requests the exact release commit. Code and repository-authored documentation use the repository's MIT license; linked papers, external archives, and the registered WSCG source retain their own boundaries.

21.3 Qualification Commands

From the repository root:

```
python -m scripts.research.proximal_distal_energy.qualify_open_release list-presets
python -m scripts.research.proximal_distal_energy.qualify_open_release validate
```

The first command exposes canonical deterministic entry points. The second validates the pinned bundle but never changes it. Maintainers regenerate the manifest only through the explicit `write` action after all source data, figures, article source, rendered PDF, and documentation are final.

21.4 Qualified and Open Claims

The release records planar interaction dynamics and negative-couple feasibility as supported at their declared tiers, geometry response as supported through reduced spatial common-state inverse dynamics, and modal reduction behavior as supported on a synthetic structural shaft case. It records forward distributed-shaft coupling as supported only for the declared synthetic planar tier. It records the finite-ground/free-moment mechanism as numerically qualified with an empty preregistered matched set, post-killswitch contact persistence as supported only in the reduced spatial carriage model, human predictions as untested, and a universal controller as unsupported.

Five release-level completion gates remain visible: three-dimensional articulated contact with calibrated unilateral foot support, force-plate comparison, grip, and shaft; equipment-calibrated beam and measured grip properties; measured tissue-level preload and slack identification; governed held-out human evaluation; and external archive deposit with a persistent identifier. Archive deposition changes external state and has not been performed. A reproducible local bundle is not described as a permanently archived release until that deposit is verified.

Chapter 22

A Common-Observable Ladder Toward Higher-Order Models

22.1 Why a Model Ladder Needs Fixed Observables

Adding degrees of freedom does not automatically strengthen a mechanism claim. It can instead change the question by changing the reference point, frame, contact definition, or reported power. A useful fidelity program must preserve the observable and declare every structural assumption changed by each comparison. Some branches below relax one assumption; others necessarily change several, so the discrepancy matrix prevents their differences from being attributed to a single factor. This chapter carries one common interaction-record schema—not one shared trajectory—through a three-coordinate chain, a prescribed mobile-hub inverse-dynamics comparison, forward rigid- and flexible-club two-hand systems, and arbitrary three-dimensional frame rotations. The reduced full-body common-state tier in Section 17 then adds nonplanar body and club inverse dynamics in two independent formulations.

The common record contains:

- model tier and time;
- Cartesian frame and reference point;
- force and equivalent couple acting on the declared distal subsystem; and
- linear and angular velocity of that same point in that same frame.

Force power, couple power, and total wrench power are derived rather than stored as unrelated fields. This makes dimensional and sign errors visible and permits exact frame and reference-transport tests. The implementation is available in `mechanism_ladder.py`, and the recorded analysis is generated by `run_mechanism_ladder_study.py`.

Figure 22.1 separates the lower-order mechanism tests from the spatial dynamics boundary. The rotated 3-D tier is a coordinate-frame audit, not an out-of-plane swing simulation; the later common-state tier supplies that nonplanar step. The historical mobile-hub tier prescribes hub motion and calculates the required reaction change. By contrast, Section 13 now evolves base translation, two-hand reactions, and club flex together. These distinctions are part of the result.

22.2 The Common Wrench–Power Contract

At reference point A, the interaction record is the wrench $(\mathbf{F}, \mathbf{M}_A)$ and twist $(\mathbf{v}_A, \omega)$. Its power is

$$P_A = \mathbf{F} \cdot \mathbf{v}_A + \mathbf{M}_A \cdot \omega. \tag{22.1}$$

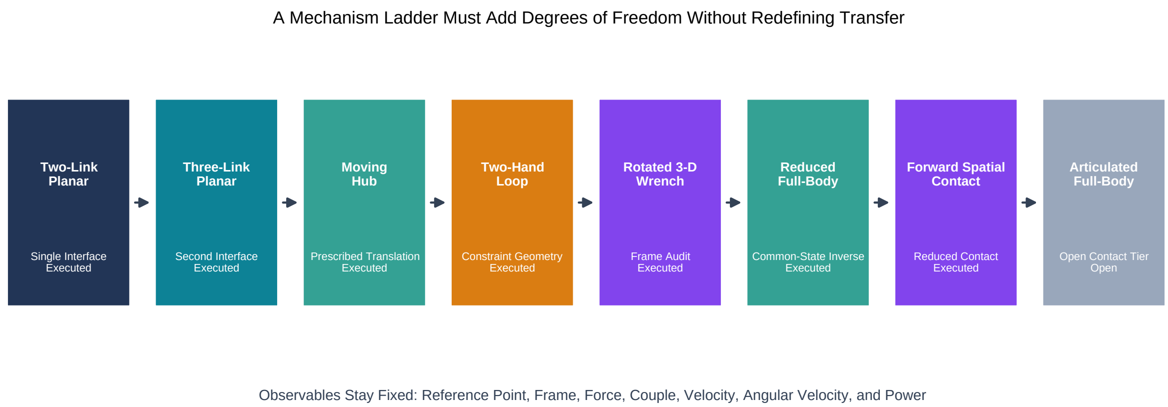

Figure 22.1: A Mechanism Ladder Must Add Degrees of Freedom Without Redefining Transfer

If the reference moves to point B, with $\mathbf{r}_{BA} = \mathbf{r}_B - \mathbf{r}_A$, then

$$\mathbf{M}_B = \mathbf{M}_A - \mathbf{r}_{BA} \times \mathbf{F}, \tag{22.2}$$

and rigid-body point kinematics require

$$\mathbf{v}_B = \mathbf{v}_A + \omega \times \mathbf{r}_{BA}. \tag{22.3}$$

Substitution into Equation 22.1 gives $P_B = P_A$. Transporting the moment without transporting the velocity, or vice versa, creates an artificial power difference. This is the power counterpart of the wrench-transport rule introduced in Section 9.4.1.

Under a proper frame rotation $\mathbf{R} \in SO(3)$, all Cartesian vectors transform by the same $\mathbf{R}$. Orthogonality then preserves vector norms and dot products. The audit applies 51 different proper rotations and a fixed reference translation to sampled three-link wrenches. Maximum force-norm, couple-norm, rotation-power, and transport-power residuals are respectively 7.1×10^{-15} N, 8.9×10^{-16} N · m, 2.4×10^{-13} W, and 5.7×10^{-14} W.

These residuals establish consistency for the tested paired rotations and reference transport. They do not show that a planar model contains the physics of a three-dimensional swing, and they cannot exclude a consistent but semantically wrong axis label inside an untested adapter. They remove the specific tested transform inconsistencies from later discrepancy explanations.

22.3 Three Coordinates and Two Internal Interfaces

The executed three-link tier reuses the reference trace from Section 12. Its bodies are the arm point mass, proximal shaft point mass, and distal head point mass. Thus it adds a second internal interface and a third coordinate, but it does not yet add an independently actuated torso. The distal interface record is evaluated at the second joint:

$$P_{23} = \mathbf{F}_{23} \cdot \mathbf{v}_{J_2} + M_{23}\omega_3. \tag{22.4}$$

At the interpolated delivery crossing, $t = 0.427252$ s. The nearest stored 0.5 ms sample has 56.37 N interface force, +4.91 N · m interface couple, 32.09 W force power, 74.60 W couple power, and 106.69 W total wrench power. The joint velocity used in these power terms is evaluated analytically from the relative-coordinate

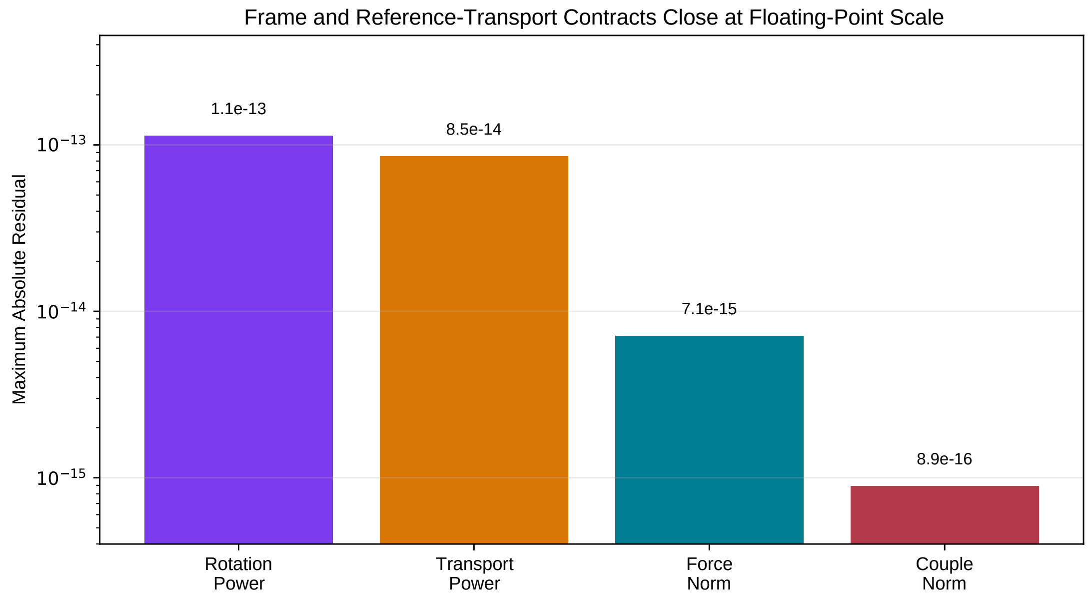

Figure 22.2: Frame and Reference-Transport Contracts Close at Floating-Point Scale

state. A second-order finite difference of the stored positions differs by as much as 0.0299 m/s over the trace, so it is retained only as a numerical comparison rather than the published velocity authority. The precise values are model outputs, not expected human ranges.

Figure 22.3 shows that the qualitative lesson from the double pendulum survives: neither force magnitude nor moment sign uniquely determines transfer. Total interface power changes sign while the force magnitude remains positive. Conversely, force and couple power can reinforce one another or oppose one another depending on velocity alignment.

The result does not prove invariance to every added link. A torso–arm–club model with an actuated first interface can alter both state history and distal reaction. What survives here is the accounting structure: force, couple, velocity, and angular velocity remain sufficient to state interface power without naming a particular generalized coordinate.

22.4 Prescribed Mobile-Hub Inverse Dynamics

A moving hub changes two parts of the interaction calculation. Its acceleration changes the force required to accelerate the supported mass, and its velocity changes the point at which force power is evaluated. For a prescribed hub acceleration $\mathbf{a}_H$ and distal supported mass m_d, the force increment in the executed comparison is

$$\Delta\mathbf{F}_H = m_d\mathbf{a}_H. \tag{22.5}$$

The corresponding interface velocity is $\mathbf{v}_{J,H} = \mathbf{v}_{J,0} + \mathbf{v}_H$. The zero-amplitude case reduces exactly to the fixed-hub trace: maximum force and power differences are both zero to stored precision.

The declared hub path has a 1.25 Hz fundamental in x and a 2.5 Hz second harmonic in y: $x = A\sin(\omega t)$ and $y = (A/2)\sin(2\omega t + 0.35)$. The x amplitudes tested are 0, 25, 50, and 100 mm; the corresponding y amplitudes are half as large. At $A = 100$ mm, the maximum distal-force shift is 2.67 N and maximum instantaneous power change is 38.09 W. The signed power difference integrated over the half-second trace is -0.174 J. These values are specific to this prescribed path and the 0.20 kg supported distal mass.

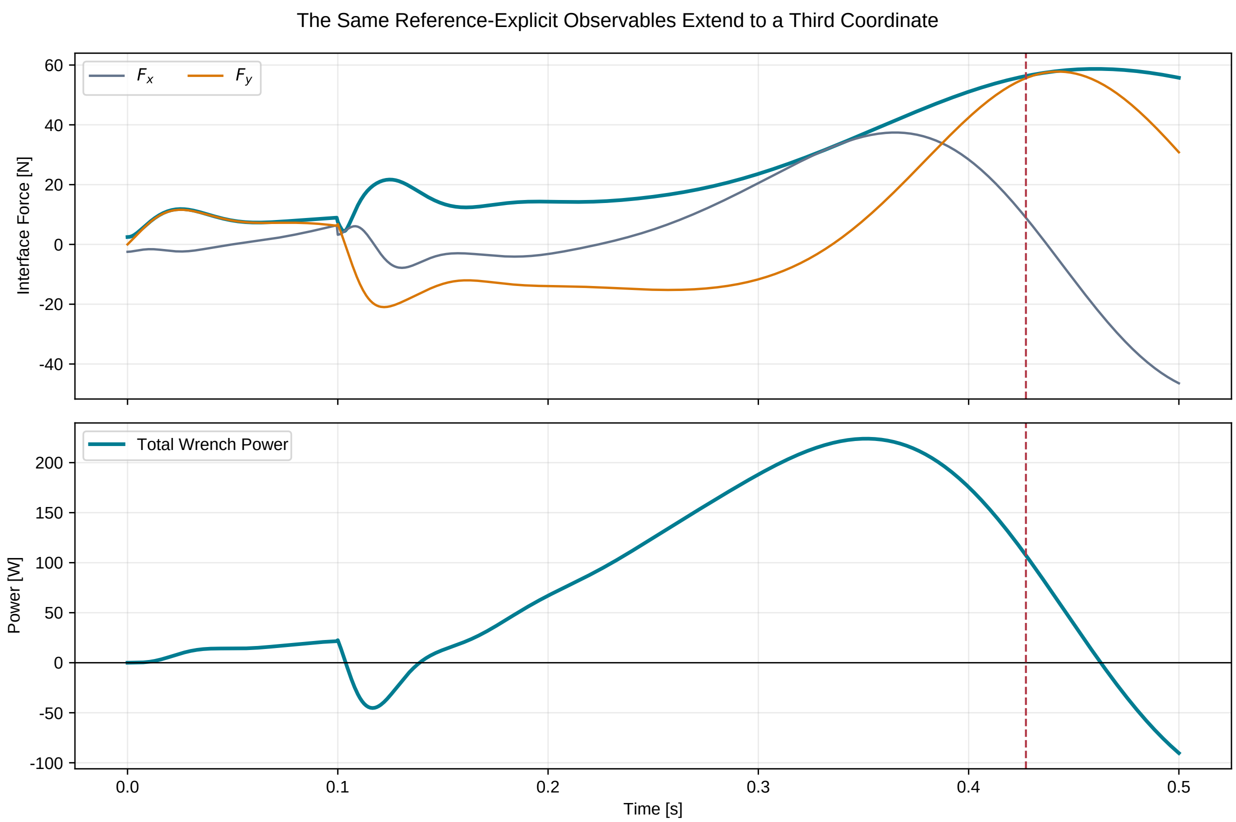

Figure 22.3: The Same Reference-Explicit Observables Extend to a Third Coordinate

Figure 22.4: Prescribed Hub Motion Changes Reaction Force and Power Without Changing the Relative Trace

The comparison is useful precisely because it is not a new forward swing. The relative trajectory is held fixed, so Equation 22.5 exposes how base motion changes the inverse-dynamics reaction. A forward torso model would also change the relative coordinates and controls. Prior hub-path studies show that such motion can materially affect model performance and inferred work (Nesbit and McGinnis 2009; Nesbit and McGinnis 2014); the present calculation supplies a transparent bridge rather than substituting for that higher-order analysis.

22.5 Forward Coupled Moving-Base Tier

The prescribed-hub audit isolates one inverse-dynamics term, while the coupled experiment in Section 13 removes its central restriction. Its finite-mass base responds to arm and club reactions; both arms remain closed to the floating grip; and shaft flex responds to the same trajectory. The model emits the same reference-explicit force, couple, point velocity, angular velocity, and power record used by the lower tiers.

This tier preserves three registered qualitative responses. A late force-generated negative couple occurs with finite hand separation, survives a 50 ms same-state zero-command branch, and collapses exactly when both contact moment arms are set to zero. Simultaneously, the contact power identity and whole-system work–energy balance close under timestep refinement. Thus the earlier prescribed-hub result remains a useful analytical audit, but it is no longer the highest executed moving-base result.

The forward tier is still planar and its base has translation but no rotation. Its one torsional flex mode is not a distributed beam. Transport to spatial dynamics is therefore evaluated separately in Section 17 rather than inferred from the planar result.

22.6 Closed-Loop Two-Hand Constraint Geometry

The two-hand wrench audit in Section 9 starts from recorded contact forces. A closed-loop model adds a prior question: which generalized velocities are compatible with maintaining both contacts? The executed planar geometry uses five coordinates,

$$\mathbf{q}_c = (\theta_L, \theta_T, x_G, y_G, \psi_G)^{\mathsf{T}}, \tag{22.6}$$

for lead- and trail-arm angles and grip pose. Two Cartesian constraints per hand give

$$\dot{\mathbf{c}} = \mathbf{J}_c(\mathbf{q}_c)\dot{\mathbf{q}}_c = \mathbf{0}, \tag{22.7}$$

with a 4×5 constraint Jacobian. At every one of 201 sampled geometries, $\mathbf{J}_c$ has rank four and a one-dimensional nullspace. The maximum residual obtained by multiplying the Jacobian by its computed nullspace vector is 6.8×10^{-16}.

The condition number remains between 9.05 and 9.46 in the declared sweep. That shows stable local velocity compatibility for this geometry. It does not determine the Lagrange multipliers or hand forces. Those require mass, acceleration, actuation, and constraint-stabilization equations. In particular, constraint rank cannot establish the sign of the equivalent couple.

This distinction connects the two evidence types cleanly:

- the constraint Jacobian defines admissible closed-loop motion;
- the dynamic solve determines contact reactions consistent with that motion;
- the equivalent wrench reduces those reactions about a declared point; and
- wrench power determines whether that action supplies or removes club energy.

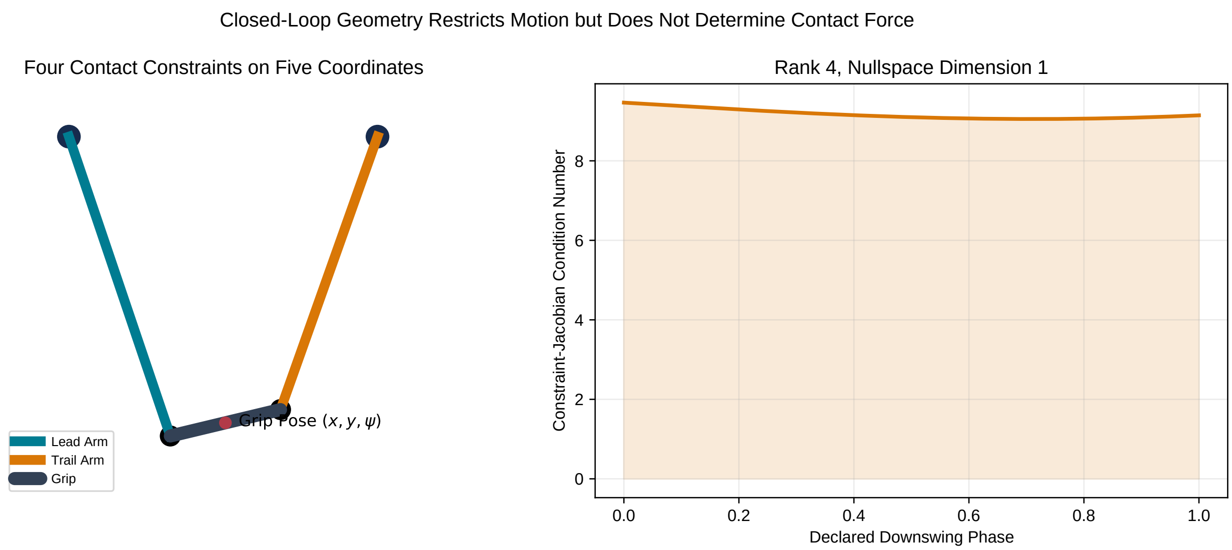

Figure 22.5: Closed-Loop Geometry Restricts Motion but Does Not Determine Contact Force

The archived WSCG tables remain the source-specific dynamic evidence evaluated in Section 9. The present Jacobian audit establishes only its kinematic geometry contract. Separate forward constrained and coupled-base models in Section 10 and Section 13 solve contact reactions dynamically; their evidence is not supplied by this rank audit.

22.6.1 Feasible Closed-Loop Orbits and Singular Margins

The preceding sweep samples Jacobians without first proving that every pose belongs to an exactly closed two-contact configuration. A separate analytical control now constructs the same-origin triangle directly. For arm lengths $L_L = 0.75$ m and $L_T = 0.78$ m and grip separation $d = 0.25$ m, the relative arm angle satisfies

$$\cos(\theta_T - \theta_L) = \frac{L_L^2 + L_T^2 - d^2}{2L_L L_T}. \tag{22.8}$$

Both signs of the inverse cosine define the two assembly branches, while a global phase rotates the entire triangle without changing its internal geometry. All 362 registered samples—181 phases on each branch—close both contacts to at most 1.66533×10^{-16} m. Under the separately declared 1 rad angular and 0.75 m translation coordinate scales, every sample has rank four and nullity one. The minimum scaled singular value is 0.202095 m, the scaled condition number is 6.45326, and the maximum singular-spectrum change under global phase rotation is below the conservative 10^{-14} m reporting bound. Expected-zero SVD residuals are published as power-of-ten upper bounds rather than platform-specific roundoff values; rank decisions and singular values are still evaluated at full precision before publication reporting.

The triangle inequality supplies two exact geometric countermodels. At $d = |L_L - L_T| = 0.03$ m and $d = L_L + L_T = 1.53$ m, the triangle becomes collinear; both exact boundaries have rank three and nullity two. A near-boundary sweep keeps position closure exact while varying the distance to the lower boundary from 10^{-4} to 10^{-12} m and the relative SVD tolerance from 10^{-12} to 10^{-4}. For example, the 10^{-8} m offset remains rank four through a 10^{-6} tolerance but is classified rank three at 10^{-4}. This is a numerical classification dependence, not a physical failure threshold.

An equivalent centimetre representation preserves rank, nullity, and condition number while multiplying the scaled singular values by 100, as required by the unit change. Three positive translation scales, three feasible geometries, three phase-grid resolutions, impossible-triangle rejections, and a manufactured row-dependency killswitch are retained in `data/closed_loop_singularity_margin.json`. These controls establish only an exact planar kinematic result. They do not establish anatomical shoulder closure, contact-force magnitude, constraint multipliers, muscle action, passive negative torque, human occurrence, or coaching guidance.

22.6.2 Phase/Event Sensitivity and Finite-Time Amplification

Local rank at isolated states does not show how perturbations grow along a finite downswing, and event-time uncertainty is not interchangeable with state amplification. The registered analytical trajectory therefore propagates the discrete variational map of the same RK4 step operator through the first positive club-vertical crossing. With declared state scale matrix $\mathbf{S}_x$, the dimensionless transition map is

$$\widetilde{\Phi}(t,0) = \mathbf{S}_x^{-1}\Phi(t,0)\mathbf{S}_x. \tag{22.9}$$

Its singular values are finite-window perturbation gains. The associated rates $\log \sigma_i / t$ are finite-time exponents, not asymptotic Lyapunov exponents. The computation refines the paper's 1 ms reference integration to 0.125 ms for this derivative audit. Central-difference step multipliers from 0.1 to 10 change the event transition by at most 6.9×10^{-6}, while three complete symmetric perturbation rollouts agree with the propagated map within a registered conservative upper bound of 4×10^{-7}. At the 0.349256 s geometric delivery event, the largest observed scaled gain is 8.33244 and the smallest is 0.093456. Thus the local map amplifies some perturbation directions while contracting others; a single label such as "stable swing" would discard that anisotropy.

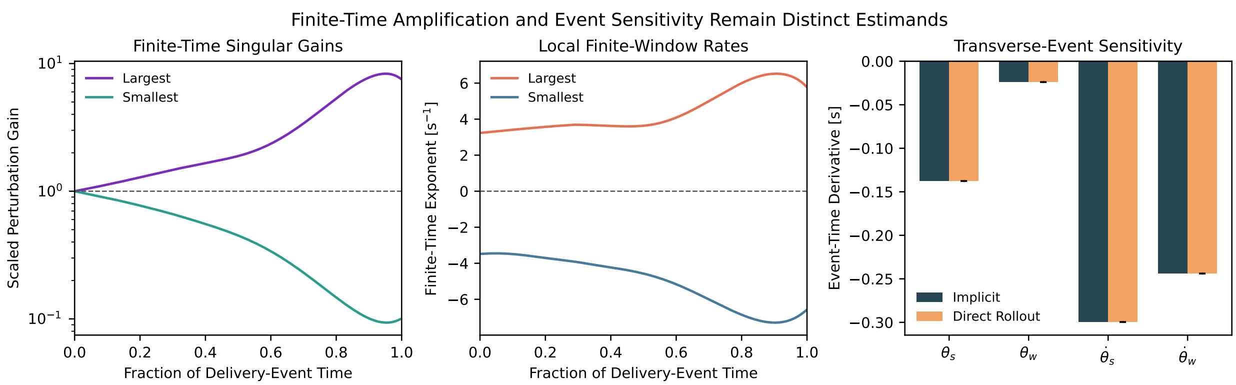

Figure 22.6: Finite-Time Amplification and Event Sensitivity Remain Distinct Estimands

For the state guard $h(\mathbf{x}) = \theta_s + \theta_w = 0$, the transverse-event derivative is obtained from the implicit relation

$$\frac{\partial t_e}{\partial \mathbf{z}_0} = -\frac{\nabla h^{\mathsf{T}}\Phi(t_e,0)\mathbf{S}_x}{\nabla h^{\mathsf{T}}\mathbf{f}(\mathbf{x}_e,\mathbf{u}_e)}. \tag{22.10}$$

The denominator is 35.0258 s^{-1} for the registered crossing. The four scaled-state derivatives are $(-0.137655, -0.0240043, -0.299636, -0.243972)$ s; direct perturbed-event estimates agree within 5.98×10^{-5} s. A constructed guard whose configuration normal is orthogonal to the event velocity has zero transversality and returns a typed near-grazing outcome rather than a derivative. Absent, multiple, and out-of-window crossings are likewise ineligible.

The time-only delivery guard in the hybrid contract has an identity reset and continuous pre-event flow, so its manufactured saltation matrix is exactly the identity; a reset corruption to 0.95 produces the expected 0.05 deviation. The event state remains 1.48546 scaled units from the initial state, far above the 10^{-6} periodicity tolerance. Floquet multipliers are therefore suppressed: no periodic orbit, orbital stability, basin, or bifurcation claim is available from this downswing. These diagnostics use one synthetic open-loop model. They do not measure neural timing demand, fatigue tolerance, participant robustness, passive negative torque, technique, or coaching efficacy.

22.6.3 Trajectory-Varying Event-Conditioned Control Authority

The finite-time transition map describes sensitivity to an initial-state perturbation. It does not answer the different question of which local state directions can be produced by a torque perturbation distributed along the trajectory. The registered input audit differentiates the same exact RK4 step operator with respect to state and input, giving

$$\mathbf{z}_{k+1} = \mathbf{A}_k\mathbf{z}_k + \mathbf{B}_k\mathbf{v}_k, \qquad \mathbf{W}_{k+1} = \mathbf{A}_k\mathbf{W}_k\mathbf{A}_k^{\mathsf{T}} + \mathbf{B}_k\mathbf{B}_k^{\mathsf{T}}. \tag{22.11}$$

State and torque coordinates are explicitly scaled. The input matrix is divided by $\sqrt{\Delta t}$ so the discrete sum represents a continuous-energy-equivalent torque perturbation rather than changing merely because the integration grid changes. At the transverse delivery guard, the fixed-time perturbation is projected to the event surface with

$$\mathbf{P} = \mathbf{I} - \frac{\mathbf{f}_e\mathbf{n}^{\mathsf{T}}}{\mathbf{n}^{\mathsf{T}}\mathbf{f}_e}, \qquad \mathbf{W}_{e,T} = \mathbf{Q}^{\mathsf{T}}\mathbf{P}\mathbf{W}_e\mathbf{P}^{\mathsf{T}}\mathbf{Q}, \tag{22.12}$$

where $\mathbf{n} = \nabla h$, $\mathbf{f}_e$ is the event velocity, and the columns of $\mathbf{Q}$ form an explicit orthonormal basis for the guard tangent space. The exact crossing has guard residual 1.31×10^{-13} and transversality $35.0258\ \mathrm{s}^{-1}$. Under the declared scales and rank tolerance, the two-channel Gramian has rank four in the four-state fixed-time space and rank three in the three-dimensional event tangent space. Shoulder-only and wrist-only input maps also have full retained rank under this local numerical contract, but their eigenvalue spectra and conditioning differ strongly. Rank therefore establishes neither equal effort nor interchangeable human strategies.

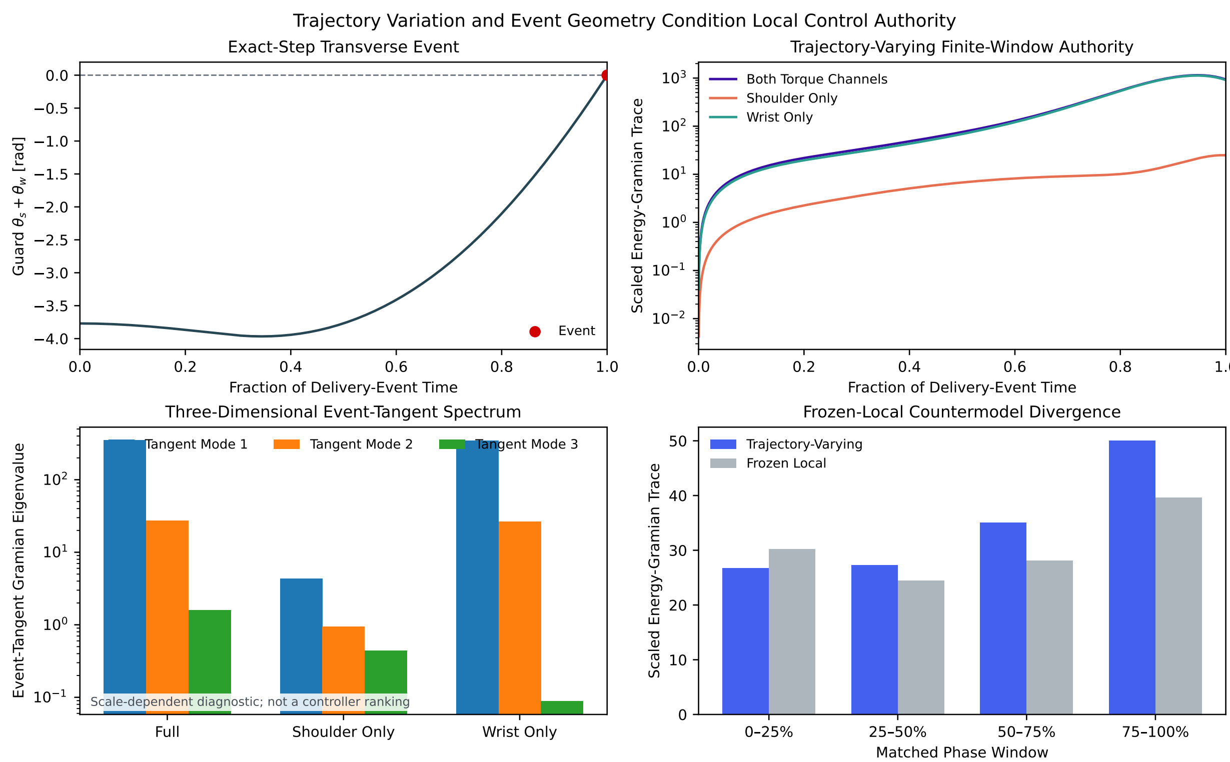

Figure 22.7: Trajectory Variation and Event Geometry Condition Local Control Authority

The result passes four registered falsification controls. Zero input produces an exactly zero Gramian; shoulder and wrist contributions add with maximum residual 5.18×10^{-12}; six direct nonlinear torque-pulse comparisons agree with their linearized step responses within 4.12×10^{-8} scaled state units; and input-step, integration-step, and equivalent-unit residuals remain below 4.12×10^{-10}, 1.27×10^{-7}, and 3.34×10^{-16}, respectively. A frozen-local countermodel evaluated on the same four phase windows differs from the trajectory-varying Gramian by 0.136–0.298 in relative norm. Thus a single operating-point approximation does not reproduce the registered finite-window authority even when phase and horizon are matched.

These are local, scale-dependent first-order diagnostics on one synthetic open-loop trajectory. They do not prove nonlinear or bounded-control reachability, controller superiority, human strength or neural allocation, passive negative torque, robustness to delay, fatigue or noise, or a coaching benefit. Those remain separate falsification gates.

22.6.4 Bounded Nonlinear Event Reachability

The next registered test replaces infinitesimal authority with finite bounded control perturbations. It uses four-interval multiple shooting and propagates every interval with the same exact RK4 operator as the parent trajectory. The decision variables are the two torque perturbations in each interval, the intermediate states, and a final partial-step duration constrained to the nominal crossing bracket. For scaled control perturbation $\delta\mathbf{u}_j$ and interval duration Δt_j, the declared objective is

$$J_u = \sum_j \Delta t_j \left\| \mathbf{S}_u^{-1} \delta\mathbf{u}_j \right\|_2^2, \tag{22.13}$$

subject to exact step continuity, the three-coordinate event-tangent target, ± 20 N m scenario bounds on each enabled torque channel, and 10,000 N m s^{-1} scenario slew limits. These bounds are model scenarios, not measurements of human torque or torque-rate capacity. An independently replayed trajectory, rather than the optimizer's internal state nodes, determines the final feasibility type.

The continuation matrix crosses seven symmetric tangent targets (0, ± 0.5, ± 1.0, and ± 2.0 mrad) with four matched channel masks: both torques, shoulder only, wrist only, and zero incremental authority. All 28 events remain unique and transverse. Thirty-two of the 38 total registered replays are feasible. The six infeasible outcomes are exactly the six displaced targets under the zero-authority killswitch; its nominal target remains feasible. Both enabled channels, either channel alone, the three- and five-segment meshes, 1, 2, and 4 ms RK4 steps, and both adverse initial states reach their registered targets. Across feasible cases, the largest independent event-tangent residual is 8.83×10^{-11}, below the declared 2×10^{-6} gate.

Feasibility does not qualify an optimum. Two converged starts for the same both-channel target return scaled objectives of 2.05356×10^{-8} and 2.56595×10^{-8}, a 24.9517% relative spread against the preregistered 5% gate. The study therefore releases the registered local feasibility result but suppresses channel, controller, effort, and optimality rankings. The fact that both one-channel masks reach all registered targets also supplies no basis for preferring a shoulder- or wrist-dominant strategy.

The result is restricted to one synthetic planar trajectory, one event guard, small tangent offsets, and an event time confined to the nominal crossing bracket. It does not map global nonlinear reachability, alternative crossing topology, delay, fatigue, noise, bilateral contact, passive negative torque, human actuation, participant behavior, or coaching benefit. Those remain separate model and governed-data falsification gates.

22.6.5 Global Event Topology, Delay, and Perturbation Robustness

The local crossing bracket is removed in the next registered test. A direction-aware global search retains every guard crossing over a common horizon and types absent, unique, multiple, grazing, initial-on-guard, and numerical-failure outcomes. It never substitutes the crossing nearest the nominal event. Causal delay uses an explicit linear-nodal policy, zero prehistory and posthistory commands, and a 0.60 s horizon long enough to retain the complete program at every delay from 0 to 200 ms.

Phase A applies matched synthetic perturbations to the initial state, sampled command, and event surface at dimensionless fractions 0.001, 0.005, and 0.01. All 6,336 nonzero replays retain one positive transverse crossing. Each cell preserves 96 of 96 independent antithetic pairs, with a 95% Wilson interval [0.961524,

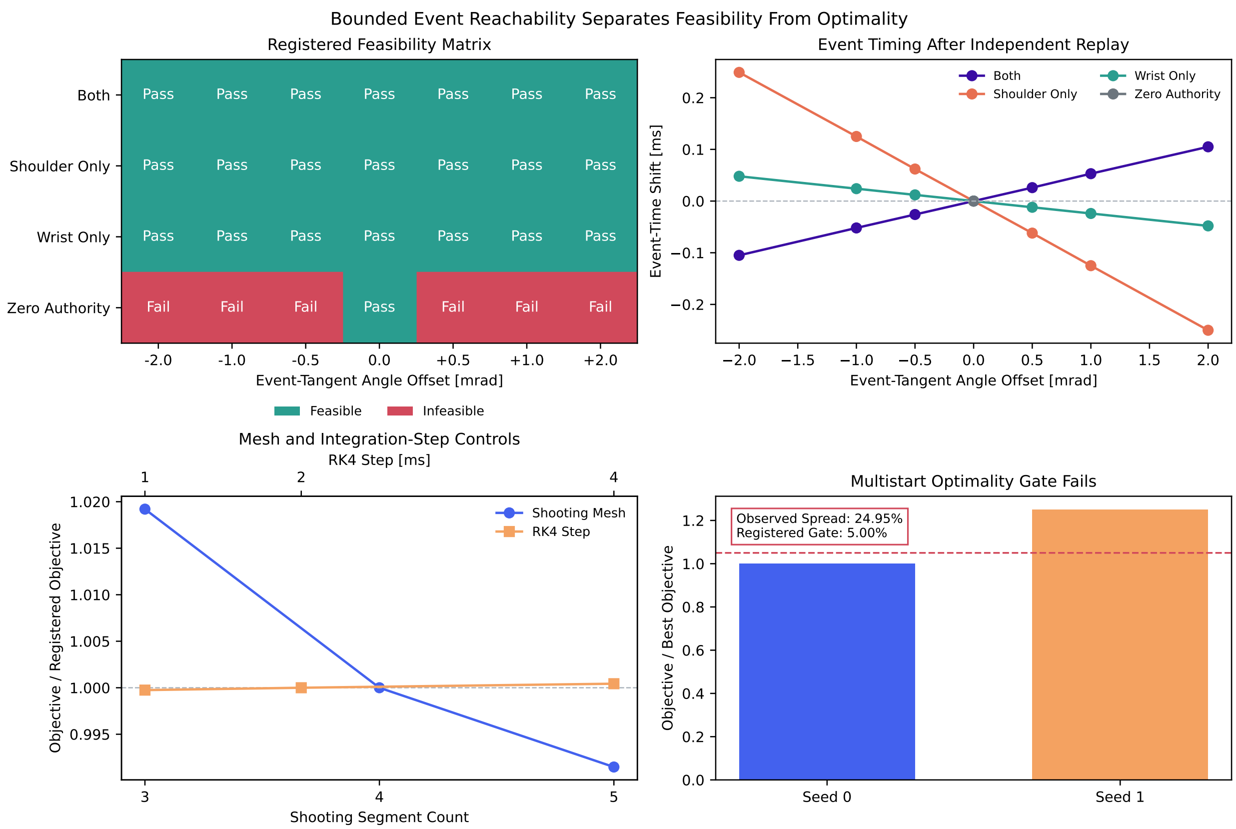

Figure 22.8: Bounded Event Reachability Separates Feasibility From Optimality

1.0]. This establishes topology preservation only for the declared small model stresses. It does not establish event-target accuracy or human robustness.

A separately preregistered Phase B extends the artificial stress ladder to 0.02, 0.05, 0.10, 0.20, and 0.50. The first topology loss occurs at fraction 0.02 and 200 ms, where one outcome is absent and 191 remain unique transverse. At fraction 0.50 and 200 ms, 118 are absent, seven have multiple crossings, and 67 remain unique transverse. Only 2 of 96 pairs preserve nominal topology. These dimensionless stresses map a synthetic failure region; they are not percentages of human motor variability.

Phase C applies the same 1% perturbation design through four generalized- coordinate masks: both torques, shoulder only, wrist only, and zero authority. Both and shoulder-only cases retain a unique positive crossing throughout. The wrist-only nominal crossing is unique through 40 ms and absent from 60 through 200 ms; zero authority is absent throughout and cannot acquire command torque through noise. Once wrist-only absence becomes nominal, its pairwise topology- preservation fraction rises again. Preserved absence is not crossing success.

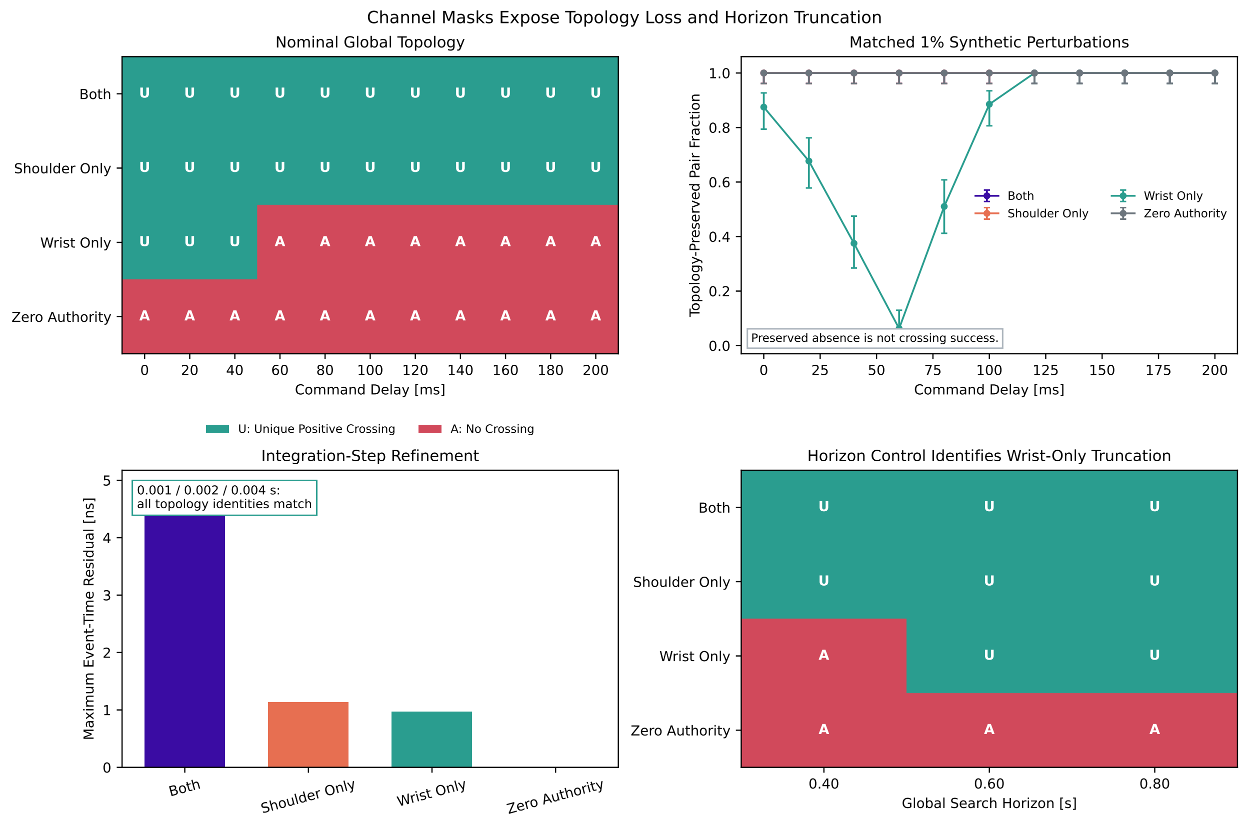

Figure 22.9: Channel Masks Expose Topology Loss and Horizon Truncation

Topology identity agrees across 1, 2, and 4 ms RK4 steps for every channel and delay. The 0.60 and 0.80 s horizons also agree. The 0.40 s horizon alone misses the wrist-only crossing that occurs at 0.579326 s on both expanded horizons; the discrepancy is therefore typed as horizon truncation rather than a mechanics threshold.

Event topology, event time/state, transversality, and clubhead speed remain separate from the parent bounded study's feasibility, target error, bound status, and control objective. Phase C has no independently registered work/power quadrature. It supports no anatomical isolation, human noise or fatigue interpretation, channel ranking, or coaching recommendation.

22.6.6 Prospective Nonlinear-Controller Qualification

The next step freezes a matched nonlinear-controller comparison without executing it. The registration digest-binds the analytical ODE plant and the trajectory-authority, bounded-reachability, and channel-topology parent artifacts. It declares nine controller families, 24 outcome-blind evaluation trials, eight disjoint tuning trials, common state and torque coordinates, scales, bounds, event logic, failure types, and a paired random-stream rule. Every family remains ineligible for ranking. Any comparability, adequacy, replay, convergence, optimality, event, or held-out failure suppresses the entire ranking rather than assigning a failed case a terminal score.

Before exposing the registered double-pendulum evaluation grid, one solver kernel is tested on a separate damped nonlinear fixture. Bounded projected first-order iLQR enforces the declared input bound inside each rollout, reduces the objective through nonincreasing accepted iterations, replays its states, controls, status, and cost exactly, and satisfies the frozen cold/warm sensitivity gate. The independent directional-derivative discrepancy is 1.05×10^{-11}, and the maximum observed bound violation is zero. A nonfinite dynamics return produces a typed failure with no trajectory. Collocation NMPC remains unimplemented; a bounded shooting method is not relabeled as that absent solver.

A separate transport test then applies four states and controls at 0.5, 1, and 2 ms. All 12 controller-facing RK4 steps match the canonical ODE backend exactly in the locked environment; repeated calls are identical, caller inputs are unchanged, and four wrong-size or nonfinite cases raise `ValueError` without a trajectory. Exact equality here is code-path parity, not independent physics validation, because both paths share the analytical equations and parameter authority.

These artifacts qualify registration, one manufactured solver kernel, and plant-step transport only. They contain zero registered double-pendulum controller evaluations and make zero methods ranking-eligible. Plant-specific derivatives, typed event and integration outcomes, outcome-blind tuning, matched replay, held-out execution, failure-region mapping, and adequate optimality evidence remain open. No result in this section establishes controller superiority, a clubhead-speed benefit, global optimality, human control, anatomy, fatigue, passive biological torque, safety, or coaching guidance.

22.7 Three-Dimensional Frame Audit

Planar vectors can be embedded in three dimensions and expressed in arbitrary proper frames. This is a necessary test because golf-model engines differ in axis conventions, quaternion ordering, angular-velocity frames, and wrench reference points. A correct adapter must preserve physical invariants even when every component changes (Featherstone 2008).

Figure 22.10 shows the delivery wrench in six rotated frames. The arrow components and apparent pose change, but force norm, couple norm, and total power do not. The transformation is performed on the complete wrench and twist, not on force alone.

This executed audit is three-dimensional algebra applied to a planar trajectory. It tests the frame-handling contract that an engine adapter must satisfy, but it does not itself exercise source-to-engine adapter parity. It also does not include out-of-plane angular velocity, long-axis club rotation, aerodynamic forces, three-dimensional joint motion, or full-body contact dynamics. Calling it a “3-D swing validation” would be incorrect.

22.8 Reduced Full-Body Common-State Inverse Dynamics

The spatial experiment in Section 17 uses 20 generalized coordinates, a separately moving six-coordinate club, bilateral arms, torso, pelvis, and lower-body mass. It evaluates 61 identical achieved states through MuJoCo and an independent Lagrange–Christoffel formulation. The common model hash, gravity, external loads, state, and required-action convention are identical.

The maximum relative generalized-action discrepancy is 2.14×10^{-11}. Reversing only the signed hand moment

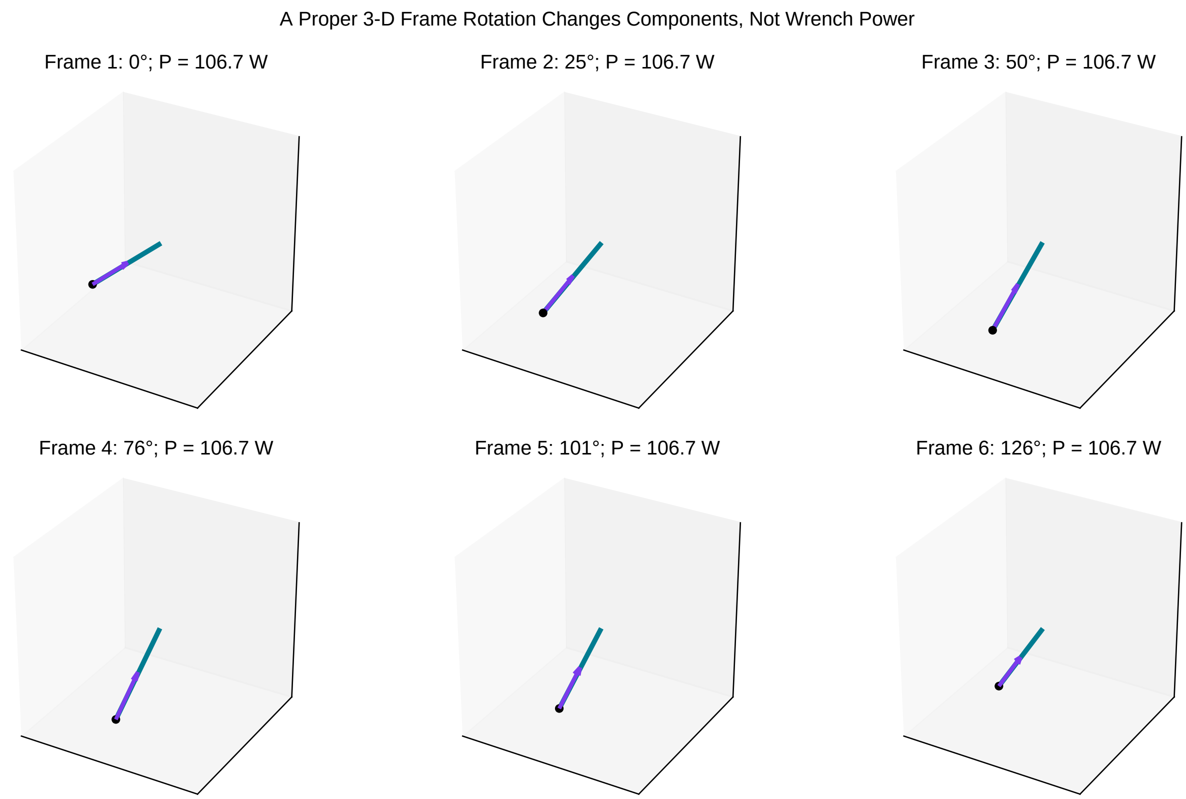

Figure 22.10: A Proper 3-D Frame Rotation Changes Components, Not Wrench Power

arm reverses the -4.32 N $\cdot$ m force-generated couple, and coincident application points remove that couple exactly. Unlike the rotated-wrench audit, this tier contains out-of-plane motion and state-dependent spatial mass and bias terms.

The result remains common-state inverse dynamics with prescribed hand loads. It does not solve closed contact, execute a zero-command forward branch, or identify passive biological load generation. The reduced forward-contact tier in Section 18 addresses the first two limitations without promoting either model to anatomical or biological evidence.

22.9 Reduced Spatial Forward Contact

The next tier replaces prescribed hand loads with two compliant point interfaces between finite-mass hand carriages and a free rigid club. MuJoCo and Pinocchio independently evaluate achieved kinematics, spatial-force mapping, mass, bias, gravity, and native forward dynamics. The two adapters share a hashed parameter record, contact law, semi-implicit update, and output schema.

In the exact same-state driver-killswitch branch, the complete grounded driver is removed at 0.180 s. The force-generated swing-normal couple remains negative for 37.5 ms in both engines and reaches approximately -0.409 N m. Coincident grips remove the couple exactly; reversed moment arms reverse its sign below 9.2×10^{-16} N m residual. Inertia-and-bias transport trajectory, wrench, orientation, and energy gates pass, and the work–energy residual decreases monotonically as timestep is halved.

This executes projected forward spatial contact at a reduced mechanism tier while transporting the same law and update through two native rigid-body operators. It does not execute independent native contact solvers or native integrators.

It does not add anatomical arms, subject-specific inertias, muscles, measured grip compliance, a distributed shaft, or human observations. The evidence boundary therefore moves from "forward contact unexecuted" to "reduced forward contact supported." The later articulated tier adds right-censored 5 ms bilateral and typed unilateral attachment results, including isolated opening and reattachment probes. Calibrated distributed contact and human transport remain untested.

22.10 What Survives, What Changes, and What Remains Open

The discrepancy matrix in Figure 22.11 summarizes the branched evidence boundary. Its cells are explicit capability memberships, not a triangular claim that every later model contains every earlier mechanism. Eleven bounded findings are supported somewhere in the executed ladder:

1. interaction force may remain nonzero under zero instantaneous distal command;
2. force magnitude does not determine power;
3. reference-point transport requires paired moment and velocity transport;
4. moving-base acceleration changes required reaction through supported mass;
5. closed-loop constraint rank determines admissible velocity dimension, not contact-force magnitude or couple sign;
6. nonplanar generalized action is reproducible across the two declared inverse-dynamics formulations;
7. reversing spatial contact moment-arm geometry reverses the force-generated club couple while coincident points remove it;
8. the negative force-generated couple persists after complete grounded-driver removal in the declared reduced spatial compliant-contact model; and
9. that forward-contact result transports through native MuJoCo and Pinocchio inertia-and-bias operators within declared trajectory, wrench, orientation, and energy regions while sharing its contact law and state update; and
10. typed dead-zone and preload choices can reverse whether the same articulated state is classified as open or taut, while explicit boundary probes reproduce opening and reattachment in both native engines; and

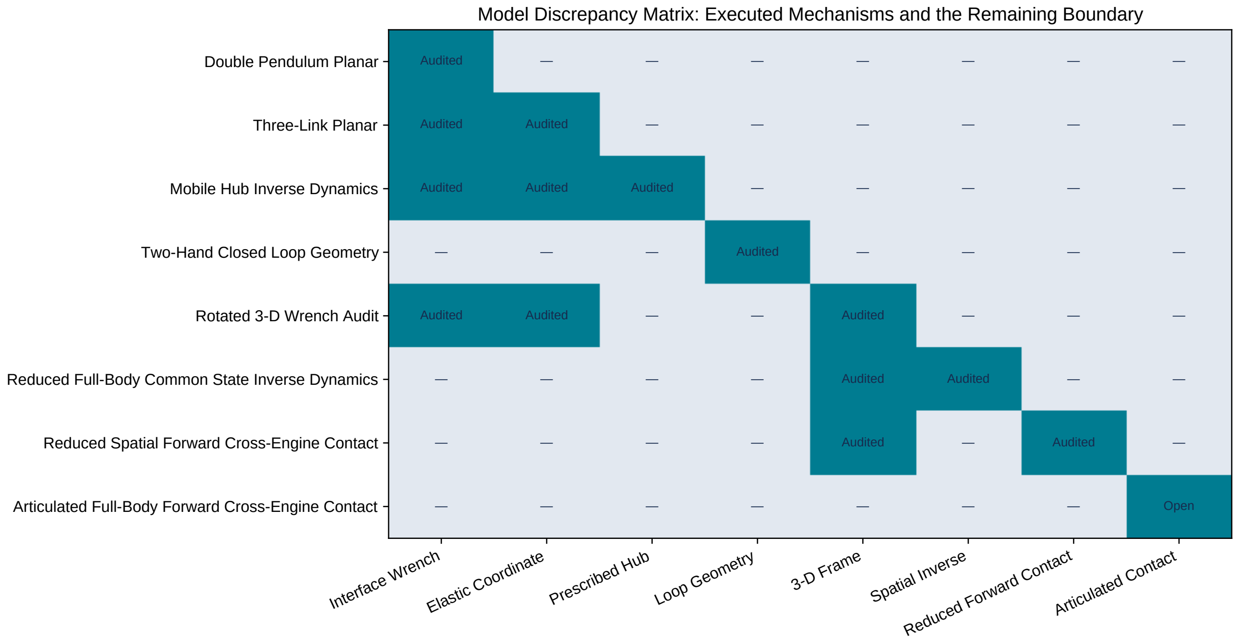

Figure 22.11: Model Discrepancy Matrix: Executed Mechanisms and the Remaining Boundary

11. finite base translation and intrinsic free moment are mechanically active under the declared passive law, although the preregistered fixed–coupled total-work match admits no cell and therefore identifies no delivery effect.

Other claims do not yet survive because they have not been tested. The present analysis does not show that the reduced result survives anatomical arms, that the synthetic shaft/support values are calibrated, or that independently authored native humanoid models produce matched human force histories. Those are separate structural and empirical questions.

22.10.1 Tier-by-Tier Interpretation

Planar Double Pendulum. This tier supplies the smallest model in which a proximal constraint force can do work on a distal body. Its strength is exact interpretability: radial and tangential projections, matched-state counterfactuals, and interface work can be checked directly. Its weakness is structural. A fixed hub and single wrist collapse torso motion, two-hand closure, and shaft deformation into omitted or prescribed effects. The tier can establish a mechanism but cannot determine its magnitude in a golfer.

Three-Coordinate Planar Chain. Adding the third coordinate introduces a second interface and an internal storage mode. The common schema remains valid, and total interface power remains the sum of force and couple power. The tier demonstrates that a locally large elastic acceleration contribution need not be a large net energy source. Because the added coordinate represents lumped shaft flex rather than an independently actuated torso, conclusions about proximal segment strategy remain provisional.

Prescribed Mobile Hub. Translating the base demonstrates that "proximal" motion changes both the reaction necessary to accelerate distal mass and the velocity used in force power. Holding the relative trace fixed isolates that inverse-dynamics effect. It also prevents a stronger claim: in a forward model, hub motion and joint motion co-evolve, so the calculated 38.09 W maximum power shift is not an expected benefit of a particular body translation.

Two-Hand Closed Loop. Constraint rank and nullspace dimension formalize the kinematic closure that a single-wrist pendulum omits. The audit shows one locally feasible velocity coordinate for the declared four-constraint, five-coordinate geometry. It does not solve for constraint multipliers. The Jacobian therefore supplies a geometry contract but no force attribution. The archived WSCG, forward constrained, and coupled-base tiers provide three separate dynamic force records with different model boundaries.

Rotated Three-Dimensional Wrench. The proper-rotation audit verifies paired wrench–twist rotations and reference transport before an engine comparison is interpreted physically. It would expose inconsistent transformation of force, moment, velocity, or angular velocity. Because it does not inject improper reflections or exercise adapter metadata, it cannot detect every semantic axis swap or source-to-engine mapping error. Passing it establishes only the tested coordinate consistency. Out-of-plane dynamics require nonplanar states and forces, not merely three stored vector components.

Reduced Full-Body Common-State Dynamics. This tier aligns the model digest, joint order, state, gravity, external loads, and inverse-dynamics estimand. It therefore isolates implementation transport and executes genuine out-of-plane dynamics. Its agreement is not anatomical validation because the model is reduced and its hand loads are prescribed.

Reduced Spatial Forward Contact. This tier adds projected two-hand compliance, state divergence, a same-state driver killswitch, long-axis rotation, swing-plane evolution, and reduced ground-pathway bookkeeping. It transports the declared mechanism through two native inertia-and-bias operators while sharing the contact law and state update. A separate MuJoCo-native equality-and-integrator control establishes a nonzero formulation discrepancy rather than contact-solver parity. The tier's hand carriages and declared contact law prevent anatomical, tissue, muscle, or human inference.

Articulated Finite Ground and Free Moment. This tier adds planar base translation and pitch to the closed-state articulated body, distributed grip, and passive first-mode shaft. The support force, intrinsic free moment, reference-transported moment, storage, damping, and augmented inertia/gravity ledger are explicit. All 576 trajectories pass their declared numerical and native-engine gates, but the primary fixed–coupled total-work match admits no cell. The tier therefore qualifies the finite-base mechanism and exposes an adverse identifiability result; it does not establish a ground-use benefit.

Articulated Full-Body Forward Contact. This tier remains open because it must replace the carriages with subject-scaled articulated arms, retain independently solved two-hand contact, and preserve event alignment without changing the observable. Contact calibration, stabilization, actuation, and anatomical uncertainty must be registered before the preferred outcome is inspected.

22.10.2 Operator-Transport Gate Definition

The executed common-state comparison did not begin with visually similar motion. It required identical model hashes and checked generalized action, wrench power, geometry interventions, and event timing. A forward comparison must retain those checks and additionally pass, at minimum:

- frame and reference-point metadata equality;
- force and moment balance residuals below declared absolute and relative tolerances;
- constraint rank and nullspace agreement away from singular events;
- wrench-power agreement after reference transport;
- matched gravity, damping, actuator, and contact settings; and
- an event-aligned comparison that distinguishes interpolation error from trajectory divergence.

Engine capability is not evidence that the comparison was run. The machine-readable discrepancy table separately marks reduced full-body common-state inverse dynamics and reduced two-engine forward contact as `executed`; articulated full-body forward contact remains `not_executed`. This split prevents a carriage-model result from silently becoming an anatomical claim.

22.11 Strategy Implications Across the Ladder

The higher-order audits reinforce a conditional strategy statement. Creating clubhead speed is not equivalent to maximizing a single joint force, delaying release by a fixed time, or producing a particular torque sign.

Useful transfer requires the complete interaction wrench to align with the distal twist during the intended delivery interval.

A moving hub can alter both reaction and force power even when relative joint motion is held fixed. A two-hand loop can restrict admissible motion while still allowing a large opposed-force mode. A third coordinate can store energy and change timing without being a net source. A frame rotation can reverse or mix plotted components without changing physical power.

The practical model-building consequence is direct: optimize and report an event-window objective with force, couple, power, work, and constraint diagnostics together. A strategy that looks favorable only in one coordinate, reference point, or instantaneous sample has not yet demonstrated robust transfer.

22.12 Limitations and Next Falsification Tests

The ladder remains deliberately incomplete:

- the three-link trace remains an arm–proximal-shaft–distal-head surrogate;
- the original hub comparison remains prescribed, although the newer coupled tier evolves a finite-mass translating base;
- the forward two-hand tiers use ideal planar point constraints and declared mechanism-study parameters rather than anatomical or contact calibration;
- the coupled club has one lumped torsional mode rather than a distributed spatial beam;
- the reduced full-body tier uses prescribed hand loads and spherical inertia elements rather than solved contact and subject-specific anatomy; and
- the reduced forward spatial tier uses two translational hand carriages; the subject-scaled articulated tier now advances one-, three-, and five-fiber tension grips through 50 ms, but those fibers remain frictionless engineering lines with state-registered free lengths rather than measured pressure, fingers, or tissue; and
- the newest articulated branch adds separately qualified first-mode bending and torsion to the distributed grip; the subsequent finite-base branch adds planar ground force and intrinsic free moment, but all shaft/support parameters remain synthetic and the ground law is linear and bilateral.

The next decisive model test replaces the synthetic bilateral support with calibrated unilateral foot contact and force-plate observations while retaining the common wrench, power, initialization, killswitch, refinement, and independent-engine schema. Failure of force/moment balance, power invariance, contact-rank agreement, refinement, or participant-held-out prediction would falsify transport of the reduced mechanism.

Chapter 23

Reference Frames, Biological Mechanisms, and the Multi-Engine Ladder

23.1 Why This Bridge Is Necessary

The preceding model ladder establishes increasingly demanding mechanical claims. It does not yet make two transitions that are essential for an advanced interpretation. First, the same physical interaction must survive changes in coordinates, point of application, and engine convention. Second, a generalized joint moment must be related to muscle activation without pretending that inverse dynamics identifies a unique biological cause.

These transitions are connected. A force, moment, velocity, or activation is only useful if its frame, reference point, sign, units, and model tier are declared. Figure 23.1 uses one semantic visual language across four phases: dark segments are the mechanical chain, green and blue segments distinguish modeled bilateral pathways, the gold point is the grip reference, the orange point is the clubhead, and the magenta arrow is the force component tangent to the club path. The drawings explain geometry; they are not reconstructed human kinematics.

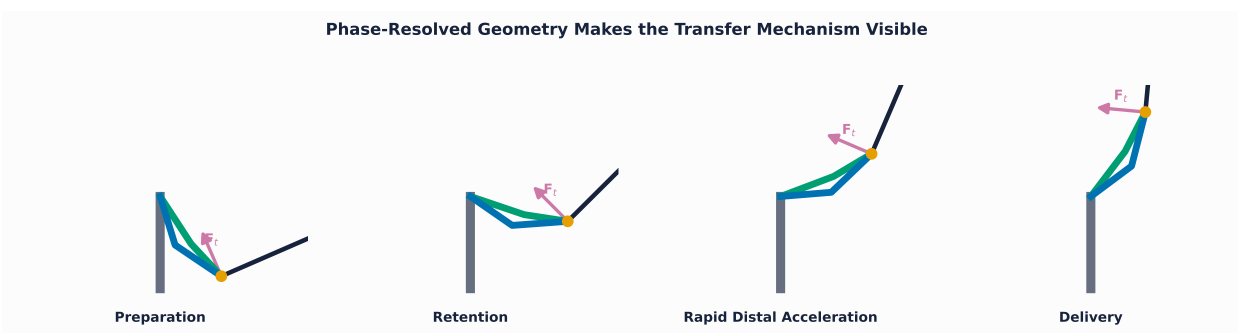

Figure 23.1: Phase-Resolved Geometry of the Advanced Model

The executable evidence is generated by `run_advanced_biological_bridge.py`, stored in the `JSON summary` and `NPZ trace archive`, and tracked under epic #8505.

23.2 The Normative Mechanical Convention

All frames in this chapter are right-handed Cartesian frames. A spatial wrench is ordered force first and couple second,

$$\mathsf{W}_A = \begin{bmatrix} \mathbf{F} \\ \mathbf{M}_A \end{bmatrix}, \tag{23.1}$$

and a spatial twist is ordered linear velocity first and angular velocity second,

$$\mathsf{V}_A = \begin{bmatrix} \mathbf{v}_A \\ \omega \end{bmatrix}. \tag{23.2}$$

The subscript is a reference point, not a coordinate index. The force and angular velocity do not change when the same physical wrench and rigid-body motion are transported from point A to point B, but the couple and point velocity do:

$$\mathbf{M}_B = \mathbf{M}_A - (\mathbf{r}_B - \mathbf{r}_A) \times \mathbf{F}, \qquad \mathbf{v}_B = \mathbf{v}_A + \omega \times (\mathbf{r}_B - \mathbf{r}_A). \tag{23.3}$$

Substitution gives the invariant scalar pairing

$$P_A = \mathbf{F} \cdot \mathbf{v}_A + \mathbf{M}_A \cdot \omega = \mathbf{F} \cdot \mathbf{v}_B + \mathbf{M}_B \cdot \omega = P_B. \tag{23.4}$$

Under a proper rotation $\mathbf{R}$, every polar vector and axial vector used here is expressed as $\mathbf{x}' = \mathbf{R}\mathbf{x}$. Consequently dot and cross products, force norm, couple norm, and total power are unchanged. This is a coordinate change. Reversing a hand moment arm, moving a physical contact, or changing a trajectory is instead a different mechanical system.

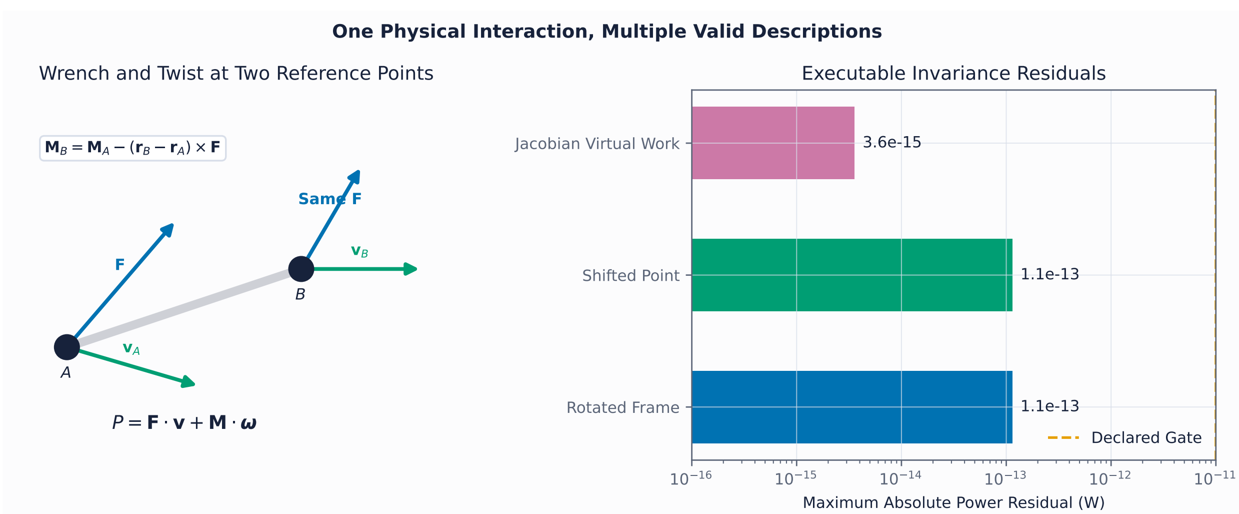

Figure 23.2: Power Is Invariant Under Consistent Frame and Reference-Point Changes

The deterministic audit in Figure 23.2 rotates two arbitrary three-dimensional samples, transports each to another point, and independently checks Jacobian virtual work. The largest rotation and point-transport power residuals are 1.14×10^{-13} W; the largest residual in

$$\tau = \mathbf{J}^T \mathsf{W}, \qquad \tau^T \dot{\mathbf{q}} = \mathsf{W}^T \mathbf{J} \dot{\mathbf{q}} \tag{23.5}$$

is 3.55×10^{-15} W. These are floating-point closure tests, not measured accuracy. They establish that an engine adapter is not allowed to change the physical power merely by changing quaternion order, angular-velocity frame, wrench order, or moment reference.

23.3 From Generalized Moments to Muscle Redundancy

Inverse dynamics supplies a net generalized moment only after the model, kinematics, inertial parameters, external loads, and constraints are fixed. It does not identify a unique muscle activation vector. For muscle forces $\mathbf{f}_m \geq 0$ and moment-arm matrix $\mathbf{R}_m(\mathbf{q})$,

$$\tau_m = \mathbf{R}_m(\mathbf{q})\mathbf{f}_m. \tag{23.6}$$

If the number of muscles exceeds the number of joint moments, any null-space component $\mathbf{N}\eta$ satisfying $\mathbf{R}_m\mathbf{N} = \mathbf{0}$ changes internal force without changing the observed moment:

$$\mathbf{f}_m = \mathbf{f}_m^{\dagger} + \mathbf{N}\eta. \tag{23.7}$$

The reduced example uses the repository's Hill-type force law and an agonist– antagonist pair at optimal fiber length and zero fiber velocity (Zajac and Gordon 1989). The activation family is selected so that positive- and negative-moment forces always produce the same 10 N m net task. Across 41 allocations, maximum moment closure error is 1.78×10^{-15} N m. Nevertheless, the declared stiffness proxy rises from 3.33 to 23.33 N m rad^{-1} and series-elastic energy from 0.208 to 5.208 J.

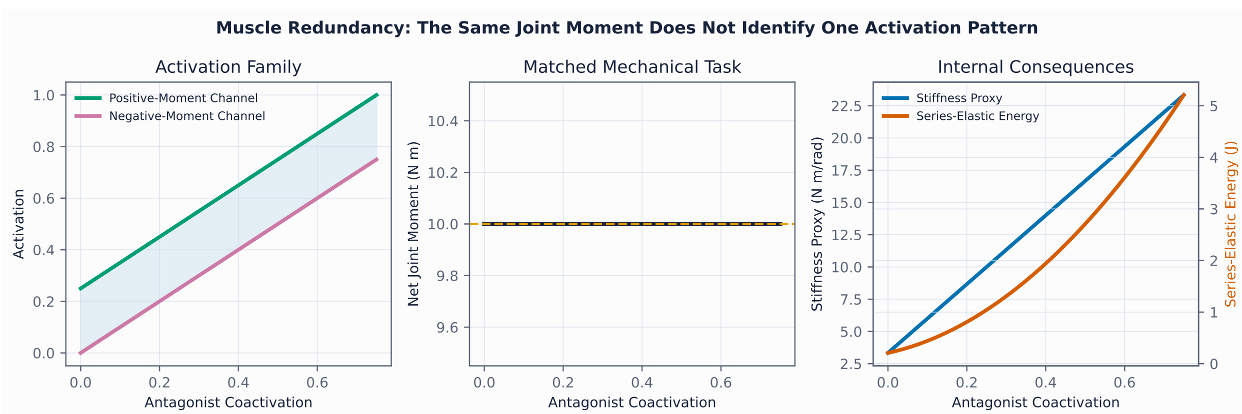

Figure 23.3: Different Muscle Activations Produce the Same Net Joint Moment

This result is an identifiability warning. It does not show that greater co-contraction is preferable. Additional internal force may improve robustness or short-range stiffness, but it also increases energetic demand and tissue loading. The objective must declare which consequence it values.

23.4 Activation Dynamics and Preparation History

The abstract dead-zone experiment in Section 14 isolates one meaning of slack. The present bridge adds a different family: first-order neural excitation-to-activation dynamics, Hill-type active force, and first-order series-force development. For muscle i,

$$\dot{a}_i = \frac{u_i - a_i}{T_i(u_i, a_i)}, \qquad F_i = F_{\max,i}\left[a_i f_{\ell,i}(\ell_i) f_{v,i}(v_i) + f_{p,i}(\ell_i)\right], \tag{23.8}$$

and the reduced transmitted series force obeys

$$\dot{F}_{t,i} = \frac{F_i - F_{t,i}}{T_{t,i}}. \tag{23.9}$$

Two programs share a 6 N m preparation target, a 10 N m delivery target, a 180 ms preparation interval, and identical muscle parameters. The persistent program retains positive arm and negative wrist channel directions. The complete role reversal changes both signs. No internal state is reset at the transition.

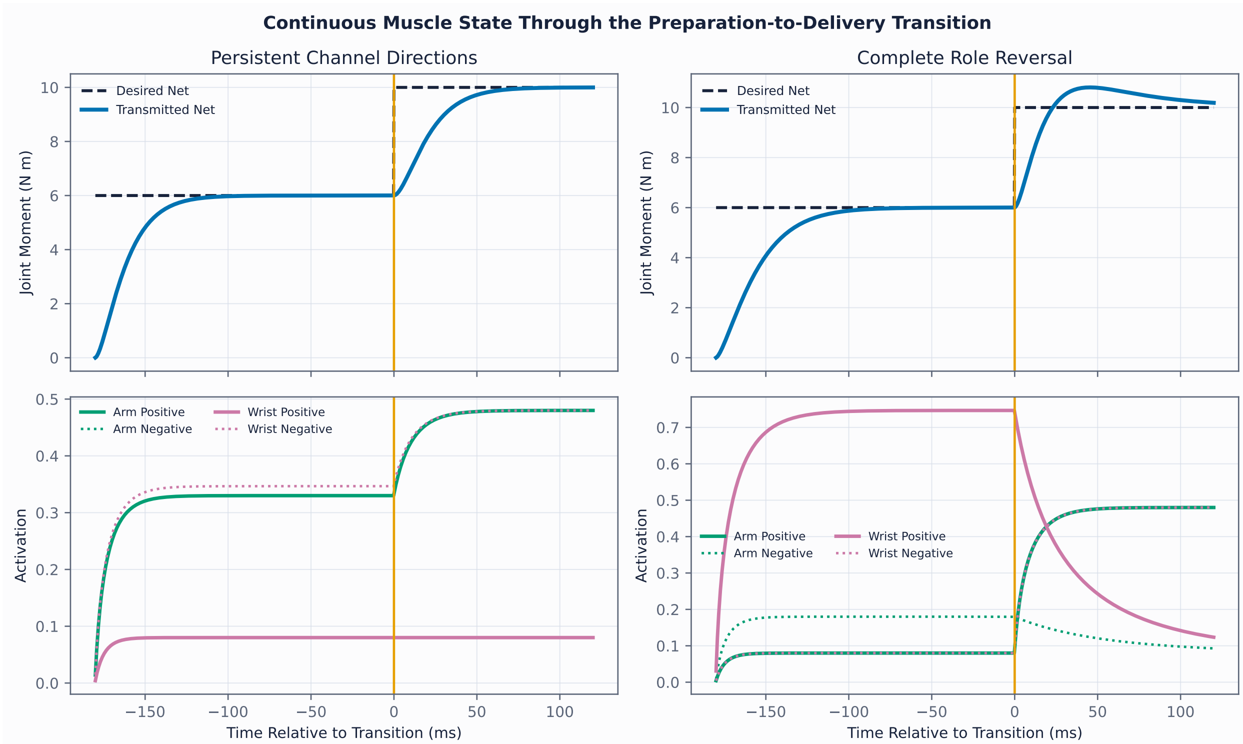

Figure 23.4: Activation and Net Moment Through Persistent and Role-Reversal Programs

The persistent program has a post-transition absolute torque-error impulse of 0.08998 N m s, versus 0.09084 N m s for complete reversal. The numerical difference is 0.94% at the published 0.2 ms step, model-dependent, and not a performance claim. Refinement from 1.0 to 0.05 ms preserves its direction but reduces its magnitude from 0.00277 to 0.000514 N m s; the advantage is therefore not numerically converged. Its defensible value is logical: activation and series-force states make role history observable even when pre- and post-transition net moments match. This example motivates a preparation-history hypothesis but does not establish a robust benefit, a scapular mechanism, or a passive wrist.

The biological term *slack* should therefore be avoided unless the measured quantity is named. Appropriate alternatives include contact gap, tendon slack length, series strain, low tangent stiffness, low activation, delayed force development, or loss of grip pressure. Those variables can have different signs and consequences.

23.5 A Question-to-Engine Model Ladder

No one backend should be treated as a truth machine. The scientific question selects the backend, while common observables make comparisons possible.

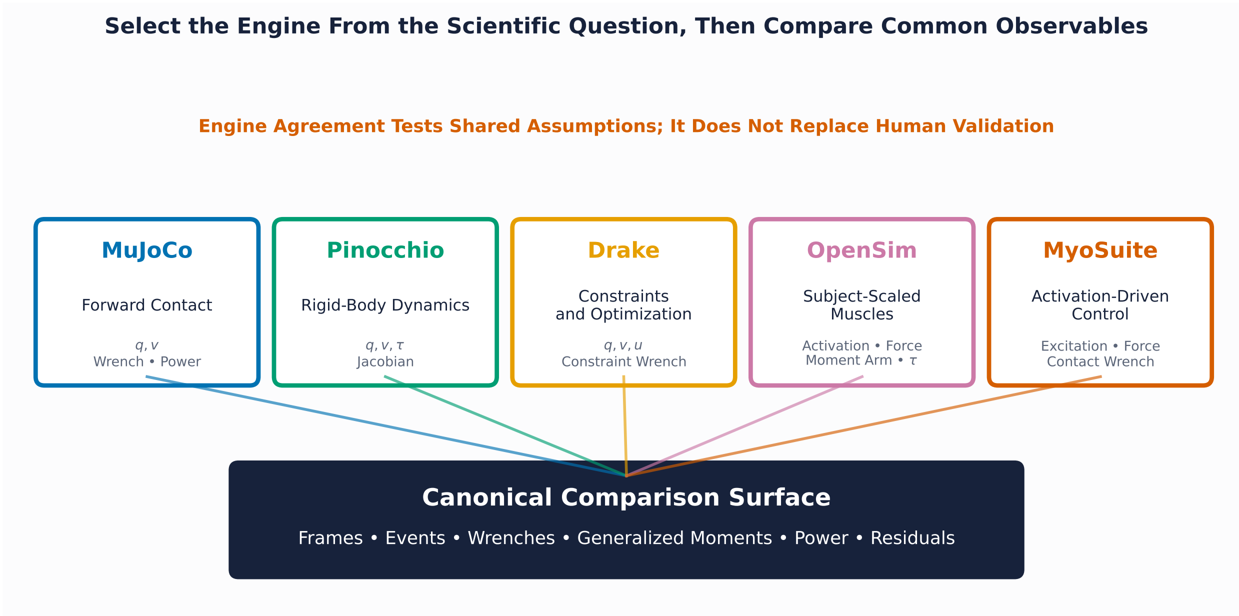

Figure 23.5: Engine Roles and Their Canonical Comparison Surface

Engine	Best-Fit Question in This Program	Current Evidence Boundary
MuJoCo	Does compliant contact generate the predicted achieved wrench in forward dynamics?	Executed for the reduced carriage–club model in Section 18; not an anatomical grip
Pinocchio	Do fast rigid-body Jacobians, RNEA, and ABA reproduce the same reduced mechanism?	Executed for the reduced forward-contact tier; contact is a declared external model
Drake	Which trajectories and constraints satisfy a registered objective under alternative contact assumptions?	Repository capability and an actionable next validation tier; no new Drake result is claimed here
OpenSim	Which subject-scaled muscle paths, moment arms, and activations can produce the inferred joint moments?	Repository capability and proposed subject-scaled validation; the reduced Hill bridge is not an OpenSim human model
MyoSuite	Can activation-driven muscles and contact reproduce the preparation and reversal effects in forward simulation?	Repository capability and proposed activation-driven validation; no human strategy has been learned or inferred

This division of labor also prevents false independence. MuJoCo and MyoSuite share important computational structure; OpenSim and the reduced bridge may share Hill-type assumptions; and every engine can inherit the same geometry, inertial, contact, or measurement error. Agreement is valuable only after the shared and differing assumptions are listed.

23.5.1 An Executed Common-Pose Convention Check

The repository's five canonical-pose adapters were exercised on one nonzero pelvis pose and four nonzero joint rotations. Each adapter encoded the same state into its native coordinate vector and decoded it back to the canonical representation. The native coordinate-vector sizes were 31 for MuJoCo, Pinocchio, and MyoSuite, 36 for Drake, and 30 for OpenSim. Across all five round trips, the maximum translation error was zero, the maximum rotation error was 3.56×10^{-15} degrees, and the maximum joint-coordinate error was 8.89×10^{-16} degrees.

This is an executed **representation** check. It verifies the adapter maps used to state a common pose; it does not execute five dynamics engines, compare contact solutions, validate anatomical coordinates, or establish trajectory parity. Those stronger claims require the common observables in the table plus model hashes, event definitions, integrator settings, and residual reports.

23.6 Connections to the AffineDrift Texts

This chapter is the application layer for several companion explanations:

- The Language of Motion introduces coordinates and velocities;
- Forces and Torques develops moments and power;
- The Affine Structure explains drift and control without assigning intent to either term;
- Constraint Forces and Parallel Mechanisms develop reaction and loop-closure mechanics;
- The Triple Pendulum adds the wrist coordinate;
- Passive and Distributed Control provides the biological-control context; and
- Induced Acceleration Analysis shows how a modeled force or moment contributes to acceleration without claiming unique anatomical causation.

The unifying AffineDrift point is precise: decompositions depend on the chosen state, inputs, constraints, and coordinates, while a correctly transported physical scalar such as instantaneous power does not. A useful decomposition must expose both its representation and its invariants.

23.7 Falsification and Next Executable Models

The current repository makes the following extensions actionable now:

1. map a common measured trajectory into the canonical pose contract and audit Jacobian, generalized moment, wrench, and power conventions in each available backend, extending the executed pose-only round trips to dynamic-state parity;
2. use OpenSim moment arms and muscle paths to replace the constant moment arms in Equation 23.6, then compare feasible activation families rather than one optimizer-selected solution;
3. reproduce the same excitation histories in MyoSuite and test whether contact, activation, force, and joint-moment traces preserve the reduced prediction;
4. use Drake to optimize registered multi-objective trajectories over speed, face/path proxy, effort, tissue load, and robustness rather than speed alone;
5. retain MuJoCo and Pinocchio as forward-contact and rigid-body cross-checks, with common event definitions and power residuals; and
6. fit no biological parameter until synchronized bilateral grip wrenches, kinematics, shaft strain, EMG, and participant identity-safe holdouts are available.

The reduced prediction is refuted if its matched moments do not close, its coordinate transformations alter power, or the sign of the preparation effect disappears under a preregistered parameter and timestep domain. Its magnitude must not be used quantitatively until a convergence study and parameter uncertainty analysis establish a stable interval. A proposed human mechanism is separately refuted if measured participants do not exhibit its preregistered force, stiffness, and activation history. Backend disagreement should first be classified as a convention, numerical, structural, parameter, or data discrepancy; it is not automatically biological evidence.

Chapter 24

Transmission Pathways, Robust Speed, and Task Stability

24.1 Why a Second Adversarial Pass Is Necessary

The preceding model ladder makes a bounded mechanical case: interaction forces, constraint reactions, separated hand forces, and elastic states can transmit power to the distal system, and delayed distal actuation can outperform early drive in several declared models. Those results do **not** establish that the fastest nominal program is repeatable, that low joint variability is desirable, that a negative torque removes energy, or that a human strategy is self-stabilizing. This chapter therefore asks a different question: *which transmission variables can be manipulated, and how do speed, variability, loading, and perturbation rejection trade against one another?*

The full finding-by-finding adjudication is published in `ADVERSARIAL_TRANSMISSION_REVIEW.md`, and the numerical record is `transmission_robustness_study.json`.

24.2 A Pathway Ledger Rather Than a Single Transfer Number

Let S be the distal subsystem and let every wrench be expressed at a declared point in a declared frame. Its mechanical-energy balance is

$$\Delta E_S = \underbrace{\int \mathbf{F}_J \cdot \mathbf{v}_J \, dt}_{W_{\text{constraint}}} + \underbrace{\int \tau_J \cdot \omega_S \, dt}_{W_{\text{direct}}} + \underbrace{\Delta U_{\text{shaft}}}_{W_{\text{elastic}}} + \underbrace{W_g}_{\text{gravity}} - \underbrace{D}_{\text{dissipation}} + \varepsilon_E.$$

For the whole constrained model, external control work, gravity (already in potential energy), damping, and projection correction replace internal contact work, which cancels by ideal-constraint power. The present 4 ms projected integrator has a worst normalized work–energy residual of 3.77%; that is a declared numerical limitation, not a machine-precision closure claim. The two-point contact-power identity itself closes to 6.40×10^{-14} W. Future strategy comparisons should report both.

This ledger produces a useful hierarchy of manipulable variables:

- **Timing and phase:** clock onset, configuration threshold, phase estimate, torque slope, and activation delay;
- **Geometry:** hand path, grip separation, moment arms, club orientation, and the reference point at which a wrench is resolved;
- **Mechanical state:** proximal angular momentum, relative wrist state, shaft strain energy, base motion, and hand-force common/differential modes;

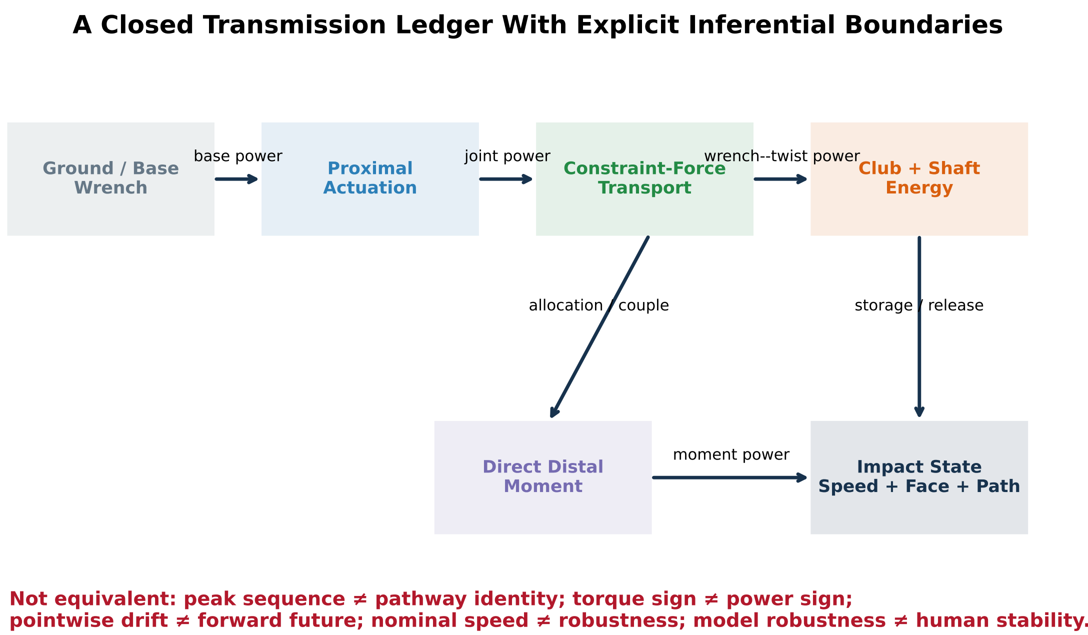

Figure 24.1: The transmission ledger distinguishes pathway identity from kinematic sequence, torque sign from power sign, pointwise drift from a forward future, and model robustness from human stability.

- **Regulation:** impedance, damping, feedback gain, sensory/observer delay, saturation, and task-dependent error coordinates;
- **Equipment and subject parameters:** inertia distribution, shaft stiffness/damping, anthropometry, strength, and contact properties.

No scalar "transfer efficiency" uniquely identifies these pathways without an explicit numerator, denominator, boundary, and time interval.

24.3 Paired Perturbations and Held-Out Evaluation

Four preregistered programs were evaluated in the existing moving-base, two-hand, compliant-club tier: clock-triggered restrain-then-drive, arm-angle-triggered handoff, the same state trigger with higher impedance, and early drive. Ten training and fifteen held-out perturbations varied initial arm and wrist angles and velocities, command scale, activation delay, shaft stiffness, and grip separation. Every program received the same samples (common random numbers). Outcomes were lower-tail delivery speed, speed dispersion, a planar face/path proxy, peak hand force, squared-torque effort, event time, late contact work, late direct-wrist work, and shaft-energy release.

All four programs remain Pareto-nondominated. Relative to the clock trigger, the state trigger increases held-out 10th-percentile delivery speed from 4.94 to 5.28 m/s, reduces mean face/path proxy error from 9.44 to 2.29 degrees, and slightly reduces delivery-speed amplification. It also raises the 90th-percentile peak hand force from 166.9 to 208.1 N. Higher impedance raises nominal speed to 5.78 m/s and reduces mean face/path proxy error to 1.26 degrees, but does not minimize speed dispersion. Early drive has the smallest speed standard deviation only because it occupies a much slower regime; low variance around a poor mean is not robust performance.

This membership is stable to the available held-out cases: recomputing all five objectives after omitting each of the fifteen cases leaves all four programs nondominated in every recomputation. That is stability of a four-program comparison, not evidence that the Pareto frontier is complete; unexamined controls can still

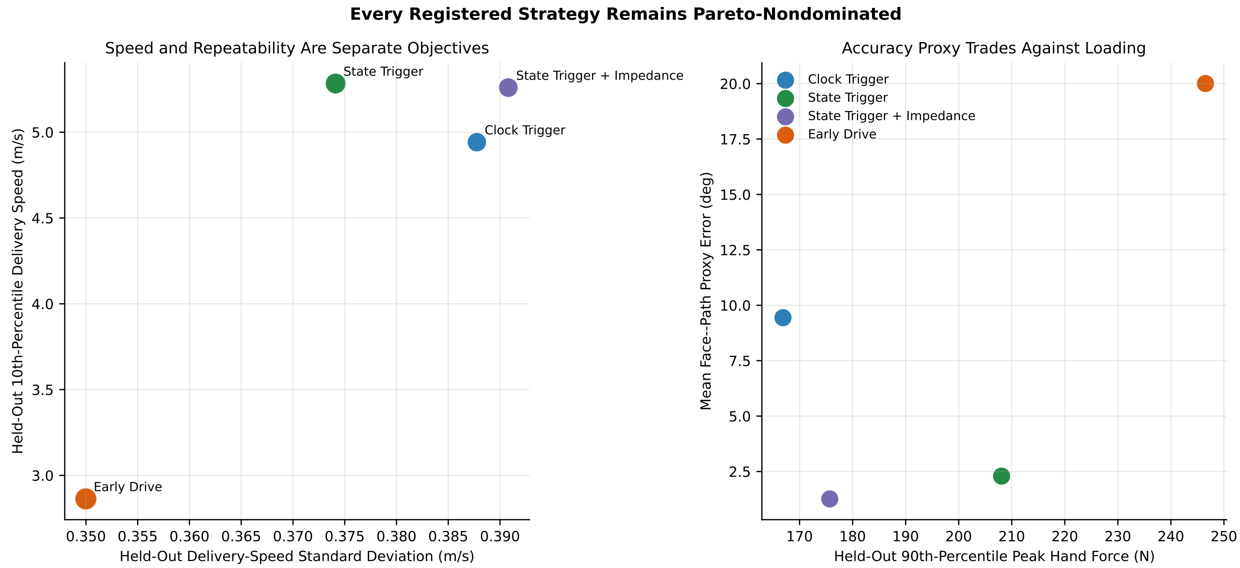

Figure 24.2: Held-out lower-tail speed and dispersion do not select the same program, and face/path error trades against peak hand force. Marker size in the left panel increases with peak-force exposure.

dominate the registered set.

These results justify only a model-conditional statement: triggering on a mechanical state can reduce sensitivity to clock-time variation because the transition follows the realized trajectory, but the same change can redirect the disturbance into contact loading. A self-stabilizing strategy must specify the task error it attenuates and the costs it is allowed to increase.

24.4 Task-Null Variability and Motor Abundance

Movement variability is not synonymous with outcome error. Golf data show that marker-trajectory variability need not correlate with ball-speed variability (Tucker, Anderson, and Kenny 2014), and uncontrolled-manifold analysis has found greater task-compatible variance in more skilled golfers (Morrison, McGrath, and Wallace 2016). This agrees with the broader principle of motor abundance: variability parallel to a task solution manifold can preserve a salient outcome, whereas variability orthogonal to it changes the outcome (Latash et al. 2010).

For local inputs $\mathbf{x}$ and task outcomes $\mathbf{y}$,

$$\delta\mathbf{y} \approx \mathbf{J}_y\,\delta\mathbf{x}, \qquad \mathcal{N} = \ker(\mathbf{J}_y).$$

The eight-input, three-outcome local map has rank three and nullity five. Under the held-out perturbation covariance, projected task-null variance is 0.1322 and task-relevant variance is 0.00466, giving the declared local index

$$\Delta V = \frac{V_{\mathcal{N}} - V_{\perp}}{V_{\mathcal{N}} + V_{\perp}} = 0.932.$$

The result is descriptive and local. Curvature can make a direction that is null infinitesimally task-relevant at larger amplitude. The correct future test is therefore trial-level covariance relative to a nonlinear, participant-specific impact manifold—not a recommendation to minimize all joint variance. The raw, unit-dependent singular values are 1141.3, 60.36, and 7.75. Relative thresholds give effective rank two at 1% and 5% of the

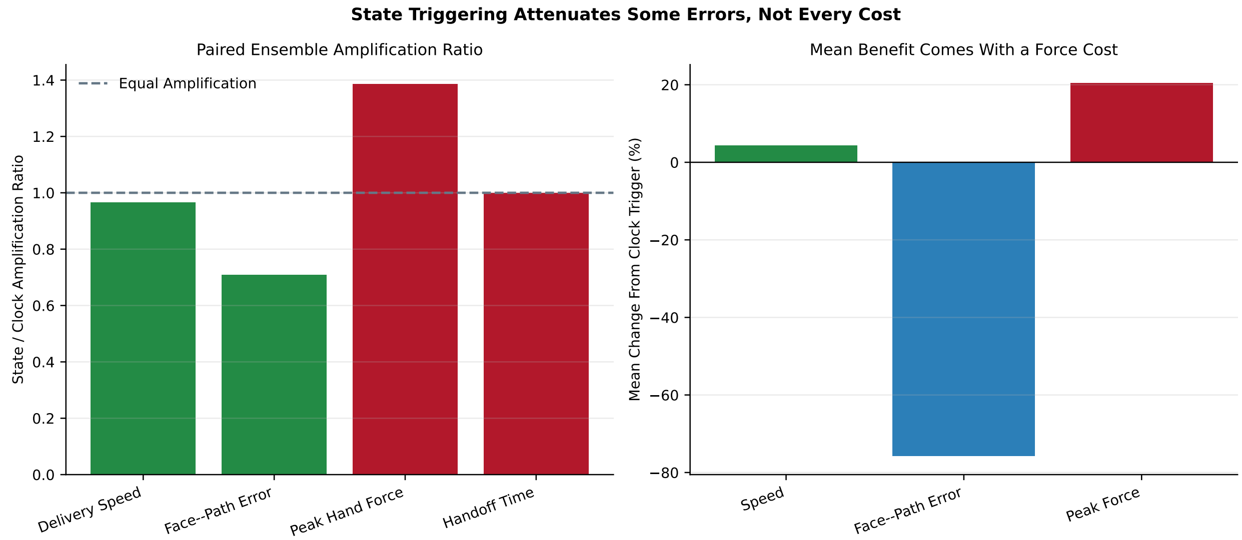

Figure 24.3: State-triggered handoff reduces speed and face/path amplification relative to clock timing but amplifies peak hand force. The right panel expresses paired mean changes as percentages so unlike units are not visually conflated.

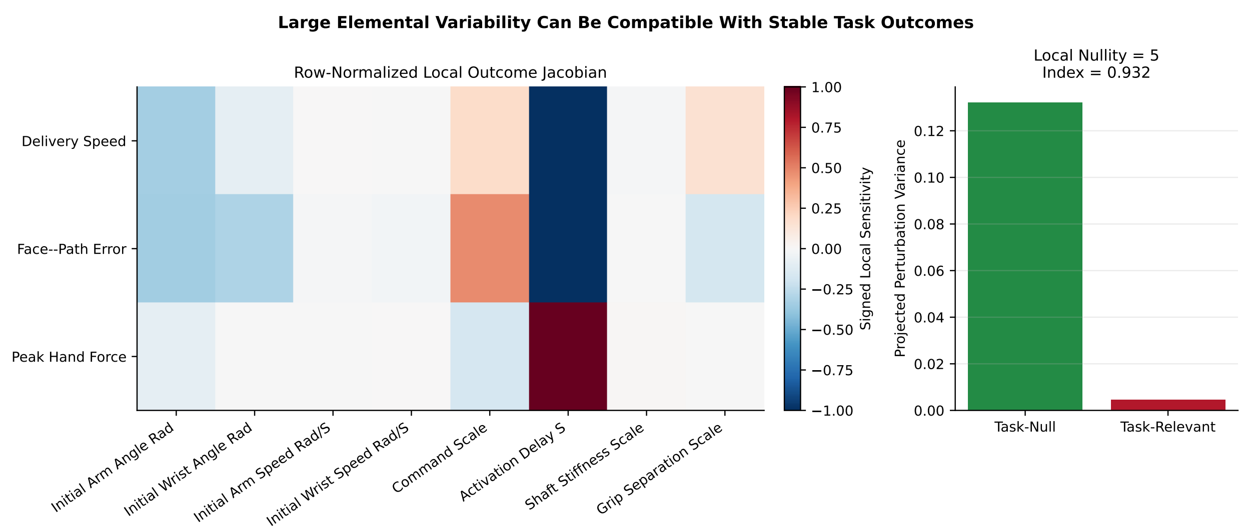

Figure 24.4: The local outcome Jacobian identifies task-sensitive input directions and a five-dimensional null space. This is a model input–outcome partition, not evidence of a neural synergy.

leading singular value, and rank one at 10% and 20%; rescaling inputs or outcomes changes these values. Moreover, applying this local linearization across the held-out envelope gives RMSE of 0.115 m/s, 2.69 degrees, and 7.48 N for speed, face/path, and peak hand force. The algebraic rank/nullity result therefore must not be promoted to a globally predictive manifold or a neural-control dimension.

24.5 Biological Realization and Impedance

Coactivation can increase endpoint stiffness and attenuate an imposed disturbance (Rugy, Loeb, and Carroll 2018), but excessive co-contraction can also be energetically inefficient and does not guarantee stability when the source is internal or feedback is delayed (Latash and Huang 2015). The reduced muscle bridge in Section 23 demonstrates redundancy and preparation history; it does not identify time-varying human impedance or reflex gains. **Human self-stabilization is untested.** Such a biological claim requires controlled, phase-registered perturbations, bilateral wrench measurement, EMG, and an identified mapping from muscle activation to endpoint impedance.

Likewise, repeatability should be evaluated above measurement noise and across sessions. Launch-monitor speed and distance can be reliable in talented golfers, but other variables have wider reliability ranges (Shaw et al. 2023). The experimental protocol must propagate device error rather than label every observed difference a motor-control effect.

24.6 Falsifiable Performance Implications

The present evidence supports a research program rather than a universal instruction:

1. **Optimize a distribution, not one trajectory.** Maximize lower-tail impact performance subject to face, path, strike, hand-force, effort, and injury- relevant constraints.
2. **Prefer state variables only when observable.** A configuration- or phase-triggered handoff can reject timing variation, but sensing delay, estimation noise, and saturation must be included.
3. **Preserve useful abundance.** Stabilize club impact variables while allowing task-null variation in joints, muscles, and hand-force allocation.
4. **Treat impedance as a tradeoff.** More stiffness may improve one error and worsen force, effort, or coupled stability.
5. **Measure the pathway.** Kinematics alone cannot distinguish proximal work, constraint-force transport, direct wrist moment, shaft release, gravity, and dissipation.
6. **Propagate to the ball.** Pure distance claims require strike location, dynamic loft, attack angle, ball speed, spin, carry, and lateral dispersion, not clubhead speed alone.

The strongest near-term experiment is participant-held-out and phase- perturbed: synchronize whole-body motion, force plates, bilateral hand wrenches, shaft response, EMG, club/ball impact, and launch; estimate task-null and task-relevant covariance; and test whether state-relative handoff predicts a better speed–dispersion–load frontier than clock-relative timing. Failure to replicate that frontier would reject the performance implication while leaving the narrower multibody mechanism intact.

Chapter 25

Empirical Evidence in Golfers

25.1 The Work and Power Budget of the Swing

Nesbit's full-body kinematic-kinetic study and the companion work-power analysis of Nesbit and Serrano provide detailed published energy budgets of the swing (Nesbit 2005b; Nesbit and Serrano 2005). Using subject-specific full-body models of four golfers of widely differing skill, they report that the trunk complex (lumbar and thoracic spine plus hips) contributes 68.7–72.2% of total swing work, the shoulder and arm joints 24.3–28%, and the modeled leg joints 3.3–3.8% (Nesbit and Serrano 2005). These fractions are conditional on the four subject models, joint partition, inverse-dynamics assumptions, and definition of work; the small leg-joint fraction is not evidence that the lower limbs or ground reactions are mechanically unimportant. Within that study, power generation and clubhead speed decreased as handicap increased, and the phase analysis placed much of the modeled torso work earlier than the late shoulder/arm and club-interface conversion. This temporal separation motivates a delayed- handoff hypothesis but does not establish that it is optimal in humans.

Ground reactions supply external forces and moments that constrain and redirect the golfer; muscular work supplies the system's internal mechanical energy. Han and colleagues characterized golfer-ground interaction in 63 skilled male golfers and reported associations between selected force and moment variables and maximum clubhead speed (Han et al. 2019). A later cross-sectional study pooled driver and 7-iron swings from 30 right-handed golfers (15 professionals and 15 amateurs) and formed principal-component constructs for hierarchical regression and mediation (Rachnavy et al. 2026). Its first regression block — early and late center-of-pressure factors **plus skill group** — explained 35.5% of clubhead-speed variance; adding trunk sequencing and the study's constructed *impulse-related energy-transfer efficiency* factor increased the final model's explained variance to 75.4%. Early center-of-pressure behavior had no significant direct association, whereas an indirect path through the transfer-efficiency factor was significant. These are model-dependent cross-sectional associations, not a demonstrated causal transmission pathway; the source itself makes that limitation explicit. They motivate measuring transfer efficiency separately from sequence order rather than treating either as a causal mechanism by definition.

25.2 Segmental Kinetic-Energy Sequencing

Two early studies calculated segment *kinetic energy* rather than inferring energy flow from angular-speed peaks, but their results do not show a simple P→D timing sequence. Anderson, Wright and Stefanyshyn analyzed driver swings from 45 male scratch golfers with a four-group kinematic model. Peak total-KE magnitudes increased from hips to club, whereas hips, torso, and arms peaked at approximately the same normalized time and only the club peaked significantly later (Anderson, Wright, and Stefanyshyn 2006). Kenny, McCloy, Wallace and Otto used measured kinematics from one elite male golfer to drive a 19-segment model and compared one driver and one 7-iron simulation. Peak-KE magnitudes again increased distally, but the reported timing order was arms, hips, torso, then club—not a proximal-to-distal sequence (Kenny et al. 2008). Thus, segment KE is a computable observable, and both studies place the club's KE peak near impact; neither demonstrates sequential body-segment energy transfer, estimates intersegment power, or independently validates the present model.

25.3 Kinematic-Sequence Evidence and Skill-Level Differences

The descriptive P→D pattern is common in sampled skilled populations, but its reported prevalence and exact ordering depend on the measurement definition. Tinmark and colleagues, studying elite golfers across full and partial shots, found a significant proximal-to-distal temporal ordering of peak speeds (pelvis → torso → hands/club) with successive amplification of peak speed at every level of effort, in both men and women (Tinmark et al. 2010). Cheetham and colleagues compared amateur recreational players with touring professionals on transition- and downswing-phase kinematic sequence parameters and found professionals showed higher peak-speed magnitudes and more consistent sequencing and timing characteristics (Cheetham et al. 2008). Zheng and colleagues' three-dimensional comparison of professional and amateur swings found systematic temporal and spatial differences, with amateurs deviating progressively more from professional norms as handicap increased (Zheng et al. 2008). Meister and colleagues provide elite rotational benchmarks (pelvis-thorax separation and its timing) against which amateurs can be compared (Meister et al. 2011), and Lindsay, Mantrop and Vandervoort review the broader catalogue of skill-level biomechanical differences (Lindsay, Mantrop, and Vandervoort 2008).

Torso-pelvis variables have sample-specific associations with ball or clubhead speed. Myers and colleagues reported moderate associations in 100 recreational golfers (Myers et al. 2008). Chu, Sell and Lephart fit event-specific regressions to 308 golfers; their selected kinematic and ground-reaction variables accounted for 44–74% of in-sample ball-speed variance (Chu, Sell, and Lephart 2010). Joyce and colleagues reported associations between three-dimensional trunk kinematics and clubhead speed across clubs (Joyce et al. 2013). These observational regressions do not establish that changing an isolated variable will reproduce the between-golfer association. For the widely coached "X-factor," Kwon and colleagues tested 18 skilled male golfers and found that three computation methods produced significantly different parameter values; none of the computed X-factor parameters was directly related to maximum clubhead velocity in that sample (Kwon et al. 2013). The studies jointly motivate explicit measurement definitions and held-out or interventional validation, not a universal torso prescription.

Three refinements prevent an overly tidy reading:

1. **Sequence Order Is Common but Not Universal — Even Among the Best.** A recent study of 14 elite right-handed men reported that slight sequence variations could yield clubhead speeds comparable to the authors' defined optimal pattern, although its regression models and unavailable public data do not establish a population-wide causal optimum (Lee, Ehrlich, and Cain 2026). On-plane analysis of 66 right-handed skilled men found associations between selected axle-chain angular-motion characteristics and clubhead speed (Madrid et al. 2020). These studies support heterogeneity and variable-level analysis; they do not show that sequence order alone determines speed.
2. **Within-Player Timing Differences Do Not Straightforwardly Explain Shot Quality.** Neal and colleagues compared player-rated well-timed and mistimed driver shots in 25 highly skilled amateurs and found no significant differences in the lags between peak angular speeds of contiguous segments (Neal et al. 2007). They did not measure pre-impact clubhead state or impact location and proposed that the ratings may have reflected contact centeredness. The result limits that five-segment peak-lag metric under the declared protocol; it does not localize a golfer's perception of timing. Reviews of golf-swing variability likewise caution that trial-to-trial variation can be structured and task-dependent (Langdown, Bridge, and Li 2012; Glazier 2011), not that every deviation is beneficial.
3. **Method Sensitivity.** Marsan and colleagues processed driver swings from 13 golfers with seven angular-velocity component definitions and obtained almost as many sequence classifications as methods for each golfer (Marsan et al. 2019). Cross-study ordering comparisons therefore require matched coordinate, component, filtering, and peak-event definitions. Historical trunk-pelvis measurements used

different specialized instrumentation and remain conditional on their own definitions (McTeigue et al. 1994).

What survives these refinements is narrower: sampled skilled groups often show higher segment-speed magnitudes and more repeatable timing, while recent cross-sectional models associate constructed transfer-efficiency measures with clubhead speed. Merely exhibiting a P→D peak order is neither unique to skill nor sufficient for it (Cheetham et al. 2008; Zheng et al. 2008; Rachnavy et al. 2026; Lee, Ehrlich, and Cain 2026). Coaching perception has partly internalized this: when surveyed systematically, coaches' key swing parameters overlap with, but do not coincide with, the parameters the biomechanical literature supports (Smith et al. 2015).

25.4 Where the Transfer Occurs

The available studies support a narrower account of where transfer may occur. Nesbit and Serrano's four subject-specific inverse-dynamics models assigned most positive joint work to the trunk complex and reported earlier torso-dominated work than the late club-interface conversion (Nesbit and Serrano 2005). Classical and later models show that wrist-cock geometry and hub-path motion can accelerate the club without requiring large simultaneous positive wrist torque (White 2006; Miura 2001; Sprigings and Neal 2000; Nesbit and McGinnis 2009). Anderson and Kenny place peak club KE near impact while explicitly rejecting simple P→D timing of body-segment KE peaks (Anderson, Wright, and Stefanyshyn 2006; Kenny et al. 2008). These model-dependent results motivate late-handoff hypotheses but do not establish a dominant human pathway. Likewise, "casting" is a model and coaching interpretation: the cited amateur cohort comparisons and Milburn's double-pendulum analysis do not by themselves show that early release causally produced the observed skill-group differences (Cheetham et al. 2008; Zheng et al. 2008; Milburn 1982). Section 29 demonstrates a related failure mode only within the registered model and command family.

Chapter 26

The Timing Question and the Counterfactual Framework

26.1 Two Strategies, Stated Precisely

At the conceptual human-system level, let $E_p(t)$ be the kinetic energy of a declared proximal subsystem. In the primary model below, however, that subsystem is only the first rigid link about a fixed hub; it is not an identified trunk-and-arms energy. Over a downswing $t \in [t_0, t_{\text{imp}}]$, and define the transfer functional $P_{\text{w}}(t)$ as the inter-segment power crossing the wrist interface — joint-force power plus moment power, in the sense of Section 2.5.2. The two strategies are:

- **S1 (transfer early):** make $P_{\text{w}}(t)$ large as soon after transition as possible; the club begins acquiring its final energy early.
- **S2 (retain early, release late):** keep $P_{\text{w}}(t)$ small early (the wrist transmits centripetal force but little power) while proximal torques maximize E_p; then allow or drive a large P_{w} concentrated in the final phase.

The double-pendulum and optimal-control studies reviewed in Section 2 provide mixed, model-dependent evidence relevant to S2. Several favor delayed release, late wrist drive, or an early negative and late positive wrist-torque program (Pickering and Vickers 1999; Sprigings and Neal 2000; Sprigings and MacKenzie 2002; Sharp 2009). White supports passive geometry-mediated transfer but reports only a second-order release-timing effect and a distance penalty for increasing constant positive wrist torque in his driven model (White 2006). The following mechanisms are therefore hypotheses to separate experimentally and computationally, not a consensus proof:

1. **Inertia management.** With the wrist cocked, the system's moment of inertia about the hub is small, so proximal torque buys angular velocity cheaply; early release raises the inertia while proximal torque is still accelerating the system (White 2006; T. P. Jorgensen 1999).
2. **Actuator timing and limits.** In Sprigings and Neal's declared torque-generator model, the optimum placed active wrist torque late, but its timing depended strongly on the assumed torque-profile shape (Sprigings and Neal 2000). Sprigings and MacKenzie separately found a small benefit from a 50 ms actively resisted delay and a much larger penalty when post-release wrist torque was removed (Sprigings and MacKenzie 2002). These simulations do not identify a muscle-level strategy.
3. **Geometry-mediated transfer.** White's undriven model demonstrates energy redistribution as the club unfolds, while Miura's translating- hub model predicts an inward-pull gain under its prescribed geometry (White 2006; Miura 2001). Whether either mechanism dominates a measured human swing requires state-resolved force and power data.
4. **Interaction dynamics can redistribute acceleration and power.** Motion-dependent terms can accelerate a distal segment while opposing a proximal segment, but they are consequences of the evolving

state and prior actuator work—not free energy (Putnam 1993; Herring and Chapman 1992). Their contribution must be evaluated from a declared decomposition.

Some cross-sectional studies report skill-group differences in release or segment-peak timing (Section 25.3), whereas Neal and colleagues found no significant difference in contiguous-segment peak-speed lags between player-rated well-timed and mistimed shots from 25 highly skilled amateurs (Neal et al. 2007). Those observations do not establish a performance plateau or locate the remaining variance in release shape, hub-path geometry, or transfer efficiency. They motivate measuring those variables directly rather than inferring them from peak order.

26.2 What Would Falsify S2?

To keep the question scientific rather than rhetorical, we state what evidence would count against the retain-early/release-late hypothesis:

- an optimal-control solution, in a validated 3D model with physiological actuator limits, whose optimal wrist-interface power is front-loaded;
- measured expert swings in which early wrist-interface power (normalized) is *positively* associated with clubhead speed across players;
- state-matched affine drift/control analyses showing that in faster swings the control term dominates club acceleration *early* rather than late;
- **or, in the direct manipulation of Section 28: torque programs that drive the wrist early outperforming programs that retain early and drive late, under matched proximal effort.**

The last test is executed in Section 29.

26.3 ZTCF and ZVCF: Definitions

Two counterfactual accelerations are defined *pointwise* at each measured state $(q, \dot{q}, \tau)$ of a swing:

$$\ddot{q}_{\text{ZTCF}} \;=\; M(q)^{-1}\,(-\,b(q,\dot{q})), \tag{26.1}$$

$$\ddot{q}_{\text{ZVCF}} \;=\; M(q)^{-1}\,(-b(q,\mathbf{0})) \;=\; M(q)^{-1}\,(-g(q)), \tag{26.2}$$

where the simplification in Equation 26.2 holds for the implemented double-pendulum bias convention because its Coriolis term (quadratic in velocity) and viscous dissipation (linear in velocity) vanish at $\dot{q} = \mathbf{0}$, leaving the declared gravity term. A different engine may include other velocity-independent terms and must be checked rather than assuming this reduction. The ZTCF (Equation 26.1) answers *"what would the declared model do right now if every included actuator switched off while the state and constraint set stayed fixed?"* — it is the **drift** field of the affine control system, containing gravity plus all retained autonomous plant dynamics. The ZVCF (Equation 26.2) answers *"what instantaneous acceleration remains at this pose when velocity and the declared applied control are both zero?"* It is not the pure control contribution. The separately named zero-velocity control-preserved evaluation is $M^{-1}(\tau - b(q, 0))$. Because Equation 2.1 is affine in τ at a fixed state and unchanged constraint set, the actual acceleration superposes exactly:

$$\ddot{q} \;=\; \underbrace{M^{-1}(-b(q,\dot{q}))}_{\text{drift = ZTCF}} \;+\; \underbrace{M^{-1}\tau}_{\text{control}}, \tag{26.3}$$

an identity enforced to numerical tolerance by the accompanying tests (Section 35).

26.4 Two Operational Variants

Two distinct operationalizations are available, and the difference matters for interpretation.

Pointwise (instantaneous) counterfactuals. The engine-agnostic Python implementation (`simulation_backends/ztcf_zvcf.py`) evaluates Equation 26.1 and Equation 26.2 at each sample of an already-measured trajectory — explicitly *not* a forward-integrated rollout. Each sample answers a local "what if"; this is the right tool for drift/control *time profiles* along a real swing, and it is the tool used in Section 29.

Legacy rerun-based pointwise sampler. The original MATLAB/Simscape pipeline (`run_ztcf_simulation.m`) reruns the full model with a torque "killswitch" applied at time t for a sweep of t values, but `run_single_ztcf_point.m` retains only the first sample at killswitch activation. It therefore samples a state-matched instantaneous torque-removal response; it does **not** tabulate a future reached after evolving with torque off. The pipeline forms the difference table DELTA = BASE − ZTCF (`process_data_tables.m`), which is an operational BASE-minus-sampled-response residual, not an isolated muscle or actuator contribution. A companion ZVCF model applies the measured torques to the same pose with velocities zeroed (`SCRIPT_ZVCF_GENERATOR.m`); the ZVCF model may be run without gravity under its documented convention so gravity is not counted in both operands. This convention must be checked against the model configuration; the script's statement that the complete multibody system is a series of linear differential equations is not correct. The acceleration split is meaningful *pointwise*, at matched states, in the sense of Equation 26.3. Separately integrated futures do not superpose at the trajectory level because M and b evolve differently once their states diverge. The MATLAB pipeline additionally computes the linear work $\int \mathbf{F} \cdot \mathbf{v}\, dt$, angular work $\int \tau \cdot \omega\, dt$, and summed work and power (`calculate_work_impulse.m`, `calculate_total_work_power.m`) for the stored tables. However, `process_data_tables.m` subtracts all BASE and ZTCF columns before `calculate_work_impulse.m` dots the resulting DELTA force with the resulting DELTA velocity. In general, $(\mathbf{F}_b - \mathbf{F}_z) \cdot (\mathbf{v}_b - \mathbf{v}_z)$ is not $\mathbf{F}_b \cdot \mathbf{v}_b - \mathbf{F}_z \cdot \mathbf{v}_z$. The optimized `calculate_total_work_power.m` also advertises fractional contributions in its header but does not calculate them. Consequently, the legacy DELTA work and power columns are **not** accepted here as an additive Robertson–Winter pathway partition. Valid pointwise contribution power must project force components onto one common achieved interface velocity, as the Python evidence does. The repository also contains a kinematic-sequence plot computed separately for the stored BASE, ZTCF, and DELTA tables (`SCRIPT_324_PLOT_ZTCF_KinematicSequence.m`).

26.5 The Counterfactual Form of the Timing Hypothesis

The affine drift/control language makes the S2 hypothesis crisp. Along a measured downswing, project acceleration components onto a declared club speed coordinate and compute power from force or moment components paired with their conjugate velocities. An acceleration projection cannot itself be integrated as energy. As a registered model hypothesis—not an empirical fact—S2 predicts:

- **Early downswing:** the *control* term should dominate energy input at proximal joints, while at the wrist the control contribution to club angular acceleration should be small or negative (restraining lag against the developing centrifugal field). The club's ZTCF profile should show the drift field already "wants" to open the wrist — control is *holding energy back*.
- **Late downswing:** the *drift* term (parametric transfer, centrifugal release) should dominate club acceleration, with a brief late window of positive wrist control power (Sprigings and Neal 2000). The active share of club-side work should concentrate before release; the passive share may account for most club energy gain after release in the declared model (White 2006).

This pattern was initially motivated by torque-removal analyses. Section 29 provides a reproducible quantitative test in a two-segment model; conversely, had the early-drive programs won the sweep, S2 would have been falsified in exactly the terms of 3. Bounded-actuator, impact-definition, and model-parameter sensitivity checks are reported here. The next chapter supplies the distinct forward matched-state killswitch test that the legacy sampler does not. Like-for-like Simscape parity, 3D full-body models, and measured swings remain future work.

Chapter 27

Computational Framework

The numerical work uses an open-source, backend-neutral implementation of a planar two-segment golf model. Model parameters are represented once and rendered to the analytical equations of motion and optional simulation backends. The present results use the deterministic analytical ODE backend; they do not depend on a proprietary solver or graphical interface.

27.1 Analysis Components

The workflow separates four responsibilities:

1. **Dynamics.** A validated mass matrix and bias-force provider advances the two generalized coordinates under specified shoulder and wrist torques.
2. **Counterfactual decomposition.** At each sampled state, acceleration is split into passive drift and applied-control components. These pointwise quantities are not presented as alternative forward trajectories.
3. **Energy accounting.** Segment kinetic and potential energies, actuator work, and wrist-interface force and moment power are evaluated with a Robertson–Winter balance check (Robertson and Winter 1980).
4. **Reproducibility.** Fixed-step integration, explicit parameter records, machine-readable outputs, and regression tests connect every reported number to a declared computation.

The source implementation and versioned data are linked once in the code and data availability statement (Section 33). Repository names are omitted from the scientific argument because software provenance is not evidence for the physical claims.

27.2 Validation Boundary

The implementation includes unit tests for drift-plus-control reconstruction, work–energy consistency, deterministic replay, impact detection, and headline ordering. The reduced full-body common-state tier now compares MuJoCo with an independent Lagrange–Christoffel implementation generated from one hashed model. That agreement reduces implementation risk for the declared inverse-dynamics estimand; it does not validate the primary planar model or remove structural limitations such as prescribed spatial hand loads, simplified inertias, missing forward contact, or simplified actuators.

Chapter 28

Computational Methods

This chapter specifies the simulation experiments whose results appear in Section 29. Everything described here is implemented in three committed modules under `scripts/research/proximal_distal_energy/` (`swing_model.py`, `interaction_forces.py`, `torque_programs.py`, `run_experiments.py`, and `run_interaction_force_stu` with figures from the paired figure scripts), and every output carries a provenance record (git SHA, integrator settings, parameter values). The reproduction commands are in Section 34.

28.1 Model

The simulated plant is a backend-neutral two-segment golf model (Section 27): an arm segment rotating about a fixed hub, hinged at the wrist to a club segment consisting of a distributed shaft plus a clubhead point mass at the tip, moving in an inclined swing plane with projected gravity. Baseline parameters are (`GolfModelParams.default()`; full table in Section 36): arm length 0.75 m and mass 7.5 kg; club length 1.0 m with 0.15 kg shaft and 0.20 kg clubhead; plane inclination 35°; viscous damping 0.4 and 0.25 $\text{N} \cdot \text{m} \cdot \text{s/rad}$ at shoulder and wrist. Angles follow the declared convention: θ_1 is the arm angle from the downward vertical in the swing plane, θ_2 the wrist angle of the club relative to the arm, and the club's absolute angle is $\theta_{\text{club}} = \theta_1 + \theta_2$.

Rollouts use the ODE reference backend (analytic dynamics, fixed-step RK4) with $\Delta t = 1$ ms over a 0.9 s horizon. Every rollout starts from the same top-of-backswing state, $\theta_1(0) = -2.2$ rad, $\theta_2(0) = -1.57$ rad (a 90° wrist cock), $\dot{q}(0) = 0$ — an arm carried well past horizontal with the club folded over the shoulder, comparable to the classical two-lever setups (T. P. Jorgensen 1999; Pickering and Vickers 1999).

28.2 Torque Programs

All programs share a constant shoulder torque τ_s active from $t = 0$ (two levels: 60 and 100 $\text{N} \cdot \text{m}$), so the sweep isolates the wrist channel. The wrist torque follows one of three profiles, parameterized by an onset time t_{on}:

- **passive**: $\tau_w(t) = 0$ throughout (free hinge) — the White limit (White 2006);
- **drive-only**: $\tau_w(t) = 0$ for $t < t_{\text{on}}$, then $\tau_w = +15$ $\text{N} \cdot \text{m}$ (opening);
- **restrain-then-drive**: $\tau_w(t) = -R$ (cock-retaining) for $t < t_{\text{on}}$ with $R \in \{5, 10\}$ $\text{N} \cdot \text{m}$, then $\tau_w = +15$ $\text{N} \cdot \text{m}$.

The onset grid is $t_{\text{on}} \in \{0, 0.025, \dots, 0.35\}$ s (15 values). With both shoulder-torque levels this yields 92 distinct programs; `drive-only` at $t_{\text{on}} = 0$ is the S1 ("transfer early") pole of the design and `restrain-then-drive` with late onset is the S2 pole. Torque magnitudes sit inside the ranges used by comparable two- and three-segment studies (Sprigings and Neal 2000; Pickering and Vickers 1999), scaled to this model's inertias. These profiles are a finite heuristic design, not a continuous optimal-control solution and not a physiological activation reconstruction. Consequently, "best" below always means grid-selected within the declared programs and endpoint rule.

E1b (actuator-bound sensitivity). Because constant torques overstate what muscle can deliver at speed, a companion sweep (`e1b_bounded_torque.py`) replaces both concentric drives with a linear torque-velocity bound, $\tau(\omega) = \tau_{\text{iso}}\,\text{clip}(1-\omega/\omega_{\text{max}}, 0, 1)$ (shoulder: $\tau_{\text{iso}} = 100$ N · m, $\omega_{\text{max}} = 20$ rad/s against arm speed; wrist: 20 N · m, 30 rad/s against opening speed; restraint constant, since eccentric torque does not taper with shortening velocity). State-dependent torques require closed-loop integration, done with the backend's own `mass_matrix`/`bias_forces` primitives under the identical RK4 settings.

E1e (finite command-rise sensitivity). A separate audit replaces each post-initial command change with an exact-discrete first-order transition at 20, 35, and 50 ms, alongside the unfiltered reference. The command at the top of the downswing is treated as preloaded; only later changes are filtered. This tests whether the ideal step switch creates the ordering. It is a command-level sensitivity, not a calcium-kinetics model, muscle identification, or OCP.

28.3 Impact Definition and Validity

Impact is the first upward crossing of $\theta_{\text{club}} = 0$ (club pointing straight down in the swing plane), linearly interpolated between samples; the score of a program is the clubhead (distal tip) speed at that instant. Because the shoulder torque is constant, a program that keeps the club folded through the bottom of the swing can postpone the crossing into a second rotation while the shoulder keeps pumping energy — an artifact, not a swing. A trial is therefore outside the registered delivery-zone estimand unless the arm angle at the crossing satisfies $\theta_1 \le 2.0$ rad (a first-pass delivery); 29 of the 92 programs were excluded by this rule, all of them heavy-restraint or very-late-onset programs. Every attempted program now records its first geometric crossing, speed, arm angle, and explicit acceptance status even when excluded. Bounds from 1.5 to 2.5 rad accept 58 to 69 of 92 programs; the grid-selected profile and onset remain unchanged at both shoulder-torque levels. This supports threshold robustness of the selected result, but it does not make 2.0 rad an anatomical cutoff or validate the endpoint as impact.

28.4 Recorded Quantities

For every program: the full state trajectory, applied controls, impact time and clubhead speed. For four representative programs at $\tau_s = 60$ N · m (passive; drive-only at $t_{\text{on}} = 0$; the best drive-only; the best restrain-then-drive), additionally:

Segment energies. Arm kinetic energy $\frac{1}{2} I_1^{\text{hub}} \dot\theta_1^2$; club kinetic energy $\frac{1}{2} m_2 \|\mathbf{v}_{c2}\|^2 + \frac{1}{2} I_2^{\text{com}} (\dot\theta_1 + \dot\theta_2)^2$ with the club centre-of-mass velocity $\mathbf{v}_{c2}$ computed analytically from the state.

Wrist-interface power accounting (E4). Following Section 2.5.2: the joint-force power $P_f = \mathbf{F} \cdot \mathbf{v}_{\text{wrist}}$, with the joint reaction force recovered from Newton's second law for the club segment, $\mathbf{F} = m_2 \mathbf{a}_{c2} - m_2 \mathbf{g}$ (centre-of-mass acceleration evaluated analytically as $J_{c2}(q)\ddot q + \dot J_{c2}(q,\dot q)\dot q$); the net wrist moment power on the club $(\tau_w - b_w \dot\theta_2)(\dot\theta_1 + \dot\theta_2)$; the wrist actuator power $\tau_w \dot\theta_2$; and the residual check that the club's total mechanical energy rate equals joint-force power plus moment power (reported as a figure in Section 29; gravity is not added separately because potential energy is included in the club's mechanical energy).

Pointwise counterfactual split (E2). At every sample, the `drift_and_control_split` (Equation 26.3) evaluated with the applied torques, yielding drift and control components of both joint accelerations; the club's absolute angular-acceleration split is the row sum.

Exact interaction-force audit (E5). Analytic club-centre-of-mass acceleration replaces finite differentiation and separates the wrist reaction force into proximal and distal tangential and centripetal terms plus gravity reaction (Section 3.3). Each vector is projected onto the analytic wrist velocity to obtain a signed power pathway. A late-downswing matched-state experiment then integrates the commanded and zero-torque futures for 120 ms, explicitly distinguishing a trajectory-level killswitch from pointwise ZTCF (Section 3.7).

Newton balance, club moment balance, force and power reconstruction, matched initial state, and initial ZTCF equivalence are unit-tested.

Matched-state counterfactual ensemble (E6). Eight cut times, including three samples bracketing the 0.100 s wrist-command switch, are crossed with four forward horizons and three fixed timesteps. Commanded and zero-torque futures share the exact interpolated source state. Divergence is recorded in generalized position and velocity, wrist force, force power, integrated force work, and terminal clubhead speed. The 80 ms subset is repeated with gravity disabled and with damping disabled. The 0.5 ms grid is the timestep reference, and the registered WSCG chart's stored DELTA series are independently reconstructed as BASE minus counterfactual after time alignment (Section 8).

Phase budgets. With the downswing divided at $t_{\text{imp}}/2$: club kinetic-energy gain, wrist actuator work, shoulder work, and integrated joint-force transfer, per half. The value at the exact split is linearly interpolated and included as the terminal point of the early integral and the initial point of the late integral, so the two trapezoidal integrals close to the unsplit integral without an omitted sample interval.

Robustness analyses (E1c and E1d). E1c re-scores the same 92 trajectories using fixed arm positions, peak horizontal clubhead velocity, peak first-pass speed, a matched arm angle, and five validity bounds. E1d repeats the four-strategy comparison after changing one model input at a time: arm length (±10%), arm mass (±15%), club length (±10%), clubhead mass (±20%), swing-plane inclination (25° and 45° versus 35°), and both damping coefficients (0.5× and 1.5×). For each E1d case, late-drive and restrain-then-drive onset are reselected on the original onset grid. E1e repeats the complete 92-program sweep under finite command transitions. These ranges test local structural sensitivity; they are not population percentiles or confidence intervals.

28.5 Design Rationale and Scope

This deliberately simple model is a planar 2-DOF chain with a fixed hub and rigid shaft. That choice is the point, not a compromise: the classical timing results were established in exactly this model class (Section 2.3), so the analysis first reproduces the class's behavior under explicit instrumentation — where every energy pathway is exactly measurable and the counterfactual contract is tested — before scaling to models where the same questions are harder to instrument. What the 2-DOF results can and cannot establish is taken up explicitly in Section 30; the extension pathway (re-simulation parity, higher-fidelity models, and motion capture) is specified in Section 32.

Chapter 29

Results

All numbers in this chapter are computed by the committed experiment suite (Section 28) from the recorded outputs in `data/` (`e1_sweep.json`, `e1e_smooth_command_sensitivity.json`, `representative_traces.npz`, `results_summary.json`); figures are generated by the registered figure scripts. Speeds are quoted to 0.1 m/s and times to 1 ms.

29.1 E1 — Timing of the Distal Handoff

Figure 29.1 shows clubhead speed at impact as a function of wrist-drive onset time for both shoulder-torque levels. Table 29.1 lists the representative programs.

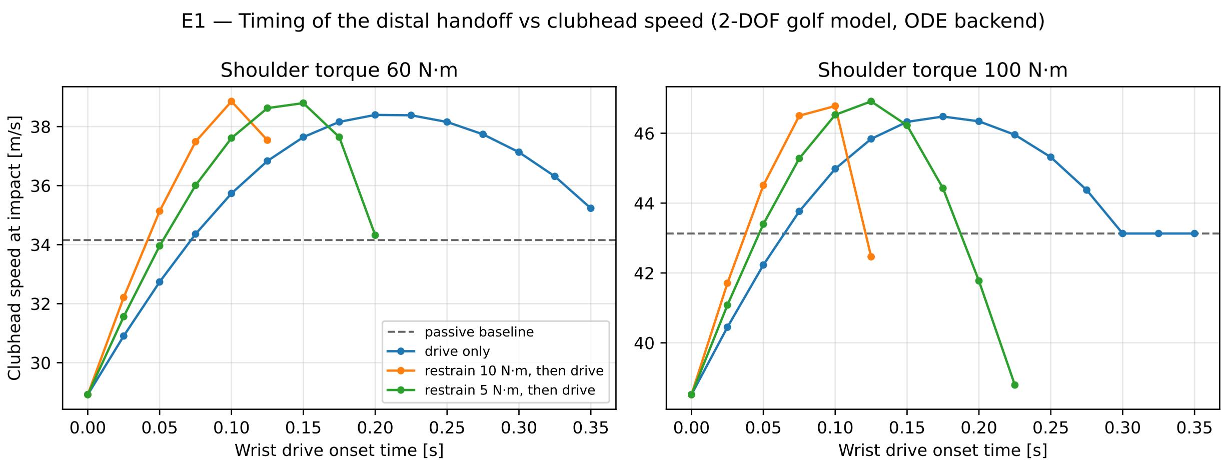

Figure 29.1: E1 sweep: clubhead speed at impact versus wrist-drive onset time, for drive-only and restrain-then-drive profiles at two shoulder-torque levels. Dashed line: fully passive wrist baseline.

Table 29.1: Representative programs at $\tau_s = 60$ N · m.

Program ($\tau_s = 60$ N · m)	t_{on} [s]	t_{imp} [s]	Clubhead speed [m/s]	vs passive
Passive wrist	—	0.370	34.2	—
Early drive (S1 pole)	0.000	0.327	28.9	**−15.3%**

Program ($\tau_s = 60$ N · m)	t_{on} [s]	t_{imp} [s]	Clubhead speed [m/s]	vs passive
Best drive-only	0.200	0.352	38.4	**+12.4%**
Best restrain-then-drive ($R = 10$)	0.100	0.349	38.9	**+13.8%**

Three findings were observed at both tested shoulder-torque levels:

1. **Driving the wrist from the top is the lowest-speed accepted program.** At $\tau_s = 60$ N · m the early-drive program reaches 28.9 m/s versus 34.2 m/s for a completely passive wrist — active early distal effort produces 15% less speed than a free hinge. The early-drive program is the lowest accepted trial in the entire 92-program sweep. At $\tau_s = 100$ N · m the pattern repeats (early drive is the minimum of its profile curve; passive baseline 43.1 m/s).

2. **The same commanded wrist-torque magnitude, applied late, produces more impact speed than the passive-wrist program in both tested cases.** Clubhead speed rises monotonically with onset time until an interior optimum ($t_{\text{on}} = 0.200$ s at 60 N · m, 0.175 s at 100 N · m — roughly the middle of the downswing, with drive active through the final ~40%), reaching 38.4 and 46.5 m/s respectively. Relative to the corresponding passive programs, the increases are 12.4% and 7.8%; the ordering repeats, but its effect size does not.

3. **Retain-early-then-drive is highest among the tested programs.** Programs that apply a *negative* (cock-retaining) wrist torque early and the identical positive drive late beat the best drive-only programs at both torque levels: 38.9 m/s ($R = 10$ N · m until 0.100 s) at $\tau_s = 60$, and 46.9 m/s ($R = 5$ N · m until 0.125 s) at $\tau_s = 100$. The margin over the best drive-only program is modest (+0.5 m/s at both levels), consistent with most of the retention benefit being achievable passively; but the ordering is strict, and heavy or over-long restraint fails the first-pass validity rule

    (2) rather than winning — the benefit is a *timed* retention, not maximal retention.

29.2 E1b — Sensitivity to Actuator Torque-Velocity Bounds

A standing objection to constant-torque sweeps is that real muscle torque falls with shortening velocity, shrinking the late-drive window (Sprigings and Neal 2000). E1b re-runs the sweep with a linear torque-velocity bound on both concentric drives (shoulder: 100 N · m isometric, zero at 20 rad/s of arm speed; wrist: 20 N · m isometric, zero at 30 rad/s of opening speed; restraint left constant as a declared modeling choice because eccentric force–velocity behavior was not modeled), integrated closed-loop with the same RK4 settings (Figure 29.2). The ordering survives intact: early drive 28.8 m/s < passive 30.8 < best late drive 34.6 (onset 0.175 s) < best restrain-then-drive 34.8 (R = 10 N · m until 0.100 s). Effect sizes compress — late drive is worth +12.2% over passive and the restraint margin narrows to +0.2 m/s — precisely the compression bounded-actuator theory predicts, while the grid-selected onsets move slightly *earlier* (0.175–0.100 s versus 0.200–0.100 s), since a velocity-limited wrist needs a slightly longer window to deliver its work. The ordering is therefore not removed by this one linear concentric bound; the experiment does not establish robustness to a calibrated human capacity surface.

29.3 Kinematic Sequence

Figure 29.3 shows arm and club angular-speed traces. All four programs produce the qualitative P→D pattern — arm speed peaks, then club speed peaks higher — as expected from interaction dynamics alone (Section 2.2). The programs differ in ways that are qualitatively comparable with, but do not validate, the skill literature (Section 25.3): the early-drive swing opens the club immediately, its arm peak is depressed, and its club peak is the lowest of the four; the retain-then-drive swing holds the club folded longest, achieves the

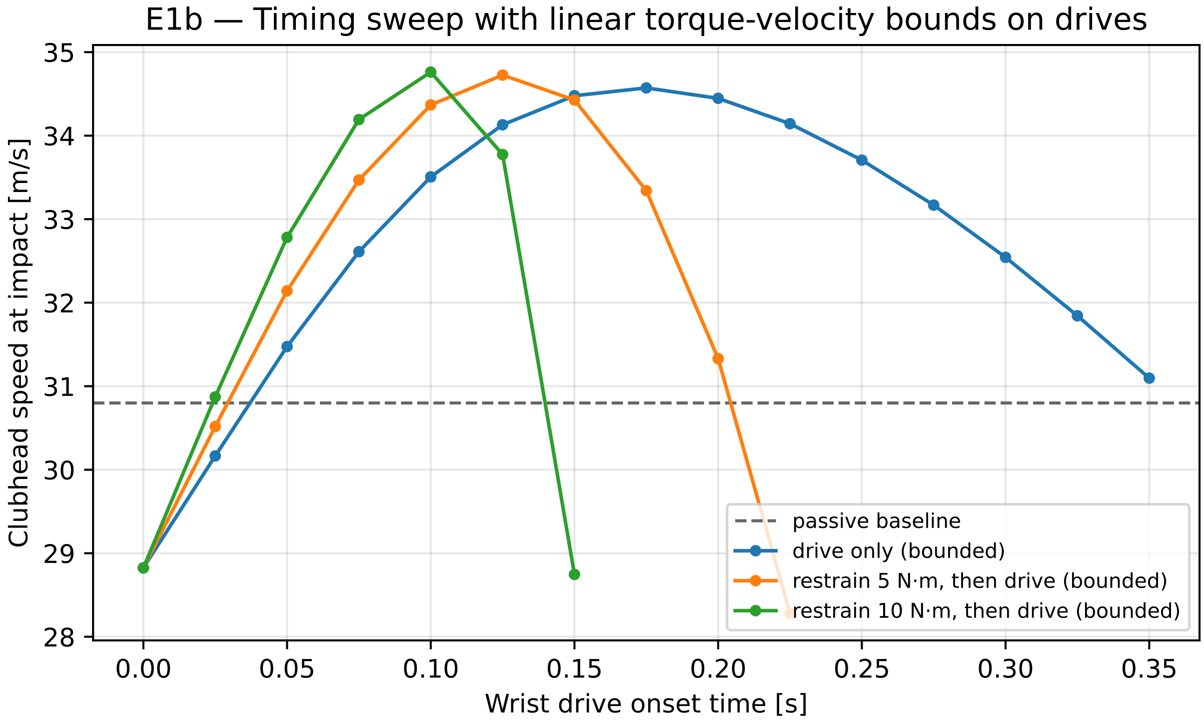

Figure 29.2: E1b: the timing sweep repeated with linear torque-velocity bounds on the shoulder and wrist drives.

highest arm speed before release, and converts it into the highest club peak. Impact in the early-drive swing occurs with the arm still 0.36 rad *short* of vertical — the clubhead has overtaken the hands before the arm arrives, the model's version of premature delivery — whereas the two highest-speed tested programs deliver impact with the arm 0.7–0.8 rad *past* vertical (hands ahead of the clubhead in this coordinate convention). This is model geometry, not a classification of a player's technique.

29.4 Segment Energies

Figure 29.5 shows arm and club kinetic-energy time courses, and Figure 29.6 the early-half/late-half budget. The energy ledger for these four selected traces is:

- **Early half.** The two grid-selected programs put the *least* energy into the club early: 5.0 J (selected restrain) and 7.3 J (selected drive-only) versus 23.0 J for the early-drive program (passive: 7.9 J). Meanwhile they bank more energy in the arm: early-half shoulder work is 55.1 J (selected restrain) and 52.0 J (selected drive) versus 34.0 J (early drive). The early-driven club's larger early energy gain coincides with less shoulder work and arm-energy accumulation. This model-local association does not by itself identify a human causal strategy.
- **Late half.** The ordering inverts: late club kinetic-energy gain is 180.5 J (selected restrain) and 174.2 J (selected drive) versus 84.3 J (early drive) and 136.3 J (passive).
- **The modeled actuator performs negative early work.** The grid-selected restrain program's early-half wrist actuator work is *negative* (−1.9 J) and its early-half joint-force transfer is likewise slightly negative (−1.0 J): the wrist interface is momentarily a net energy *withdrawer* from the club while the proximal segment accelerates. This is the literal sign of work under the imposed torque command, not evidence of muscle intent, eccentric physiology, or an observed human retention strategy.

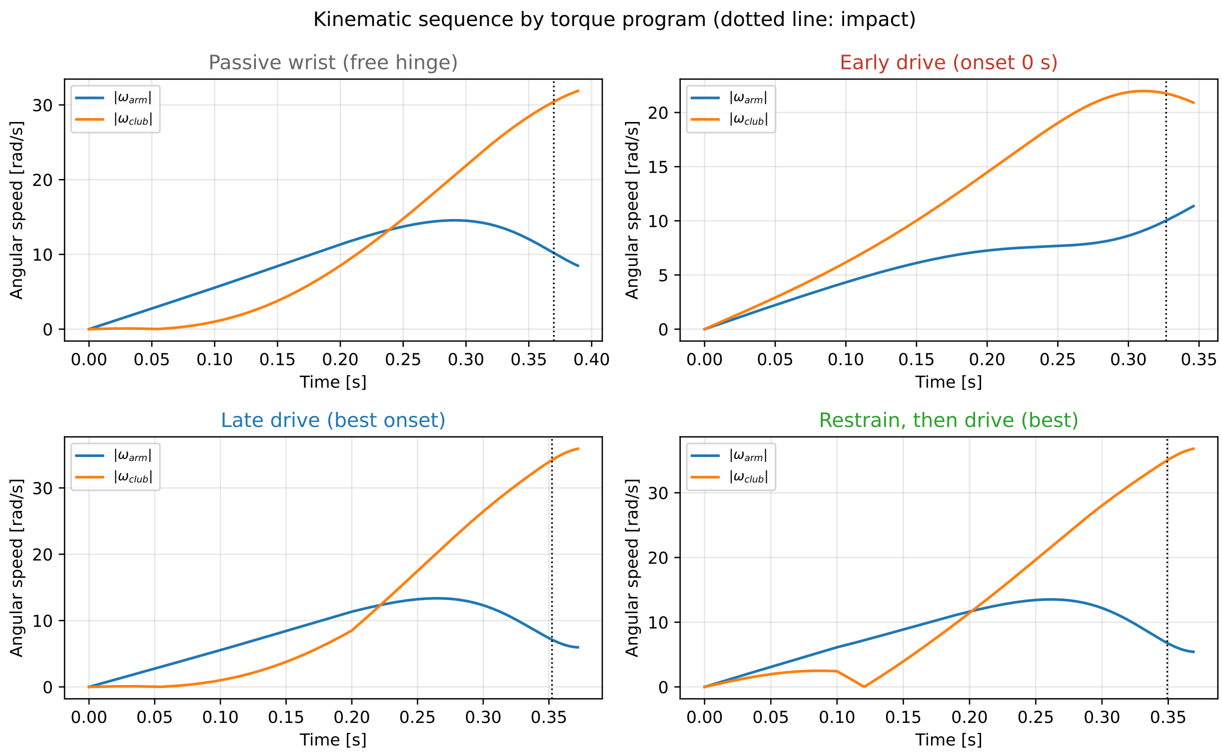

Figure 29.3: Kinematic sequence (arm and club angular speeds) for the four representative programs at $\tau_s = 60\ \mathrm{N \cdot m}$. Dotted vertical line: impact.

29.5 E4 — Wrist-Interface Power Accounting

Figure 29.7 (left) shows the Robertson-Winter interface powers for the grid-selected restrain-then-drive swing. The joint-force power — energy carried into the club *through the joint force*, the pathway that requires no wrist torque at all — is small and briefly negative early, then surges in the final ~0.1 s to dominate the two reported interface channels supplying the club (late-half integral 131.7 J versus 25.7 J of late wrist actuator work). The wrist moment channel contributes a brief late pulse, qualitatively consistent with the late window modeled by Sprigings and Neal (Sprigings and Neal 2000); this timing resemblance is not an independent validation. The right panel verifies the accounting: the club's mechanical-energy rate tracks the sum of joint-force and moment power across the swing pointwise after analytic COM acceleration replaces sampled velocity differentiation, confirming the implementation of the segmental balance of Section 2.5.2.

29.6 E2 — Counterfactual Drift/Control Split

Figure 29.8 shows the pointwise drift/control decomposition (Equation 26.3) of the club's absolute angular acceleration for the S1 pole (early drive) and the grid-selected S2 program (restrain-then-drive). In the early-drive swing, the control term supplies a large share of club acceleration from the first instant — the S1 signature — and the drift term never develops the late surge seen elsewhere. In the restrain-then-drive swing the picture reverses: early, the control term *opposes* the drift term at the club (restraint holding back a drift field that locally accelerates release); late, the drift term — the instantaneous zero-command vector field evaluated at that same state — dominates the club's angular acceleration, with the control term a small additive assist. This is a pointwise signature, not a forward zero-torque trajectory. The matched-state futures in Section 8 quantify how the tangent-field statement diverges after a cut.

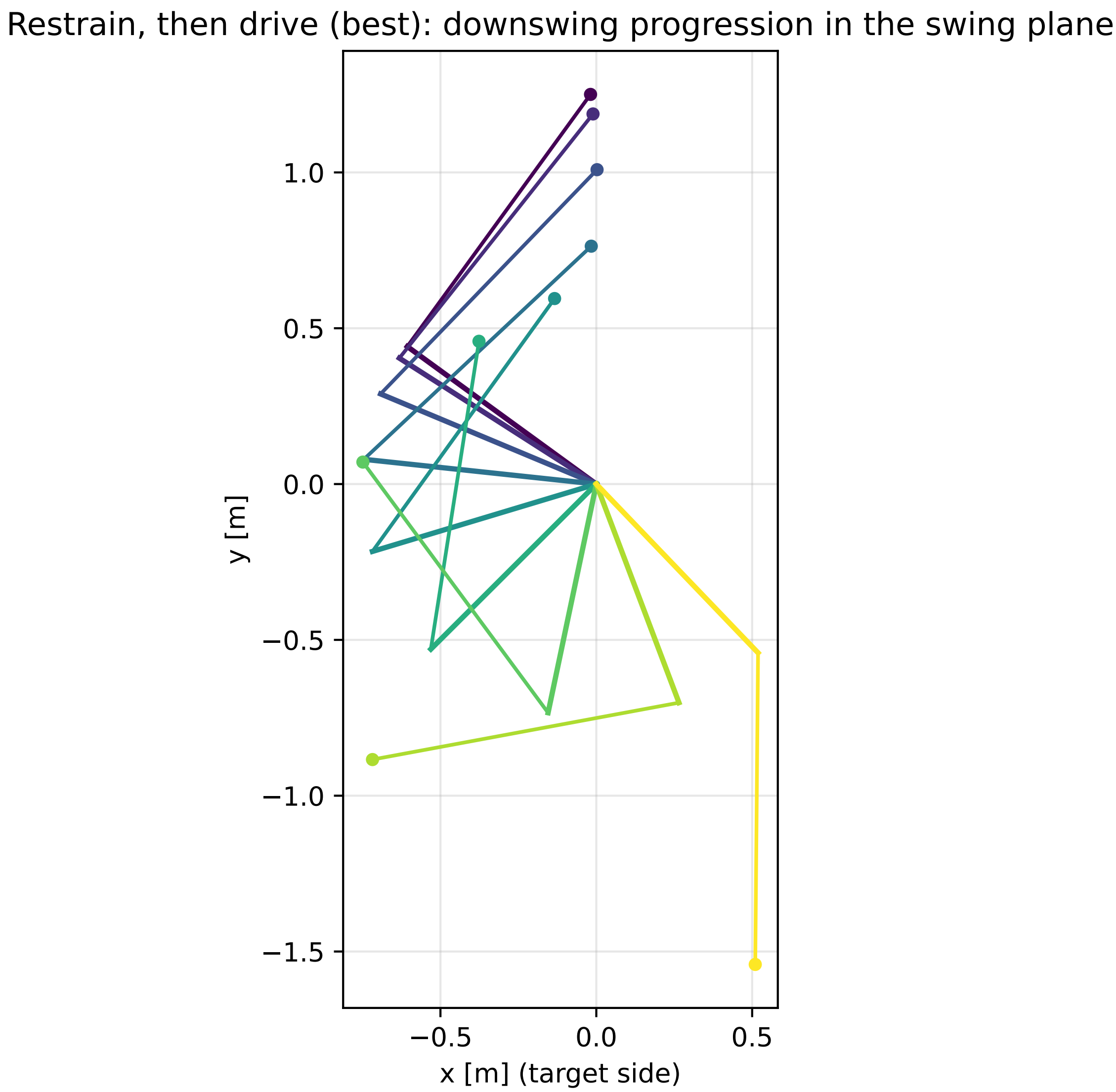

Figure 29.4: Stick-figure montage of the grid-selected restrain-then-drive swing in the swing plane (downswing progression at equal time steps).

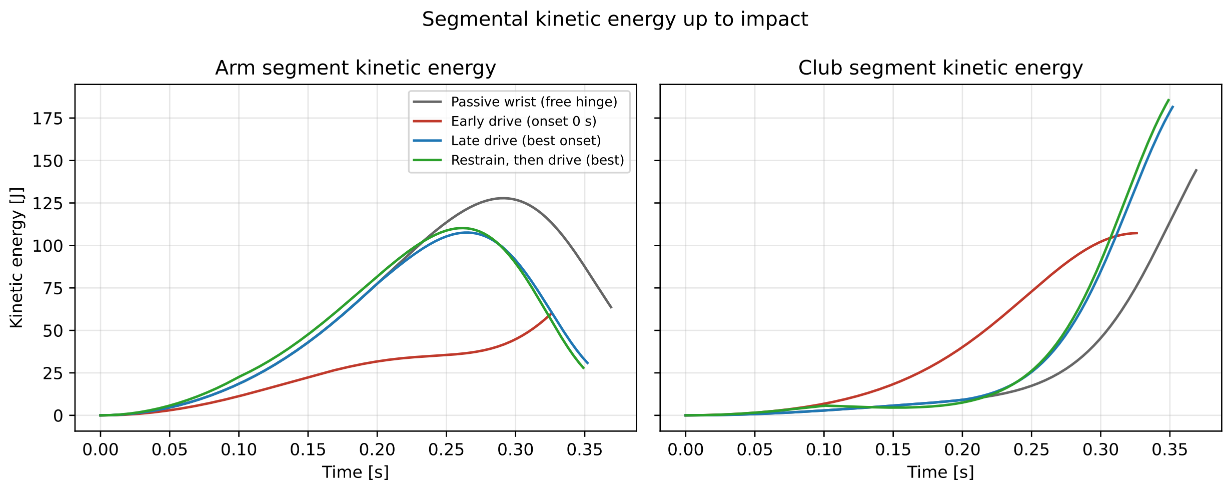

Figure 29.5: Segmental kinetic energies up to impact for the four representative programs.

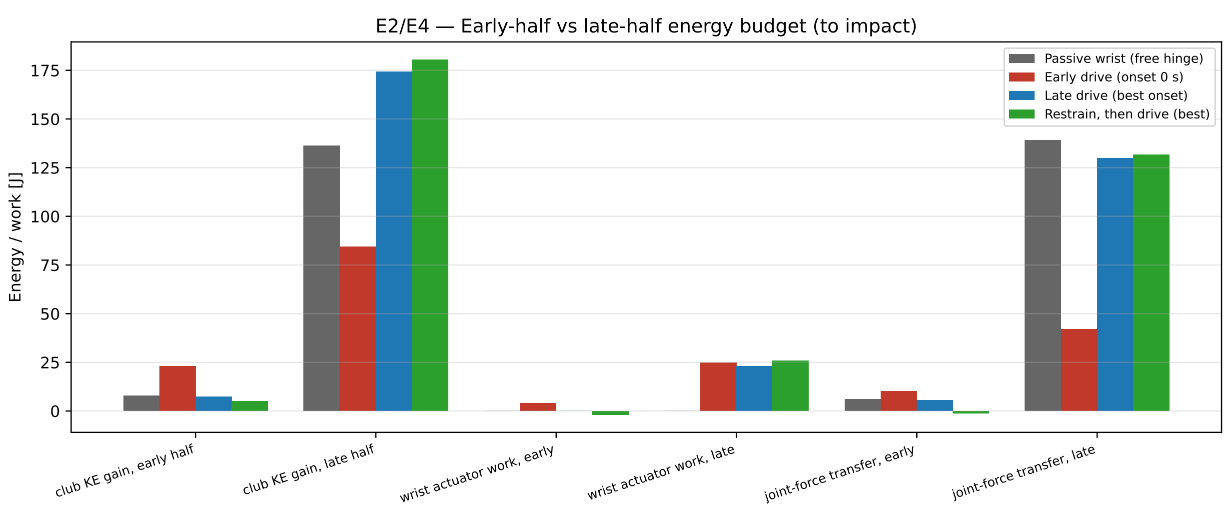

Figure 29.6: Early-half versus late-half energy budget (club kinetic-energy gain, wrist actuator work, integrated joint-force transfer) for the representative programs.

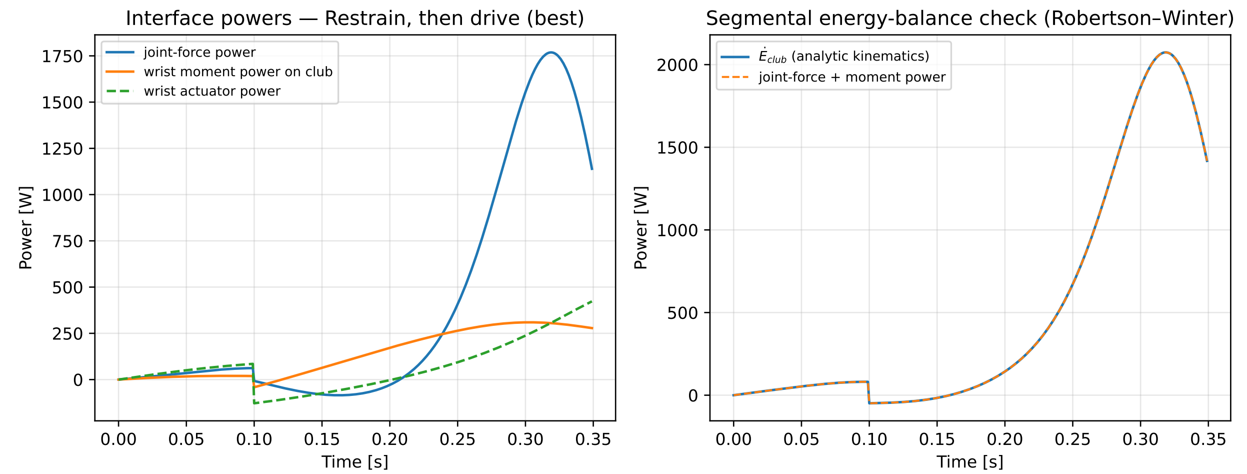

Figure 29.7: Left: wrist-interface powers for the best restrain-then-drive swing. Right: segmental energy-balance check — club mechanical-energy rate versus the sum of interface powers. The right-panel equality is pointwise after replacing sampled-velocity differentiation with analytic COM acceleration.

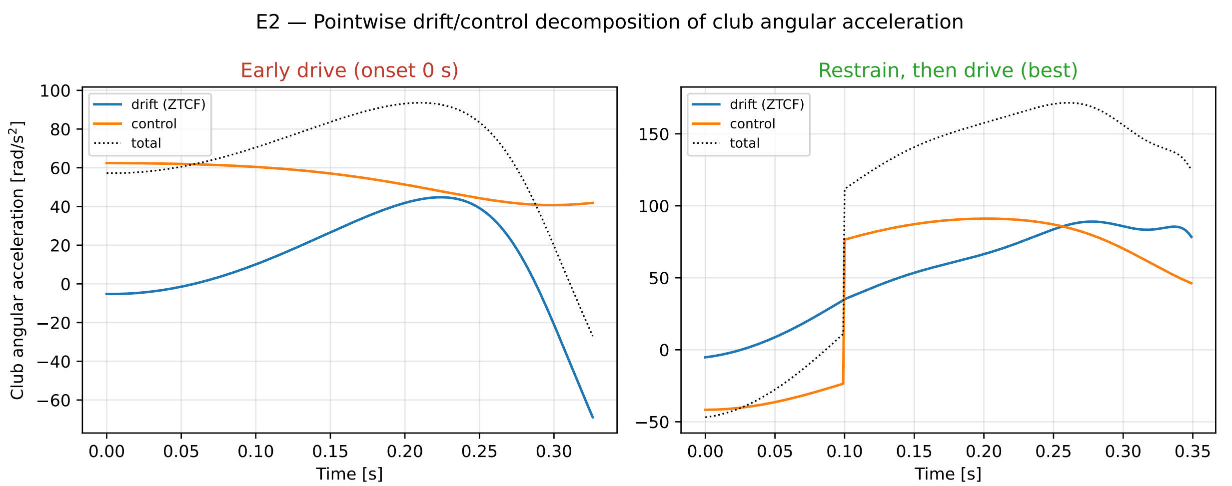

Figure 29.8: Pointwise drift (ZTCF) versus control decomposition of club absolute angular acceleration, for the early-drive (left) and best restrain-then-drive (right) programs.

29.7 E1c, E1d, and E1e — Robustness to Scoring, Parameters, and Command Rise Time

Re-scoring all trajectories under five alternative families of impact criteria preserved the qualitative strategy ordering. This rules out the specific concern that the result was created by the club-vertical impact definition, but it does not test unmodeled impact physics.

The one-at-a-time parameter study also preserved the ordering in all 13 cases. Across those cases, clubhead-speed ranges were 26.4–31.3 m/s for early drive, 32.9–35.6 m/s for the passive wrist, 36.5–40.6 m/s for the best late drive, and 36.8–41.3 m/s for the best restrain-then-drive program. The best drive onset shifted from 0.175 to 0.225 s, while the best restrained onset shifted from 0.100 to 0.150 s.

The stable ordering supports a mechanism-level interpretation within the local parameter neighborhood. The shifting optimum argues against treating one onset time as a general prescription. Because parameters were varied individually, the study does not characterize interaction effects or a population distribution.

The 2.0 rad registered bound accepted 63 and excluded 29 programs. Across bounds from 1.5 to 2.5 rad, accepted counts ranged from 58 to 69 while the selected winner at each shoulder torque remained unchanged. All 92 rows retain the unfiltered first-crossing candidate and a reason-coded status, so exclusion cannot silently remove an attempted outcome.

E1e then applied 20, 35, and 50 ms first-order transitions to every command change after the initial preload. The registered ordering was preserved at both shoulder torques for all four time constants. At 60 $N \cdot m$, selected late drive changed from 38.40 m/s at 0 ms to 38.07 m/s at 50 ms, and selected restrain-then-drive changed from 38.85 to 38.66 m/s; selected onset and restraint also changed. The result rejects a single-sample step artifact for this filter family, but does not establish a muscle activation history or a global optimum.

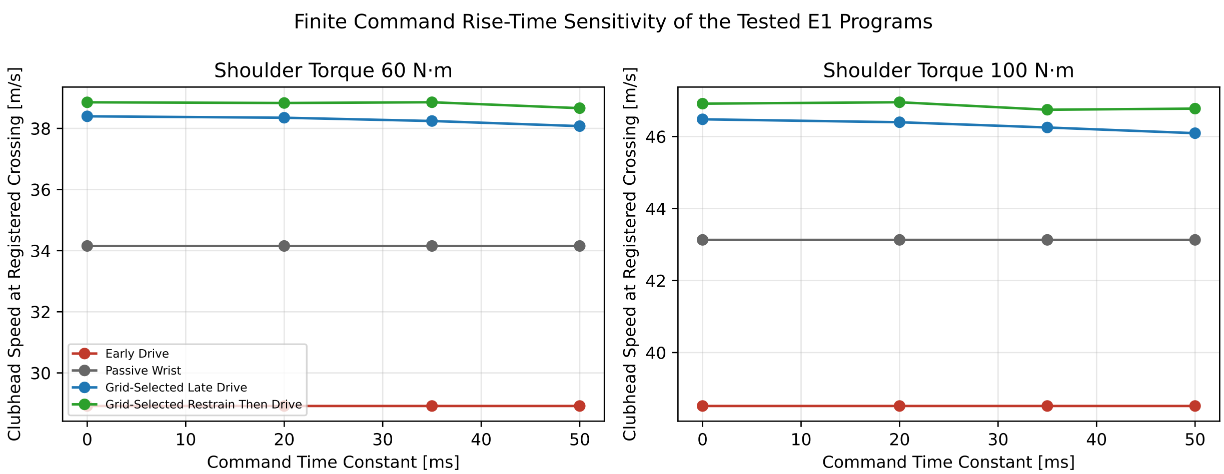

Figure 29.9: Finite Command Rise-Time Sensitivity of the Tested E1 Programs

29.8 Summary of Findings

Within this model class and finite tested command family, under matched proximal effort and a consistently defined first-pass impact: (i) early distal drive is lower than the passive condition (-15.3% at 60 $N \cdot m$ and -10.7% at 100 $N \cdot m$); (ii) the same distal command applied late is $+12.4\%$ and $+7.8\%$ above the corresponding passive programs; (iii) a timed restrain-then-drive command is highest at both effort levels, with its early-phase modeled wrist work negative; (iv) the late club energy supply in the reported interface ledger is dominated by joint-force power rather than the applied wrist-moment channel; (v) the counterfactual split shows control acting early as restraint and drift delivering late — the S2 pattern of Section 26.5 in full; and (vi) the entire ordering survives linear torque-velocity bounds, alternative scoring definitions, the declared one-at-a-time parameter perturbations, and 20–50 ms command transitions, although effect sizes and selected onset times change (Section 29.2, Section 29.7).

Chapter 30

Discussion

30.1 Agreement With the Literature

Several results of Section 29 are directionally comparable with studies in Section 2, but their magnitudes are not directly exchangeable. The harm of the tested early-drive program is consistent with the delayed-release results of Pickering and Vickers and of Sprigings and MacKenzie (Pickering and Vickers 1999; Sprigings and MacKenzie 2002) and with Milburn's account of delayed uncocking (Milburn 1982). It is not a replication: the models, objectives, admissible torques, and impact definitions differ. The +12.4% and +7.8% late-drive contrasts should likewise be compared cautiously with Sprigings and Neal's approximately 9% enabled-versus-disabled wrist-generator contrast (Sprigings and Neal 2000), and not with the 1.6% forced-delay contrast reported by Sprigings and MacKenzie (Sprigings and MacKenzie 2002). The dominance of the passive late energy pathway (joint-force transfer of 131.7 J versus 25.7 J of late wrist work in the grid-selected swing) is White's parametric transfer made explicit in Robertson-Winter accounting (White 2006; Robertson and Winter 1980). The early-delivery geometry of the early-drive swing — clubhead overtaking the hands before the arm reaches vertical — is consistent with release differences documented across skill-level studies (Cheetham et al. 2008; Zheng et al. 2008). The two selected programs instead have the hands ahead in the model's coordinate convention, with the arm 0.7–0.8 rad past vertical. These are geometric comparators, not player classifications. Finally, the drift/control time signature — control as early restraint, drift as late delivery — is the counterfactual pattern proposed in Section 26.5, now exhibited by this model.

30.2 Why the Selected Retention Program Is Faster: A Mechanistic Reading

Within this registered model and intervention family, the energy budgets localize two mechanisms associated with the ordering. Early wrist drive raises the system's moment of inertia about the hub while the shoulder is still accelerating (so the same shoulder torque buys less arm speed — the early-drive program banks 21 J less early shoulder work than the retain program despite identical τ_s). It also changes wrist work and joint-force transfer at a different state; the present comparison does not isolate an independent "amplification" factor. Timed restraint is faster in the tested family: it holds the compact configuration slightly longer than a free hinge would (the drift field already wants to open the wrist — the restraint is fighting centrifugal release, not gravity), banks that margin as arm speed, and then releases into a fully developed motion-dependent field where the registered joint-force channel transfers arm energy to the club rapidly. The negative early wrist work (−1.9 J) is small in absolute terms and diagnostic only of this simulated command: the imposed negative actuator torque opposes the modeled joint's opening velocity. It distinguishes active model restraint from zero model torque, consistent with the restraining-torque role in Jorgensen's fitted swing and Sprigings–Neal-type actuator solutions (T. P. Jorgensen 1999; Sprigings and Neal 2000; Herring and Chapman 1992). It does not identify a muscle, neural intent, eccentric physiology, or a human retention technique.

Two qualifications temper this reading. Active restraint adds only +0.5 m/s over the selected passive-then-drive program; most of the modeled benefit comes from not driving early. Heavier or longer restraint crosses outside the registered delivery zone. Neither result prescribes human timing.

30.3 What the 2-DOF Model Cannot Establish

The results chapter demonstrates the S2 pattern in the model class where the classical timing literature lives; it does not yet demonstrate it for a golfer. The specific gaps, each with a tracked remediation:

- **Spatial Body and Distributed-Club Dynamics.** The hub-path and inward-pull mechanisms (Miura 2001; Nesbit and McGinnis 2009; Nesbit and McGinnis 2014), shaft dynamics (MacKenzie and Sprigings 2009; Betzler et al. 2012; Osis and Stefanyshyn 2012), and long-axis rotations (Marshall and Elliott 2000) are outside the primary 2-DOF model. The forward two-hand and coupled moving-base/flexible-club tiers address planar closure, translation, and one lumped flex mode; base rotation, distributed beams, and the reduced full-body common-state tier now addresses nonplanar inverse dynamics. The reduced MuJoCo/Pinocchio forward-contact tier adds compliant spatial closure, long-axis rotation, swing-plane evolution, and a reduced ground-pathway proxy. Subject-scaled articulated arms, base–ground dynamics, and a coupled distributed beam remain appropriate staged extensions.
- **Simplified Actuator Models.** E1b shows the S2 ordering survives a linear torque-velocity bound on the drives with compressed margins (Section 29.2), but activation-rate limits, history dependence, and eccentric-side detail remain unmodeled. The coupled study adds pure delay, first-order activation, rate limits, torque–velocity bounds, and an impedance proxy, but these remain command-level surrogates; full optimal-control treatments with physiological actuators are the appropriate refinement (Sprigings and Neal 2000; Sharp 2009; McNally and McPhee 2018).
- **Coupled Sensitivity Is a Screening Tier.** Alternative impact definitions and single-parameter perturbations preserved the ordering (Section 29.7). The 12-input Latin-hypercube study now exposes coupled effects, parameter non-identifiability, and held-out strategy tradeoffs. Its ranges are engineering envelopes and its sample is small; measurement uncertainty and population distributions remain unmodeled.
- **Counterfactuals Remain Model-Tier Specific.** The Python pathway now includes both pointwise ZTCF profiles and forward same-state killswitches in the double-pendulum and constrained two-hand tiers. The coupled extension now preserves the finite negative-couple branch with endogenous base translation and club flex. The spatial common-state tier transports the geometry response across independent inverse-dynamics formulations. The reduced spatial forward tier then preserves a negative contact couple after complete driver removal under both native inertia-and-bias operators, with one shared projected contact law and state update. Its hand carriages and declared contact law do not establish persistence in anatomical arms or human dynamics.
- **No Human Data Yet.** The decisive observational test — wrist interface power time courses across skill levels from motion capture
  (3) — awaits an appropriately governed motion-capture study.

30.4 Implications, Cautiously Stated

For modeling, counterfactual and energy-level accounting make the timing question testable without treating peak order as energy transfer. A recent cross-sectional study likewise found its constructed transfer-efficiency factor associated with clubhead speed, but its mediation analysis does not establish a causal human transfer mechanism (Rachnavy et al. 2026). The program names denote finite model inputs, not coaching cues or novelty over delayed-release literature (Cochran and Stobbs 1968; T. P. Jorgensen 1999). No recommendation follows. Player-specific translation requires governed human evidence spanning physical constraints, injury history, and functional timing variability (Cole and Grimshaw 2016; Hume, Keogh, and Reid 2005; Neal et al. 2007; Langdown, Bridge, and Li 2012; Glazier 2011).

Chapter 31

Critical Momentum-Transfer Questions

The model ladder now permits bounded answers to several recurring questions, but it does not support a single transfer percentage, a universal release time, or a preferred human technique. Table 31.1 separates present results from the observations needed to change them. The prospective experiment definitions are machine-readable in `momentum_transfer_experiment_registry.json`, and their broader rationale is documented in the open `question program`.

Table 31.1: Current answer and falsification map for the critical momentum-transfer questions. "Conditional" denotes model- and estimand-bounded evidence rather than a human strategy.

Question	Present Assessment	What Would Change the Assessment?
How much transfer is drift-mediated?	Conditional on the observable, coordinate and frame, event window, model, and decomposition. Signed drift shares may exceed 100% when control opposes the pathway; pointwise attribution is not forward persistence.	A common acceleration/force/impulse/power/work ledger across tiers, same-state killswitches, uncertainty propagation, and participant-held-out bilateral-wrench evaluation.
Which geometry matters?	Relative-link and force–velocity angles create exact sine/cosine gates; bilateral couple varies with signed grip separation and transverse differential force. Existing moving-base and two-engine spatial controls reproduce coincident-grip zeros and moment-arm reversals. A six-profile audit rejects prescribed states that miss closure by 0.171–0.616 m; a bounded follow-up closes all 234 registered reduced-tree configurations. The articulated distributed-grip and passive-shaft tiers advance twelve selected states through 50 ms. A finite-base extension then adds translation and intrinsic free moment; all numerical gates pass, but none of 384 coupled–fixed cells meets the primary load–total-work match.	Calibrate grip, shaft, unilateral foot contact, and force-plate support; propagate initialization and parameter uncertainty; then repeat the horizon, geometry, killswitch, matched-outcome, and held-out human bilateral-wrench tests.

Question	Present Assessment	What Would Change the Assessment?
Which timing patterns matter?	Early distal release changes the available geometry; proximal rate, acceleration, braking, and release timing interact nonmonotonically. "Casting" is not one universal event.	Factorial interventions on proximal acceleration, distal release, and braking under matched state and work, with multiple preregistered casting definitions and adverse-load tests.
Does a drift-mediated strategy require less timing precision?	Not supported in the registered moving-base planar comparison. On a common nominal phase grid, the clock policy retained four of five robust task-viable points and 45 ms of contiguous width; the delayed/noisy state trigger retained one point and no multi-point span. This does not measure neural timing demand.	Continuous phase-volume studies with independently identified observers, spatial impact outcomes, subject scaling, and participant-held-out perturbations.
Is a strategy self-correcting?	Not established. The earlier screen produced 13–20% sustained recovery, whereas the expanded phase/load screen produced none in 60 cases. No tested policy has a recovery-qualified viable region.	Continuous attraction-region studies with independently identified observers, stronger feedback families, external-contact disturbances, and human perturbations without hidden load-cost increase.
Should proximal velocity be maximized?	No general rule is supported. Exact equal-energy rate sweeps are nonmonotonic. A 216-program common-time screen yields 46 disjoint work/load-matched pairs with 20 favorable and 26 adverse higher-rate outcomes. An identical-state acceleration sweep also reverses the club-acceleration response before impact.	Full-delivery-state-matched forward rate and acceleration interventions, extended across spatial and subject-scaled models and held-out participants.
Is slack beneficial or necessary?	Partly answered at a synthetic constitutive tier. Five declared classes have been exercised separately, but no global benefit, necessity, intentionality, or delivery advantage is supported. One scalar output nearly confounds contact disengagement with the biological-compliance surrogate.	Embed one class at a time in moving-base, two-hand, and spatial delivery models under matched state, work, and load; add stateful backlash and subject-specific tissue models; acquire independent contact, shaft, tendon, activation, and bilateral-wrench measurements.

31.1 Geometry Gates and Null Controls

The geometry atlas in Figure 31.1 makes three independent gates explicit. First, force power is $Fv\cos\phi$: the same force magnitude is positive, zero, or negative as the force–velocity angle crosses 0, 90, or 180 degrees. Second, the distal tangential and centripetal projections have distinct $\cos\theta$ and $-\sin\theta$ gates, so one can vanish while the other is maximal. Third, an ideal bilateral differential-force couple is the signed grip-separation vector crossed with differential force. It vanishes for coincident contacts and axial differential force and reverses with the moment arm or transverse force.

These are not merely symbolic checks. The existing moving-base planar control gives exactly zero couple for coincident grips; the rotating-base tier changes +1.351 to -1.351 N m under signed arm reversal; and the independently authored MuJoCo and Pinocchio spatial-contact tier retains a maximum reversal residual below 9.2×10^{-16} N m. Proper 3-D rotations preserve total wrench power to the registered numerical

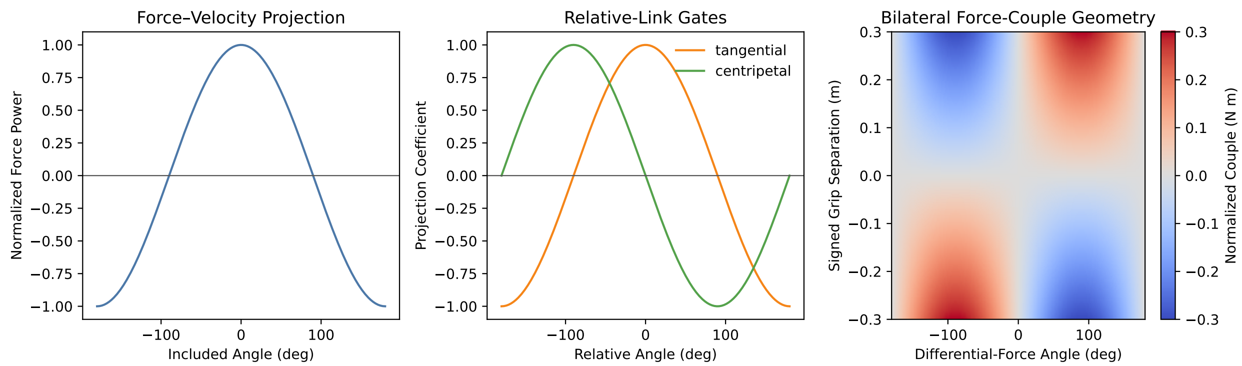

Figure 31.1: Geometry Atlas for Force Power, Relative-Link Projection, and Bilateral Force-Couple Sign.

tolerance. The remaining anatomical question is therefore not whether these geometric identities hold, but which subject-scaled configurations, forces, velocities, and compliant contacts are feasible and used by people. The subject-scaled audit in Section 17.6 makes that distinction quantitative: all local constraint Jacobians retain rank six, yet the prescribed anatomical hand points remain 0.171–0.616 m from the grips. Full local rank is not contact closure.

The bounded inverse-kinematics follow-up separates unclosed prescription from reduced-tree reachability. All 234 profile/span/phase configurations close both point contacts with fixed club coordinates, rank-six achieved constraint Jacobians, positive engineering-limit margins, and positive coarse bounding-sphere clearances. That result clears only the next geometric gate: the bounds are not clinical ranges, the collision screen is not anatomy, and no contact forces or delivery outcomes are solved.

31.2 Timing and Common Failure Descriptions

The terms *casting*, *weak early body acceleration*, and *late release* are useful only after translation into observables. The registered timing study therefore treats at least four quantities independently: proximal-acceleration onset, distal-angle or distal-rate threshold crossing, proximal-braking onset, and the impact or delivery event. A result is not robust if it depends on one arbitrary casting threshold. Work-matched and delivery-state-matched controls are both required because either matching rule can alter the apparent benefit.

31.3 Timing Demand and Self-Correction

A mechanism can be mechanically passive at an instant while its preparation or regulation remains demanding. Timing demand is therefore reported as the width or volume of a viable event-time region, outcome sensitivity to phase error, lower-tail performance, and degradation under observer delay and noise. Self-correction has the stronger requirement that a declared physical or feedback mechanism return a perturbed state toward a viable set. Repeatable open-loop behavior does not meet that definition.

The delayed-observer experiment makes that distinction executable. Each policy received the same nuisance parameters and deterministic sensor-noise realization in an unperturbed reference and a matched initial-state perturbation. All policies briefly crossed the half-error threshold in most cases, but most later left it. Requiring sustained recovery through delivery reduced return fractions to 0.20 for the clock and delayed/noisy policies and 0.13 for perfect-state and higher-impedance policies. Median terminal error remained 0.79–0.84 of the initial perturbation. Figure 31.2 thus rejects the shortcut from transient error reduction or low outcome variance to self-correction; it does not rank human strategies.

The common-phase extension maps both policies onto the same nominal release coordinate. Clock commands use offsets from 0.140 s; state thresholds are the right-shoulder angles reached at those same target times on one common nominal trajectory. The comparison therefore does not confuse seconds with arbitrary angle

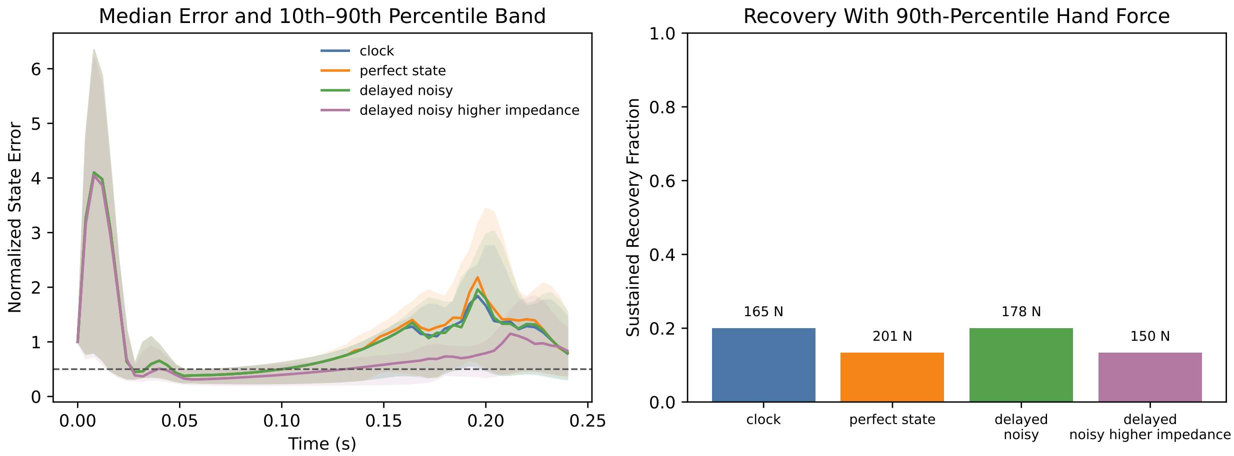

Figure 31.2: Trajectory-Level Recovery Under Matched Initial-State Perturbations. Bands show the held-out engineering envelope; labels above the recovery bars give 90th-percentile individual-hand force.

thresholds. Six named cohorts preserve nominal dynamics, a 15% heavier distal club, 20% lower shaft stiffness, 12 ms additional actuator delay, a 50% larger initial perturbation, and a combined adverse case. Every policy, load, and phase has paired reference and perturbed trajectories.

Under the primary task guards—at least 95% of the load-matched clock baseline speed, no more than 2 degrees additional face/path error, no more than 10% additional peak individual-hand force or squared-torque effort, and a 5% normalized numerical-residual ceiling—the clock policy is viable at four of five phase points across the intersection of all loads. Its largest contiguous sampled span is 45 ms. The delayed/noisy state trigger is robustly viable only at the latest point and therefore has no multi-point span. Strict, primary, and lenient guards retain the same ordering. Requiring sustained half-error recovery makes both regions empty: none of the 60 perturbed cases recovers through delivery. This is evidence against a state-trigger timing or self-correction advantage in this declared model, not evidence that people should use clock timing. Half-step checks change delivery speed by 0.029–0.034 m/s and reduce the normalized residual from 0.014–0.022 to 0.008–0.012.

31.4 Proximal Velocity as a Dose, Not a Maxim

The existing planar evidence is sufficient to reject the rule "maximize proximal velocity" at those declared tiers, but not to specify a human optimum. An apparent speed benefit must be considered together with relative motion, control work, interface power, braking work, bilateral load, club orientation, and the matching rule. The registered analysis searches explicitly for plateaus, interior optima, and reversals rather than forcing a monotonic fit. The exact energy-matched state sweep retains 36 later-phase cases with maximum energy residual 5.7×10^{-14} J; no phase is monotonic, and the pre-impact fitted slope falls from 283.74 to 5.70 W/(rad/s) relative to the co-varying-energy rule. The initial eight reused work-only pairs favor the lower-rate member by 4.31–9.28 m/s. The follow-on 216-program common-time factorial resolves that load confound: its primary thresholds produce 109 candidate and 46 disjoint work/load-matched pairs, of which 20 higher-rate members are faster and 26 are slower. All nine tolerance cells retain both signs. This mixed result rejects a monotonic rate rule but does not isolate a causal rate effect because actuator commands and full delivery state differ. The separate 45-case acceleration intervention holds the entire state and distal torque fixed. Before impact, increasing proximal acceleration raises interface power yet reduces club angular acceleration; the required proximal torque spans -69 to +189 N m. Acceleration is therefore neither a free input nor a monotonic substitute for proximal rate.

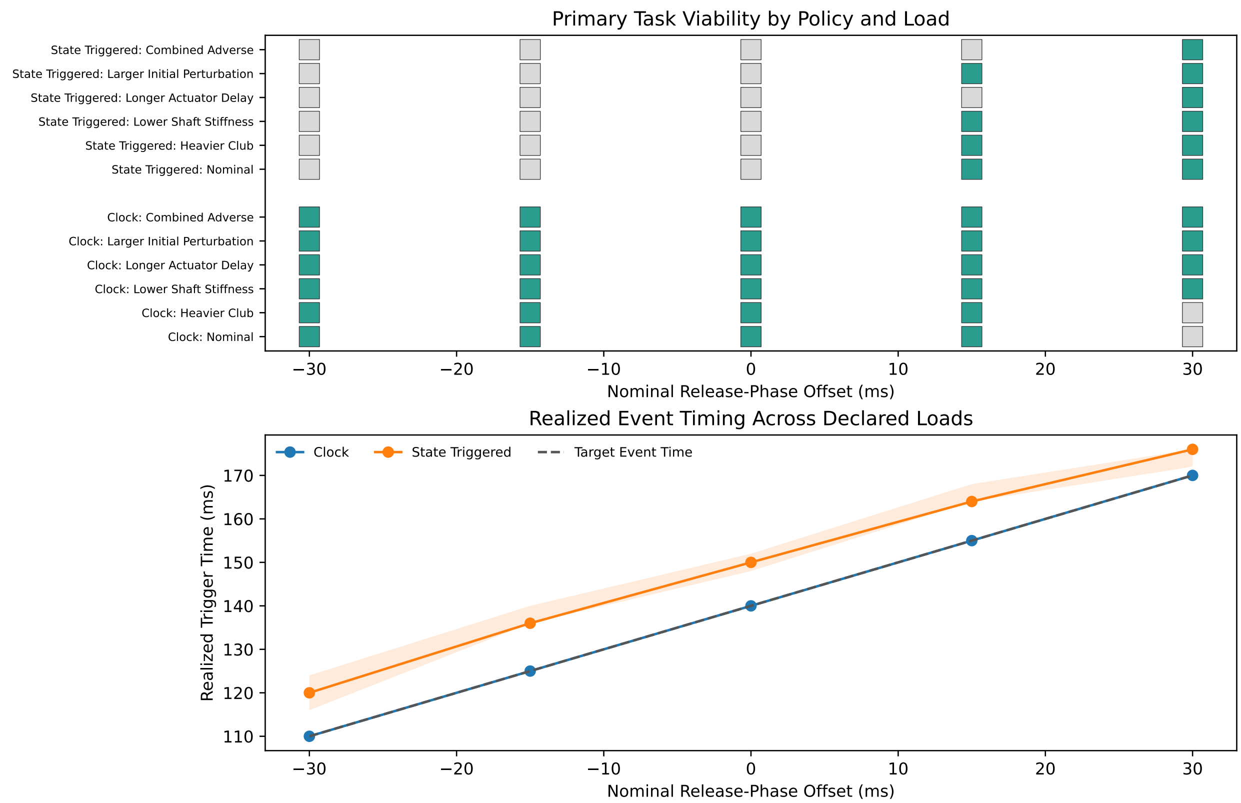

Figure 31.3: Task Viability and Realized Trigger Timing Across the Common Phase Grid and Declared Adverse Loads. Green cells satisfy common speed, face/path, force, effort, and numerical guards; recovery is reported separately and is absent in all registered cases.

31.5 Five Distinct Slack Hypotheses

1. **Contact slack** is temporary loss or weakening of a hand-grip constraint.
2. **Transmission slack** is backlash or a dead zone before torque transmission.
3. **Structural slack** is compliant preload and elastic deformation.
4. **Biological series compliance** is a muscle-tendon state with stored and released energy.
5. **Control slack** is an activation deadband, delay, or co-contraction reserve.

The dynamic constitutive audit now exercises all five classes separately under a slow closed-cycle sine and a richer multisine with repeated reversals. The four mechanical surrogates satisfy the registered passivity and work-energy closure checks; the largest absolute closure residual is 5.13×10^{-10} J. The control deadband is deliberately treated as a delayed command-transmission map, so mechanical passivity and stored energy are not assigned to it.

The richer excitation improves the local scaled-sensitivity conditioning of every mechanical surrogate. Each three-parameter local Jacobian is full rank, but that result does not identify the generating class. Under the registered multisine, contact disengagement and the biological-compliance surrogate differ by only 1.96% normalized transmitted-output RMSE. Independent contact, tissue, shaft, activation, and bilateral-wrench measurements are therefore necessary to distinguish mechanisms rather than fitting one output channel. The transmission element remains a memoryless dead-zone-plus-damping surrogate, not a stateful rate-independent play operator, and the biological element is a unilateral Kelvin-Voigt surrogate rather than a subject-specific tendon model.

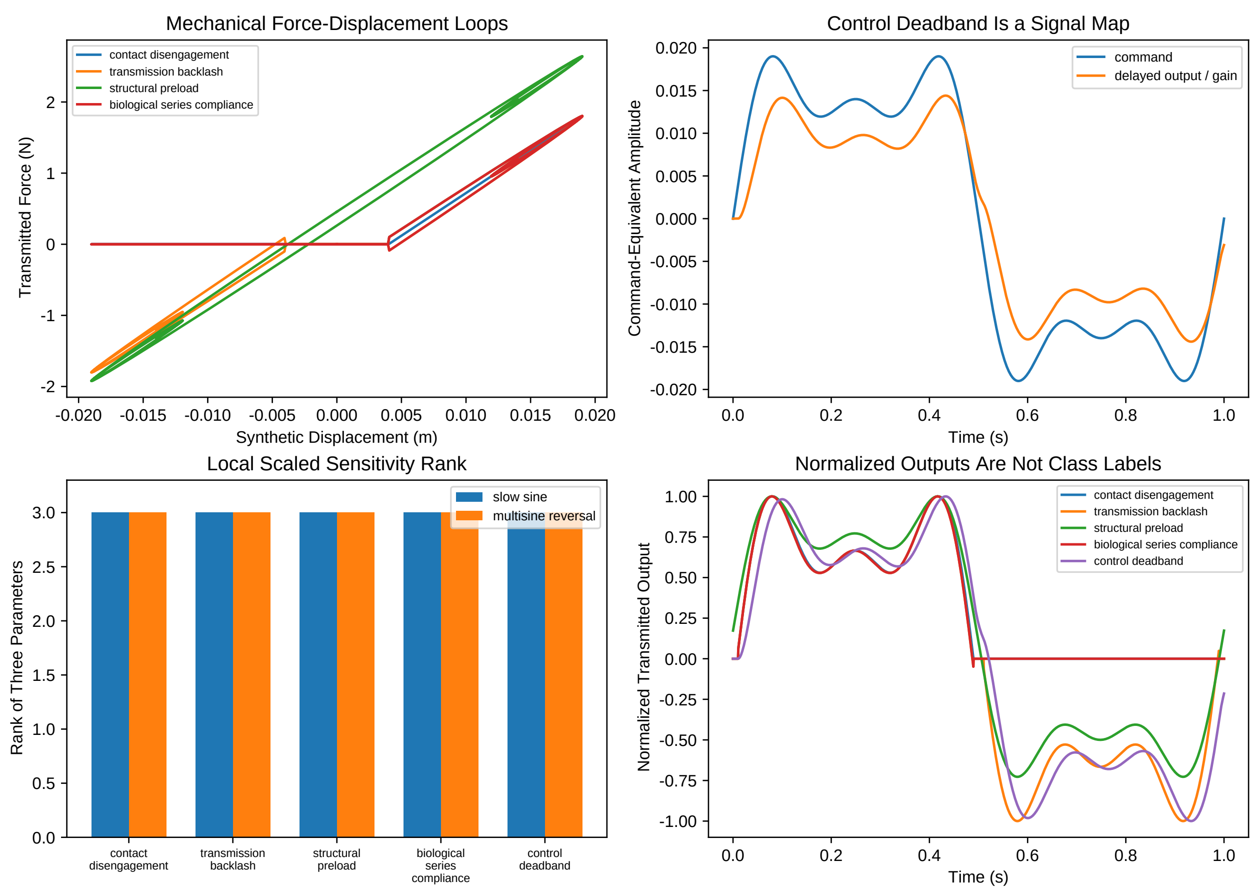

Figure 31.4: Typed Slack Dynamic Audit. Mechanical force-displacement loops, the delayed control boundary, local scaled-sensitivity ranks, and normalized outputs are shown for the registered synthetic excitations.

This evidence supports only a typed experimental program. It does not show that slack is good, bad, intentional, required, or beneficial for delivery. The articulated forward atlas now performs the first of those transport tests: bilateral, tension-only, and two dead-zone laws are compared under common displacement and approximately matched radial extension across 1,944 bounded trajectories. The 1.5 mm law remains open under the common 1 mm displacement but taut under matched extension; natural branches show no transition before 5 ms, while isolated boundary probes qualify opening and reattachment. This shows why preload matching changes the answer, not that either condition is beneficial. Any benefit proposal must still survive longer matched-work/load delivery, stateful hysteresis, calibrated distributed contact, and independent human measurement.

The next articulated atlas crosses frictionless and equipment-provisional $\mu = 0.35$ tension-fiber comparators with one, three, and five stations per hand while holding total stiffness and damping fixed. Its 576 trajectories pass nested 4, 10, 25, and 50 ms power, energy, refinement, geometry-null, and MuJoCo–Pinocchio gates. Separate probes record opening and reattachment with exact engine agreement, but begin disengaged and do not qualify an attached-to-open first failure. Finite-friction minus frictionless 50 ms speed differences have mixed signs. The result therefore demonstrates sensitivity, not a physical benefit of friction, slack, or distributed pressure. A mass-metric impulsive perfect-stick control bounds instantaneous kinetic-energy capture at 9.84×10^{-9}–0.37665 J while enforcing tangential velocity below 9.65×10^{-11} m/s with exact stored-precision engine parity. It does not test static-friction feasibility or subsequent stick–slip evolution. Attached-to-open first failure, measured contact, coupled shaft/ground work, matched tasks, and governed human outcomes remain necessary.

The following articulated shaft atlas then retains the five-fiber grip and adds rigid, bending-only, torsion-only, and coupled passive-club branches. Its 384 trajectories pass the registered 0.25/0.125 ms work–energy, small-deformation, killswitch, and native-engine gates through 50 ms; 1.0 and 0.50 ms torsion probes fail closed outside the declared linear domain. Of 384 coupled–rigid cells, 126 meet the predeclared 5% peak-load and dissipated-work match. Their final-speed differences include 82 negative and 44 positive values. Passive shaft response is therefore a state-dependent pathway in this synthetic model, not a general speed advantage. Equipment calibration, higher mode adequacy under fast loading, ground work, impact, and human outcomes remain open.

31.6 Evidential Boundary

These experiments are designed to make the framework easier to disprove. Synthetic studies can reject a mechanism within a declared model and can qualify software, but they cannot establish a coaching instruction or human control strategy. The participant-held-out stage remains blocked until a governed dataset contains synchronized full-body and club kinematics, force plates, bilateral six-axis grip wrenches, grip/contact state, and impact outcomes. Substituting synthetic traces would erase the question the human stage is intended to answer.

31.7 Point-by-Point Readiness Audit

The handwritten agenda contains nine testable points after its nested timing examples are separated: drift contribution; geometry; casting; early-downswing proximal acceleration; segment release; timing precision; self-correction and noise robustness; proximal-velocity maximization; and slack. The executable readiness audit preserves all nine rather than allowing a broad question to hide an unplanned subquestion. Eight presently have a model-bounded answer or a negative general-rule result. The unresolved point is the broader timing-precision claim: the registered planar comparison is adverse to a state-trigger advantage, but spatial and human timing demand remain untested. All nine have a registered model experiment and a participant-held-out human stage, but the latter remains blocked by the bilateral-wrench data boundary.

The machine-readable authority is `momentum_transfer_readiness_audit.json`. It is regenerated from the question and experiment registries and validated in CI. A missing source point, missing falsifier, invalid evidence status, absent human stage, or experiment linked to the wrong question is a hard failure.

Table 31.2: Readiness assessment for every point transcribed from the source agenda. "Partly answered" never denotes a human or coaching conclusion.

Source Point	Present Scientific State	Next Decisive Model Test
Drift contribution	Partly answered; observable- and window-specific only	Common cross-tier estimand table with uncertainty
Geometry dependencies	Partly answered through reduced spatial controls; the first subject-scaled audit rejects contact feasibility of the prescribed common states	Closed-contact inverse kinematics, calibrated contact, and independent forward integration
Casting	Partly answered: no single event definition is defensible; human causal interpretation remains open	Multiple preregistered event definitions under matched controls
Early proximal acceleration	Partly answered pointwise; nonmonotonic	Forward factorial intervention with full-state/work/load matching
Segment release	Partly answered; objective- and constraint-dependent	Viable-region mapping across proximal and distal control families
Timing precision	Unresolved beyond an adverse planar result; a state-trigger volume advantage is not supported in the registered planar tier	Continuous common-phase spatial and subject-scaled comparison
Self-correction and noise robustness	Partly answered negatively at the registered planar tier; no sustained recovery in 60 cases	Continuous attraction regions with identified observers and external-contact loads
Proximal-velocity maximization	Not supported as a general planar rule	Causal full-delivery-state-matched spatial dose response
Slack	Partly answered at a synthetic constitutive tier; no global benefit and one-channel class identification is not established	One-class-at-a-time moving-base and spatial delivery tests with stateful backlash, subject-specific tissue, and independent measurements

Chapter 32

Conclusions and Research Priorities

32.1 Conclusions

The literature does not support equating proximal-to-distal peak order with a requirement to transfer mechanical energy outward as early as possible. Interaction dynamics, optimal-control studies, and segmental energy measurements instead motivate a timing hypothesis: retain a compact proximal configuration while proximal speed develops, then accelerate the distal handoff later in the downswing.

The present simulations provide model-derived support for that mechanism. Under matched shoulder torque in a planar two-link model, early wrist drive reduced clubhead speed relative to a passive wrist, whereas grid-selected late drive increased it. A small early restraining torque followed by late drive was best among the tested programs. Energy and counterfactual accounting located the modeled mechanism in early arm-energy retention and late joint-force transfer rather than in early active wrist work.

This conclusion is conditional. The result survived torque-velocity bounds, alternative scoring rules, 13 one-at-a-time parameter cases, and declared 20–50 ms command transitions, but the selected onset shifted across cases. The study therefore supports a robust ordering within a local model neighborhood, not a universal timing value or an individual coaching prescription. Planar motion, simplified actuators, and absence of human data remain material limitations. The finite sweep is not a continuous optimal-control solution, and the command filters are not muscle activation models.

The forward constrained two-hand extension resolves one previously open mechanistic question. Starting from the exact same 0.200 s state, the force-generated club couple remains negative for 50 ms after all applied joint torques are removed. The effect disappears exactly when both grip moment arms are removed and remains stable under timestep and projection refinement. This supports finite passive-couple persistence in the declared planar model, not a claim about muscle inactivity or human technique.

The coupled moving-base/flexible-club extension resolves the next structural question at the planar tier. Base translation, shaft flex, and both grip forces evolve in one forward constrained solve. The negative force-generated couple survives the same-state zero-command intervention, while coincident grip points remove it exactly; constraint, contact-power, and work–energy residuals close under timestep refinement. This transports the mechanism beyond a fixed base and rigid club without promoting it to a spatial or physiological result.

The distributed-shaft comparison closes a narrower structural gate. A one-mode reduction and six-mode Euler–Bernoulli reference share the same assembled mass, stiffness, damping, tip inertia, and loads. The reduced model closely follows slow loading but misses higher-mode history under a short force-and-moment pulse, even when their peak deflections are similar. Synthetic modal identification, mesh convergence, and work–energy closure pass. This does not calibrate equipment or show that the result survives coupling the beam into the two-hand constrained solve.

The articulated finite-base extension closes the next numerical mechanism gate while producing an adverse primary inference result. Across 384 pathway and 192 independent-control trajectories, the native inertia-and-bias operators remain within the registered transport bounds, energy residuals decrease with step refinement, and all declared shaft/base domains hold through 50 ms. Ground force and intrinsic free moment are mechanically active, but none of 384 coupled–fixed comparisons meets the preregistered 5% peak-load and total-dissipated-work match. A post-hoc non-ground-dissipation sensitivity admits 60 cells with both speed-difference signs. The experiment therefore qualifies finite-base coupling and rejects a universal delivery interpretation; it does not identify a ground-use strategy or human benefit.

The reduced full-body common-state extension resolves implementation transport for a narrower spatial estimand. MuJoCo and an independent Lagrange–Christoffel formulation agree across 20 coordinates and 61 nonplanar states to 2.14×10^{-11} relative error. Reversing the hand moment arm reverses the force-generated couple and coincident points remove it exactly. Because the forces are prescribed and the state is shared, this supports spatial inverse-dynamics and geometry transport but leaves passive forward contact inconclusive at that tier.

The subject-scaled contact-closure audit rejects a tempting shortcut at that same tier. Six deterministic de Leva profiles retain a full-row-rank local contact Jacobian, yet the prescribed anatomical hand points remain 0.171–0.616 m from the declared grips. Rank and conditioning therefore cannot substitute for closed feasible anatomy. The next articulated spatial tier must solve bilateral closed-contact inverse kinematics with joint-limit and collision checks before its forward contact, timing, recovery, or slack results can be interpreted. The registered inverse-kinematics follow-up now clears that reduced-tree gate in all 234 profile/span/phase samples while holding the club pose fixed. Its minimum engineering-limit margin is 0.103 rad and its minimum coarse bounding-sphere clearance is 30.9 mm. These are screening results, not measured anatomical ranges or mesh-level clearance; they advance the next test to calibrated compliant forward contact from the closed states.

A paired arm-only intervention now isolates one omitted structure. With trunk and club pose fixed, the fixed-shoulder branch closes none of 54 registered states, whereas a bounded scapula-on-ellipsoid surrogate reaches the contact residual in 31 states and satisfies both residual and solver-termination gates in 16. Full rank persists while coordinate nullity rises from two to ten, so the result supports the importance of scapular geometry but also strengthens the non-identifiability boundary. It is not an anatomical, muscular, or human strategy result.

The reduced spatial forward-contact extension resolves that narrower mechanism gate. Native MuJoCo and Pinocchio independently supply rigid-body kinematics, mass, bias, gravity, and continuous-time acceleration for two finite-mass hand carriages and a free rigid club without direct club actuation. Both branches share the projected compliant interfaces and project-authored state update. Their baseline and same-state killswitch trajectories satisfy the declared position, orientation, wrench, and energy regions. Removing the complete grounded driver leaves a negative force-generated swing-normal couple for 37.5 ms in both engines; coincident and reversed-moment-arm controls close exactly, and the work–energy residual decreases under timestep refinement. This supports reduced spatial contact persistence and inertia-and-bias transport, not independent contact-solver equivalence, anatomical arms, muscles, calibrated grip tissue, equipment, or human strategy. A separate MuJoCo-native equality and `mj_step` control produces a nonzero discrepancy from the projected formulation and is reported as a formulation difference, not a parity success.

The closed-state validity-horizon extension further shows that the same two engines remain inside the declared trajectory, wrench, energy-discrepancy, and work–energy closure gates for all 2,160 registered cases through 50 ms. The matrix spans all profile–span–phase states plus one-factor stiffness, damping, hand-mass, timestep, and immediate-driver-off branches. No failure is observed inside the registered interval, so the result is right-censored at 50 ms. It strengthens the reduced numerical reference but does not turn the hand-carriage model into articulated anatomy or a full delivery simulation.

The coupled uncertainty/control phase rejects two additional shortcuts. A net planar wrench cannot uniquely identify both hand forces, and six summary observables cannot identify the complete 12-parameter vector. Separate training and held-out ensembles leave objective-dependent tradeoffs among all eight command programs. Early restraint improves held-out lower-tail speed relative to late drive but increases the planar face/path error, so the result supports a conditional model mechanism rather than a universal or physiological strategy.

The experimental phase is preregistered but not empirically executed. Its machine-readable protocol fixes six synchronized modalities, participant-level holdout, identity-safe provenance, filtering and residual sensitivities, and four prediction-specific falsifiers. The synthetic dry run passes all intake and fail-closed controls, but it cannot advance H1–H4. Governed human data are still required.

The open-resource layer now supplies model-tier presets, a hash-pinned release manifest, standard checksums, a data dictionary, citation metadata, and a claim-first reviewer workbench. Validation fails closed on artifact drift. The bundle remains a qualified local release candidate rather than a persistent archive: articulated subject-scaled contact, equipment-calibrated beam coupling, governed human evaluation, and external identifier deposit remain open.

32.2 Research Priorities

The next work should reduce the largest inferential risks in dependency order:

1. **Articulated Spatial Forward-Contact Counterfactual.** Replace the executed hand-carriage reference with subject-scaled articulated arms and calibrated grip interfaces. Start from the executed bilateral closed-contact, engineering-limit, and coarse collision-qualified configurations, replace those screens with subject-specific anatomy where available, then preserve the two-engine same-state killswitch, force, couple, power, work, pathway, and closure observables.
2. **Calibrated Uncertainty and Constrained Control.** Extend the executed multivariable screen with population-informed distributions, measurement error, profile-likelihood or Bayesian calibration, larger held-out ensembles, and a constrained optimal-control comparator.
3. **Spatial Model-Fidelity Ladder.** Extend the executed planar base rotation, intrinsic free moment, distributed grip, and passive shaft into a three- dimensional club/body solve with calibrated unilateral foot contact and force-plate comparison without changing the registered interface observables. Each rung should carry conservation checks and cross-engine tolerance gates.
4. **Execute the Frozen Human-Data Protocol.** Acquire governed synchronized measurements that pass the fixed inclusion, residual, missingness, participant-holdout, and provenance gates. Sequence order alone must not be treated as evidence of energy transfer.
5. **Arm–Wrist Allocation and Preload Falsification.** Execute the bilateral grip-wrench, pressure, activation, stiffness, and participant-holdout tests registered in Section 14. Treat the dead-zone mechanism as rejected if its predicted gap is absent under documented low tangent stiffness or if any performance difference disappears on holdout.
6. **Open-Resource Release.** Maintain deterministic commands, machine-readable results, data dictionaries, checksums, citation metadata, and explicit license boundaries. Archive validated releases with a persistent identifier.

The implementation roadmap and acceptance criteria are tracked in the open research epic. The matched-task allocation and transmission program is tracked separately in its falsification epic.

Code and Data Availability

Analysis code, tests, figures, machine-readable outputs, and parameter records are available in the open-source repository. The repository name identifies provenance only; none of the scientific claims depend on adoption of the broader software project. The principal summary is recorded in `data/results_summary.json`, and the parameter-sensitivity results are recorded in `data/e1d_parameter_sensitivity.json`. The spatial common-state evidence is recorded in `data/spatial_full_body_study.json`. The two-engine spatial forward-contact evidence is recorded in `data/spatial_forward_contact_study.json`. The uncertainty, identifiability, and control evidence is recorded in `data/uncertainty_control_study.json`. The distributed-shaft structural evidence is recorded in `data/shaft_beam_reference.json`. The forward distributed-modal shaft and arm–wrist allocation evidence are recorded in `data/moving_base_modal_shaft_study.json` and `data/torque_allocation_preload_study.json`. The frozen experimental protocol and synthetic readiness classification are recorded in `data/experimental_protocol_v1.json` and `data/experimental_protocol_readiness.json`. The finite-ground initialization, preregistered atlas, and labeled post-hoc matching sensitivity are recorded in `data/articulated_ground_diagnostic.json`, `data/articulated_ground_atlas.json`, and `data/articulated_ground_posthoc_sensitivity.json`.

32.3 Normalized Claim Adjudication

The current census contains 328 material claims. The normalized outcome applies only to each claim's declared estimand, model domain, and uncertainty boundary. A `supported` model-conditional claim is not thereby independently replicated, empirically validated, or converted into a human strategy recommendation.

The absence of a `contradicted` row does not mean that every mechanism survived every adverse test. Claims that accurately report null, mixed, or adverse model results can themselves be supported. The complete finding-level reasons, falsifiers, locators, and boundaries are available in the reviewer JSON and reviewer CSV.

32.3.1 Outcome Counts

Table 32.1: Outcome Counts for the Current Claim Census.

Normalized Outcome	Claim Count
`inconclusive`	5
`supported`	308
`untested`	15

32.3.2 Evidence Tier Counts

Table 32.2: Evidence Tier Counts for the Current Claim Census.

Evidence Tier	Claim Count
bibliographic_record	3
external_empirical_human	34
external_methods_or_measurement	10
external_modeling_or_simulation	15
external_review_or_synthesis	10
project_derivation_or_document	113
project_executable_or_generated	299
prospective_or_unexecuted	15

32.3.3 Source Independence Counts

Table 32.3: Source Independence Counts for the Current Claim Census.

Source Independence	Claim Count
multiple_independent_external_support	20
project_only	274
single_independent_external_support	34

32.3.4 Model Tier Counts

Table 32.4: Model Tier Counts for the Current Claim Census.

Model Tier	Claim Count
articulated_spatial	35
compliant_shaft	66
cross_tier_synthesis	77
declared_model_tier_unclassified	12
finite_ground_or_base	16
human_or_external_evidence	46
planar_reduced	150
spatial_reduced	76
two_hand_or_bilateral	94
uncertainty_or_control	10

32.3.5 Unresolved Replication Counts

Table 32.5: Unresolved Replication Counts for the Current Claim Census.

Replication Class	Claim Count
external_validation_open	1
full_text_or_original_source_open	5
governed_human_data_unavailable	11
independent_reimplementation_open	12
mixed_or_insufficient_evidence	5

Replication Class	Claim Count
none_declared	284
prospective_experiment_open	15
statistical_reanalysis_or_replication_open	9
systematic_review_open	2

32.3.6 Claim-Family Source Concentration

Table 32.6: Claim-Family Source Concentration Flags; the tuple is project only / one independent work / two or more independent works.

Claim Family	Claims	Source-Category Tuple	Flag
ch01 introduction	2	0 / 2 / 0	external support concentrated
ch02 mechanics	33	5 / 17 / 11	mixed independence
ch03 evidence	14	1 / 10 / 3	mixed independence
ch03 interaction forces	10	8 / 1 / 1	mixed independence
ch03b hand path attribution	11	7 / 2 / 2	mixed independence
ch03ba coordinate force sources	3	3 / 0 / 0	project authored only
ch03c ground reaction drift	8	4 / 2 / 2	mixed independence
ch03d shoulder velocity transfer	18	18 / 0 / 0	project authored only
ch04 counterfactual ensemble	6	6 / 0 / 0	project authored only
ch04 counterfactuals	5	4 / 0 / 1	mixed independence
ch05 two hand wrench	21	21 / 0 / 0	project authored only
ch05a interactive workbench	1	1 / 0 / 0	project authored only
ch05b forward two hand	15	15 / 0 / 0	project authored only
ch06 shaft contributions	15	15 / 0 / 0	project authored only
ch06b coupled base flex	14	14 / 0 / 0	project authored only
ch06bb shaft beam reference	2	2 / 0 / 0	project authored only
ch06bbb forward modal shaft	7	7 / 0 / 0	project authored only
ch06bc torque allocation preload	7	7 / 0 / 0	project authored only
ch06c spatial cross formulation	44	44 / 0 / 0	project authored only
ch06ca articulated ground	1	1 / 0 / 0	project authored only
ch06cb spatial cross tail	6	6 / 0 / 0	project authored only
ch06cc spatial forward contact	8	8 / 0 / 0	project authored only
ch06cd articulated attribution	3	3 / 0 / 0	project authored only
ch06d uncertainty control	10	10 / 0 / 0	project authored only
ch06e experimental protocol	1	1 / 0 / 0	project authored only

Claim Family	Claims	Source-Category Tuple	Flag
ch06f open release	2	2 / 0 / 0	project authored only
ch07 model ladder	32	32 / 0 / 0	project authored only
ch07 results	7	7 / 0 / 0	project authored only
ch07b frames biology engines	5	5 / 0 / 0	project authored only
ch07c transmission robustness	5	5 / 0 / 0	project authored only
ch08b momentum transfer questions	10	10 / 0 / 0	project authored only
ch09 conclusions	2	2 / 0 / 0	project authored only

Evidence-tier, model-tier, and unresolved-replication labels are nonexclusive, so those totals can exceed the claim count. Source independence is an exact one-category partition derived from the canonical-work review. No governed participant outcome is present; human validation remains an external-data boundary.

Chapter 33

Software and Data Availability

The open-source implementation separates the analytical model, torque programs, counterfactual evaluation, energy accounting, robustness analyses, and figure generation. The scientific entry points are collected under `scripts/research/proximal_distal_energy/`, with shared model parameters and dynamics under `simulation_backends/`. This is a provenance statement, not a capability claim about the surrounding software.

The current evidence boundary includes these known limitations:

- A multi-phase matched-state torque-killswitch ensemble is complete for one declared torque program; other torque programs, model classes, and uncertainty distributions remain necessary before making general persistence claims.
- The archived two-hand ZTCF remains pointwise along the BASE state history. Separate forward rigid-club and coupled moving-base/flexible-club models now demonstrate finite zero-command persistence. A reduced full-body spatial common-state tier now tests nonplanar inverse dynamics, but passive spatial contact and human variants remain open validation steps.
- The primary model has two planar links and a fixed hub; torso, hub-path, long-axis rotation, and closed-loop arm effects are absent.
- The shaft extension is a three-coordinate point-mass surrogate with one linear torsional mode. It is not a calibrated distributed-beam or equipment model, and extreme low-stiffness deflections exceed its linear premise.
- The coupled actuator adds delay, first-order activation, rate and torque–velocity limits, and impedance, but it remains a nonphysiological command surrogate.
- Coupled uncertainty is screened over declared engineering envelopes; population distributions and measurement uncertainty are not estimated.
- No human motion or force data are analyzed; the result is mechanistic and model-derived, not a skill-group effect.
- The model ladder now executes reduced and subject-scaled forward two-hand contact, distributed grip, passive first-mode shaft, and planar finite-base ground/free-moment tiers in MuJoCo and Pinocchio. The interfaces and support law remain synthetic, bilateral, and uncalibrated; three-dimensional unilateral foot contact and governed human validation remain unexecuted.

Chapter 34

Reproducibility Guide

From the repository root (Python 3.11+ with the project dependencies):

```
# Primary sweep, counterfactuals, and interface-power analysis
python3 -m scripts.research.proximal_distal_energy.run_experiments

# Registered WSCG source extraction and interaction-force analysis
python3 -m scripts.research.proximal_distal_energy.extract_wscg_charts
python3 -m scripts.research.proximal_distal_energy.run_interaction_force_study
python3 -m scripts.research.proximal_distal_energy.run_counterfactual_ensemble
python3 -m scripts.research.proximal_distal_energy.run_two_hand_wscg_analysis
python3 -m scripts.research.proximal_distal_energy.run_shaft_contribution_study
python3 -m scripts.research.proximal_distal_energy.run_mechanism_ladder_study
python3 -m scripts.research.proximal_distal_energy.run_forward_two_arm_study
python3 -m scripts.research.proximal_distal_energy.run_moving_base_flexible_study
python3 -m scripts.research.proximal_distal_energy.run_shaft_beam_reference
python3 -m scripts.research.proximal_distal_energy.run_spatial_full_body_study
python3 -m scripts.research.proximal_distal_energy.run_articulated_manufactured_solution
python3 -m scripts.research.proximal_distal_energy.run_articulated_native_constraint_discrepancy
python3 -m scripts.research.proximal_distal_energy.make_articulated_native_constraint_discrepancy_figur
python3 -m scripts.research.proximal_distal_energy.run_articulated_ground_diagnostic
python3 -m scripts.research.proximal_distal_energy.run_articulated_ground_atlas
python3 -m scripts.research.proximal_distal_energy.run_articulated_ground_posthoc_sensitivity
python3 -m scripts.research.proximal_distal_energy.run_uncertainty_control_study
python3 -m scripts.research.proximal_distal_energy.run_experimental_protocol_dry_run
python3 -m scripts.research.proximal_distal_energy.qualify_open_release validate

# Robustness analyses
python3 -m scripts.research.proximal_distal_energy.e1b_bounded_torque
python3 -m scripts.research.proximal_distal_energy.e1c_impact_sensitivity
python3 -m scripts.research.proximal_distal_energy.e1d_parameter_sensitivity

# Figures and document
python3 -m scripts.research.proximal_distal_energy.make_figures
python3 -m scripts.research.proximal_distal_energy.make_interaction_force_figures
python3 -m scripts.research.proximal_distal_energy.make_counterfactual_figures
python3 -m scripts.research.proximal_distal_energy.make_two_hand_wscg_figures
python3 -m scripts.research.proximal_distal_energy.make_shaft_contribution_figures
python3 -m scripts.research.proximal_distal_energy.make_mechanism_ladder_figures
```

```
python3 -m scripts.research.proximal_distal_energy.make_forward_two_arm_figures
python3 -m scripts.research.proximal_distal_energy.make_moving_base_flexible_figures
python3 -m scripts.research.proximal_distal_energy.make_articulated_ground_figure
python3 -m scripts.research.proximal_distal_energy.make_shaft_beam_reference_figures
python3 -m scripts.research.proximal_distal_energy.make_spatial_full_body_figures
python3 -m scripts.research.proximal_distal_energy.make_uncertainty_control_figures
cd docs/research/proximal_distal_energy_transfer
quarto render proximal_distal_energy_transfer.qmd --to pdf
cd ../../..
python3 -m scripts.research.proximal_distal_energy.optimize_article_pdf
```

Outputs land in `data/` (JSON and NPZ with integrator and parameter provenance) and `figures/` (PDF and SVG). The open-chain analyses use fixed-step RK4; the forward constrained two-hand analysis uses velocity Verlet with mass-metric projection. The analyses contain no stochastic elements. Re-runs should reproduce the recorded values up to floating-point environment differences. The final optimizer requires PyMuPDF, performs lossless object/stream compaction, and refuses an artifact that changes the page count, URI-link count, or outline-entry count.

Chapter 35

Validation Evidence

Tests exercise analytical double-pendulum ground truth, optional cross-backend agreement, drift-plus-control reconstruction, work–energy consistency, deterministic replay, impact edge cases, headline values, and the parameter-case contract. The wrist-interface balance also checks that the club mechanical-energy rate matches the summed interface powers to the finite-difference tolerance. These checks reduce numerical and implementation error; they do not validate the structural model assumptions.

Chapter 36

Model Parameters and Program Definitions

Table 36.1: Baseline model parameters and experiment constants.

Parameter	Value	Notes
Arm length l_1	0.75 m	baseline
Arm mass m_1	7.5 kg	both arms lumped
Arm COM ratio	0.45	$l_{c1} = 0.3375$ m
Arm inertia about COM	$0.3516\ \mathrm{kg \cdot m^2}$	about hub: $1.2059\ \mathrm{kg \cdot m^2}$
Club length l_2	1.0 m	grip to clubhead
Shaft mass	0.15 kg	COM ratio 0.43
Clubhead mass	0.20 kg	point mass at tip
Club composite mass m_2	0.35 kg	$l_{c2} = 0.7557$ m
Club inertia about COM	$0.0403\ \mathrm{kg \cdot m^2}$	about wrist: $0.2402\ \mathrm{kg \cdot m^2}$
Plane inclination	35°	projected gravity $8.033\ \mathrm{m/s^2}$
Damping (shoulder, wrist)	$0.4, 0.25\ \mathrm{N \cdot m \cdot s/rad}$	viscous
Integrator	RK4, $\Delta t = 1$ ms	analytical ODE backend
Initial state	$\theta_1 = -2.2$, $\theta_2 = -1.57$ rad, $\dot{q} = 0$	top of backswing
Shoulder torque τ_s	$60\ /\ 100\ \mathrm{N \cdot m}$	constant from $t = 0$
Wrist drive	$+15\ \mathrm{N \cdot m}$ from t_{on}	onset grid 0–0.35 s, step 0.025
Wrist restraint R	$5\ /\ 10\ \mathrm{N \cdot m}$ before t_{on}	restrain-then-drive only
Impact	first $\theta_1 + \theta_2 = 0$ crossing	valid iff $\theta_1 \leq 2.0$ rad

Recorded outputs:

- `data/e1_sweep.json` — one row per torque program plus provenance.
- `data/representative_traces.npz` — representative state, control, counterfactual, energy, speed, and interface-power traces.
- `data/results_summary.json` — representative impacts and phase budgets.
- `data/e1b_bounded_sweep.json` — torque-velocity-bounded sweep.
- `data/e1c_sensitivity.json` — alternative impact-definition results.
- `data/e1d_parameter_sensitivity.json` — 13 one-at-a-time parameter cases.
- `data/interaction_force_mechanisms.npz` — exact force, power, geometry, and matched-state kill-switch arrays.
- `data/interaction_force_summary.json` — headline force, work, and divergence metrics with counterfactual contracts.

- `data/wscg_2024_hand_force_series.csv` — hash-verified values from the source presentation's embedded chart cache.
- `data/wscg_2024_source_provenance.json` — source hashes, series inventory, and interpretation boundary.
- `data/counterfactual_ensemble.json` — 96 baseline cut/horizon/timestep rows, gravity and damping ablations, convergence metrics, and WSCG DELTA checks.
- `data/counterfactual_selected_traces.npz` — commanded and zero-torque state, force, and power traces for three representative cuts.
- `data/wscg_two_hand_raw/*.csv` — portable, column-labeled exports of the archived BASE, ZTCF, and DELTA two-hand tables.
- `data/two_hand_wscg_analysis.json` — source hashes, wrench-reconstruction residuals, reversal times, sensitivity results, and interpretation boundary.
- `data/two_hand_wscg_analysis.npz` — local force modes, moment and power decompositions, poses, and geometry-counterfactual arrays.
- `data/bilateral_wrench_identifiability_study.json` — three-dimensional point-force and full bilateral-wrench ranks, null spaces, grip-span sweep, proper-rotation audit, sensing boundary, and explicit nonhuman claims.
- `data/constraint_internal_force_diagnostics.json` — source-hash-bound planar closure and bilateral wrench-map ranks, explicit coordinate/wrench scales, singular and coincident-contact controls, tolerance sensitivity, and nonhuman inference boundaries.
- `data/closed_loop_singularity_margin.json` — exact same-origin closure on both assembly branches, full-phase scaled singular margins, exact triangle degeneracies, and phase, geometry, scale, unit, tolerance, impossible- geometry, and manufactured-rank controls.
- `data/phase_event_stability.{json,npz}` — nondimensional finite-time state transitions, singular gains and exponents, transverse-event derivatives, direct perturbation controls, near-grazing rejection, saltation controls, equivalent-unit checks, and the fail-closed periodicity/Floquet gate.
- `data/trajectory_control_authority.{json,npz}` — exact-step trajectory-varying input maps, continuous-energy-equivalent Gramians, event-tangent projection, channel masks, direct nonlinear pulse controls, frozen-local countermodels, refinement, additivity, zero-input, and equivalent-unit gates.
- `data/bounded_event_reachability.{json,npz}` — finite event-tangent continuation, exact-RK4 multiple shooting and independent replay, four channel masks, declared amplitude/slew limits, typed failures, and multistart, mesh, step, zero-authority, and adverse-state controls.
- `data/event_topology_robustness.{json,npz}` — global direction-aware event enumeration, eleven-delay continuation, matched small synthetic perturbations, pair-level adequacy intervals, and full retained events.
- `data/event_topology_stress_extension.{json,npz}` — separately preregistered fixed stress-to-failure ladder with absent and multiple crossings retained rather than selected away.
- `data/event_topology_channel_matrix.{json,npz}` — both, shoulder-only, wrist-only, and zero-authority delay/noise maps; event-state and speed arrays; integration-step refinement; and global-horizon truncation controls.
- `data/nonlinear_controller_comparison_registration.json` — outcome-blind tuning/evaluation split, nine declared families, matched plant, constraints, objectives, typed failures, ranking suppression, and single-worker identity.
- `data/nonlinear_controller_solver_qualification.json` — one bounded projected first-order iLQR kernel with derivative, bound, descent, replay, initialization-sensitivity, and typed nonfinite-dynamics gates; collocation NMPC remains unavailable.
- `data/nonlinear_controller_plant_transport.json` — 12 controller-to-ODE parity cases across three integration steps, exact replay, immutable inputs, typed invalid cases, and zero ranking authority.
- `data/double_pendulum_identifiability.json` — exact seven-coefficient inverse- dynamics factorization, analytic physical-map rank witness, three exact nonunique parameter families, dimensionless finite-record rank, unit and scale audits, conditional noise bounds, and a zero-motion killswitch.
- `data/shaft_contribution_study.json` — matched rigid/flexible results, termwise acceleration and power summaries, ablations, 120 robustness cases, endpoint windows, timestep convergence, and interpretation boundaries.

- `data/shaft_contribution_traces.npz` — reference, rigid, and ablation state, speed, force, acceleration-contribution, power, work, and energy traces.
- `data/mechanism_ladder_study.json` — common-schema invariance residuals, prescribed mobile-hub cases, closed-loop constraint diagnostics, and the fail-closed model-discrepancy table.
- `data/mechanism_ladder_traces.npz` — three-link interface, mobile-hub, and closed-loop conditioning arrays used by the higher-order figures.
- `data/forward_two_arm_study.json` — forward model parameters, command, closure, killswitch ensemble, negative control, and numerical sensitivities.
- `data/forward_two_arm_study.npz` — baseline and representative branch states, contact forces, force modes, moments, power, energy, and solver residuals.
- `data/moving_base_flexible_study.{json,npz}` — coupled base/flex branch, negative control, parameter screen, convergence, states, forces, and energy.
- `data/shaft_beam_reference.{json,npz}` — synthetic modal identification, finite-element convergence, paired one/six-mode responses, and work–energy closure; not equipment calibration.
- `data/spatial_full_body_study.{json,npz}` — common-model hashes, prescribed wrench interventions, two-formulation inverse dynamics, and spatial states.
- `data/articulated_manufactured_solution.json` — independent analytical, MuJoCo, and Pinocchio inverse-dynamics residuals; three-level Richardson estimates; measured free-subtree conservation drift; and the corruption killswitch contract.
- `data/articulated_native_constraint_discrepancy.{json,npz}` — one same-state MuJoCo-native bilateral `connect/mj_step` branch and one projected Kelvin–Voigt/shared-mass-and-bias branch, including the equality-disabled killswitch, six-row native-constraint gate, refinement, attachment separation, generalized force, and nonzero state discrepancy.
- `data/uncertainty_control_study.{json,npz}` — declared design, actuator contract, uncertainty intervals, PRCC screen, identifiability audit, training/held-out program comparison, closure, and rollout arrays.
- `data/experimental_protocol_v1.json` — frozen inclusion, measurement, processing, participant-split, prediction, and inference contract.
- `data/experimental_protocol_{dry_run,readiness}.json` — synthetic-only intake fixture and fail-closed readiness classification; no human observations.
- `release_manifest.json` and `CHECKSUMS.sha256` — exact release artifact inventory, model-tier presets, claim status, open gates, hashes, and sizes.

References

Anderson, Brady C., Ian C. Wright, and Darren J. Stefanyshyn. 2006. "Segmental Sequencing of Kinetic Energy in the Golf Swing." In *The Engineering of Sport 6*, 1:167–72. New York, NY: Springer. https://doi.org/10.1007/978-0-387-46050-5_30.

Araz, Matthew, Sven Weidner, Fabio Izzi, Alexander Badri-Spr"owitz, Tobias Siebert, and Daniel F. B. Haeufle. 2023. "Muscle Preflex Response to Perturbations in Locomotion: In Vitro Experiments and Simulations with Realistic Boundary Conditions." *Frontiers in Bioengineering and Biotechnology* 11: 1150170. https://doi.org/10.3389/fbioe.2023.1150170.

Ball, Kevin A., and Russell J. Best. 2007. "Different Centre of Pressure Patterns Within the Golf Stroke i: Cluster Analysis." *Journal of Sports Sciences* 25 (7): 757–70. https://doi.org/10.1080/02640410600874971.

Balzerson, Daniel, Joydeep Banerjee, and John McPhee. 2016. "A Three-Dimensional Forward Dynamic Model of the Golf Swing Optimized for Ball Carry Distance." *Sports Engineering* 19: 237–50. https://doi.org/10.1007/s12283-016-0197-7.

Berret, Bastien, Dorian Verdel, Etienne Burdet, and Frédéric Jean. 2024. "Co-Contraction Embodies Uncertainty: An Optimal Feedforward Strategy for Robust Motor Control." *PLoS Computational Biology* 20 (11): e1012598. https://doi.org/10.1371/journal.pcbi.1012598.

Betzler, Nils F., Stuart A. Monk, Eric S. Wallace, and Steve R. Otto. 2012. "Effects of Golf Shaft Stiffness on Strain, Clubhead Presentation and Wrist Kinematics." *Sports Biomechanics* 11 (2): 223–38. https://doi.org/10.1080/14763141.2012.681796.

Bourgain, Maxime, Philippe Rouch, Olivier Rouillon, Patricia Thoreux, and Christophe Sauret. 2022. "Golf Swing Biomechanics: A Systematic Review and Methodological Recommendations for Kinematics." *Sports* 10 (6): 91. https://doi.org/10.3390/sports10060091.

Bunn, John W. 1972. *Scientific Principles of Coaching*. 2nd ed. Englewood Cliffs, NJ: Prentice-Hall.

Carpentier, Justin, Guilhem Saurel, Gabriele Buondonno, Joseph Mirabel, Florent Lamiraux, Olivier Stasse, and Nicolas Mansard. 2019. "The Pinocchio C++ Library: A Fast and Flexible Implementation of Rigid Body Dynamics Algorithms and Their Analytical Derivatives." In *2019 IEEE/SICE International Symposium on System Integration (SII)*, 614–19. https://doi.org/10.1109/SII.2019.8700380.

Cheetham, Phillip J., Gregory A. Rose, Richard N. Hinrichs, Robert J. Neal, Rob E. Mottram, Paul D. Hurrion, and Peter F. Vint. 2008. "Comparison of Kinematic Sequence Parameters Between Amateur and Professional Golfers." In *Science and Golf v: Proceedings of the World Scientific Congress of Golf*, edited by Debbie Crews and Rafer Lutz. Mesa, AZ: Energy in Motion. https://www.researchgate.net/publication/252236426.

Choi, Hyeob, and Sukyung Park. 2020. "Three Dimensional Upper Limb Joint Kinetics of a Golf Swing with Measured Internal Grip Force." *Sensors* 20 (13): 3672. https://doi.org/10.3390/s20133672.

Chu, Yungchien, Timothy C. Sell, and Scott M. Lephart. 2010. "The Relationship Between Biomechanical Variables and Driving Performance During the Golf Swing." *Journal of Sports Sciences* 28 (11): 1251–59. https://doi.org/10.1080/02640414.2010.507249.

Cochran, Alastair, and John Stobbs. 1968. *Search for the Perfect Swing*. Philadelphia: J. B. Lippincott.

Cole, Michael H., and Paul N. Grimshaw. 2016. "The Biomechanics of the Modern Golf Swing: Implications for Lower Back Injuries." *Sports Medicine* 46 (3): 339–51. https://doi.org/10.1007/s40279-015-0429-1.

Coleman, Simon, and Alan J. Rankin. 2005. "A Three-Dimensional Examination of the Planar Nature of the Golf Swing." *Journal of Sports Sciences* 23 (3): 227–34. https://doi.org/10.1080/02640410410001730179.

De Groote, Friedl, Jessica L. Allen, and Lena H. Ting. 2017. "Contribution of Muscle Short-Range Stiffness to Initial Changes in Joint Kinetics and Kinematics During Perturbations to Standing Balance.” *Journal of Biomechanics* 55: 71–77. https://doi.org/10.1016/j.jbiomech.2017.02.008.

Dillman, Charles J., and Gregory W. Lange. 1994. “How Has Biomechanics Contributed to the Understanding of the Golf Swing?” In *Science and Golf II: Proceedings of the World Scientific Congress of Golf*, edited by Alastair J. Cochran and Martin R. Farrally. London: E & FN Spon. https://doi.org/10.4324/9780203474709-2.

Featherstone, Roy. 2008. *Rigid Body Dynamics Algorithms*. New York, NY: Springer. https://doi.org/10.1007/978-1-4899-7560-7.

Feltner, Michael E. 1989. “Three-Dimensional Interactions in a Two-Segment Kinetic Chain. Part II: Application to the Throwing Arm in Baseball Pitching.” *International Journal of Sport Biomechanics* 5 (4): 420–50. https://doi.org/10.1123/ijsb.5.4.420.

Feltner, Michael E., and Jesús Dapena. 1986. “Dynamics of the Shoulder and Elbow Joints of the Throwing Arm During a Baseball Pitch.” *International Journal of Sport Biomechanics* 2 (4): 235–59. https://doi.org/10.1123/ijsb.2.4.235.

———. 1989. “Three-Dimensional Interactions in a Two-Segment Kinetic Chain. Part i: General Model.” *International Journal of Sport Biomechanics* 5 (4): 403–19. https://doi.org/10.1123/ijsb.5.4.403.

Fradkin, Andrea J., Caroline A. Sherman, and Caroline F. Finch. 2004. “How Well Does Club Head Speed Correlate with Golf Handicaps?” *Journal of Science and Medicine in Sport* 7 (4): 465–72. https://doi.org/10.1016/S1440-2440(04)80265-2.

Glazier, Paul S. 2011. “Movement Variability in the Golf Swing: Theoretical, Methodological, and Practical Issues.” *Research Quarterly for Exercise and Sport* 82 (2): 157–61. https://doi.org/10.1080/02701367.2011.10599742.

Han, Ki Hoon, Christopher Como, Jemin Kim, Sangwoo Lee, Jaewoong Kim, Dae Kyoo Kim, and Young-Hoo Kwon. 2019. “Effects of the Golfer–Ground Interaction on Clubhead Speed in Skilled Male Golfers.” *Sports Biomechanics* 18 (2): 115–34. https://doi.org/10.1080/14763141.2019.1586983.

Hellström, John. 2009. “Competitive Elite Golf: A Review of the Relationships Between Playing Results, Technique and Physique.” *Sports Medicine* 39 (9): 723–41. https://doi.org/10.2165/11315200-000000000-00000.

Herring, R. M., and A. E. Chapman. 1992. “Effects of Changes in Segmental Values and Timing of Both Torque and Torque Reversal in Simulated Throws.” *Journal of Biomechanics* 25 (10): 1173–84. https://doi.org/10.1016/0021-9290(92)90073-A.

Horan, Sean A., and Justin J. Kavanagh. 2012. “The Control of Upper Body Segment Speed and Velocity During the Golf Swing.” *Sports Biomechanics* 11 (2): 165–74. https://doi.org/10.1080/14763141.2011.638390.

Hume, Patria A., Justin Keogh, and Duncan Reid. 2005. “The Role of Biomechanics in Maximising Distance and Accuracy of Golf Shots.” *Sports Medicine* 35 (5): 429–49. https://doi.org/10.2165/00007256-200535050-00005.

Jobe, Frank W., James Perry, and Marilyn Pink. 1995. “Electromyographic Analysis of Scapular Muscles During a Golf Swing.” *The American Journal of Sports Medicine* 23 (1): 19–23. https://doi.org/10.1177/036354659502300104.

Joo, Su-Bin, Seung Eel Oh, and Joung Hwan Mun. 2016. “Improving the Ground Reaction Force Prediction Accuracy Using One-Axis Plantar Pressure: Expansion of Input Variable for Neural Network.” *Journal of Biomechanics* 49 (14): 3153–61. https://doi.org/10.1016/j.jbiomech.2016.07.029.

Jorgensen, Theodore. 1970. “On the Dynamics of the Swing of a Golf Club.” *American Journal of Physics* 38 (5): 644–51. https://doi.org/10.1119/1.1976419.

Jorgensen, Theodore P. 1999. *The Physics of Golf*. 2nd ed. New York: Springer / AIP Press.

Joyce, Christopher, Angus Burnett, Jodie Cochrane, and Kevin Ball. 2013. “Three-Dimensional Trunk Kinematics in Golf: Between-Club Differences and Relationships to Clubhead Speed.” *Sports Biomechanics* 12 (2): 108–20. https://doi.org/10.1080/14763141.2012.728244.

Kenny, Ian C., Alex J. McCloy, Eric S. Wallace, and Steve R. Otto. 2008. “Segmental Sequencing of Kinetic Energy in a Computer-Simulated Golf Swing.” *Sports Engineering* 11 (1): 37–45. https://doi.org/10.1007/s12283-008-0005-0.

Koike, Sekiya. 2016. “Measurement of Individual Hand Forces Exerted on a Golf Club Grip.” In *International Symposium on Biomechanics in Sports*. https://ojs.ub.uni-konstanz.de/cpa/article/view/6828.

Kwon, Young-Hoo, Christopher S. Como, Kunal Singhal, Sangwoo Lee, and Ki Hoon Han. 2012. "Assessment of Planarity of the Golf Swing Based on the Functional Swing Plane of the Clubhead and Motion Planes of the Body Points." *Sports Biomechanics* 11 (2): 127–48. https://doi.org/10.1080/14763141.2012.660799.

Kwon, Young-Hoo, Ki Hoon Han, Christopher S. Como, Sangwoo Lee, and Kunal Singhal. 2013. "Validity of the X-Factor Computation Methods and Relationship Between the X-Factor Parameters and Clubhead Velocity in Skilled Golfers." *Sports Biomechanics* 12 (3): 231–46. https://doi.org/10.1080/14763141.2013.771896.

Lampsa, Michael A. 1975. "Maximizing Distance of the Golf Drive: An Optimal Control Study." *Journal of Dynamic Systems, Measurement, and Control* 97 (4): 362–67. https://doi.org/10.1115/1.3426951.

Langdown, Ben L., Matthew Bridge, and François-Xavier Li. 2012. "Movement Variability in the Golf Swing." *Sports Biomechanics* 11 (2): 273–87. https://doi.org/10.1080/14763141.2011.650187.

Latash, Mark L., and Xian-Geng Huang. 2015. "Neural Control of Movement Stability: Lessons from Studies of Neurological Patients." *Neuroscience* 301: 39–48. https://doi.org/10.1016/j.neuroscience.2015.05.075.

Latash, Mark L., Mindy F. Levin, John P. Scholz, and Gregor Schöner. 2010. "Motor Control Theories and Their Applications." *Medicina* 46 (6): 382–92. https://doi.org/10.3390/medicina46060054.

Lee, Junghoon, Justin Ehrlich, and Christopher Cain. 2026. "The Effects of Different Kinematic Sequences of the Elite Golf Swing on Clubhead Speed." *International Journal of Sports Science & Coaching*. https://doi.org/10.1177/17479541261429479.

Lindsay, David M., Shannon Mantrop, and Anthony A. Vandervoort. 2008. "A Review of Biomechanical Differences Between Golfers of Varied Skill Levels." *International Journal of Sports Science & Coaching* 3 (Suppl. 1): 187–97. https://doi.org/10.1260/174795408785024117.

Luo, Y., R. Cooke, and E. Pate. 1994. "Effect of Series Elasticity on Delay in Development of Tension Relative to Stiffness During Muscle Activation." *American Journal of Physiology* 267 (6): C1598–1606. https://doi.org/10.1152/ajpcell.1994.267.6.C1598.

MacKenzie, Sasho J., Matthew McCourt, and Luc Champoux. 2020. "How Amateur Golfers Deliver Energy to the Driver." *International Journal of Golf Science* 8 (1). https://www.golfsciencejournal.org/article/12640-how-amateur-golfers-deliver-energy-to-the-driver.

MacKenzie, Sasho J., and Eric J. Sprigings. 2009. "A Three-Dimensional Forward Dynamics Model of the Golf Swing." *Sports Engineering* 11 (4): 165–75. https://doi.org/10.1007/s12283-009-0020-9.

Madrid, Braden, Marco A. Avalos, Nicholas A. Levine, Noelle J. Tuttle, Kevin A. Becker, and Young-Hoo Kwon. 2020. "Association Between the on-Plane Angular Motions of the Axle-Chain System and Clubhead Speed in Skilled Male Golfers." *Applied Sciences* 10 (17): 5728. https://doi.org/10.3390/app10175728.

Marino, Simeone, Ian B. Hogue, Christian J. Ray, and Denise E. Kirschner. 2008. "A Methodology for Performing Global Uncertainty and Sensitivity Analysis in Systems Biology." *Journal of Theoretical Biology* 254 (1): 178–96. https://doi.org/10.1016/j.jtbi.2008.04.011.

Marsan, Thibault, Patricia Thoreux, Maxime Bourgain, Olivier Rouillon, Philippe Rouch, and Christophe Sauret. 2019. "Biomechanical Analysis of the Golf Swing: Methodological Effect of Angular Velocity Component on the Identification of the Kinematic Sequence." *Acta of Bioengineering and Biomechanics* 21 (2): 115–20. https://doi.org/10.5277/ABB-01318-2019-02.

Marshall, Robert N., and Bruce C. Elliott. 2000. "Long-Axis Rotation: The Missing Link in Proximal-to-Distal Segmental Sequencing." *Journal of Sports Sciences* 18 (4): 247–54. https://doi.org/10.1080/026404100364983.

Mayfield, Dean L., Andrew G. Cresswell, and Glen A. Lichtwark. 2016. "Effects of Series Elastic Compliance on Muscle Force Summation and the Rate of Force Rise." *Journal of Experimental Biology* 219 (20): 3261–70. https://doi.org/10.1242/jeb.142604.

McKay, M. D., R. J. Beckman, and W. J. Conover. 1979. "A Comparison of Three Methods for Selecting Values of Input Variables in the Analysis of Output from a Computer Code." *Technometrics* 21 (2): 239–45. https://doi.org/10.1080/00401706.1979.10489755.

McNally, William, and John McPhee. 2018. "Dynamic Optimization of the Golf Swing Using a Six Degree-of-Freedom Biomechanical Model." In *Proceedings*, 2:243. 6. https://doi.org/10.3390/proceedings2060243.

McPhee, John. 2022. "A Review of Dynamic Models and Measurements in Golf." *Sports Engineering* 25. https://doi.org/10.1007/s12283-022-00387-0.

McTeigue, Michael, Steven R. Lamb, Robert Mottram, and Francis Pirozzolo. 1994. "Spine and Hip Motion Analysis During the Golf Swing." In *Science and Golf II: Proceedings of the World Scientific*

Congress of Golf, edited by Alastair J. Cochran and Martin R. Farrally, 50–58. London: E & FN Spon. https://doi.org/10.4324/9780203474709-9.

Meister, David W., Amy L. Ladd, Erin E. Butler, Betty Zhao, Andrew P. Rogers, Conrad J. Ray, and Jessica Rose. 2011. "Rotational Biomechanics of the Elite Golf Swing: Benchmarks for Amateurs." *Journal of Applied Biomechanics* 27 (3): 242–51. https://doi.org/10.1123/jab.27.3.242.

Milburn, Peter D. 1982. "Summation of Segmental Velocities in the Golf Swing." *Medicine and Science in Sports and Exercise* 14 (1): 60–64. https://doi.org/10.1249/00005768-198201000-00012.

Miura, Ken. 2001. "Parametric Acceleration — the Effect of Inward Pull of the Golf Club at Impact Stage." *Sports Engineering* 4 (2): 75–86. https://doi.org/10.1046/j.1460-2687.2001.00071.x.

Morrison, Andrew, Denise McGrath, and Eric S. Wallace. 2016. "Motor Abundance and Control Structure in the Golf Swing." *Human Movement Science* 46: 129–47. https://doi.org/10.1016/j.humov.2016.01.009.

Myers, Joseph, Scott Lephart, Yung-Shen Tsai, Timothy Sell, James Smoliga, and John Jolly. 2008. "The Role of Upper Torso and Pelvis Rotation in Driving Performance During the Golf Swing." *Journal of Sports Sciences* 26 (2): 181–88. https://doi.org/10.1080/02640410701373543.

Neal, Robert J., Ryan Lumsden, Mark Holland, and Bruce Mason. 2007. "Body Segment Sequencing and Timing in Golf." *International Journal of Sports Science & Coaching* 2 (Suppl. 1). https://doi.org/10.1260/174795407789705497.

Nesbit, Steven M. 2005b. "A Three Dimensional Kinematic and Kinetic Study of the Golf Swing." *Journal of Sports Science and Medicine* 4 (4): 499–519. https://pmc.ncbi.nlm.nih.gov/articles/PMC3899667/.

———. 2005a. "A Three Dimensional Kinematic and Kinetic Study of the Golf Swing." *Journal of Sports Science and Medicine* 4 (4): 499–519. https://pubmed.ncbi.nlm.nih.gov/24627665/.

Nesbit, Steven M., and Ryan McGinnis. 2009. "Kinematic Analyses of the Golf Swing Hub Path and Its Role in Golfer/Club Kinetic Transfers." *Journal of Sports Science and Medicine* 8 (2): 235–46. https://www.jssm.org/volume08/iss2/cap/jssm-08-235.pdf.

Nesbit, Steven M., and Ryan S. McGinnis. 2014. "Kinetic Constrained Optimization of the Golf Swing Hub Path." *Journal of Sports Science and Medicine* 13 (4): 859–73. https://pmc.ncbi.nlm.nih.gov/articles/PMC4234956/.

Nesbit, Steven M., and Monika Serrano. 2005. "Work and Power Analysis of the Golf Swing." *Journal of Sports Science and Medicine* 4 (4): 520–33. https://www.jssm.org/volume04/iss4/cap/jssm-04-520.pdf.

Olson, Dieter. 2024. "Evaluation of the Effect of Momentum on Interaction Forces in a Linked System." World Scientific Congress of Golf / International Sports Engineering Association presentation. https://www.mathworks.com/matlabcentral/fileexchange/169071-two-hand-golf-swing-model.

Osis, Sean T., and Darren J. Stefanyshyn. 2012. "Golf Players Exhibit Changes to Grip Speed Parameters During Club Release in Response to Changes in Club Stiffness." *Human Movement Science* 31 (1): 91–100. https://doi.org/10.1016/j.humov.2011.02.006.

Penner, A. Raymond. 2003. "The Physics of Golf." *Reports on Progress in Physics* 66 (2): 131–71. https://doi.org/10.1088/0034-4885/66/2/202.

Pickering, W. M., and G. T. Vickers. 1999. "On the Double Pendulum Model of the Golf Swing." *Sports Engineering* 2 (3): 161–72. https://doi.org/10.1046/j.1460-2687.1999.00028.x.

Putnam, Carol A. 1991. "A Segment Interaction Analysis of Proximal-to-Distal Sequential Segment Motion Patterns." *Medicine and Science in Sports and Exercise* 23 (1): 130–44. https://pubmed.ncbi.nlm.nih.gov/1997807/.

———. 1993. "Sequential Motions of Body Segments in Striking and Throwing Skills: Descriptions and Explanations." *Journal of Biomechanics* 26 (Suppl. 1): 125–35. https://doi.org/10.1016/0021-9290(93)90084-R.

Rachnavy, Pornthep, Khemchat Chaemklan, Dipak Kumar Agrawal, Soodkhet Pojprapai, Hathairat Rachnavy, and Thanomsak Senakam. 2026. "Foot–Ground Interaction and Clubhead Speed: Impulse-Based Energy Transfer as the Key Mechanism in the Golf Swing." *Frontiers in Sports and Active Living* 8. https://doi.org/10.3389/fspor.2026.1790645.

Raue, Andreas, Clemens Kreutz, Thomas Maiwald, Julie Bachmann, Marcel Schilling, Ursula Klingmüller, and Jens Timmer. 2009. "Structural and Practical Identifiability Analysis of Partially Observed Dynamical Models by Exploiting the Profile Likelihood." *Bioinformatics* 25 (15): 1923–29. https://doi.org/10.1093/bioinformatics/btp358.

Reinkensmeyer, David J., Peter S. Lum, and Steven L. Lehman. 1992. "Human Control of a Simple Two-Hand

Grasp." *Biological Cybernetics* 67 (6): 553–64. https://doi.org/10.1007/BF00198762.

Robertson, D. Gordon E., and David A. Winter. 1980. "Mechanical Energy Generation, Absorption and Transfer Amongst Segments During Walking." *Journal of Biomechanics* 13 (10): 845–54. https://doi.org/10.1016/0021-9290(80)90172-4.

Robinson, Patrick G., Howie J. Carson, Jim Richards, Andrew Murray, Andrew D. Duckworth, and Doug Campbell. 2023. "What Differences Exist Between the Lead and Trail Wrist in Extensor Carpi Ulnaris Activity and Golf Swing Joint Kinematics in Sub-Elite Golfers?" *Journal of Sports Sciences* 41 (17): 1596–1604. https://doi.org/10.1080/02640414.2023.2285121.

Rugy, Aymar de, Gerald E. Loeb, and Timothy J. Carroll. 2018. "Muscle Patterns Underlying Voluntary Modulation of Co-Contraction." *PLoS ONE* 13 (10): e0205538. https://doi.org/10.1371/journal.pone.0205538.

Seth, Ajay, Ricardo Matias, Antonio P. Veloso, and Scott L. Delp. 2016. "A Biomechanical Model of the Scapulothoracic Joint to Accurately Capture Scapular Kinematics During Shoulder Movements." *PLOS ONE* 11 (1): e0141028. https://doi.org/10.1371/journal.pone.0141028.

Sharp, Robin S. 2009. "On the Mechanics of the Golf Swing." *Proceedings of the Royal Society A: Mathematical, Physical and Engineering Sciences* 465 (2102): 551–70. https://doi.org/10.1098/rspa.2008.0304.

Shaw, James, Zachariah I. Gould, Jon L. Oliver, and Rhodri S. Lloyd. 2023. "Within- and Between-Session Reliability of Golf Swing Variables Using the TrackMan Launch Monitor in Talented Golfers." *Journal of Strength and Conditioning Research* 37 (12): 2431–37. https://doi.org/10.1519/JSC.0000000000004554.

Smith, Aimée, Jonathan Roberts, Eric S. Wallace, Pui Wah Kong, and Steph Forrester. 2015. "Golf Coaches' Perceptions of Key Technical Swing Parameters Compared to Biomechanical Literature." *International Journal of Sports Science & Coaching* 10 (4): 739–55. https://doi.org/10.1260/1747-9541.10.4.739.

Sohn, M. Hongchul, J. Lucas McKay, and Lena H. Ting. 2013. "Defining Feasible Bounds on Muscle Activation in a Redundant Biomechanical Task: Practical Implications of Redundancy." *Journal of Biomechanics* 46 (7): 1363–68. https://doi.org/10.1016/j.jbiomech.2013.01.020.

Sprigings, Eric J., and Sasho J. MacKenzie. 2002. "Examining the Delayed Release in the Golf Swing Using Computer Simulation." *Sports Engineering* 5: 23–32. https://doi.org/10.1046/j.1460-2687.2002.00094.x.

Sprigings, Eric J., and Robert J. Neal. 2000. "An Insight into the Importance of Wrist Torque in Driving the Golfball: A Simulation Study." *Journal of Applied Biomechanics* 16 (4): 356–66. https://doi.org/10.1123/jab.16.4.356.

Sturdy, Jordan T., Anne K. Silverman, and Nathan T. Pickle. 2022. "Automated Optimization of Residual Reduction Algorithm Parameters in OpenSim." *Journal of Biomechanics* 137: 111087. https://doi.org/10.1016/j.jbiomech.2022.111087.

Tinmark, Fredrik, John Hellström, Kjartan Halvorsen, and Alf Thorstensson. 2010. "Elite Golfers' Kinematic Sequence in Full-Swing and Partial-Swing Shots." *Sports Biomechanics* 9 (4): 236–44. https://doi.org/10.1080/14763141.2010.535842.

Todorov, Emanuel, Tom Erez, and Yuval Tassa. 2012. "MuJoCo: A Physics Engine for Model-Based Control." In *2012 IEEE/RSJ International Conference on Intelligent Robots and Systems*, 5026–33. https://doi.org/10.1109/IROS.2012.6386109.

Tucker, Catherine B., Ross Anderson, and Ian C. Kenny. 2014. "Is Outcome Related to Movement Variability in Golf?" *Sports Biomechanics* 13 (3): 343–54. https://doi.org/10.1080/14763141.2013.873817.

Vu, Van Hoan, Brice Isableu, and Bastien Berret. 2016. "Adaptive Use of Interaction Torque During Arm Reaching Movement from the Optimal Control Viewpoint." *Scientific Reports* 6: 38845. https://doi.org/10.1038/srep38845.

Watson, Andrew, Andrew Murray, Alex Ehlert, Jiaqing Xu, Steve Williams, Abbie Spiegelhalter, Daniel Coughlan, Anthony Turner, and Chris Bishop. 2026. "Ground Reaction Force and Centre of Pressure During the Golf Swing and Associations with Clubhead Speed and Skill Level: A Systematic Review." *Sports Medicine*. https://doi.org/10.1007/s40279-025-02391-3.

Werling, Keenon, Nicholas A. Bianco, Michael Raitor, Julia Stingel, Jennifer L. Hicks, Steven H. Collins, Scott L. Delp, and C. Karen Liu. 2023. "AddBiomechanics: Automating Model Scaling, Inverse Kinematics, and Inverse Dynamics from Human Motion Data Through Sequential Optimization." *PLOS ONE* 18 (11): e0295152. https://doi.org/10.1371/journal.pone.0295152.

White, Rod. 2006. "On the Efficiency of the Golf Swing." *American Journal of Physics* 74 (12): 1088–94. https://doi.org/10.1119/1.2346688.

Winter, David A. 2009. *Biomechanics and Motor Control of Human Movement*. 4th ed. Hoboken, NJ: John Wiley & Sons.

Worsfold, Paul, Neal A. Smith, and Rosemary J. Dyson. 2008. "Low Handicap Golfers Generate More Torque at the Shoe–Natural Grass Interface When Using a Driver." *Journal of Sports Science and Medicine* 7 (3): 408–14. https://pubmed.ncbi.nlm.nih.gov/24149910/.

Zajac, Felix E., and Michael E. Gordon. 1989. "Determining Muscle's Force and Action in Multi-Articular Movement." *Exercise and Sport Sciences Reviews* 17: 187–230. https://pubmed.ncbi.nlm.nih.gov/2676547/.

Zajac, Felix E., Richard R. Neptune, and Steven A. Kautz. 2002. "Biomechanics and Muscle Coordination of Human Walking. Part I: Introduction to Concepts, Power Transfer, Dynamics and Simulations." *Gait & Posture* 16 (3): 215–32. https://doi.org/10.1016/S0966-6362(02)00068-1.

Zatsiorsky, Vladimir M., and Mark L. Latash. 2008. "Multifinger Prehension: An Overview." *Journal of Motor Behavior* 40 (5): 446–76. https://doi.org/10.3200/JMBR.40.5.446-476.

Zheng, Naiquan, Steve W. Barrentine, Glenn S. Fleisig, and James R. Andrews. 2008. "Kinematic Analysis of Swing in Pro and Amateur Golfers." *International Journal of Sports Medicine* 29 (6): 487–93. https://doi.org/10.1055/s-2008-1038732.